POLITECNICO
MILANO 1863

SCUOLA DI INGEGNERIA INDUSTRIALE
E DELL'INFORMAZIONE

Coupling of membrane reactor and electrolyzer for green hydrogen production: carbon neutral and carbon negative solutions

TESI DI LAUREA MAGISTRALE IN
ENERGY ENGINEERING
INGEGNERIA ENERGETICA

Author: **Francesco Lardaioli**

Student ID: 962919
Advisor: Prof. Marco Binotti
Co-advisors: Ing. Gioele Di Marcoberardino, Ing. Michele Ongis
Academic Year: 2021-2022

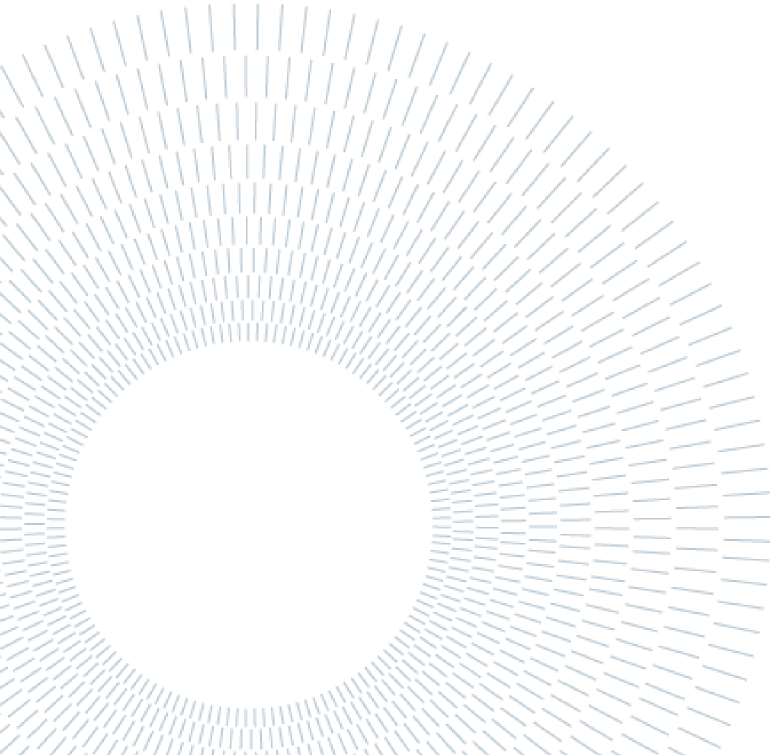

Abstract

Membrane reactors could support the tremendous growing low-carbon hydrogen production required in the future years. The core of this thesis is a green hydrogen producing plant from biogas through autothermal reforming (ATR) in fluidized bed membrane reactor. The first goal has been to quantify the performance improvement by switching oxidizing agent, from air to oxygen; secondly, to perform techno-economic analysis of different coupling solutions between ATR plant and PEM electrolyzer, to produce oxygen in situ. The results have been compared to air-fed benchmark case LCOH, to understand if an economic convenience of feeding oxygen, instead of air, is achieved.

A comparison between oxygen-fed case and air-fed case, at same operative conditions, but at different membranes number, have been performed. Results provide an increase in HRF from 68.29% to 71.39% and an increase of system efficiency from 60.25% to 65.42%.

Different coupling solutions of PEM-ATR plant have been assessed: on-grid, on-grid assisted by PV field, on-grid assisted by PV field and Li-ion battery system and off-grid. In off-grid case the plant is powered by PV field and by a battery pack, with an oxygen tank installed to decouple oxygen production and consumption. When oxygen is fed, from retentate flue gas, after water separation, a rich-CO_2 stream is obtained. Two scenarios have been detailed: the first considers selling CO_2 at ambient conditions (worthing 35 €/tonCO_2), while, in the second, CO_2 is injected into a pipeline (worthing 50 €/tonCO_2), obtaining a carbon-negative plant.

Lowest LCOHs have been achieved when PEM-ATR plant is powered by the grid and assisted by PV field, with values equal to 4.82 €/kgH_2 (if CO_2 is sold at ambient condition) and equal to 4.86 €/kgH_2 (carbon-negative plant case), that are lower or very close to air-feeding benchmark LCOH, which is equal to 4.83 €/kgH_2 when it is assisted by a PV field. Thus, the feasibility and the techno-economic convenience of oxygen-feeding case have been demonstrated. A final remark should be done for carbon-negative plant, which LCOH is slightly higher than air-feeding value, but the overall environmental benefits are increased.

Key-words: Green hydrogen production; Membrane reactor; Carbon-negative; Biogas.

Abstract in italiano

Produrre idrogeno sostenibile è un prerogativa per raggiungere la neutralità carbonica. I reattori a membrana possono supportare questa crescente richiesta. Il fulcro di questo progetto è un impianto per la produzione di idrogeno da biogas con autothermal reforming (ATR) in un reattore a membrane a letto fluido. Il primo scopo è quantificare il miglioramento delle prestazioni alimentando, come agente ossidante, ossigeno anziché aria. In seguito, sono state investigate varie soluzioni di accoppiamento fra l'impianto ATR ed un elettrolizzatore PEM per produrre O_2 in loco. I risultati tecnico-economici sono stati comparati ad un caso di riferimento alimentato con aria.

Il confronto aria-ossigeno è stato effettuato con le stesse condizioni operative, e si evidenzia: un aumento dell'HRF da 68.29% a 71.39%, un aumento dell'efficienza di sistema da 60.25% a 65.42% ed un minor numero di membrane adottate.

L'accoppiamento PEM-ATR è stato valutato: collegato alla rete, assistito da campo fotovoltaico, assistito da campo PV e da batterie ed in isola. In isola l'impianto PEM-ATR viene alimentato solo dal campo PV e dalle batterie; al fine di disaccoppiare la produzione ed il consumo di ossigeno è stato installato un serbatoio per accumulare O_2. Quando la combustione del retentato viene svolta con ossigeno si può ottenere un flusso di CO_2 dai gas combusti. Due scenari sono stati valutati: nel primo (caso A), la CO_2 viene venduta a condizioni ambiente (35 €/tonCO_2), nel secondo (caso B), viene immessa in pipeline (50 €/tonCO_2) ottenendo un impianto ad emissioni di CO_2 negative. Le migliori prestazioni economiche si ottengono quando l'impianto PEM-ATR è assistito dal solo campo PV, raggiungendo LCOH pari a 4.82 €/kgH_2 (caso A) e pari a 4.86 €/kgH_2 (caso B). Questi risultati sono prossimi al LCOH (4.83 €/kgH_2) nel caso in cui l'impianto ATR viene alimentato con aria e assistito da fotovoltaico. Si conclude che la fattibilità e la convenienza tecnico-economica di alimentare ossigeno anziché aria è stata dimostrata. L'impianto ad emissioni negative merita una nota di riguardo: ha LCOH prossimo a quello del caso con aria, ma genera benefici ambientali grazie al sequestro della CO_2.

Parole chiave: Produzione idrogeno verde; Reattori a membrana; Emissioni CO_2 negative; Biogas.

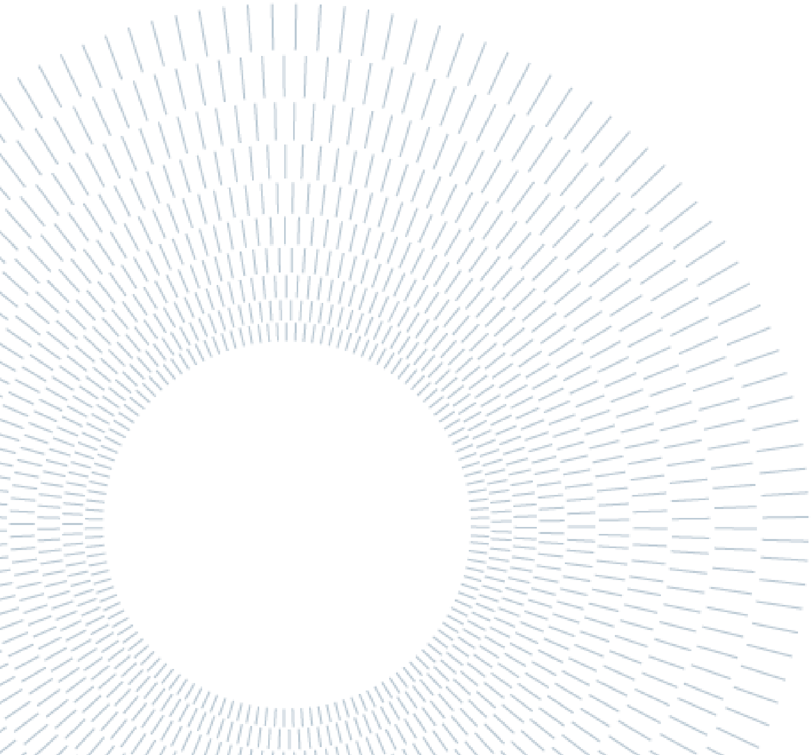

Contents

Abstract i
Abstract in italiano iii
Contents vii
1 Introduction 2
- 1.1. Hydrogen production overview 2
  - 1.1.1. Hydrogen demand 4
  - 1.1.2. Hydrogen supply 5
- 1.2. Biogas 6
  - 1.2.1. Biowaste-to-bioenergy 6
  - 1.2.2. Biogas production process 6
  - 1.2.3. Biogas utilization 8
- 1.3. Membrane reactor 8
  - 1.3.1. Current hydrogen production 8
  - 1.3.2. Hydrogen production through membranes reactor: features and classification 10
  - 1.3.3. Hydrogen production through membranes reactor: working principle 11
  - 1.3.4. Membrane reactors 13
- 1.4. Electrolyzer 14
  - 1.4.1. Electrolyzers: working principle and main features 15
  - 1.4.2. Alkaline electrolyzer 16
  - 1.4.3. Proton exchange membrane electrolyzer 17
  - 1.4.4. Solid oxide electrolyzer 18
  - 1.4.5. Anion exchange membrane electrolyzer 21
- 1.5. Solar photovoltaic technology 22
  - 1.5.1. Working principle 22
  - 1.5.2. Types of PV cell 23
  - 1.5.3. Current and future applications 25

2 Methodology 27
- 2.1. General process introduction 27
- 2.2. Comparison description between air and oxygen 28

2.2.1. Air configuration 31
2.2.2. Oxygen configuration 34
2.3. Oxygen production addition 37
3 Fluidized bed membrane reactor model 43
3.1. Introduction and general assumptions 43
3.2. Features and model 44
4 Electrolyzer 49
4.1. Electrolyzer Model: $i - V$ curve 49
4.1.1. Open circuit voltage (OCV) 50
4.1.2. Activation Losses 52
4.1.3. Ohmic Loss 53
4.1.4. Diffusion losses 54
4.1.5. Polarization Curve 55
4.1.6. Effect of temperature 56
4.1.7. Effect of pressure 57
4.1.8. Effect of Exchange Current Density 58
4.2. Hydrogen and Oxygen production 60
4.2.1. Fundamentals of Hydrogen and Oxygen production 60
4.2.2. Efficiency of H_2 production – Effect of Temperature 61
4.2.3. Efficiency of H_2 production – Effect of Pressure 62
4.2.4. Efficiency of H_2 production – Effect of cell number and cell area 62
4.3. PEM power – PEM production relations 63
4.3.1. Cell Voltage – PEM Power relation 64
4.3.2. Current density – Cell Voltage relation 65
4.3.3. Hydrogen and oxygen production 65
4.3.4. Minimum power relation 65
4.3.5. Electrolyzer auxiliaries consumption 66
4.3.6. System Efficiency 67
5 Photovoltaic field and auxiliaries 69
5.1. Solar radiation data 69
5.2. Electricity production estimation 70
5.2.1. Land utilization 71
5.3. Battery Energy Storage System 72
5.4. Oxygen tank 73
5.5. CO_2 removal and injection in pipeline 74
6 Economic analysis 77
6.1. General description 77

6.2. Photovoltaic field cost 79
6.3. PEM Electrolyzer cost 80
6.4. Battery Energy Storage System cost 81
6.5. O_2 Tank cost 81
6.6. ATR cost 82
6.6.1. Reactor Cost 82
6.6.2. Components cost 83
6.6.3. O&M Cost 84
6.7. CO_2 removal and utilization 85
7 Results 87
7.1. Oxygen-air comparison 88
7.1.1. Technical comparison results 88
7.1.2. Economic comparison results 96
7.2. PEM-ATR configuration 101
7.2.1. Configuration set-up 101
7.2.2. Results 104
7.3. PV-PEM-ATR configuration 111
7.3.1. Configuration set-up 111
7.3.2. Results 113
7.4. PV-BESS-PEM-ATR configuration 117
7.4.1. Configuration set-up 117
7.4.2. Results 119
7.5. Sensitivity analysis on electricity prices 121
7.5.1. Results 122
7.6. Off-grid configuration 124
7.6.1. Configuration set-up 124
7.6.2. Results 127
8 Conclusion 141
Bibliography 151
A Appendix A 161
A.1. Oxygen-air comparison 161
B Appendix B 165
B.1. Flow-chart 166
List of Figures 169
List of Tables 174
List of symbols 177

Acronyms 185

1 Introduction

Our times are characterized by decisive moments to tackle the ongoing climate change. Energy transition cannot be postponed further and, in order to achieve 2050 Net Zero Emission (NZE) scenario, great efforts must be taken by everyone. According to the Stated Policies Scenario (STEPS) computed by IEA (International Energy Agency), considering that emissions trend remains unvaried, the temperature will raise of 2.7°C by 2100 (with a 50% of probability) [1]. Energy system is one of the biggest contributor to GHGs emissions, thus a challenging and difficult transition has been involving it.

Hydrogen is considered one of the key player to achieve a decarbonized society in the following years. Recently, a growing attention gathered around it, potentially being a clean, reliable and sustainable energy vector [2]. In particular, it is addressed to be the missing link between renewable energy and hard-to-abate sector, powering those applications which are difficult to be decarbonized [3].

Among the different technologies addressed to green hydrogen production, which demand is going to continuously increase in the next years, fluidized bed membrane reactor did not reach full commercial maturity yet. For this purpose, due to the remarkably interesting development and performance of this technology, especially for small-scale production, further analysis are necessary to optimize possible configurations and to provide efficient coupling with other promising technologies.

For each technology involved, in this work, a brief overview has been presented in the following sections.

1.1. Hydrogen production overview

Hydrogen is already deeply used as feedstock in different industrial sectors, like refinery, chemical, iron and steel production. Its generation is strongly based on fossil fuels, indeed low carbon production, thus from electrolysis and from fossil fuels with carbon capture technologies, accounts for less than 1%[4]. Nowadays, hydrogen production is settled around 90 Mt, but a prevision of 200 Mt in 2030, is expected with low-carbon production that should grow up to 70%, according to NZE scenario [1].

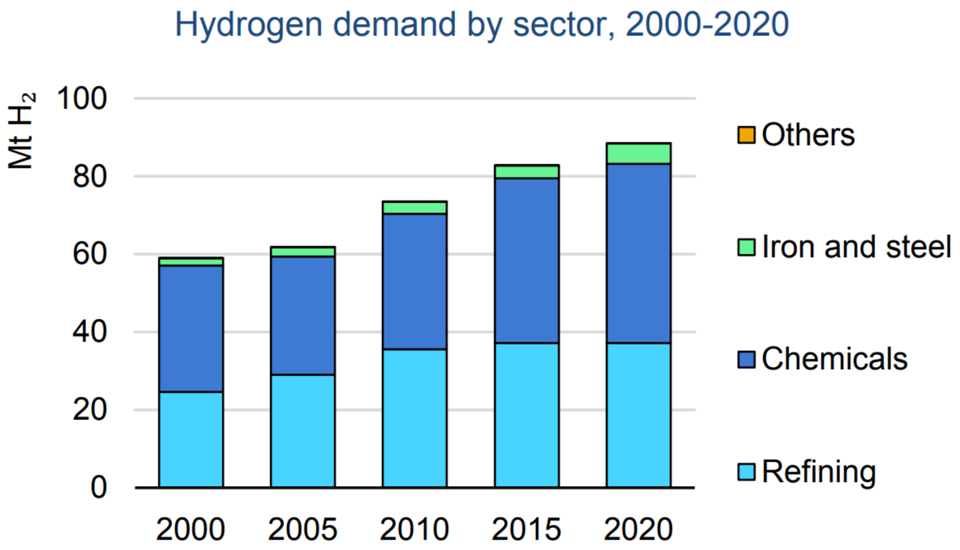

Figure 1.1 - Hydrogen demand by sector (2000-2020) [4].

Besides being used as industry feedstock, new sectors like transport, building and sustainable fuel production, will drive the previously mentioned production growth, as can be seen in Figure 1.2. Concerning power production sector, different applications could be implemented. One of the most promising is to use hydrogen as energy storage, converting excess renewable energy into hydrogen through electrolysis, and converting it back into power through fuel cell technology.

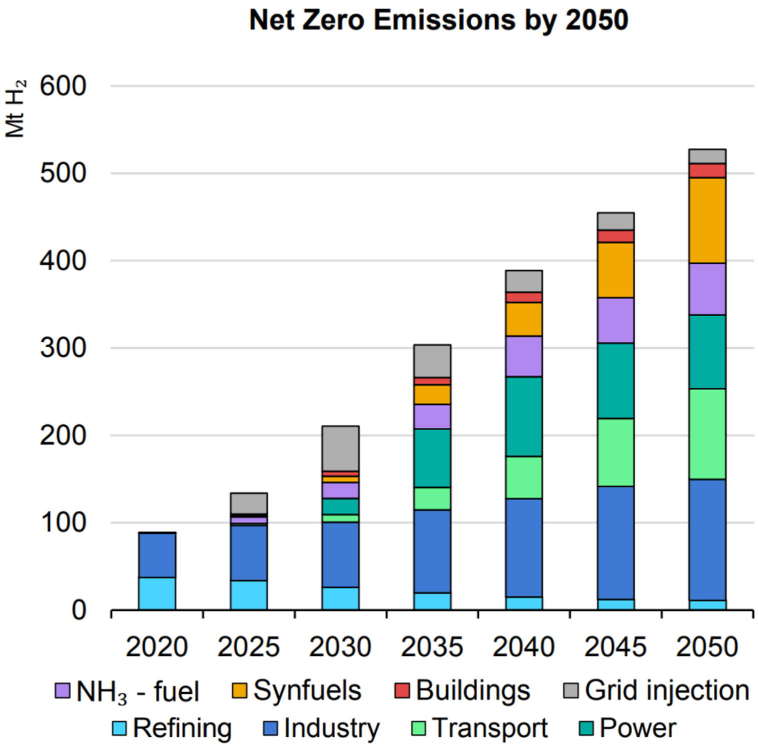

Figure 1.2 - Energy demand prevision according to NZE scenario (adapted from “Global Hydrogen Review”, 2021 [4]).

1.1.1. Hydrogen demand

Well-established hydrogen consuming sector, like refining and industry should replace the fossil fuel based hydrogen used, with eco-friendly hydrogen, but to favor this switch, a reduction of green hydrogen cost is required.

Refinery is the only field that foresees a reduction in the utilization, especially because hydrogen is used to treat oil and oil-derived compounds; therefore, with a suggested decrease in oil utilization, refinery hydrogen consumption will reduce too. Anyway, this expected cut of products needed in the market, is delaying a transformation towards green hydrogen utilization, even if the expertise in fuel production could be a possibility to drive syn-fuel development [4].

Industry field is the other large hydrogen consuming sector, accounting for 51 Mt in 2020. It is used in chemical production (mostly for producing ammonia and methanol), but also in iron and steel production as reducing agent.

More challenging is the adoption of hydrogen in the sectors where currently is not used; this requires the biggest transformation in hydrogen world.

Transport sector GHGs emission contribution is around 22% and it is dominated by oil-products, while hydrogen applications are currently negligible. An alternative solution to internal combustion engine is therefore necessary [5].

Regarding road transportation, two main possibility stood out: battery electric vehicles (BEVs) and fuel cell electric vehicles (FCEVs), which requires hydrogen and oxygen (from air) consumption to generate electricity. FCEVs are going to occupy heavy-duty, long range and high-utilization transport field, being a possible solution for train and buses too [5].

In transport world, the more difficult task is asked to maritime transport and aviation. Fuel cell ships are currently at demonstration stage, with the advantage that fuel cell can act as power provider too. Several EU projects, involving fuel cell for ships, ferries and tug boat are under development with a partnership aiming to test a 23 MW of hydrogen fuel cell powered ferry [4]. Other possibilities are involving ammonia and methanol fueled engines. Methanol is a near-term solution being compatible with existing engine, but ammonia engine implementation would offer a large decarbonization impact [4].

Aviation sector is going towards a deep transformation too. According to industry group ATAG (air transport action group) other solutions, besides fuel cells, should be implemented. Longer-haul flight could be addressed towards sustainable drop-in aviation fuels (hydrogen-based fuels and bio-fuels) utilization. While short and medium-haul ones, could adopt hydrogen combustion, but in this case NO_x treatment should be probably adopted [4].

Regarding building and heating sector, which accounts for around 12% of global CO_2 emissions, hydrogen use is currently being tested through injection in the existing natural gas grid, in order to reduce GHGs emissions [5]. An injection up to 20% could be achieved in an easy way in the current infrastructure, avoiding 145 Mt of CO_2 [5]. Other hydrogen applications in building field could involve hydrogen boilers, fuel cells to generate heat and power and hybrid heat pump (combination of boiler and heat pump) [4]. Another possible low carbon solution, which does not take into account hydrogen use, could be the installation of solar heating and/or heat pump.

1.1.2. Hydrogen supply

Fossil fuel based hydrogen is the dominant pathway for the current hydrogen production, accounting for 99% of total production, causing around 900 Mt of CO_2 emission[4]. The main source is natural gas, which is the feedstock of steam reforming, through which 59% of the total hydrogen produced is generated in 2020 [4].

Low-carbon hydrogen production should have a steep boost in order to meet 2050 NZE. According to this scenario, 60% of hydrogen should be produced by water electrolysis, corresponding to 3600 GW of electrolyzers capacity, while the capture rate of CCUS should reach 1.5 $GtCO_2$/year [4].

The current hydrogen market price is set by steam reforming production, in which the disclaimer is mainly the natural gas price, which is fluctuating according to the geographical area. This variation of natural gas price affects the hydrogen price, which is settled between 0.5 USD/kgH_2 and 1.70 USD/kgH_2 [4]. Green hydrogen from electrolysis price is set by the cost of the electrolyzer technology which has not already reached its full degree of commercial maturity and by renewable electricity cost. The market price for green hydrogen with this production chain is between 3 USD/kgH_2 and 8 USD/kgH_2 according to "Global Hydrogen Review" in 2021 [4], although price up to 10 USD/kgH_2 are reported in [3].

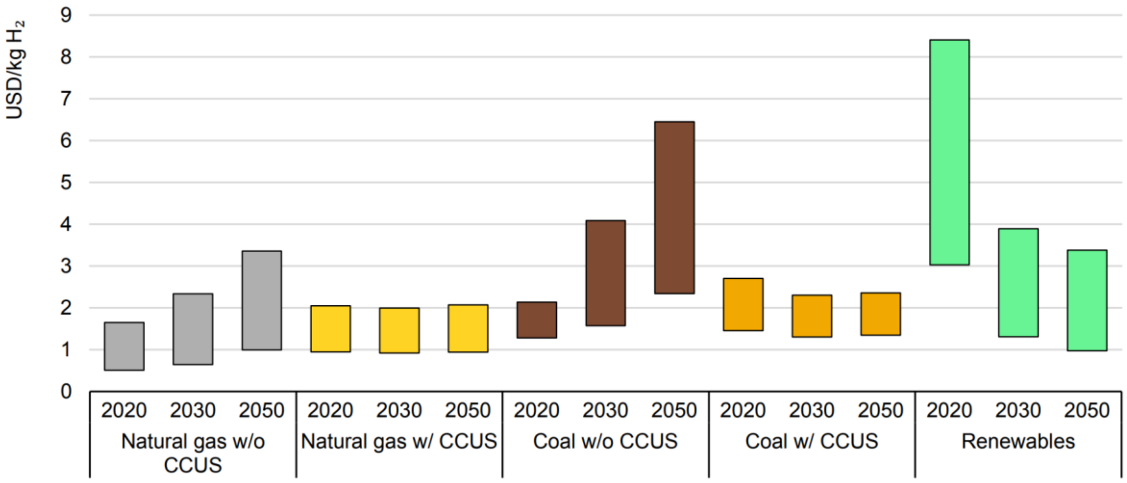

Figure 1.3 – LCOH by technology in 2020, and in the NZE scenario, 2030 and 2050 [4].

1.2. Biogas

1.2.1. Biowaste-to-bioenergy

The continuously growing energy demand, coupled with decarbonization necessity, requires the implementation of green solutions to satisfy the future society requirements.

Furthermore, in this context of impulsive consumption, a problem of waste management arises. The conventional treatments of waste, like incineration and landfill, are not compliant with a reduction of greenhouse gases policy.

These two challenges could be partially managed, in a scientific way, adopting biowaste-to-bioenergy (BtB) technologies. This method foresees a biowaste, like forest and agricultural residues, animal wastes and municipal wastes, that is going under conversion obtaining biogas, biodiesel, bioalcohol and others products, depending on the conversion process (anaerobic digestion, transesterification…) [6].

1.2.2. Biogas production process

Biogas is a gas mixture which contains mainly methane and carbon dioxide, but traces of water and other gas like N_2,O_2 and CO are typically present; however, its composition depends on the feedstock and on the production process. Typically a value of methane between 45-75% is achieved, while the remaining fraction is mostly CO_2. As a consequence, its LHV is variable, ranging from 16 MJ/m^3 to 28 MJ/m^3 [7].

Different feedstocks can be used to produce biogas, and this is a great advantage, opening to biogas production practically everywhere. The most common feedstocks are: crop residues, animal manure, organic fraction of municipal solid waste (MSW) and wastewater sludge [7].

Biogas is commonly produced through anaerobic digestion or landfilling. Landfilling is the oldest method of waste disposal, which consists in a burial of the garbage. Natural anaerobic decomposition happens thanks to microbes, producing methane and carbon dioxide. If the produced gases are collected through a gas recovery system, biogas has an energetic and an economic value, otherwise, they are going to be dispersed in atmosphere, provoking GHGs emissions, especially methane, which has 20 times the impact of CO_2 in global warming [6].

Anaerobic digestion (AD) is a stepwise process, which happens in a biodigester, whose conditions are controlled in order to manage pH and temperature, which are fundamental parameters to ensure the conversion performed by microorganisms.

In a biodigester four steps are necessary to perform waste conversion into biogas, and they are shown in Figure 1.4:

1. Hydrolysis: the feedstock is composed by different complex polymeric materials that is going to be converted in simpler molecules (sugars, amino acids and fatty acids) thanks to hydrolases produced by microbes.
2. Acidogenesis: the simpler molecules generated by hydrolysis are fermented by acidogenic bacteria into various volatile fatty acids (VFAs) and gaseous components (H_2 and CO_2).
3. Acetogenesis: the components produced are converted into acetic acids through acetogenesis bacteria.
4. Methanogenesis: in this last step the intermediate products are converted in methane, carbon dioxide and water.

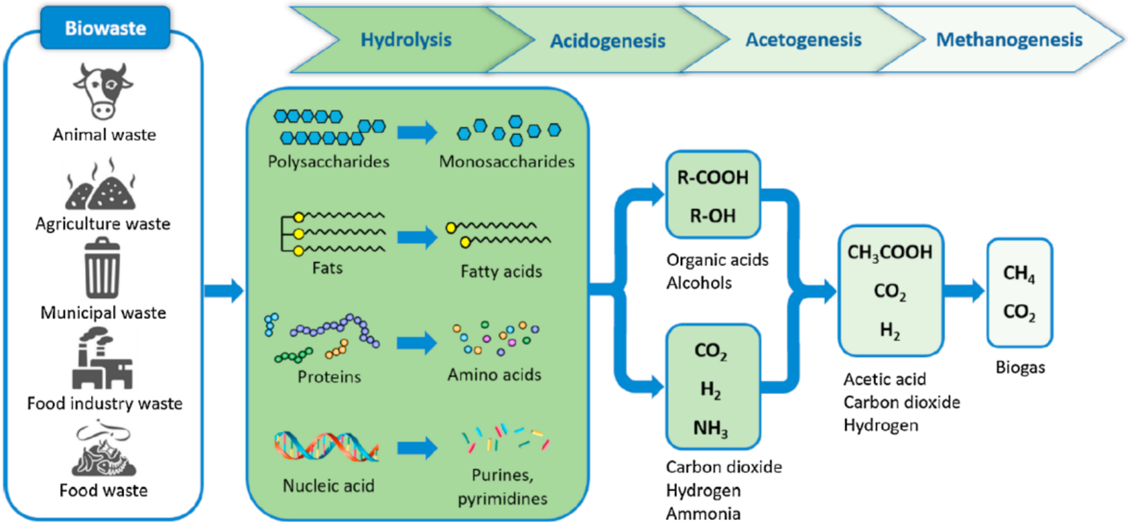
Biowaste
Animal waste
Agriculture waste
Municipal waste
Food industry waste
Food waste
Hydrolysis
Acidogenesis
Acetogenesis
Methanogenesis
Polysaccharides
Monosaccharides
Fats
Fatty acids
Proteins
Amino acids
Nucleic acid
Purines, pyrimidines
R-COOH
R-OH
Organic acids
Alcohols
CO2
H2
NH3
Carbon dioxide
Hydrogen
Ammonia
CH3COOH
CO2
H2
Acetic acid
Carbon dioxide
Hydrogen
CH4
CO2
Biogas

Figure 1.4 - Anaerobic digestion process [6].

The final biogas composition is affected by different factors, but above all, by the feedstock composition, the pH and the temperature inside the digester.

In particular, the conversion can be maintained at different operating temperature range, in which different microorganisms will be active and will perform the degradation of biomass into biogas: psychrophilic condition (12-16°C) are typical for landfilling production, while anaerobic digestion is typically performed in mesophilic condition (35-37 °C) or in thermophilic condition (55-60°C). High temperature operation allows to have the advantage of thermal destruction of pathogenic bacteria, which involves residence time, that it is going to be reduced, but it reduces the process stability and it requires large amount of heat too [8].

Regarding pH condition the bacteria performing the different steps foresee different optimal range, like 6.5-7.2 for methanogenesis bacteria, or 4.0-8.5 the fermentative ones, so typically it is a value in this range.

1.2.3. Biogas utilization

Biogas is considered a CO_2-neutral fuel because, during its life, it absorbs the same quantity of carbon dioxide that is released during its combustion. Whether a carbon capture technology is implemented, the application is then carbon-negative.

Currently, biogas is adopted mainly as fuel in CHP plant, for power and heat cogeneration, but a small percentage is addressed to upgrading steps, producing biomethane. In biogas upgrading plant the CO_2 contained is removed, saving CH_4, thus obtaining a methane rich stream, which is carbon-neutral, or even carbon-negative if CCUS is present [9].

Recently, a growing interest has gathered around the so called second-generation upgrading technology. In this case, the carbon dioxide removed from biogas is not a waste, but it is seen as by-product which is used to produce carbon-containing energy carriers, being then a carbon source. This mentioned upgrading could be performed through Fischer-Tropsch catalytic synthesis, which can convert CO_2 and renewable hydrogen into a sustainable fuel.

1.3. Membrane reactor

1.3.1. Current hydrogen production

Hydrogen plays a fundamental role in the ongoing energy transition, being addressed as one of the possible solutions to solve several problems in the current decarbonizing scenario, especially in hard-to-abate sectors. Nevertheless, almost the whole hydrogen production comes from fossil fuels, in particular adopting natural gas as feed of reforming process.

Steam Reforming process (SR) is an endothermic reaction, performed at 800-850°C, which produces a stream which contains around 50% of hydrogen (on dry-basis) and around 40-45% of carbon monoxide according to reaction (R.1.1)[10].

$$CH_4 + H_2O \leftrightarrow 3H_2 + CO \tag{R.1.1}$$

The flow from reforming unit is sent to a purification chain, which upgrades its hydrogen purity through different processes, performed in several units. The first treatment is a high-temperature (350-400°C) Water Gas Shift (HT-WGS), followed by low-temperature (220-300°C) Water Gas Shift (LT-WGS), which converts carbon monoxide. Water gas shift is a slightly exothermic reaction and it is shown in reaction (R.1.2).

$$CO + H_2O \leftrightarrow CO_2 + H_2 \tag{R.1.2}$$

A further upgrading is realized in Pressure Swing Adsorption (PSA) stage, in order to separate hydrogen from other gases, and whether the user requires a very high-purity stream (like fuel cells) an additional purification step could be involved.

Since SR reaction requires energy to be realized, autothermal reforming becomes an option: an oxidizing agent, typically air, is fed to ignite methane oxidation (R.1.3); indeed, a small amount of methane fed is going to be burned providing the required energy to activate SR.

$$CH_4 + 2O_2 \rightarrow CO_2 + 2H_2O \qquad \text{(R.1.3)}$$

As previously mentioned, traditional steam reforming is the most spread technology for hydrogen production, even though several limits can be pointed out [11]:

- Reversible reactions, like SR, are limited by thermodynamic equilibrium, meaning that methane conversion into hydrogen cannot be pushed over this limit.
- Heat transfer management is a relevant matter in steam reforming, indeed, being the reaction performed at high temperature, the tubes and the reactor have to cope with high temperature streams.
- Deactivated catalyst due to carbon formation (enhanced at high temperature) affects process efficiency.
- CO_2 and NO_X are extensively produced during the process.

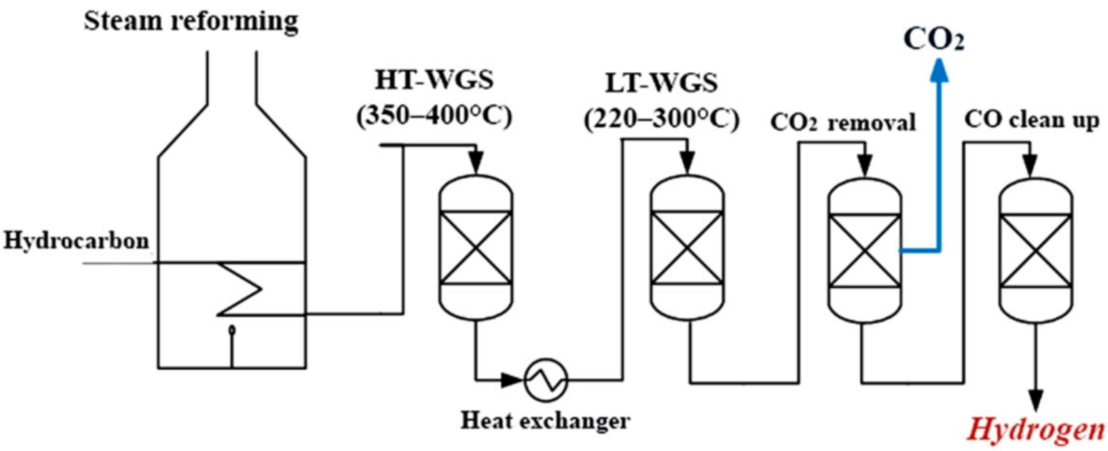

Figure 1.5 - Hydrogen production through SR ("Membrane Reactor for Hydrogen Production", 2017 [10]).

Membranes reactor is a technology belonging to Process Intensification Strategy (PIS), because it allows to perform hydrogen reaction and separation in the same unit. Besides, ensuring the reduction of required devices, thus presumably the reduction of capital and material costs too, another important advantage of adopting a membranes reactor is the achievement of the same performance of traditional reactor at milder condition (circumventing equilibrium limited conversion of conventional process and inhibiting unwanted reactions). Furthermore, performing the reactions at lower temperature enables new heating strategies.

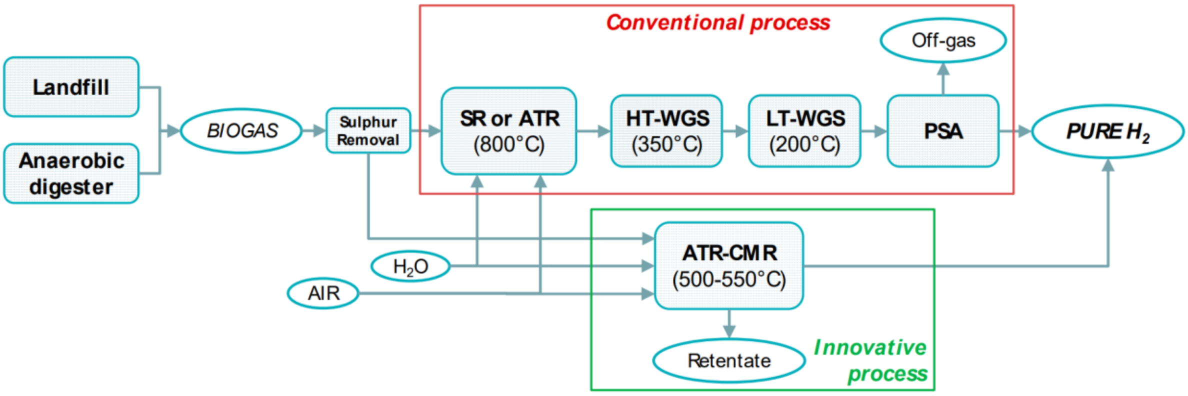

Figure 1.6 - Comparison of traditional reforming process and membrane reactor-assisted process, taken from [12].

In order to understand why membranes reactor are more performant from a technical point of view, the main characteristics and the working principle of membranes reactor are furtherly presented.

1.3.2. Hydrogen production through membranes reactor: features and classification

Membranes are barriers that should allow the flux of the chosen component only, in this case hydrogen. Therefore, it is evident that membranes should have been manufactured in order to provide a high selectivity towards hydrogen, allowing only this component to pass through and thus collecting a pure H_2 stream in the permeate side, while the other components of the reactions should be confined in the retentate side. Another evidence is that membranes should allow high flux of hydrogen, meanwhile being mechanically and chemically stable and hopefully having a low cost.

In F. Gallucci et al. [13] membranes for hydrogen separation are classified, based on material used, into different categories: polymeric membranes, porous membranes, dense metal membranes and proton conducting membranes. Dense metal and dense ceramic ones are considered the most suitable membranes due to their high H_2 selectivity; furthermore, Pd-alloys are used, because they allow to decrease embrittlement and poisoning of H_2S and CO phenomena [14].

Membranes can be also classified based on their geometry: the most common used are planar and tubular geometry, widely adopted respectively in laboratory and industrial applications, indeed tubular geometry offer higher surface area-to-volume ratio with respect to planar ones. However, other geometries like plate and frame and spiral wound are under development [13].

Another classification of membranes can be done depending on the membrane whether it is supported or unsupported [13]. Unsupported membranes have mechanical stability problems, which force the membrane to be thick, but this typically increases the overall cost and penalizes hydrogen permeance. Supported membranes have not mechanical stability problems because it is ensured by a porous support (ceramic or metallic). The hydrogen permeance is higher than unsupported ones, thus the membrane area required is lower, as well as the membrane cost. Anyway, the porous support manufacturing cost is not negligible, particularly with very thin film membranes.

1.3.3. Hydrogen production through membranes reactor: working principle

Dense inorganic membranes are expensive, but the permeation mechanism, which involves solution-diffusion, is more efficient than others, like molecular sieving [13].

Solution-diffusion permeation mechanism has been extensively studied [13], [15]. The first step is the (I) diffusion of hydrogen molecules towards the membrane surface on the feed side; once reached the metal surface of the membrane (II) dissociation in atomic hydrogen and consequent adsorption on the surface. After the adsorption phase, the atomic hydrogen is going under (III) dissolution through the bulk metal, and then it is going to (IV) diffuse towards permeate side. Once the metal surface on low pressure side is reached, the (V) association of atomic hydrogen and consequently the formation of H_2 molecule is realized. Afterwards, the molecular hydrogen leaves the metal surface through (VI) desorption, followed by (VII) diffusion of H_2 through the permeate side.

One of the main advantage of membranes reactor for hydrogen production is the possibility to circumvent thermodynamic equilibrium, by applying the so called "shift effect", performed through product removal.

In reversible reactions (R.1.4) the conversion of reactants is limited by equilibrium condition, expressed through equilibrium constant K, computed in Equation (1.5). In this particular state, the direct reaction rate and the inverse reaction rate are equal, with the overall reaction rate which is zero ($r = \vec{r} - \overleftarrow{r} = 0$), providing no changes in molar fraction, temperature or pressure at equilibrium.

$$aA + bB \leftrightarrow cC + dD \tag{R.1.4}$$

$$K = \frac{[C]^c[D]^d}{[A]^a[B]^b} \tag{1.5}$$

Equilibrium constant has a specific value which depends on the conditions at which the reaction is performed, meaning that if an endothermic reaction is performed at high temperature the conversion of reactants will be higher (higher equilibrium constant) than the case if it would be performed at low temperature. K is computed through Van't Hoff Equation, reported in Equation (1.6) [16], with ΔH^0 which is the standard enthalpy change for the reaction.

$$\frac{dlnK}{dT} = \frac{\Delta H^0}{RT^2} \tag{1.6}$$

Once the equilibrium condition is reached, the reactants conversion into products is stopped. Nevertheless, this conversion value is related to that precise conditions of temperature, pressure and feed concentration, meaning that if products are removed the reaction is not anymore in equilibrium and the conversion of the feed is increased ($r = \vec{r} - \overleftarrow{r} \neq 0$).

Membranes reactor foresees the possibility of product removing, thus the thermodynamic equilibrium limit on the conversion is circumvented.

In membranes reactors for hydrogen production, the equilibrium conditions are avoided adopting a sweep gas or a vacuum pump, which modifies the partial pressure of hydrogen in permeate side. Indeed, the driving force of hydrogen permeation and diffusion is related to the partial pressure difference, as shown in Equation (1.7), which rules the flux of hydrogen permeating flux $J_{H_2}^{Permeating}$ through Pd-based membranes [16].

$$J_{H_2}^{Permeating} = \frac{P_{H_2}}{t}\left(p_{H_2 retentate}^{n} - p_{H_2 permeate}^{n}\right) \tag{1.7}$$

Where t is the membrane thickness, $p_{H_2 retentate}$and $p_{H_2 permeate}$ are the hydrogen partial pressure respectively on retentate and on permeate side, while $n = [0.5; 1]$ is the hydrogen partial pressure exponent, which depends on the rate limiting step. If hydrogen diffusion through the lattice (step IV of solution-diffusion mechanism) is the rate limiting step, n is equal to 0.5, and Equation (1.7) becomes the Sieverts-Fick law. Instead, if the surface effects assume a relevant role in permeation mechanism, n is increasing, with Knudsen diffusion mechanism which dominates hydrogen transport, reaching 1 if surface-reactions are the rate limiting step.

Hydrogen membrane permeability P_{H_2} is computed thanks an Arrhenius like equation:

$$P_{H_2} = P_{H_2}^{0} \cdot e^{\frac{-E_a}{RT}} \tag{1.8}$$

With R, which is the universal gas constant, T is the temperature, E_a is the apparent activation energy and $P_{H_2}^{0}$ is pre-exponential factor.

1.3.4. Membrane reactors

Currently, the most important membrane reactors are nickel-based catalyst bed ones, distinguished in fixed bed reactor or fluidized bed reactor, depending on the gas velocity. If gas velocity reaches the minimum fluidization velocity (u_{mf}), fluidization regime is achieved, followed by the involvement of bubbling regime for greater superficial velocity $\left(\frac{u_0}{u_{mf}} < 10\right)$; typically, bubbling regime is avoided in standard operation, because it triggers large instabilities and vigorous mixing of solid [17]. Instead, low superficial velocity is typical of fixed bed regime (Figure 1.7), which has several drawbacks, like bed-to-wall mass transport limitation (the catalytic bed is crossed by the gas like if it would be a porous media), and increasing pressure drop with the velocity. Other matters to be pointed out are: the heat management, which has several degrees of complexity, and the temperature profiles, which are difficult to be avoided, with consequent loss in efficiency and thermal stability issues [13].

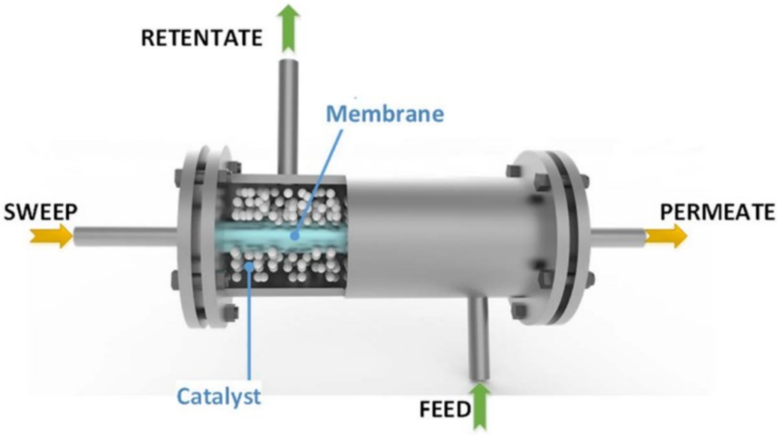

Figure 1.7 - Packed bed MR ("Membrane Reactor for Hydrogen Production", 2017 [10]).

Fluidized bed MR (Figure 1.8) are capturing attention because: internal mass and heat transfer limitations are practically null, indeed, due to negligible pressure drop, smaller particles are used; heat and temperature profiles are easier to be managed, since higher transfer rate are developed; bed-to-wall mass transfer limitations are reduced [18]. The main drawback of fluidized bed reactor is the constraint of maintaining the minimum fluidization velocity, which means that a minimum gas flow rate should be always ensured.

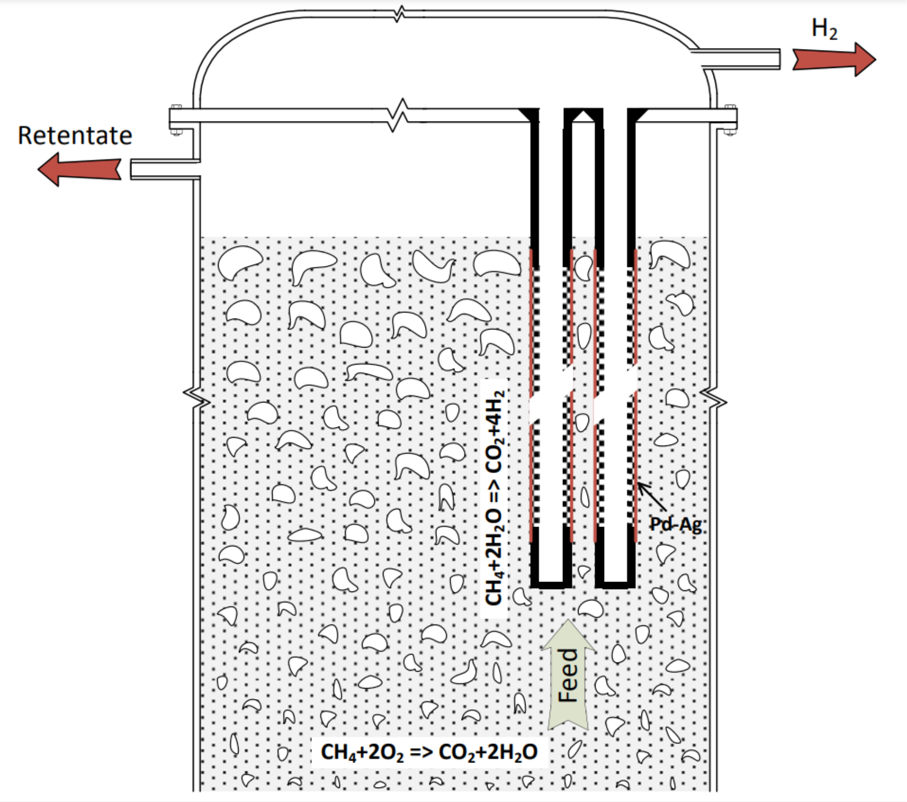

Figure 1.8 - Fluidized bed MR scheme [18].

1.4. Electrolyzer

Water electrolysis is a fundamental process to keep up with the 2050 carbon neutral goal, indeed, if an electrolyzer is fed with non-fossil electricity, it allows to harvest high-purity, eco-friendly hydrogen, with oxygen as by-product [19].

Jan Rudolph Deiman and Adriaan Paets van Troostwijk realized the first water electrolysis experiment in 1789, and, after a slow growth, several hundreds of industrial applications have been implemented by 1902 [20].

A water electrolysis cell is an assembled technology which performs water electrolysis reaction, consisting in water splitting in hydrogen and oxygen.

$$H_2O \rightarrow H_2 + \frac{1}{2}O_2 \tag{R.1.9}$$

It is composed by three main components, that are two electrodes (anode and cathode) and an electrolyte, in order to separate them and to conduct the ions generated by the reactions, which are realized onto the electrodes, embedded with catalyst to enhance the kinetics of the two reactions.

Depending on electrolyte solution composition, it is possible to identify two families of electrolytes that could be used: alkaline and acidic electrolyte. According to electrolyte pH, two reactions pathways could be performed for Hydrogen Evolution Reaction (HER) and Oxygen Evolution Reaction (OER), and they are reported in Table 1.1. Both in alkaline and in Proton Exchange Membrane (PEM) electrolyzer hydrogen production happens through HER at the cathode, while OER is performed at the anode. The electrodes are then connected by an external electrical circuit, through which electrons, generated by OER, could flow.

	Acidic Electrolyte	Alkaline electrolyte
HER	$4H^+ + 4e^- \leftrightarrow 2H_2(g)$	$4H_2O\ (l) + 4e^- \leftrightarrow 2H_2(g) + 4OH^-$
OER	$2H_2O\ (l) \leftrightarrow 4H^+ + O_2(g) + 4e^-$	$4OH^- \leftrightarrow O_2(g) + 2H_2O\ (l) + 4e^-$

Table 1.1 - Half-reactions in different electrolyte type.

An electrolyzer device contains a large number of cells, which are series-connected forming a stack. One cell is separated by the adjacent one by the bipolar plate, which connects the negative electrode of a cell with the positive electrons of the other one; at the extremes of the stack an end plate is placed.

1.4.1. Electrolyzers: working principle and main features

Water electrolysis is an endothermic and non-spontaneous reaction (R.1.9) at standard conditions ($\Delta G_R^0 = 237.2 \frac{kJ}{mol}$ [21]), and to produce hydrogen and oxygen, through hydrogen evolution reaction and oxygen evolution reaction respectively, a DC source of electricity is required to provide the energy to overcome the reversible cell potential and the irreversible losses which are generated during functioning [19].

The reversible cell voltage, under standard and ideal conditions, E_{rev}^0, is the difference between anode and cathode potential and it corresponds to the minimum electrical work to enable water splitting (if the required thermal energy is available [19]).

$$H_2O_{(l)} + electricity\left(237.2\frac{kJ}{mol}\right) + heat\left(48.6\frac{kJ}{mol}\right) \rightarrow H_2 + \frac{1}{2}O_2 \qquad (1.10)$$

$$E_{rev}^0 = \frac{\Delta G_R^0}{n_{el}F} = 1.229\ V \qquad (1.11)$$

During the stack functioning, inside the cell, irreversible losses happen and a voltage greater than the reversible cell potential must be provided.

Once that favourable conditions are presents, water electrolysis half-reactions start on the surface of the two electrodes, the ions are transported through the electrolyte and the separation of the product gases starts.

The electrolyte, and as consequence the chemical charges transported, are key features to discriminate the four type of electrolyzer: alkaline, proton exchange membrane, anion exchange membrane and solid oxide electrolyzer. Indeed, as previously mentioned, different reactions pathways for (HER) and (OER), with different ions transferred, are found, depending on the pH of the electrolyte, as explicated in Table 1.1. In acidic environment, H^+ is the electrochemical charge carrier, transferred from the anode to the cathode, while in alkaline electrolyte, the electrochemical charge carrier is the hydroxyl group (OH^-), which is moving from the cathode to the anode [22].

The different environment and the various possible operating conditions characterize the different types of electrolyzers, with a brief deepening for the most relevant technology in the next paragraphs.

1.4.2. Alkaline electrolyzer

Alkaline electrolyzer devices are the most mature and most industrial diffused technology between water electrolysis ones.

The two electrodes are drowned in a liquid alkaline electrolyte, composed of 20-30% by potassium hydroxide (KOH), which is going to transport OH^-. Water is fed at the cathode, where reduction happens generating OH^- ions that will be transported towards the anode, starting oxidation reaction.

$$Anode: 4OH^- \leftrightarrow 2H_2O + O_2 + 4e^- \tag{R.1.12}$$

$$Cathode: 4H_2O + 4e^- \leftrightarrow 2H_2 + 4OH^- \tag{R.1.13}$$

Between the two electrodes a porous inorganic diaphragm (permeable to hydroxide ions and water molecules) is inserted, with the goal of reducing gas crossover, ensuring the safety of the system and good value of efficiency [21]. Typically thick diaphragm is installed, generating high resistance, thus reducing the efficiency of the device. Nevertheless oxygen crossover towards cathode chamber is not completely avoided, and when this happens, the gas is catalysed back to water, reducing the efficiency.

Another important aspect to point out, regarding gas crossover, is the possibility of reaching lower explosion limit of hydrogen concentration; this situation has high probability of happening when oxygen production rate decreases, meaning at partial load. In order to avoid unsafe operation, a minimum load, around 40%, is respected for alkaline electrolyzer [21].

Besides the low load range of alkaline electrolyzers, which penalizes the coupling with intermitting energy sources, like most of renewable ones, other two drawbacks can be remarked, and they are related to the presence of liquid electrolyte. Indeed, alkaline electrolyzer maximum current density value is low with respect to the other technologies, due to high ohmic loss at high current density. Furthermore, liquid electrolyte makes alkaline electrolyzer unsuitable to work at high pressure, in order to ensure a safe functioning.

Despite these limitations, alkaline electrolyzers are spread in industrial applications due to the low cost of material, indeed, working with non-corrosive material avoids adopting expensive element inside the electrolysis cell.

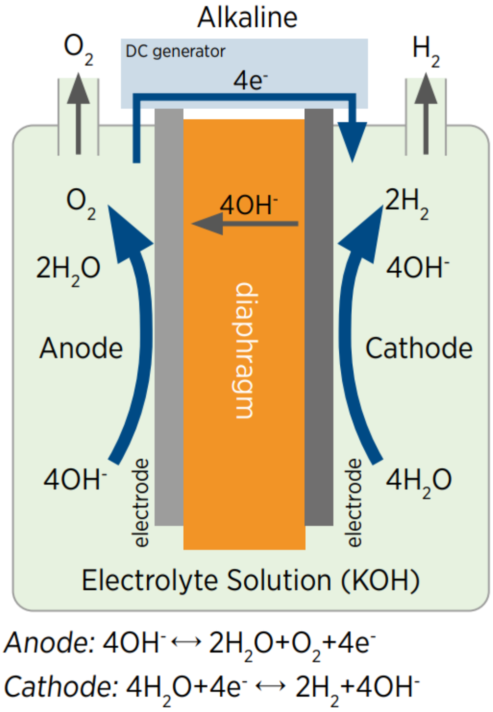
Alkaline
O_2
DC generator
$4e^-$
H_2
O_2
$4OH^-$
$2H_2$
$2H_2O$
$4OH^-$
Anode
diaphragm
Cathode
$4OH^-$
electrode
electrode
$4H_2O$
Electrolyte Solution (KOH)
Anode: $4OH^- \leftrightarrow 2H_2O+O_2+4e^-$
Cathode: $4H_2O+4e^- \leftrightarrow 2H_2+4OH^-$

Figure 1.9 - Alkaline water electrolysis cell [23].

1.4.3. Proton exchange membrane electrolyzer

Researchers, deepening alkaline electrolyzer drawbacks, started to imagine a solid polymer electrolyte, in order to circumvent limitations on pressure and on partial load. General Electric developed in 1960 the first PEM electrolyzer, where the acronym could refer to Proton Exchange Membrane or to Polymer Electrolyte Membrane too [21].

In this device water is fed at the anode where oxidation is developing, producing ions H^+ which are going to be reduced at the cathode, with the following reactions path:

$$Anode: 2H_2O \leftrightarrow O_2 + 4H^+ + 4e^- \tag{R.1.14}$$

$$Cathode: 4H^+ + 4e^- \leftrightarrow 2H_2 \tag{R.1.15}$$

Adopting a solid polymer as membrane provides several remarkable benefits. First of all, the gas crossover rate is strongly reduced, since the proton transport has a fast answer to the power input, thus the operating load range is remarkably expanded, with minimum partial load reported value by Carmo et al. [21] equal to 10%, but value equals to 0% are declared by other work [20]. Another advantage, due to low thickness of the membrane, thus low ohmic loss at high current density are detected, is the maximum current density, which increases up to 2 A/cm^2 [21] or even 3 A/cm^2 [20].

A strong interest has been grown around electrochemical compression, which can be performed in an easier way in PEM electrolyzer with respect to alkaline, with declared maximum operating pressure up to 350 bar [20], [21].

Nevertheless, the cost of this technology is quite high, because the electrolyzer works in a corrosive acidic regime and it has to withstand to high operating cell voltage (higher than 2 V) at high current density. These necessities requires that expensive and scarce materials (Platinum, Iridium, Ruthenium…) should be used, increasing the cost up to 700-1400 USD/kW with respect to 500-1000 USD/kW for alkaline ones [23].

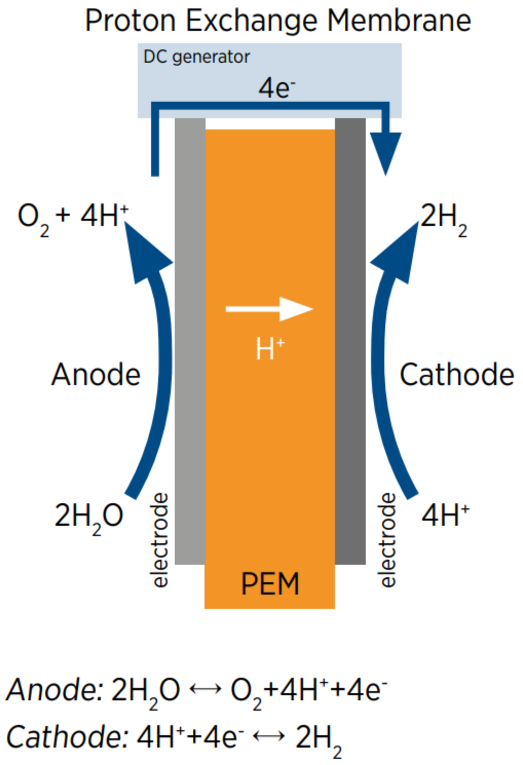

Figure 1.10 – Proton Exchange Membrane (PEM) water electrolysis cell [23].

1.4.4. Solid oxide electrolyzer

Alkaline and PEM water electrolyzer are nearly ambient temperature operating device, with cell temperature between 40-90°C for alkaline and between 20-100°C for PEM ones [21].

Solid Oxide Electrolyzer (SOEC) perform water splitting at high temperature, typically between 800-1000°C, exploiting the thermodynamic analysis of water splitting reaction, which requires less electrical input at high temperature, indeed Gibbs free energy change of the reaction is reducing at increasing temperature, providing a reduction in electrical consumption [20], as displayed in Figure 1.11.

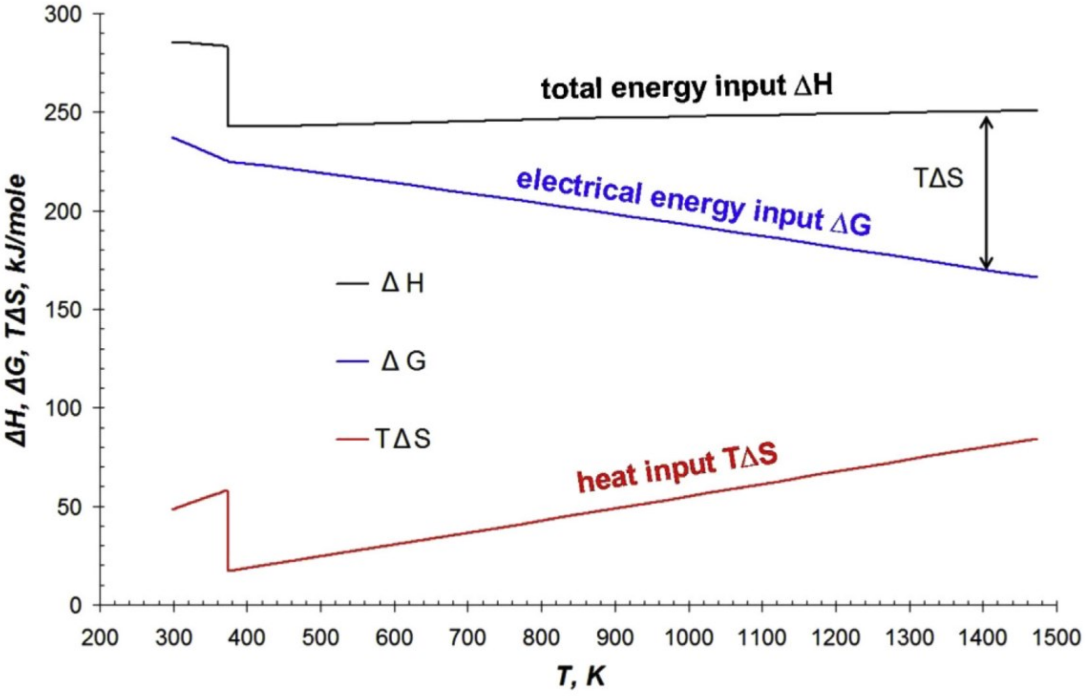

Figure 1.11 – Thermodynamic parameters change with temperature [20].

Therefore, working at high temperature provokes a reduction on electricity consumption and an improvement on mass transport limitation, allowing to reach very high efficiency, near to 100% [20], [21].

The reactions of reduction and oxidation are based on oxygen ion transport from cathode to anode, executing the following reaction:

$$Anode: 2O^{2-} \leftrightarrow O_2 + 4e^- \tag{R.1.16}$$

$$Cathode: 2H_2O + 4e^- \leftrightarrow 2H_2 + 2O^{2-} \tag{R.1.17}$$

The membrane is built with ceramic material, in order to be an oxygen-ion-conductor; anode and cathode are placed on the two side of the ceramic membrane, with separator equipped by flow fields that helps water vapour circulation and gas collection.

Currently SOEC technology has several important limits, indeed it is the less commercial and more recent technology compared to PEM and alkaline electrolyzer.

Working at this range of temperature gives rise to different problems regarding heat management and degradation of the cell components like: the slow turn-on and turn-off procedure, the loss of oxygen-ion conductivity, the corrosion provoked by the presence of high temperature oxygen and the inability to operate in pressurized condition (manufacturing problems of cell gasket realization at high temperature) [20].

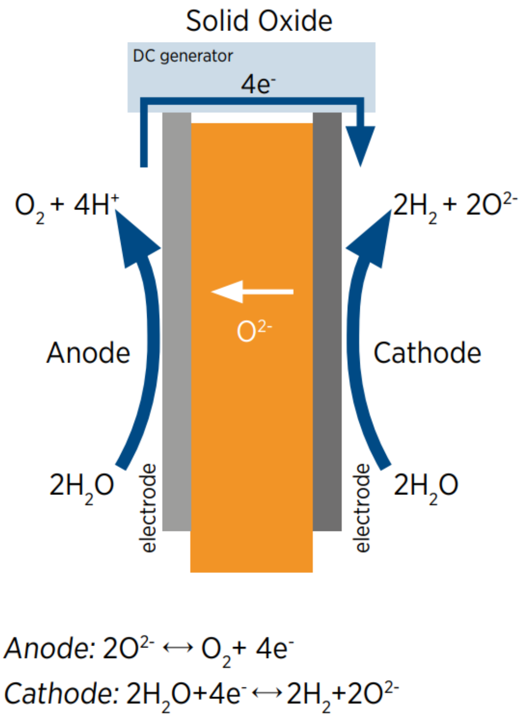
Solid Oxide
DC generator
4e-
O2 + 4H+
2H2 + 2O2-
O2-
Anode
Cathode
2H2O
2H2O
electrode
electrode
Anode: 2O2- ↔ O2+ 4e-
Cathode: 2H2O+4e- ↔ 2H2+2O2-

Figure 1.12 - Solid Oxide water electrolysis cell [23].

Alkaline, PEM and SOEC electrolyzer are the more mature technologies and typical values of performance are summarized in Table 1.2, highlighting the limitations and the benefits of each one.

	Alkaline	PEM	SOEC	Ref.
P-range [bar]	1-200	1-350	1-5	[20]
Current density [A/cm^2]	0.2-0.5	0-3	0-2	[20]
Efficiency [%] (at $i \frac{A}{cm^2}/V_{cell}/T\ °C$)	60-80% 0.2-0.25/2/80	80% 1.0/1.8/65	100% 3.6/1.48/950	[20]
Capacity [Nm^3/h]	1-500	1-250	1	[20]
Durability [hours]	100000	10000–50000	500-2000	[20]
System electrical efficiency [kWh/kgH$_2$]	50-78	50-83	40-50	[23]
System Capital Cost (>1 MW) [USD/kW]	500-1000	700-1400	>2000	[23]

Table 1.2 - Comparison of the different electrolyzer technologies.

1.4.5. Anion exchange membrane electrolyzer

Anion Exchange Membrane (AEM) electrolyzer technology is still at an early development stage. The idea behind AEM is to merge the advantages of alkaline (low cost due to alkaline environment) and of PEM (high performance).

Water is fed at the cathode side where reduction is executed, generating hydrogen and hydroxyl ions. OH^- will diffuse through the anode chamber, in which oxidation happens, forming back water and generating oxygen.

An alkaline polymer membrane is used to transport hydroxyl ions, providing a reduction of gas crossover issue, a more mechanically stable component and the possibility to work at higher pressure.

Anyway the performances are not as good as expected yet; this is mainly due to low membrane conductivity and slow catalyst kinetics. Moreover the membrane has not a stable lifetime profile, indeed chemical, but also mechanical stability, is still an issue in AEM [24].

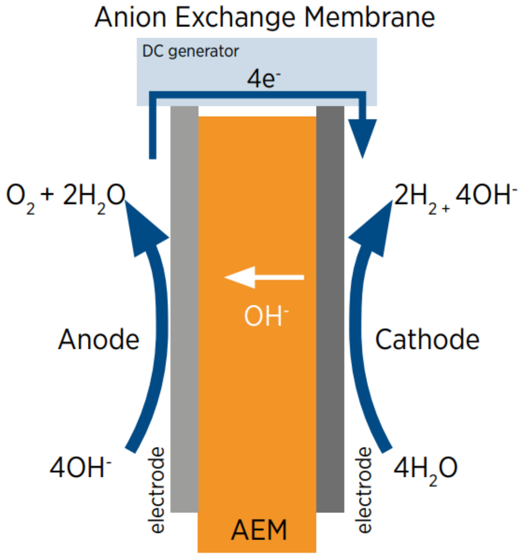

$$\textit{Anode: } 4OH^- \leftrightarrow 2H_2O + O_2 + 4e^-$$

$$\textit{Cathode: } 4H_2O + 4e^- \leftrightarrow 2H_2 + 4OH^-$$

Figure 1.13 - Anion Exchange Membrane water electrolysis cell [24].

1.5. Solar photovoltaic technology

Solar energy conversion technologies, and in particular solar photovoltaic one, are everyday detected as one piece of solution to decarbonize energy sector, especially in those areas with a remarkable solar radiation throughout the year.

In 1839 Alexandre-Edmund Becquerel identified, for the first time, the photovoltaic effect, meaning the generation of electrical current from certain light-induced chemical reactions [25]. However, it is just after 1958, when solar cells have been tested on an orbiting satellite, that solar photovoltaic technology, as it is currently known, started its development [25].

1.5.1. Working principle

Photovoltaic effect is exploited in the solar cell, which is the essential unit of a solar module, where sunlight is directly converted in electric energy. Electric current is detected when a flow of electrons is generated, thus solar cell requires material in which electrons can jump to a higher energy state when the sunlight is absorbed, and then, whether an external circuit is provided, an electric current is generated.

The basic functioning of a solar cell is granted by the p-n junction, where semiconductor materials are used. Conventional cells are composed by a main component, typically silicon (Si), which has four electrons in the outer shell. If atoms with three electrons on the outer shell (like B, Ga…) replace some Si atom, a zone with several atoms with a missing electrons, with respect to Si atoms, is realized. Instead, if another zone of the lattice is doped by pentavalent impurities (like P, As…), there will be a local excess of electrons. Thus, a p-n junction is formed because there will be an excess of positive charges in a zone, and on the adjacent one, there will be an excess of negative charges. It is evident that, if these two zones will be close to each other, the electrons in excess of the n-side are going to migrate towards the p-side, neutralizing the electric charges, forming the depletion zone, where there are not mobile charge carriers. Due to this migration, the n-side will be positively charged, while the p-side will be negatively charged, producing an electric field.

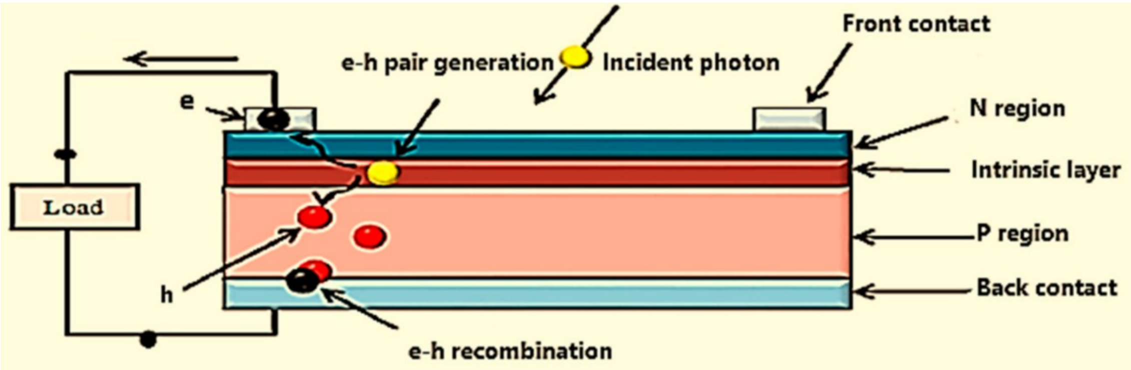

Figure 1.14 – Solar cell p-n junction [26].

At this point, the electric field attracts the electrons towards the n-side of the junction (positively charged), while the hole will be attracted towards the p-side, thus, a potential difference between the two junction is created.

When a photon is absorbed in p-n junction, if its energy is greater than the energy gap between valence and conduction band, the electron will leave the valence band, leaving there a hole, forming the electron-hole pair. Electron, now free to move, is going out across the n-region, while the hole is attracted towards the p-region. If an external circuit between the two sides is placed, an electrons flow, from n-side to p-side, is generated, providing electric current. The n-side is thinner than the p-side in order to reduce recombination effect, which reduces the efficiency of the conversion current [26].

A single PV cell is practically useless because the voltage generated is too low, around 0.5 V [26]; thus a PV module is composed by a series-parallel structure, indeed a series of cells provides a voltage which is the sum of the single cell voltage, while the current is increased whether cells work in parallel. By displacing a certain number of PV cells, depending on the series-parallel arrangement, a different voltage, current and consequently power is provided by the PV module.

1.5.2. Types of PV cell

Silicon has been widely used in photovoltaic industry, characterizing the first generation of PV module and holding 95% share of PV module production [27]. Silicon photovoltaic modules are mainly labelled as mono-crystalline (when a single ingot is adopted in manufacturing process) or poly-crystalline. Adopting crystalline-Si cells has been typically a cost-effective solution, because an increase of efficiency (current value between 15-22% [28]) and a continuous falling of manufacturing cost have been detected [27].

Typically poly-crystalline cells are less efficient and cheaper than mono-crystalline one [28]. Their manufacturing process does not require the extraction stage for ingot formation, but the number of impurities are higher, which reduces the efficiency of conversion [28].

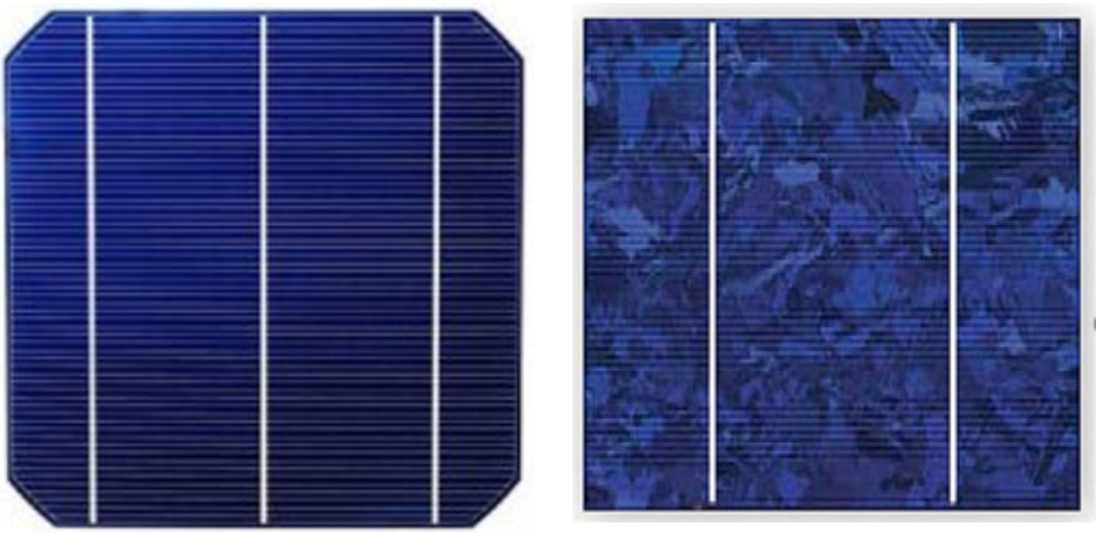

Figure 1.15 - Mono-crystalline and poly-crystalline cell [28].

An advanced solution of crystalline-Si cell is represented by Passivated Emitter and Rear Cell (PERC) technology. PERC cell manufacturing process is similar to mono-crystalline one, but a key improvement is realized: an integration of a back-surface passivation layer. PERC cell provides an increase of efficiency with respect to conventional crystalline-Si because the recombination of electrons is reduced, the absorption of sun radiation is increased, and it enables higher internal efficiency. In particular an efficiency gain, up to 1% and up to 0.8%, has been detected with respect to mono-crystalline and poly-crystalline respectively.

The radiation that are not absorbed by silicon will pass through, reaching the backside of the cell, thus it represents a waste of energy. If the backside of the cell is equipped with a dielectric layer, some of the radiation will be reflected and a part of it, will be absorbed, increasing the harvesting efficiency [28].

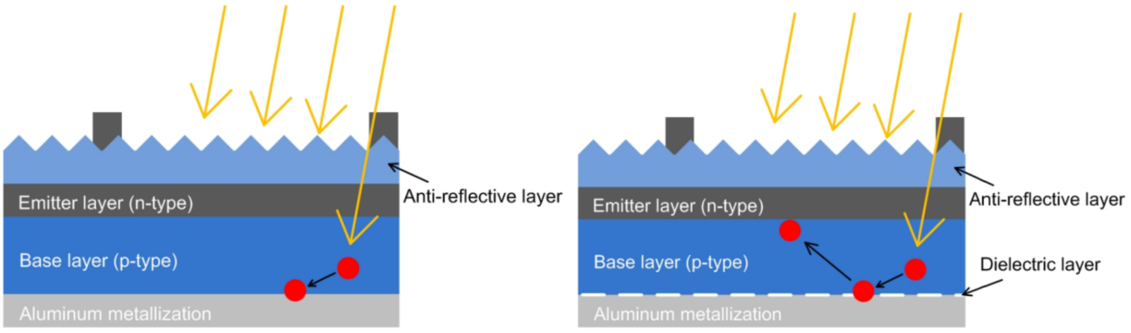
Emitter layer (n-type)
Base layer (p-type)
Aluminum metallization
Anti-reflective layer
Emitter layer (n-type)
Base layer (p-type)
Aluminum metallization
Anti-reflective layer
Dielectric layer

(a) (b)

Figure 1.16 - Comparison of a conventional cell (a) and a PERC cell (b) [28].

Despite its recent development, PERC technology become the new standard industry for mono-crystalline cell [27].

Another PV module generation, known as second generation, is represented by thin film technologies. Thin film PV modules are characterized by a lower cost with respect to crystalline-Si panels, because the amount of semiconductor material is remarkably lowered. Unlike first generation PV cell manufacturing process, where semiconductor materials are placed between glass panels, in thin film production, a thin layer of semiconductor materials is deposited on glass or stainless steel. The thickness of the layer is strongly reduced, passing from hundreds of micron to less than ten micron, reducing the manufacturing cost. Anyway, using less semiconductor material reduces the possibility of absorbing sunlight, thus the efficiency of thin film technology is lower than crystalline silicon technology [25]. Among thin film technologies two main groups can be distinguished like: silicon-based thin film (amorphous and micromorph silicon) and non-silicon based, like perovskites, cadmium telluride (CdTe) and copper-indium-gallium-diselenide (CIGS) [28].

The sun emits radiations with different wavelengths and only a part reaches the Earth surface. In order to absorb most of the sunlight hitting a PV module, a cell composed by a stack of different crystalline layers, thus by different materials with different band gap energy, can be tailored. From this concept, compound semiconductor PV cell production emerged. Piling up different layers an hetero-junction device is realized, which is able to exploit a wider band of solar spectrum with respect to a cell with a single semiconductor [25]. Indeed, if a band of solar radiation is not converted into electricity, it passes towards the beneath layer, which electrons are going to be excited by different wavelengths, thus increasing the probability of absorbing sunlight. Efficiency is obviously greater than crystalline-silicon and thin film technologies, reaching values up to 46%, but manufacturing cost and material cost are remarkably high, due to the expensive materials that are used [27].

Recently, advanced module technologies have been proposed, like bifacial solar cells, half-cells and others (multi-busbars, solar shingles…).

Half-cell concept arises from the fact that the cell area directly affects the cell current, which is related to resistive losses. Conventional crystalline silicon modules are composed by 60 or 72 cells, while half-cell PV modules are made of 120 or 144 cells. Reducing the cell area allows to increase the efficiency, since resistive loss, related to the cell current, are lowered, and secondly, the hot-spot probability is reduced [28].

Bifacial solar cells are capable of converting the sunlight which is reflected to the back of the cell too, and up to now they are the most promising technology among these previously mentioned.

1.5.3. Current and future applications

Fields and rooftops applications are matured implementation of PV modules for electric power generation. Nevertheless, the necessity of increasing renewable penetration gives rise to new possibilities of implementation.

Floating PV modules is an opportunity that has already been adopted in several area. The largest floating photovoltaic plant is currently in China, in which 70 MW of PV modules have been installed. This application has risen interest in the last years, because land cost is typically higher than water surface cost, the presence of water offers a cooling effect which is beneficial for PV cell performance and the evaporation rate is remarkably reduced. The drawbacks are related mainly to installation and maintenance cost and to the design of anchoring system [29].

Another installation possibility is related to building integration. Building-integrated solar panel (BIPV) applications are growing in number as both active and passive functions could be exploited. Indeed, besides electricity production that can be exploited inside the building, also other functionality are typically included, like thermal and acoustic insulation [29].

Recently attention has grown around agrophotovoltaic (APV) applications, where PV modules and growing crops share the same land. It is typically a win-win situation because the shade offered by PV modules is beneficial for crops growth. Moreover, since crops transpire water during the growing process, the PV modules temperature does not reach high values, increasing harvesting efficiency [29].

Unlike floating PV, BIPV and agrophotovoltaic, which are already well-developed applications, solar trees are not diffuse yet. Solar trees concept arises in order to reduce land consumption, with PV modules installed through a structure which resembles a tree. The application allows to harvest the same amount of energy, occupying 100 times less ground space, providing a possibilities of installing PV modules in those zone with scarcity of land availability.

2 Methodology

2.1. General process introduction

Membrane Reactor performance are strictly related to hydrogen production and separation through the membranes. Hydrogen separation happens when hydrogen is permeating from retentate side towards permeate side; this permeation is driven by hydrogen partial pressure difference between the two sides of the membrane.

Therefore, an interesting possibility to improve the performance of membranes reactors, is to increase the difference of hydrogen partial pressure between retentate side and permeate side.

In this thesis work, where hydrogen production from biogas through autothermal reforming is assisted by membrane reactor, an opportunity to increase the partial pressure difference between the two membrane sides is represented by feeding pure oxygen, instead of air. Indeed autothermal reforming behaviour is ensured by the heat supplied by a small amount of biogas that is burned. If the combustion is performed in air, a relevant amount of nitrogen will be present in overall reactions product stream. This high amount of N_2 in product stream, besides the fact that inert concentration (CO_2 molar fraction in biogas is around 40-50%) in biogas is already high, is reducing the hydrogen partial pressure in retentate side. Therefore, the goal of feeding pure oxygen as oxidizing agent is to avoid N_2 in reactions product stream, increasing hydrogen partial pressure in retentate side, thus, increasing hydrogen permeation driving force.

The first aim is to quantify plant performance improvement when oxygen, instead of air, is fed as oxidizing agent. Secondly, different layouts of an ATR-FBMR plant coupled with a Proton Exchange Membrane (PEM) electrolyzer to produce oxygen in situ and PV panels, have been techno-economically evaluated, considering both on-grid and off-grid solutions. The O_2-feeding ATR-FBMR configuration chosen to be coupled with PEM electrolyzer is the one with the highest system efficiency from the results of air-O_2 comparison.

Furthermore, since the off-gases from ATR plant mainly consist of CO_2 and water, a simple CCS system has been included to separate a rich-CO_2 stream, providing valuable incomes.

The ATR-FBMR plant functioning is simulated in Aspen Plus [30], with an integrated Aspen Custom Modeler unit for the FBMR reactor. The Aspen flowsheet solve energy and mass balance of this section while the integration of the electrolyser, PV panels, BESS and the grid is developed with a specific VBA tool in Microsoft Excel to solve components control strategy, annual energy and mass balance and to optimize the components size.

Hydrogen yearly productions have been evaluated through a hourly simulation performed in Microsoft Excel, where electrolyzer model has been developed too. Solar radiation data (reference year is 2019) have been taken from PVgis tool, obtaining a yearly hourly profile of PV electricity generation in kWh/kW$_P$ for Catania (Sicily). This procedure has been detailed in [31], where a coupling between PV and PEM has been performed.

2.2. Comparison description between air and oxygen

The first aim of this project is to quantify the performance improvement by changing the feed, from ambient air to oxygen, for an autothermal reforming plant (ATR) assisted by membrane reactor placed in Catania, Sicily.

In order to do that, a comparison, varying the number of membranes, has been performed at same operating conditions (enlisted in Table 2.1), with fixed minimum fluidization velocity and the goal of producing 100 kg of pure hydrogen per day (actually hydrogen produced is slightly greater, but not all the H_2 produced can be completely separated).

Reactor functioning simulations have been performed in Aspen Plus, that allows to compute and to solve mass and energy balances. Membrane reactor is not a commercial technology yet, therefore a model has been developed in Aspen Custom Modeler during previous projects, and it has been adopted in this work too. The model adopted to simulate the functioning of the membrane reactor has been detailed in chapter *3 Fluidized bed membrane reactor model*.

The oxidizing agent (air or oxygen) is going to be calibrated in order to the ensure autothermal behaviour of the reactor, while the amount of steam required is regulated to have a Steam-Carbon-Ratio (S/C), which is the ratio between molar flow rate of steam and molar flow of methane, at the beginning of the membrane region (5 cm from the distributor plate of the reactor [30].

The biogas consumed is assumed to be originated from anaerobic digestion process, with properties and composition explicated in Table 2.2.

Parameter	Unit	Value
Reactor temperature	°C	500
Reactor pressure	bar	12
Permeate Pressure	bar	0.1
S/C	-	3
Pure H_2 produced	kg/day	100
Operative Hours	hours/year	7500

Table 2.1 - Operating conditions to compare air and oxygen as feed.

Species	Unit	Value
CH_4	%mol	58.1
CO_2		33.9
N_2		3.8
O_2		1.1
H_2		-
CO		-
H_2O		Saturated
LHV	MJ/kg	17.79
p / T	bar / °C	1.013 / 15

Table 2.2 - Biogas composition and characteristic.

In order to understand the goodness of replacing oxidizing agent, from air to oxygen, several parameters will be compared, performing a sensitivity analysis on membranes number.

Membrane reactor goal is to produce and to separate the hydrogen generated from reforming reaction, thus, a method to understand how good the performances are, is to quantify the hydrogen permeated, with respect to the maximum amount of hydrogen that could be produced. This concept is expressed by Hydrogen Recovery Factor (HRF), calculated as in Equation (2.1) [30]. Hydrogen Recovery Factor is the main Key Performance Indicator (KPI) to evaluate FBMR performance. It is defined as the ratio between the pure hydrogen separated ($\dot{n}_{H_2,perm}$) and the maximum theoretical amount of hydrogen that can be separated if:

i. all CH_4 fed (excluding the amount burned to ensure autothermal behaviour) is converted according to reactions,(R.1.1), (R.1.2) and (R.1.3), so 4 moles of H_2 are produced for each mole of CH_4.
ii. all hydrogen produced is separated from the membrane; this is an ideal conditions, since, even if complete chemical reactions are performed, it would possible only with zero pressure at permeate side.

$$HRF = \frac{\dot{n}_{H_2,perm}}{4 \cdot (\dot{n}_{CH_4,in} - \dot{n}_{CH_4,ox})} \tag{2.1}$$

An important technical parameter to assess the technical performance of the plant is the system efficiency, defined in Equation (2.2), which evaluates the energy output contained in the hydrogen produced, with respect to biogas and primary energy input [32].

$$\eta_{sys} = \frac{\dot{m}_{H_2} \cdot LHV_{H_2}}{\dot{m}_{BG,f} \cdot LHV_{BG} + \frac{W_{aux}}{\eta_{el,ref}}} \tag{2.2}$$

In particular:

- LHV_{H_2} has a value of 120 MJ/kg.
- LHV_{BG} has been already introduced in Table 2.2.
- W_{aux} is the input power to feed all the auxiliaries of the plant (i.e. compressors, pump, control system).
- $\eta_{el,ref}$ is assumed equal to 45%, like the average electric efficiency of the power generating park.

Besides the technical aspect, an economic analysis provides relevant information too.

Commonly, the economic convenience of a hydrogen producing plant, is assessed through Levelized Cost of Hydrogen (LCOH), considering all the components forming the autothermal reforming plant and the yearly hydrogen production; it is computed as in Equation (2.3).

$$LCOH_{ATR} = \frac{TPC_{ATR} \cdot CCF_{ATR} + C_{O\&M-ATR}}{kg_{H_2-ATR}} \tag{2.3}$$

In Equation (2.3): TPC_{ATR} is the total plant cost, CCF_{ATR} is the carrying charge factor (assumed equal to 16% [32]), while $C_{O\&M-ATR}$ represents yearly fix and variable operational and maintenance cost.

Once that the comparison between oxygen-fed case and air-fed case has been done, it is possible to evaluate which is the number of membranes that minimizes the LCOH for the two plants.

The configuration which minimizes LCOH in air-fed case has been taken as reference case, which assumptions are detailed in paragraph *2.2.1 Air configuration*, and it will be used for other comparison analysis further explained. Oxygen case assumptions, where FBMR is fed by pure oxygen, have been described in paragraph *2.2.2 Oxygen configuration*. Oxygen fed-case minimum LCOH is an incomplete index, because in the first comparison oxygen has been assumed as available in situ, thus next analysis, in which oxygen production is introduced, will be more meaningful from a techno-economic point of view.

2.2.1. Air configuration

Air-case, where air is used as oxidizing agent, is going to be the main benchmark for this work, and it has been developed in EU funded MACBETH project; its layout is represented in Figure 2.1, and it is here furtherly explained.

The air is going to be compressed in a three-stage intercooled compressor, from ambient conditions (15°C, 1 bar) to 12 bar, which is the operating pressure of the reactor, assuming negligible pressure drop in the whole plant.

The biogas, with composition detailed in Table 2.2, is compressed in similar way from ambient conditions to 12 bar. The detail to execute the compression of air and biogas are available in Table 2.3 and Table 2.4; the compression ratio has been set in order to avoid temperature greater 150°C.

	Stage 1	Stage 2	Stage 3
Discharge Pressure [bar]	2.40	5.40	12
β	2.40	2.25	2.22
Outlet Temperature [°C]	30	30	140.14
Isentropic Efficiency	0.70	0.70	0.70
Mechanical Efficiency	0.85	0.85	0.85

Table 2.3 - Input parameter to simulate air compression.

Air and biogas are going to be mixed and heated up by flue gas of burned retentate, which are going to exchange energy with water too, providing hot steam at 700°C at the inlet of the reactor. Water is retrieved at ambient condition (15°C, 1 bar) and pumped up to 12 bar, assuming the pressure drop negligible in the whole air-feeding configuration. The reactor feed is entering the bottom region at 448°C and 12 bar (reactor operating pressure), where combustion is ignited and reforming process is going to start.

	Stage 1	Stage 2	Stage 3
Discharge Pressure [bar]	2.5	6	12
β	2.5	2.4	2
Outlet Temperature [°C]	50	70	147.60
Isentropic Efficiency	0.70	0.70	0.70
Mechanical Efficiency	0.85	0.85	0.85

Table 2.4 - Input parameter to simulate biogas compression.

The retentate, therefore, is burned and it is used as heat source to produce high temperature steam. The cold flue gas are going to be flashed to separate water from them; the final composition is mainly characterized by nitrogen compounds (molar fraction greater than 60%) and carbon dioxide (around 27%), the left fraction is water and oxygen.

The hydrogen separated in permeate side is then used as heat source in a first economizer, and then cooled down to 40°C in an air cooler. A vacuum pump is going to compress it up to 1 bar, while a compressor increases hydrogen pressure up to 20 bar, considered as battery limit of the plant. Vacuum pump efficiencies are the same of the hydrogen compressor ones, which features are reported in Table 2.5.

	Stage 1	Stage 2	Stage 3	Stage 4
Discharge Pressure [bar]	2.12	4.47	9.46	20
β	2.12	2.12	2.12	2.12
Outlet Temperature [°C]	30	30	30	141.32
Isentropic Efficiency	0.70	0.70	0.70	0.70
Mechanical Efficiency	0.85	0.85	0.85	0.85

Table 2.5 - Features of hydrogen compressor.

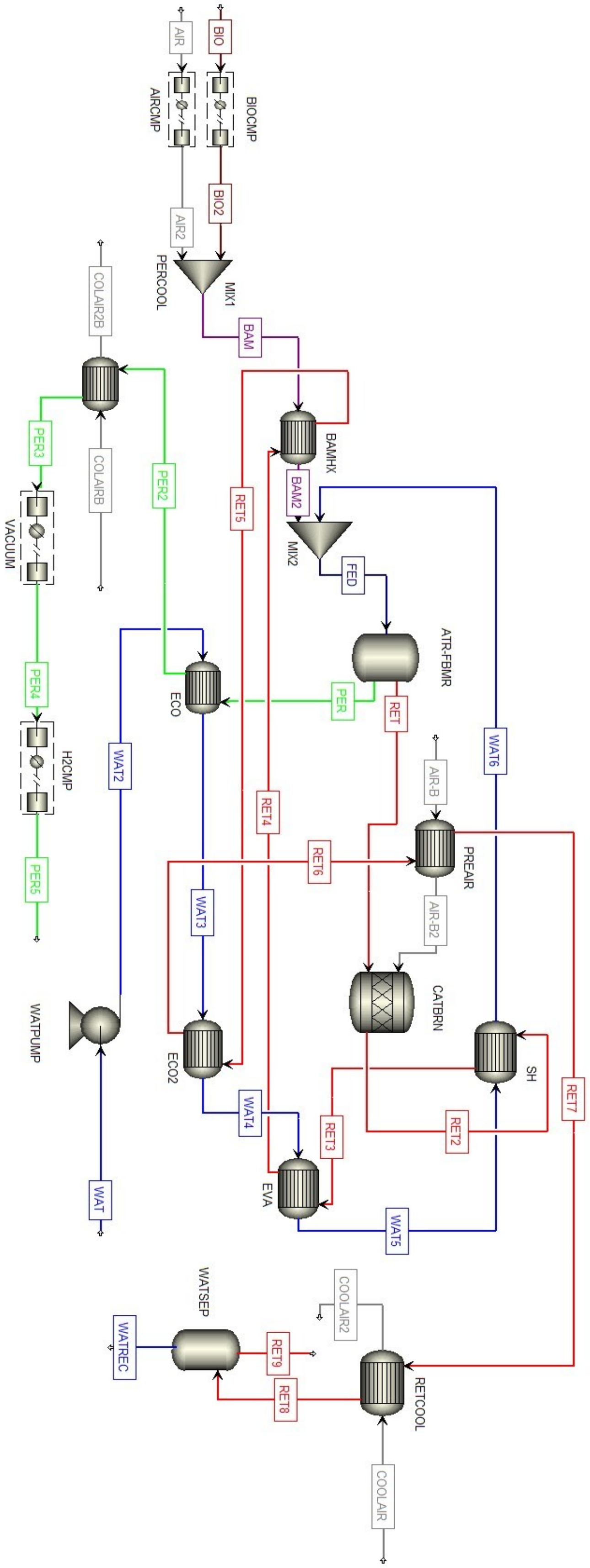
AIR
BIO
AIRCMP
BIOCMP
AIR2
BIO2
PERCOOL
MIX1
BAM
COLAIR2B
COLAIRB
PER3
VACUUM
PER2
RET5
BAMHX
BAM2
MIX2
FED
ATR-FBMR
PER
RET
WAT6
ECO
PER4
H2CMP
WAT2
RET4
AIR-B
PREAIR
RET6
PER5
WAT3
AIR-B2
CATBRN
WATPUMP
ECO2
SH
RET7
WAT4
RET3
RET2
EVA
WAT
WAT5
WATSEP
COOLAIR2
WATREC
RET9
RET8
RETCOOL
COOLAIR

Figure 2.1 - ATR plant in air configuration, taken from MACBETH Project.

Several constraints to obtain the required production, but also to avoid inconvenient results, are implemented in Aspen Plus, through Design-Specification (DS) tool. The constraints adopted in air-feeding configuration are reported in Table 2.6.

DS Name	Objective variable	Varying
DS-BG	$\dot{m}_{H_2} = 100 \pm 0.1 \, \frac{kg_{H_2}}{day}$	$\dot{n}_{biogas} \in (1.11 - \ 3.21)$
DS-H2O	$\frac{S}{C} = 3 \pm 0.05$	$\dot{n}_{water} \in (1.11 - \ 6.11)$
DS-UMF	$u_0/u_{mf,min} = 1.55 \pm 0.05$	$D_{reactor} \in (0.4 - 0.6)$
DS-AIR	$Q_{ATR} = 0 \pm 0.1$	$\dot{n}_{air} \in (0.51 - \ 2.51)$
DS-AIR BURNER	$x_{O_2}^{fluegas-retentate} = 0.05 \pm 0.01$	$\dot{n}_{air}^{burner} \in (0.51 - 3.11)$

Table 2.6 - Constraints imposed in air-case, with Design-Specification tool.

2.2.2. Oxygen configuration

Oxygen configuration is developed having as reference air-feeding case, adopting several common assumptions, in order to have a fair comparison too. In this configuration, oxygen is assumed to be given at ambient temperature (15°C) and at the reactor operating pressure (12 bar). Indeed, in next analysis, oxygen production through PEM electrolysis, at pressure greater than 12 bar, will be performed. Thus, this preliminary evaluation has been made mainly with the goal of quantifying the performance improvement by changing the oxidizing agent.

The configuration shown in Figure 2.2 is the one adopted for the oxygen-case, in which O_2 is used for autothermal reforming and to burn the retentate.

Biogas entering the plant is compressed with the same specifications reported in Table 2.4, while oxygen is considered at ambient temperature and at reactor operating pressure. They are mixed and heated up to 300 °C (considered a safe ignition limit with oxygen-gas mixture according to [33]), in order to provide the feed at a temperature close to reactor operating temperature.

Steam is generated by retentate burned fuel gas used as heat source, as well as, by the cooling down of the permeate, in a first superheater (SH1) and in a first economizer (ECO1), reaching the same temperature of air-configuration, imposed to be 700°C. The retentate combustion is performed in pure oxygen environment, provided directly by PEM electrolyzer, thus a valve is placed to reduce oxygen pressure.

Being the combustion realized with pure oxygen, the flue gas composition will be mainly carbon dioxide and water. Thus, after a cooling down of this stream, and after a separation by water condensation, it is possible to obtain rich-CO_2 stream. At this point, it could be sold or it could be compressed to be injected into a pipeline, realizing a carbon-negative plant; both cases will be taken into account. The CO_2 compressor has been modeled to reach injection condition, as mentioned in *5.5 CO2 removal and injection in pipeline*, and its main features are enlisted in Table 2.7.

	Stage 1	Stage 2	Stage 3	Stage 4	Stage 5
Discharge Pressure [bar]	2.63	6.90	18.12	47.59	125
β	2.63	2.63	2.63	2.63	2.63
Outlet Temperature [°C]	35	35	35	35	25
Isentropic Efficiency	0.70	0.70	0.70	0.70	0.70
Mechanical Efficiency	0.85	0.85	0.85	0.85	0.85

Table 2.7 - Features of CO_2 compressor.

Water, as in air case, is pumped from ambient conditions to 12 bar, which is the reactor operating pressure. In oxygen configuration, pressure drops in the plant are neglected in order to provide a fair comparison with air-case developed in MACBETH project. The permeated hydrogen is going to be cooled down in two heat exchangers, as previously mentioned, and then compressed through a vacuum pump and then through a compressor, with the same specifications of air-case, up to 20 bar.

In analogous way of air configuration, Design Specification tool is used to respect several constraints; they are reported in Table 2.8.

DS Name	Objective variable	Varying
DS-BG	$\dot{m}_{H_2} = 100 \pm 0.1 \frac{kg_{H_2}}{day}$	$\dot{n}_{biogas} \in (1.1 - 4.1)$
DS-H_2O	$\frac{S}{C} = 3 \pm 0.05$	$\dot{n}_{water} \in (1.1 - 4.1)$
DS-UMF	$u_0/u_{mf,min} = 1.55 \pm 0.05$	$D_{reactor} \in (0.3 - 0.6)$
DS-O_2	$Q_{ATR} = 0 \pm 0.1\ kW$	$\dot{n}_{O_2} \in (0.1 - 1.1)$
DS- O_2 BURNER	$x_{O_2}^{fluegas-retentate} = 0.05 \pm 0.01$	$\dot{n}_{air}^{burner} \in (0.05 - 1.05)$

Table 2.8 - Constraints imposed in oxygen configuration, with Design-Specification tool.

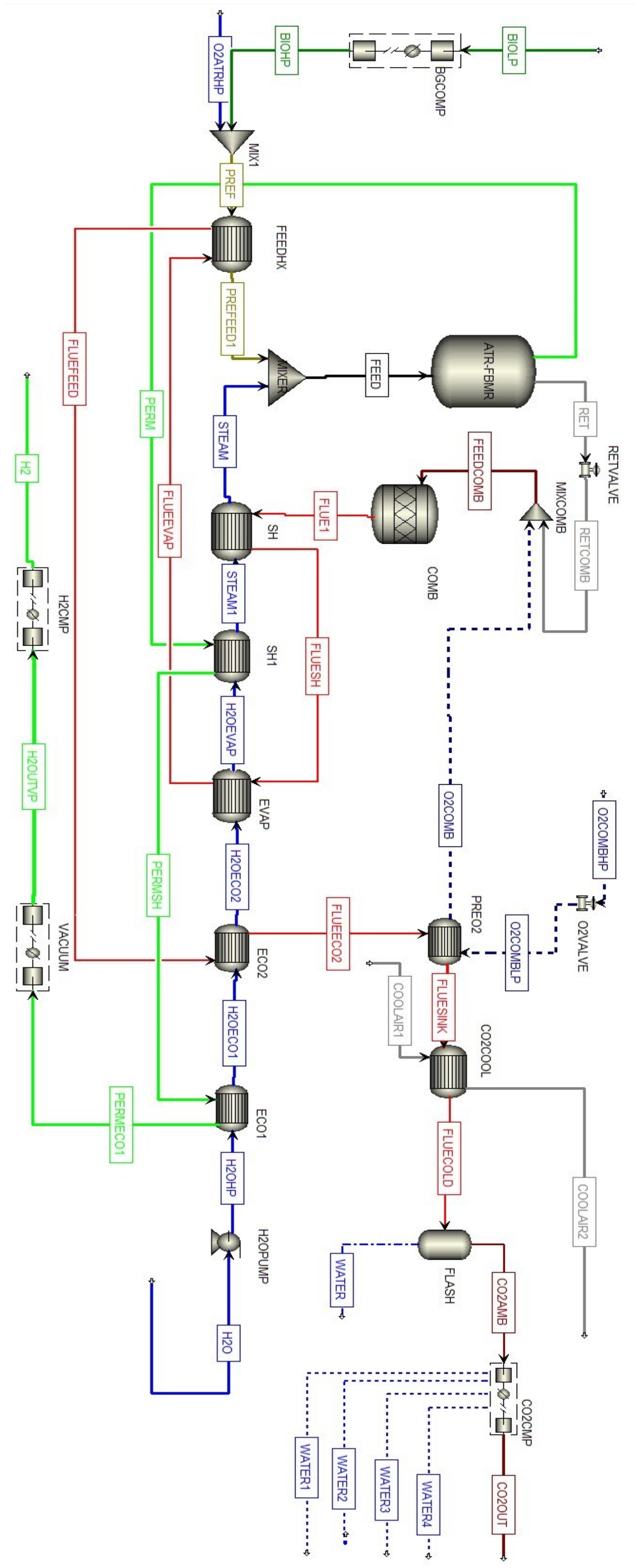
O2ATRHP
BIOHP
BGCOMP
BIOLP
MIX1
PREF
FEEDHX
PREFEED1
MIXER
FEED
ATR-FBMR
RET
RETVALVE
RETCOMB
MIXCOMB
FEEDCOMB
COMB
FLUE1
STEAM
SH
STEAM1
SH1
FLUESH
H2OEVAP
EVAP
FLUEEVAP
FLUEFEED
PERM
H2
H2CMP
H2OUTVP
VACUUM
PERMSH
H2OECO2
ECO2
FLUEECO2
PREO2
O2COMB
O2COMBLP
O2VALVE
O2COMBHP
FLUESINK
COOLAIR1
CO2COOL
COOLAIR2
H2OECO1
ECO1
PERMECO1
H2OHP
H2OPUMP
H2O
FLUECOLD
FLASH
WATER
CO2AMB
CO2CMP
WATER1
WATER2
WATER3
WATER4
CO2OUT

Figure 2.2 - ATR plant in oxygen configuration.

2.3. Oxygen production addition

The previously mentioned comparison has been made considering oxygen as available in situ, nevertheless, this gas must be produced, therefore the autothermal reforming with air will be compared, in further sections, with a plant which foresees oxygen production too.

In particular, in this work, a Proton Exchange Membrane (PEM) electrolyzer has been chosen as suitable technology to produce the amount of oxygen required by autothermal reforming. The model of a PEM electrolyzer has been developed in Microsoft Excel and explained in chapter *4.Electrolyzer*.

PEM electrolyzer, through water electrolysis reaction, provides oxygen generation, with a further hydrogen production, that will be added to the one performed by autothermal reforming, providing an LCOH which takes into account oxygen production too.

Electrolyzer requires a source of energy to enable water electrolysis reaction, and depending on the electricity sources, different configurations will be modelled, and finally compared with autothermal reforming performed with air, taken as benchmark case.

The first configuration studied is the simple introduction of a PEM electrolyzer to the autothermal reforming plant, where the electricity needed is withdrawn by the grid, with a purchasing price assumed (for every case further explained) equal to 120 €/MWh [32].

In order to properly design the electrolyzer size, a constraint on the oxygen production has been set. From Aspen Plus results, the oxygen needed, to perform the autothermal reforming and the combustion of retentate, is obtained, thus PEM electrolyzer must provide the exact quantity, at suitable conditions of pressure and temperature, for each FBMR working hour.

Starting from this oxygen production constraint, an optimization procedure, varying cells number and cell area, has been performed through a computational code in Visual Basic (developed for all the configurations analysed and furtherly detailed), which allows to easily compute efficiency, LCOH and other variables, for each combination of cell area and cell number, respecting the electrolyzer constraints explicated in chapter *4.Electrolyzer*. The procedure outcome is the size of the electrolyzer which minimizes the LCOH of the whole plant (PEM electrolyzer and autothermal reforming plant).

Since PEM electrolyzer produces hydrogen too, this surplus generation should be taken into account in LCOH formulation:

$$LCOH_{PEM\,\&\,ATR} = \frac{TPC_{ATR} \cdot CCF_{ATR} + C_{O\&M-ATR} + TPC_{PEM} \cdot CCF_{PEM} + C_{O\&M-PEM}}{kg_{H_2-ATR} + kg_{H_2-PEM}} \tag{2.4}$$

In similar way the system efficiency formulation is updated and computed as in Equation (2.5), where W_{aux} considers electrolyzer consumption too.

$$\eta_{sys} = \frac{(\dot{m}_{H_2^{ATR}} + \dot{m}_{H_2^{PEM}}) \cdot LHV_{H_2}}{\dot{m}_{BG,f} \cdot LHV_{BG} + \frac{W_{aux}}{\eta_{el,ref}}} \tag{2.5}$$

The following configuration, as the previous one, foresees the possibility of withdrawing by the grid, but also the availability of an electricity generation source in situ, studying the techno-economic convenience of installing a photovoltaic field. A yearly hourly PV electricity generation profile (kWh/kW_p) has been obtained by using PVgis tool (the reference year is 2019), thus LCOH computation has been based on yearly hourly profile, considering ATR-FBMR operative hours equal to 7500 h/y. In this case, an optimization on PV modules, electrolyzer cells number and electrolyzer cells area is performed too, in order to identify the configuration which minimizes the LCOH of the whole plant. Concerning LCOH of the plant it will be calculated introducing PV plant cost too, as in Equation (2.6). Contribution of CCF_i is going to be detailed in chapter *6 Economic analysis.*

$$LCOH_{PLANT} = \frac{TPC_{ATR} \cdot CCF_{ATR} + C_{O\&M-ATR} + \sum_i^N TPC_i \cdot CCF_i + C_i^{O\&M}}{kg_{H_2-ATR} + kg_{H_2-PEM}} \tag{2.6}$$

On a third case, the implementation of Battery Energy Storage System (BESS) is evaluated from a techno-economical point of view. The goal of introducing storage system is to reduce the withdrawing from the grid, especially during night-time, exploiting the electricity generated by PV field. In every case which adopts PV field, also the possibility of revenues by electricity injection into the grid is enabled, assuming an electricity selling price of 60 €/MWh [31]. LCOH has been computed as in Equation (2.6), accounting for BESS introduction too.

Being the selling electricity price and purchasing electricity price relevant parameter a sensitivity analysis on these values has been performed and it is reported in paragraph *7.5 Sensitivity analysis on electricity prices*.

A sketch of configuration with the main players of the plant is presented in Figure 2.3; this sketch is obviously incomplete, but with a glance it allows to represent all the most important components in an on-grid configuration; more detailed configuration will be provided in the next chapters.

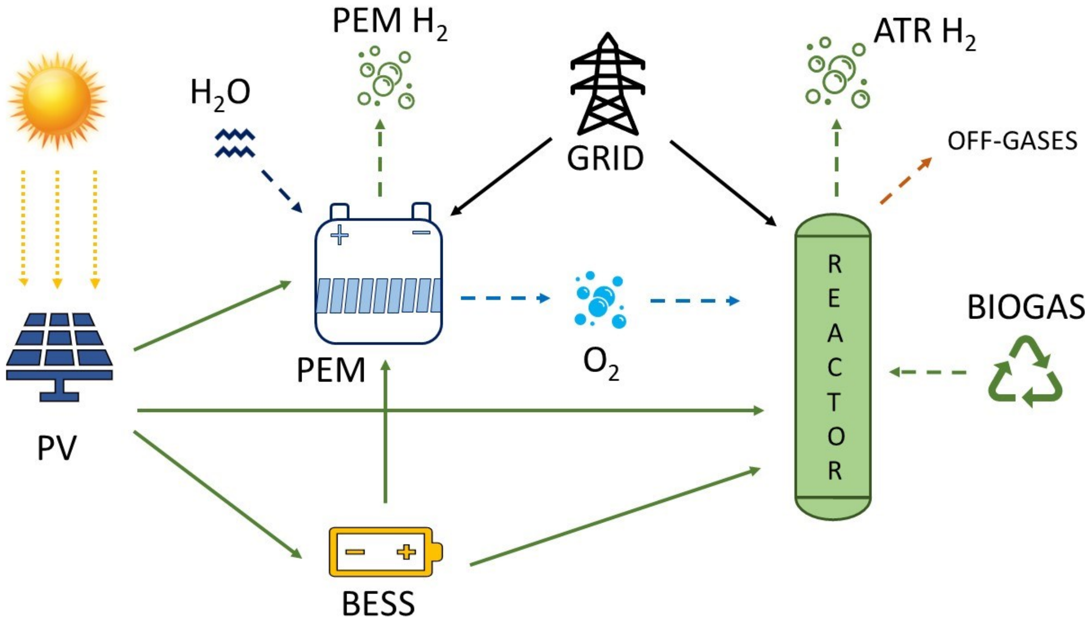

Figure 2.3 - Sketch of on-grid complete configuration.

Another possibility is to work off-grid. In this case the only electricity source is PV field, which is going to feed PEM electrolyzer and ATR plant auxiliaries and meanwhile is recharging the battery to allow hydrogen production during some night hours too. Indeed, in this configuration an oxygen tank is installed, allowing PEM electrolyzer of producing oxygen in excess with respect to the strictly constraint of producing the exact quantity needed by autothermal reforming plant, decoupling oxygen production and oxygen consumption; its schematic representation is displayed in Figure 2.4. LCOH in off-grid has been computed as in Equation (2.6) too.

By decoupling oxygen production and consumption, situation where an excess of oxygen is produced could be possible, meaning that in a certain hour oxygen production allows to feed FBMR and oxygen tank is already full. In this case oxygen would be wasted, but since it is a valuable by-product, it has been decided to sell it when an oxygen surplus is generated. A value of 150 €/tonO_2 is indicated as minimum selling price for industrial use of oxygen, but medical oxygen could be more expensive [34], [35], [36].

Feeding oxygen to the plant provokes that the burned retentate is mainly composed by CO_2 and H_2O, thus the possibility of selling carbon dioxide, nearly at ambient condition or by pipeline injection is investigated too, upgrading the plant from being carbon-neutral to be carbon-negative. The selling price is assumed equal to 35 €/tonCO_2 [37] or 50 €/tonCO_2 whether injected in a pipeline [38].

In order to provide a clear comprehension of the different cases analysed, a summary of the different configuration investigated and detailed in chapter 7 *Results* is provided in Table 2.9.

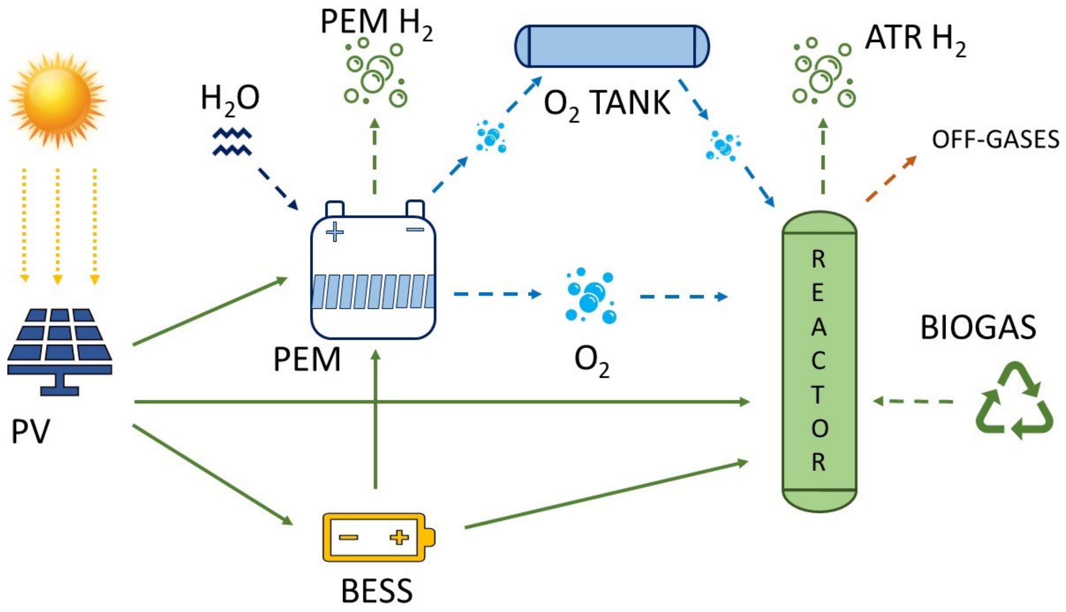

Figure 2.4 - Sketch of off-grid configuration.

Case name	Description
Air case	It is the benchmark case where air is fed to FBMR (developed in MACBETH project). It is an on-grid configuration
PV-Air case	It is the benchmark case, but it is assisted by a PV field, besides the grid
Oxygen case	Oxygen is fed to FBMR. Since O_2 is assumed available in situ, this case has been used to quantify the improvement of FBMR performance when oxidizing agent is oxygen instead of air.
PEM-ATR	It is an on-grid configuration where O_2 production through PEM electrolyzer is introduced, thus a fair techno-economic comparison with air-case can be performed.
PV-PEM-ATR	It is an on-grid configuration assisted by a PV field. Oxygen is still produced by PEM electrolyzer to feed ATR plant.
PV-BESS-PEM-ATR	It is an on-grid case assisted by a PV field and by a Battery Energy Storage System (BESS).
OFF-GRID	Being off-grid the electricity is provided by PV field and BESS only. An oxygen tank to decouple PEM oxygen production and FBMR oxygen consumption has been introduced.

Table 2.9 - Summary of the cases analyzed.

In all the configurations where FBMR is fed by oxygen, two cases will be detailed: a case in which CO_2 is sold at ambient conditions and a case in which CO_2 is injected into a pipeline, making the plant carbon-negative.

3 Fluidized bed membrane reactor model

Autothermal reforming assisted by membrane reactor is the core of the analysis performed in this project, being the main player of plant optimization. In this chapter an overview of membrane reactor model has been presented.

3.1. Introduction and general assumptions

The adopted model is simulating a fluidized bed membrane reactor (FBMR), which general features and working principle have been briefly introduced in *1.3 Membrane reactor*.

Fluidized bed membrane reactor model used in this project has been developed in EU funded project MACBETH through Aspen Custom Modeler (ACM) software. The model describes in detail the functioning of a membrane reactor with its theoretical and experimental fundamentals based on a collection of several previous works [17], [39], [30], [40]. Being FBMR model developed in ACM, it can be easily integrated in Aspen Plus, a software able to solve heat and mass balances and which includes a wide dataset of properties and equations of state. Aspen Plus is the software through which the simulation of the overall plant has been performed.

The FBMR model, simulating hydrogen production and separation from biogas autothermal reforming, includes the following chemical components: CH_4, H_2O, CO_2, CO, H_2, O_2, N_2. Considering that membranes adopted for hydrogen separation would not withstand H_2S presence and that it is typically removed for conventional reforming too, it has been decided to not include this compound. As common practice in hydrocarbons involving process, Peng-Robinson equation of state has been adopted to compute thermodynamic properties. In order to properly design biogas autothermal reforming, methane steam reforming (R.1.1), water gas shift reaction (R.1.2) and methane oxidation (R.1.3) and have been included in FBMR model [40].

As briefly introduced in *1.3.1 Current hydrogen production*, WGS is a slightly exothermic reaction, while SR is an endothermic one, which required heat is provided by methane oxidation. Besides the heat to be supplied for SR activation, other energy should be taking into account for heating the feed up to reactor operating temperature. A feed temperature as close as possible to reactor operating temperature is beneficial for FBMR operation. Feed heating is supplied by retentate combustion in a catalytic burner.

Biogas, together with steam and air/oxygen is composing the reactor feed, and its characteristics have an important impact concerning the performance of the plant [32]. Biogas is assumed to be originated in anaerobic digester and its composition has been reported in Table 2.2. Operating conditions adopted have been introduced in Table 2.1; besides these parameters the dilution factor (DF), defined as the ratio between the total solid mass (catalyst and filler material) and the mass of catalyst, has been set equal to 2, meaning that only half of the solids are catalytic particles.

3.2. Features and model

The developed model consists in a cylindrical vessel in which membranes are vertically placed and they have been inserted from the top part of the reactor. The feed, instead, is inserted from the bottom flowing towards the top, and the products which do not permeate through the membranes will compose the retentate.

Membranes have a mesoporous ceramic protective layer which increases their resistance to impact with catalytic particles. Due to this additional layer, the adopted membranes are called double-skin membranes, which parameters for the permeation model are reported in Table 3.1 [30]. In FBMR model, an infinite selectivity for hydrogen has been assumed, due to the very high selectivity of dense membranes [13].

Parameter	Units	Value
$P^0_{H_2}$(pre-exponential factor of membrane permeability)	$\frac{mol}{s \cdot m \cdot bar^{0.5}}$	$5.87 \cdot 10^{-10}$
$E_{a,perm}$ (activation energy related to permeation process)	$\frac{kJ}{mol}$	7.81
n (exponent in hydrogen flux expression)	-	0.749
t_{SL} (thickness of membrane selective layer)	μm	2.5
Membranes length	cm	45
Membranes external diameter	cm	1.4
Membranes internal diameter	cm	0.7
Minimum membranes distance	cm	2
Minimum membranes pitch	cm	3.4

Table 3.1 - Double-skin membranes parameters used in Richardson equation [30]

The catalyst adopted is composed by Rhodium over a zirconia oxide support (ZrO_2), with catalyst parameter for reactions rate equations taken from [40]. Catalyst particles should be dragged by the gas flowing in the reactor, therefore, it should have enough superficial velocity to generate a bubbling fluidization regime. Concerning catalyst amount, in order to ensure a correct fluidization regime, the model equations directly computes the total amount of solids.

Minimum membrane distance, shown in Figure 3.1, it is an important constraint to be respected, and several analysis will be furtherly detailed to investigate the trend of membranes number with membranes minimum distance. This value has been set equal to 2 cm because, from experimental results, it has been observed that below that value hydrogen concentration at the membranes surface can be remarkably reduced by interference with nearby membranes.

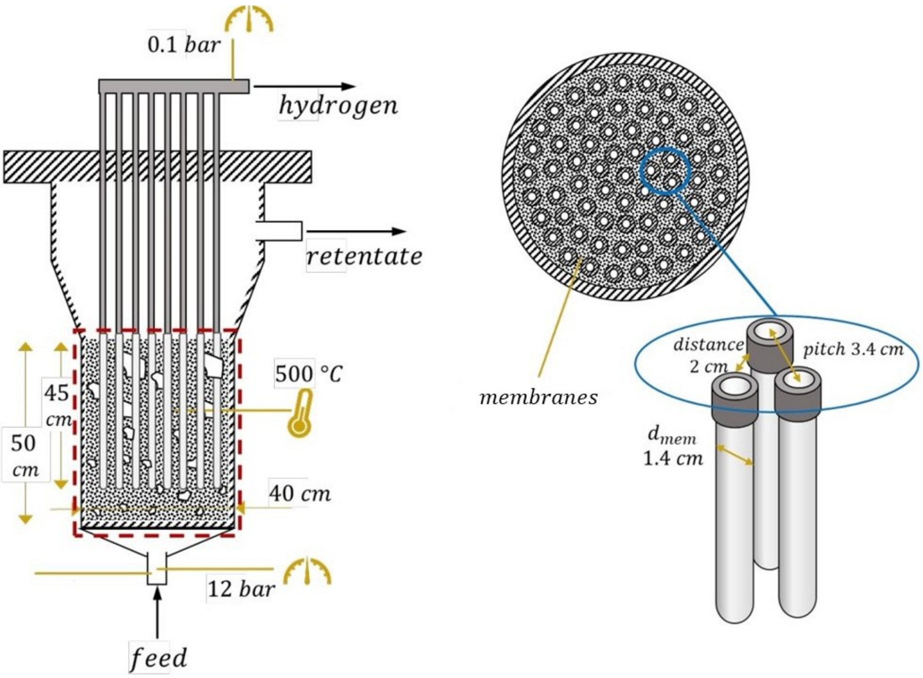

Figure 3.1 – FBMR layout with modeled region contoured in red, with catalyst (black dots) and membranes (in white) clearly represented. Layout adapted taken from [30].

Three reactor regions could be identified: bottom region, membranes region and freeboard region. In the bottom region only the chemical reactions occurs, then the hydrogen produced permeates in membranes region, while the freeboard region is a zone where the bed is expanded but with a negligible presence of the solid particles and no membrane area, meaning that conversion is neglected in this zone and it has not been modeled in ACM model.

Two phase has been assumed: emulsion and bubble phase. The first one is always in minimum fluidization condition, then the whole amount of excess gas that is passing through the bed in bubble form, forming the bubble phase. Bubbles have been modeled as spheres without catalyst particle inside them. The model also includes the wake phase, calculated starting from the bubble-phase fraction but with the same characteristics of the emulsion phase (same void fraction and then presence of catalytic particles).

The functioning of hydrogen production and separation through FBMR, is described by a 1D continuous model, referred to coordinate z (representing the vertical length of the reactor), in which material balances in each element dz and an overall energy balance have been performed.

The overall energy balance is included in the model to ensure the autothermal behaviour of the reactor, and it is reported in Equation (3.1), where $\dot{n}$ represents the molar flow rate, while h is the molar enthalpy.

$$\dot{n}_{feed} \cdot h_{feed} = \dot{n}_{retentate} \cdot h_{retentate} + \dot{n}_{H_2,permeate} \cdot h_{H_2,permeate} \qquad (3.1)$$

In each element dz material balance is performed and it is reported in Equation (3.2).

$$\frac{\partial \dot{n}_i(z)}{\partial z} = A_R(z) \cdot \rho_p \cdot \left(1 - \varepsilon_{mf}(z)\right) \cdot \delta_{e/w} \sum_{j}^{NR} r_{R,j}(z) \nu_{j,i} \pm A_R \cdot \delta_b(z) K_{be}(z) \left(C_{i,b}(z) - C_{i,e}(z)\right) - F_{H_2,perm}(z) \qquad (3.2)$$

Material balance is performed for each chemical component i and both for emulsion or wake ($\delta_{e/w}$) and bubble phase (δ_b) and it considers inlet-outlet variation in the single element for the molar flow of each component $\dot{n}_i(z)$. The variation of the single component molar flow depends on two main terms, which are related to:

- the components production/consumption in the reaction j. Reaction rates $r_j(z)$ formulation has been detailed in [30], for SMR and for WGS reaction and they are multiplied by stochiometric coefficient of component i in reaction j ($\nu_{j,i}$). Instead, for methane oxidation oxygen is assumed to be totally converted in the first 5 cm, due to the faster development of methane oxidation. In this term: $A_R(z)$ is the reactor cross section area, ρ_p is the density referred to catalyst particle, while $\varepsilon_{mf}(z)$ is the void fraction in minimum fluidization conditions.
- the concentration difference of component i between bubble (sign plus is used) and emulsion phase (sign minus is used) ($C_{i,b}(z) - C_{i,e}(z)$), which generates a flux between these two phase. In this term $K_{be}(z)$ is the exchange coefficient between bubble and emulsion phase.

If the mass balance is performed for hydrogen, an additional term related to permeated hydrogen for unit of membrane length ($F_{H_2,perm}(z)$) should be considered. Its formulation is displayed in Equation (3.3), and its amount is obviously affected by diameter ($d_{membranes}$) and number of membranes ($N_{membranes} \cdot$).

$$F_{H_2,perm}(z) = N_{membranes} \cdot \pi \cdot d_{membranes} \cdot J_{H_2,perm}(z) \qquad (3.3)$$

Computing an integration, as shown in (3.4), along the whole membrane, of the hydrogen permeated, it is possible to compute the whole amount of hydrogen separated, and then produced, by the plant.

$$\dot{n}_{H_2,perm} = \int_{start\ mem}^{end\ mem} F_{H_2,perm}(z) \cdot dz \tag{3.4}$$

In Equation (3.3) and in Equation (3.4), hydrogen permeation flux per unit of membrane area ($J_{H_2,perm}(z)$) is introduced and it is evaluated as in through Richardson's equation, shown in Equation (3.5). Hydrogen permeation flux, as previously introduced, is driven by difference of partial pressure between the two sides of the membrane. It is related also to exponent n, hydrogen permeance, modeled through an Arrhenius type equation and to an activation energy $E_{a,perm}$, derived by experiments. Computational values adopted are taken from Table 3.1.

$$J_{H_2,perm}(z) = \frac{P_{H_2}^0 \cdot exp\left(\frac{-E_{a,perm}}{RT}\right)}{t_{SL}} \cdot \left(p_{H_2,retentate}^n(z) - p_{H_2,permeate}^n(z)\right) \tag{3.5}$$

Besides energy and mass balances, fluid dynamics relation to describe the behaviour of fluidized bed membrane reactor are needed to complete the model. The relations adopted have been reported in [30].

FBMR model provides a large variety of variables suitable for different analysis and different goals. The performance of membrane reactors in different operating conditions are typically assessed through HRF, already introduced in chapter *2.Methodology* and computed through Equation (2.1) which is the main Key Performance Indicator (KPI). Besides HRF, pure hydrogen production, which is the mass of hydrogen separated per unit time, is another important performance indicator.

4 Electrolyzer

In this chapter the model, developed in Microsoft Excel, of the PEM electrolyzer used for oxygen production is explained in detail and it is based on modelling PEM electrolyzer polarization curve.

4.1. Electrolyzer Model: $i - V$ curve

The performance of an electrolyzer are typically represented by $i - V_{cell}$ curve (also called polarization curve), where the current density i forms the x-axis, while the cell voltage V forms the y-axis of the plane. Each couple of current density and cell voltage belonging to this curve is a specific operating point, which will provide different values of overall current and overall voltage, depending on the area of the cell and on their number, according to Equation (4.1) and to Equation (4.2), since the cells are placed in series to form the stack.

$$I = i \cdot A_{cell} \tag{4.1}$$

$$\Delta V = V_{cell} \cdot N_{cell} \tag{4.2}$$

Once that the operating point, the number of the cells and their area are defined, the power P required by the electrolyzer is simply given by Equation (4.3) [41]:

$$P = I \cdot \Delta V \tag{4.3}$$

This logic flow could be applied also in a reverse way, meaning that, once an electric power, inside the operating range of the given electrolyzer, is provided, it is possible to obtain the current density and the cell voltage for the single cell.

The polarization curve of an electrolyzer represents its performance, since an operating point provides us the power needed to produce a certain amount of hydrogen, and this power is higher than the one that would be used in ideal conditions. Indeed, during functioning, losses are presents, and greater the losses are, greater the power required is.

Thus, the different losses provoke an increase of the reversible cell voltage E that should be provided to the cell, according to Equation (4.4) [21].

$$V = E + V_{act} + V_{ohm} + V_{trans} \tag{4.4}$$

The reversible cell voltage E, also called open circuit voltage (OCV), represents the voltage to be provided to the electrolyzer in ideal conditions; in the reality this only happens when the current density i is zero, therefore the reversible cell voltage is the offset in y-axis of $i - V$ curve; an example is provided by Figure 4.1.

V_{act} is the activation voltage, a voltage increase (overvoltage) to break the molecular bonds, therefore, it is needed to activate the electrochemical reaction [21]. V_{ohm} represents the ohmic losses, provoked by the resistance to the electrons flow and to the protons' conduction, respectively inside the current collector and the separator plates, and through the membrane; V_{trans} (also called diffusion voltage) is an overvoltage due to mass transport resistance inside the porous electrode [42]. All these losses are summed up to identify the real voltage required in order to have a certain current density and hence a certain hydrogen production.

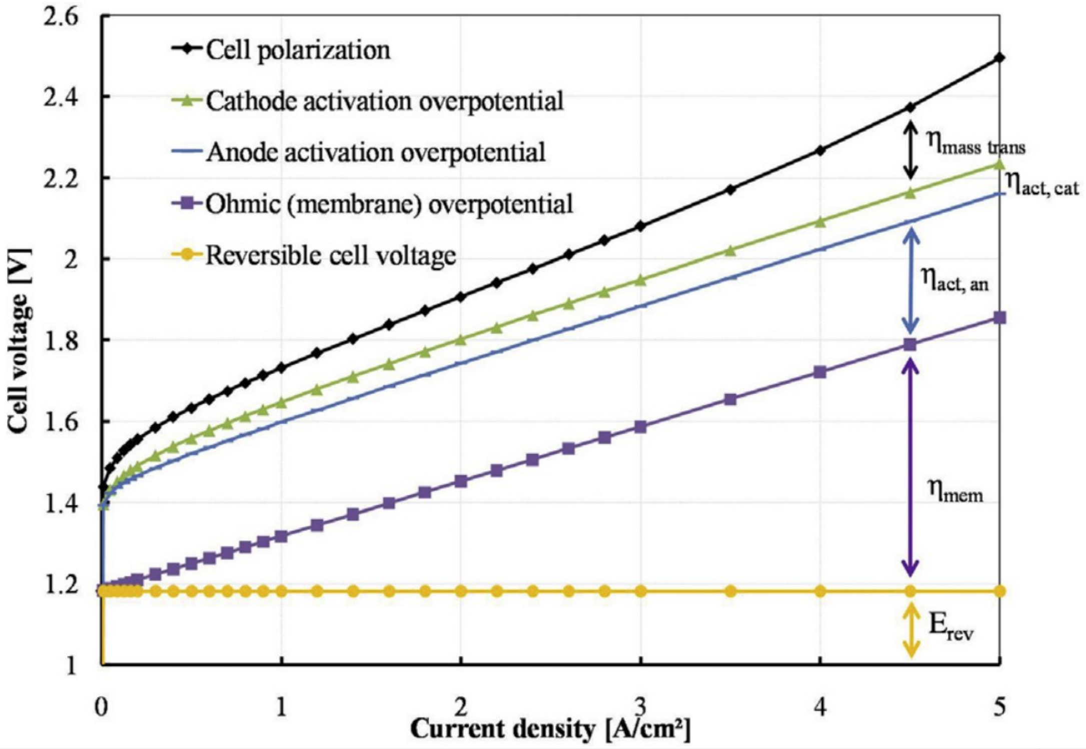

Figure 4.1 - Example of polarization curve at 80°C and 1 bar [43].

Therefore, in order to properly simulate the functioning of a PEM electrolyzer, a polarization curve should be modeled in each part, starting from OCV in Section 4.1.1.

4.1.1. Open circuit voltage (OCV)

The reversible cell voltage E is typically computed through Nernst Equation (Equation (4.5)), but Gibbs Free Energy equation procedure could be used too [21], [44].

$$E = E_0 + \frac{RT}{z_{el}F}\ln\left(\frac{\alpha_{H_2}\alpha_{O_2}^{0.5}}{\alpha_{H_2O}}\right) \tag{4.5}$$

In Equation (4.5) E_0 is the reversible voltage at standard pressure, computed as in Equation (4.6) [21], $R = 8.314\frac{J}{mol\cdot K}$ is the universal gas constant, T is the average temperature at which the electrolyzer works, z_{el} is the mole number of electrons transferred to fulfill the reactions ($z_{el} = 2$ in this case), $F = 96485.3\frac{C}{mol}$ is the Faraday constant, and α_i is the activity of the species i, equal to 1 for liquid water and equal to $\alpha_i = P_i/P_0$ for ideal gas, where P_i is the partial pressure of species i and P_0 is the standard atmospheric pressure [42].

$$E_0 = 1.229 - 0.9\cdot 10^{-3}\cdot(T - 298) \tag{4.6}$$

From Equation (4.5) and Equation (4.6) it is easy to point out that the open circuit voltage is affected by both temperature and pressure and their effect are shown in Figure 4.2, which are computed through the previously mentioned equations.

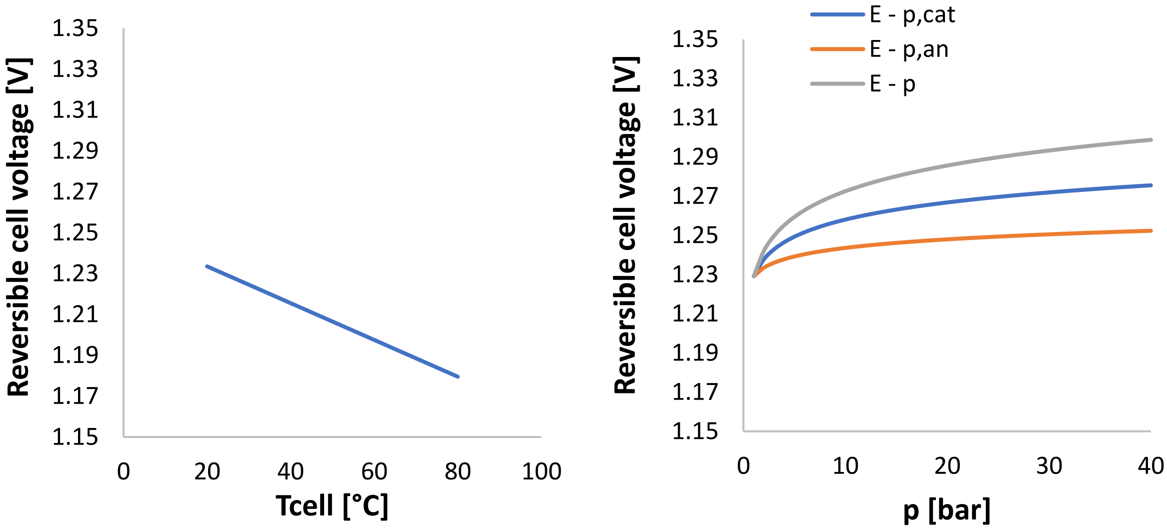

Figure 4.2 – Left: E_0 at standard pressure as function of cell temperature. Right: effect of varying pressure (at cathode only, at anode only, both) at standard temperature.

It is easy to understand that operation at high temperature and low pressure is more convenient from an electricity consumption point of view, since a lower voltage should be provided.

The chosen range of temperature (20°C-80°C) in Figure 4.2 is the typical one for proton exchange membrane electrolyzer, even if temperature around 100°C are reported too [45], [21].

Unlike temperature, increasing the operative pressure provokes a greater energy consumption, because the voltage trend, at standard temperature, as function of pressure is growing up. The pressure affects the activity of the species, and since it is possible to operate PEM electrolyzer in unbalanced pressure condition (cathode pressure greater than anode pressure [46]), in Figure 4.2 also the increasing of the pressure at a single electrode is shown. The biggest potential increase is obviously present when both cathode and anode pressure are rising up, and this will be the case of this project since both hydrogen and oxygen are required to be at medium-high pressure.

4.1.2. Activation Losses

Activation overpotential represents a loss which takes into account the need of providing a certain amount of potential to overcome the energy of the molecular bonds and therefore to activate the reactions.

It is given by two contributions (as explicated in Equation (4.7)) which are related to the two electrodes where the electrochemical reactions happen, and they are modeled in Equation (4.8) and in Equation (4.9) thanks to the Butler-Volmer equation applied to the single electrode [19], [21].

$$V_{act} = V_{act,cat} + V_{act,an} \tag{4.7}$$

$$V_{act,cat} = \frac{RT_c}{\alpha_c F} \operatorname{arcsinh}\left(\frac{i}{2i_{0,cat}}\right) \tag{4.8}$$

$$V_{act,an} = \frac{RT_a}{\alpha_a F} \operatorname{arcsinh}\left(\frac{i}{2i_{0,an}}\right) \tag{4.9}$$

In Butler-Volmer equation $R = 8.314 \frac{J}{molK}$ is the universal gas constant, $F = 96485.3 \frac{C}{mol}$ is the Faraday constant, T_c and T_a are the temperatures at the cathode and at the anode, $\alpha_c = 0.5$ and $\alpha_a = 2$ are typical values for the charge transfer coefficient at the cathode and at the anode respectively [21].

Regarding the exchange current density at the cathode ($i_{0,cat}$) and at the anode ($i_{0,an}$) there is not agreement in literature, founding values with discrepancy of seven order of magnitude too [21], [44]. They have an important role in the activation losses, because they define the electrochemical reaction rate at equilibrium [47], and their value is affected by different factors like temperature, catalyst material, utilization and loading [21]. The effect of exchange current density is that: greater their values are, lower the activation potentials will be, thus better the performance of the electrolyzer are achievable [47].

The values, assuming Pt based catalysts, have been chosen from Han et al. [42], since similar ranges of operating pressure and temperature have been tested, and they are equal to $i_{0,cat} = 1.0 \cdot 10^{-1} \frac{A}{cm^2}$ and $i_{0,an} = 2 \cdot 10^{-6} \frac{A}{cm^2}$; anyway, seen the disagreement in literature among the values for these variables, and the difficulty to properly assess them, a further analysis with other values is reported in Section 4.1.8.

In Figure 4.3 the contribution of activation losses at $T = 25\,°C$ and $P = 101325\,Pa$ are shown, and it is possible to point out that the main dissipation source is present at the anode, where the energy required to drive the electrochemical reaction is greater than the one at the cathode, this because the kinetics of water splitting reaction, happening at the anode side, is slower than the hydrogen evolution reaction, as expressed in [48], [49].

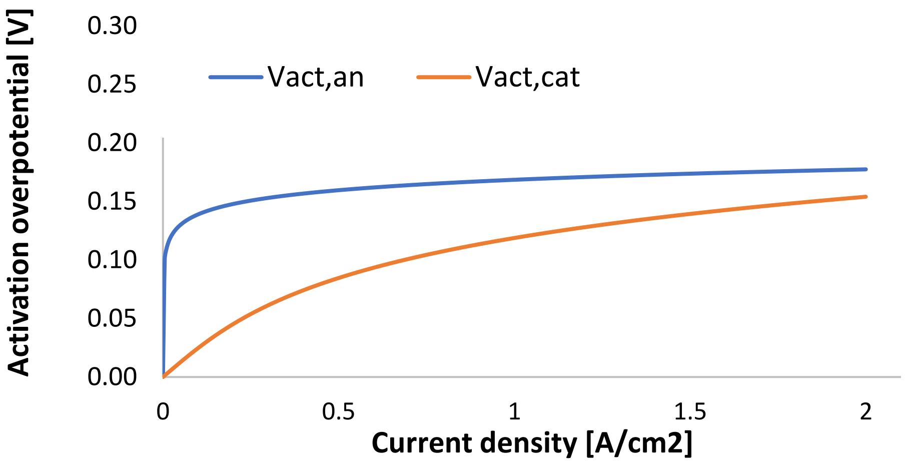

Figure 4.3 - Contribution in terms of overvoltage of activation losses.

4.1.3. Ohmic Loss

The material resistance to proton flux inside the membrane (which is the predominant dissipation with respect to electrons flux resistance) is widely computed through a standard Ohm's Law, as reported in Equation (4.10), evaluating this loss as proportional to the current density [19], [21], [42], [50]. The membrane thickness δ_m has been assumed equal to 183 μm, value taken from the most used membrane, which is N117 [51].

$$V_{ohm} = \frac{\delta_m}{\sigma_m} \cdot i \tag{4.10}$$

It is evident that the membrane properties are fundamental in assessing the ohmic overpotential, in particular the thickness δ_m and the conductivity σ_m, which is affected by the membrane hydration λ_m and the temperature, as reported in Equation (4.11) and in Equation (4.12). In Equation (4.12) a is the membrane water activity which is always equal to 1 for electrolyzer, since they operates under 100% of relative humidity [50].

$$\sigma_m = (0.005139 \cdot \lambda_m - 0.003260) \cdot exp^{\left[1268\left(\frac{1}{303}-\frac{1}{T}\right)\right]} \tag{4.11}$$

$$\lambda_m = 0.043 + 17.81 \cdot a - 39.85 \cdot a^2 + 36 \cdot a^3 \tag{4.12}$$

In Figure 4.4 it is possible to appreciate the effect of temperature on the membrane resistivity: higher the temperature, higher the conductivity, lower the ohmic loss.

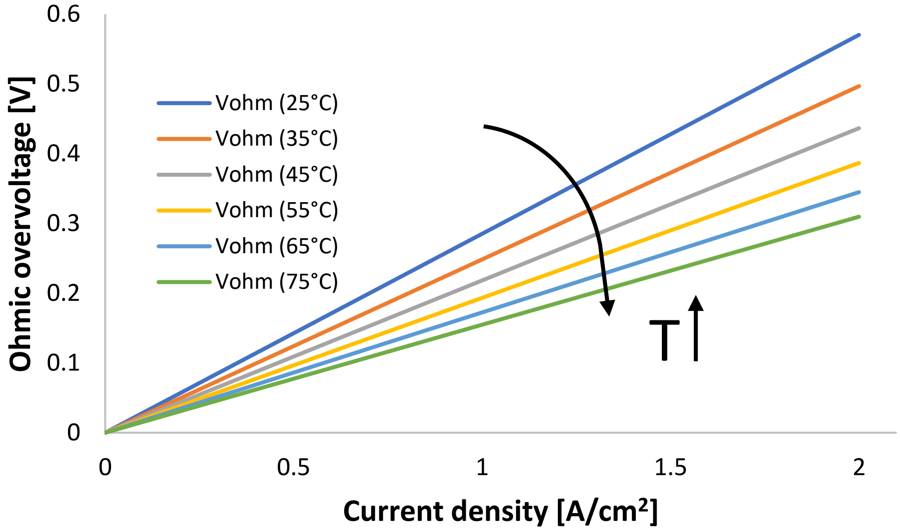

Figure 4.4 - Ohmic losses at different temperature.

4.1.4. Diffusion losses

Diffusion loss is caused by the opposition to mass transport of gas and of liquid water between the electrodes' surface and the electrolyte [48], [42].

This loss could be neglected at low current density, but it becomes remarkable at high value of current density $\left(i > 1.6\frac{A}{cm^2}\right)$ [52]. Indeed, at high current density the molecules reacting is increasing and they could impede the access towards active site, slowing down the reaction [19]. This effect could be also seen in Figure 4.5.

This transfer loss is modelled through an expression based on current density limit i_{lim}, assumed equal to $i_{lim} = 2.01\frac{A}{cm^2}$ [21], it is typically used [50], [19]:

$$V_{trans} = -\frac{RT}{n_{el}F}\ln\left(1 - \frac{i}{i_{lim}}\right) \tag{4.13}$$

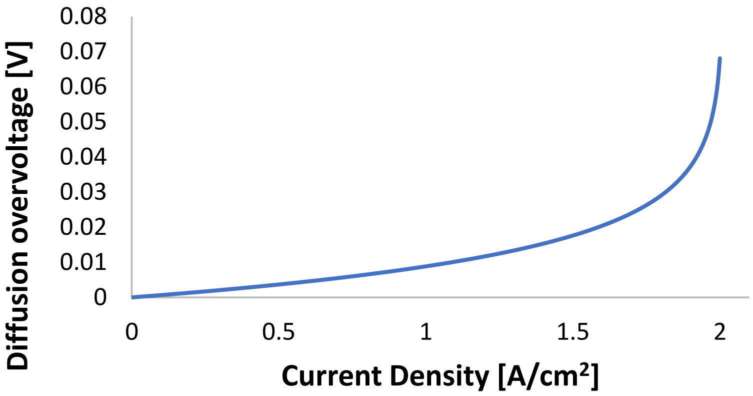

Figure 4.5 - Diffusion overpotential contribution.

4.1.5. Polarization Curve

Once the losses are modelled, the polarization curve is defined too, as in Figure 4.6. From the $i - V$ curve (voice "V" in Figure 4.6) it is possible to appreciate the different contribution of each single loss, at fixed conditions of temperature and pressure. The different losses are affected by several factor, and their percentage on the total sum of losses varies depending on the operating conditions, the current density and so on, as in Figure 4.7.

Similar polarization curve, to the one reported in Figure 4.6, in terms of losses contribution and general trend can be found in literature [43], [48], [53], hence the model of the $i - V$ curve could be assumed reliable.

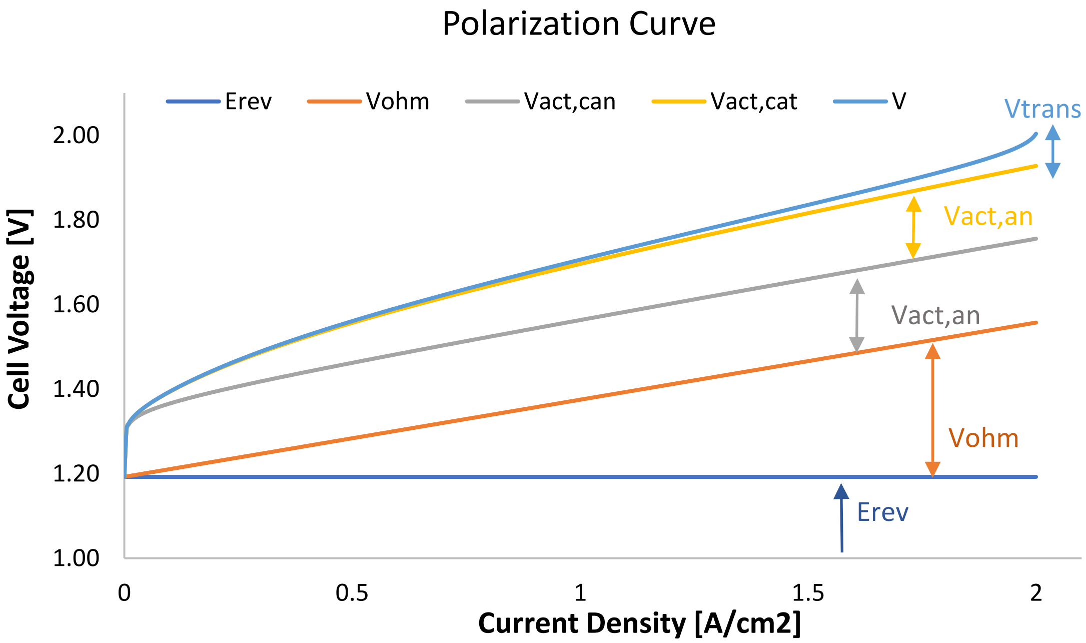

Figure 4.6 - Polarization curve and contribution of the different losses at 60 °C and 1 atm

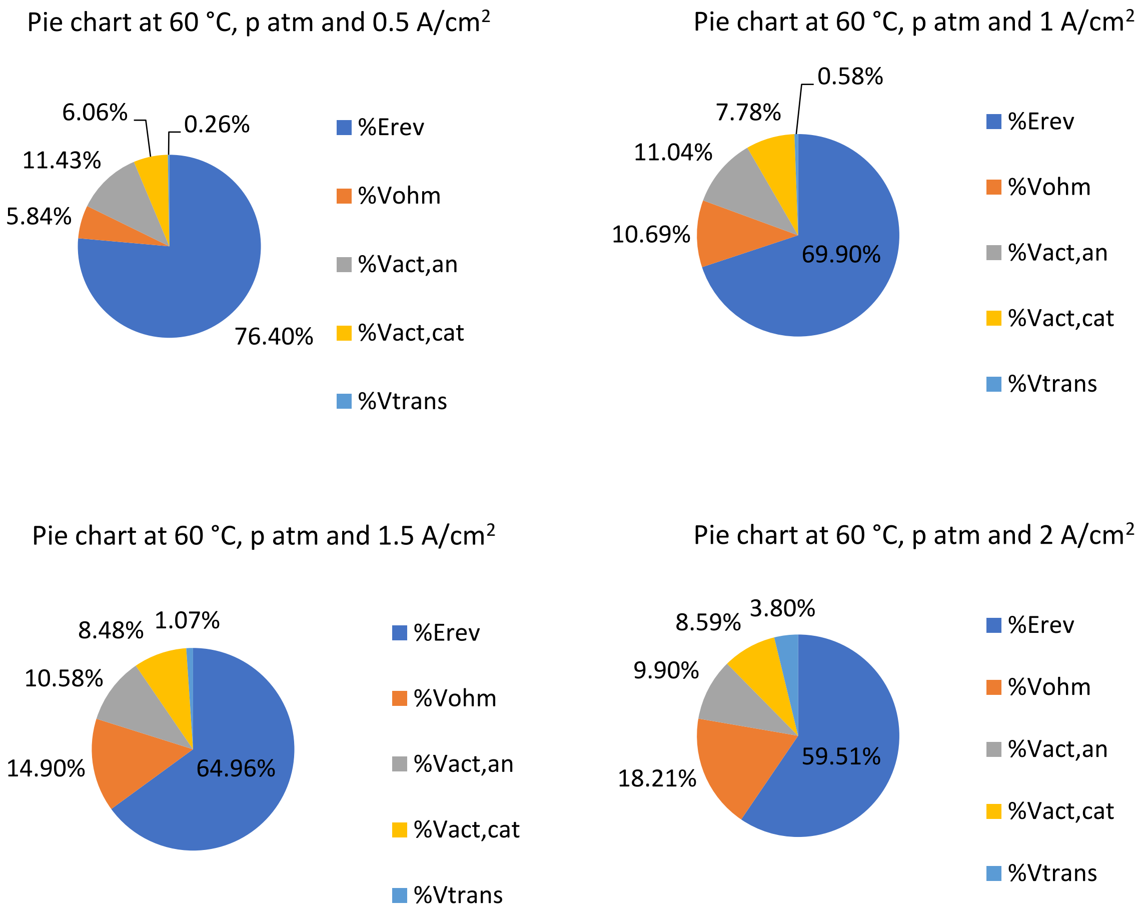

Figure 4.7 - Losses contributions at 60 °C, 1 atm and at different current density

4.1.6. Effect of temperature

To furtherly validate the developed model, an evaluation concerning the effect of temperature is carried out. The temperature affects the polarization curve directly varying the open circuit voltage Equation (4.5), Equation (4.6), the activation overpotential (Equation (4.8), Equation (4.9), the diffusion overvoltage (Equation (4.13)) and the conductivity of the membrane influencing the ohmic loss (Equation (4.11)).

Increasing the temperature is beneficial for the performance of the electrolyzer, since the voltage required at the same current density is reducing, like in Figure 4.8. This happens because raising up the operating temperature is decreasing every loss but the activation overpotential [42].

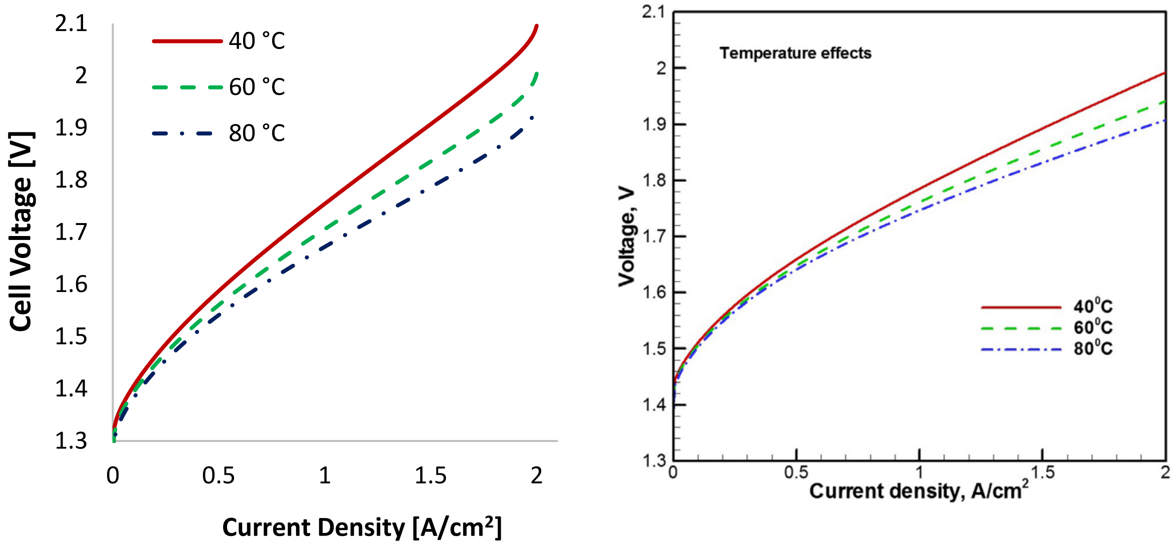

Figure 4.8 – Left: effect of temperature at 1 atm on the modeled polarization curve. Right: effect of temperature at 1 atm in [42].

Similar results, as shown in Figure 4.8, are obtained in [42] or in [48], hence the modeled $i - V$ curve is reacting well to temperature change.

The small differences between the two figures are due to a lower membrane thickness used in [42] and due to the hypothesis of membrane hydration λ_m always equal to 22 (thus better humidification) and not calculated through Equation (4.12).

4.1.7. Effect of pressure

Another analysis should concern the effect of pressure on the polarization curve and a comparison with literature's examples could furtherly validate the developed model. In Figure 4.9 the effect of cathode pressure with anode at atmospheric condition and cell temperature at 80°C is shown; these conditions are chosen in order to have a fair comparison with Bo Han et al. [42] analysis. Since the trends are similar, it is possible to state that the developed model is reacting well to change of pressure.

The pressure surely affects open circuit voltage (Equation (4.5)), but a pressurization operation would hinder diffusion movement of ions and water too, therefore losses are greater at high pressure; anyway an electrolyzer typical works at medium-high pressure, in order to exploit electrochemical compression and then to avoid the need of a further compression [42].

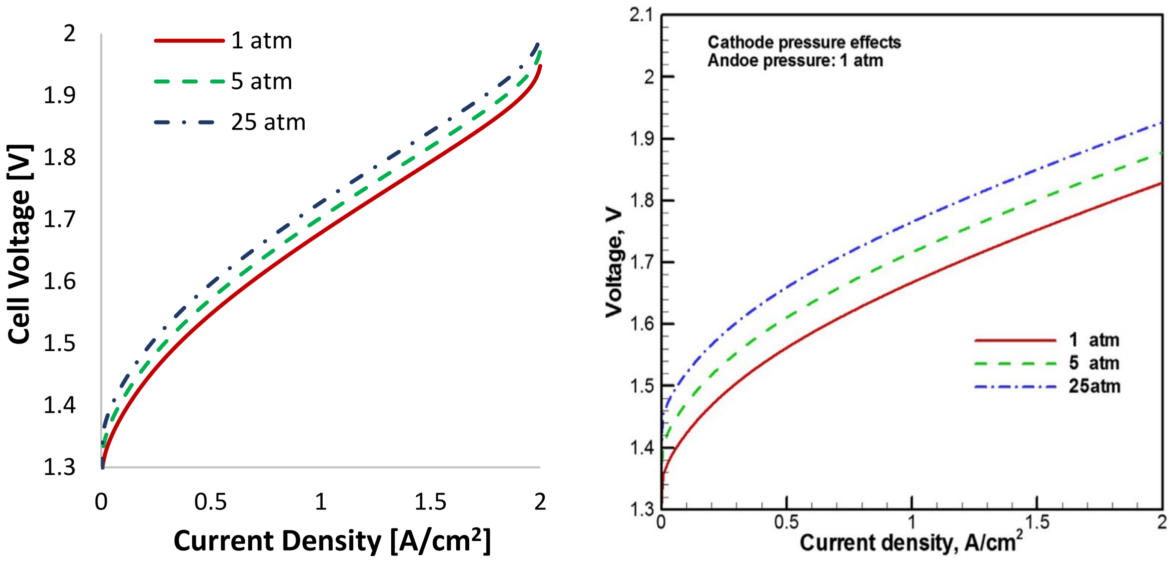

Figure 4.9 – Left: cathode pressure effect on the modeled polarization curve at 80°C and anode at 1 atm. Right: cathode pressure effect at 80°C and anode at 1 atm in [42].

4.1.8. Effect of Exchange Current Density

As said in Section 4.1.2, there is large variety of exchange current density (ECD) for PEM electrolyzer in literature, even with seven order of magnitude of discrepancy [21], [44]. In order to validate the developed model, comparing it with literature's examples, and to properly understand the effect of these characteristics, different values for anode and cathode exchange current density have been tested, in accordance with [42].

Bo Han et al. [42] proposed to test the values reported in Table 4.1, obtaining the results shown in Figure 4.10 and in Figure 4.11. The modeled polarization is tested under the same exchanged current density values reported in Table 4.1, and the resulting trend are reported in Figure 4.10 and in Figure 4.11.

$i_{0,an}$	$i_{0,cat}$
$1 \cdot 10^{-6}$	$1 \cdot 10^{-1}$
$1 \cdot 10^{-8}$	$1 \cdot 10^{-3}$
$1 \cdot 10^{-10}$	$1 \cdot 10^{-5}$

Table 4.1 - Exchange current density values tested in [42].

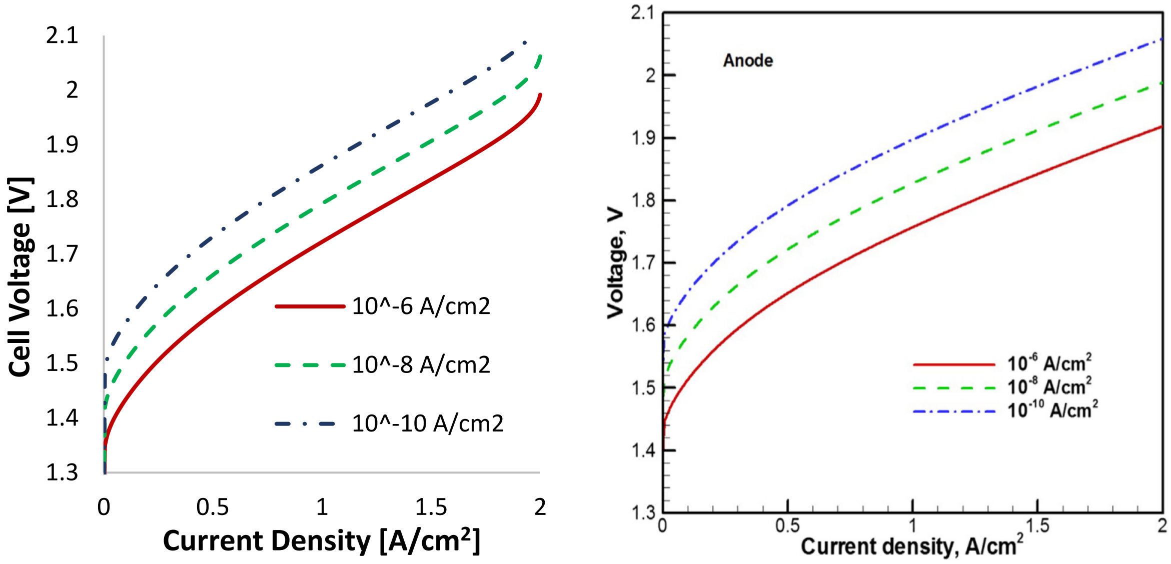

Figure 4.10 – Left: anode ECD effect on the modeled polarization curve at 80 °C, anode at 1 atm, cathode at 13.6 atm. Right: anode ECD effect on polarization curve at 80 °C, anode at 1 atm, cathode at 13.6 atm in [42].

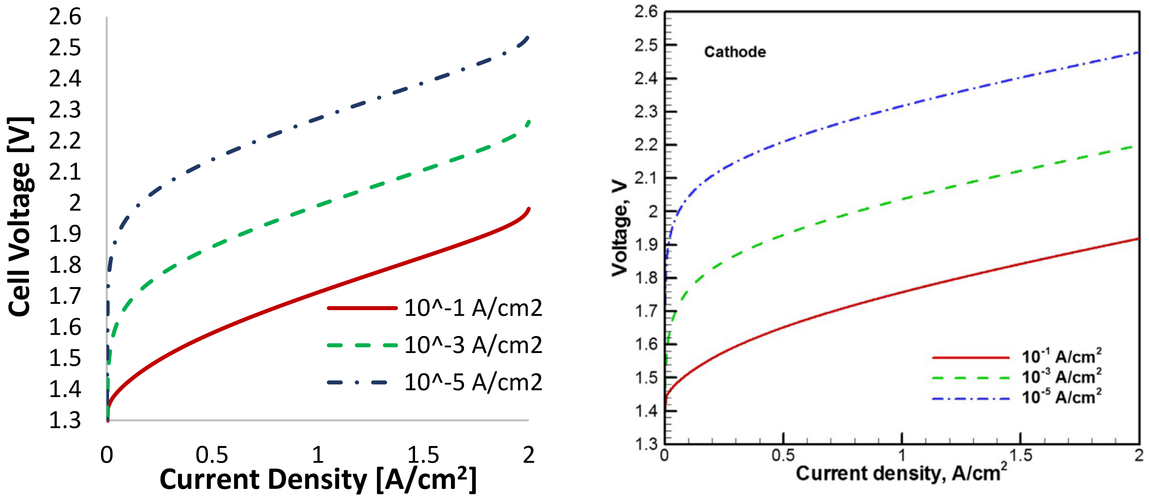

Figure 4.11 - Left: cathode ECD on the modeled polarization curve at 80 °C, anode at 1 atm, cathode at 13.6 atm. Right: cathode ECD on polarization curve at 80 °C, anode at 1 atm, cathode at 13.6 atm in [42].

The modeled polarization curve in equal condition of pressure and temperature, but in different conditions regarding the structuring of the electrolyzer (thickness of membrane…), is performing in a coherent way the change of different current density, hence the modeled $i - V$ curve is reacting in a satisfactory way.

4.2. Hydrogen and Oxygen production

4.2.1. Fundamentals of Hydrogen and Oxygen production

Once that a certain electric power (inside the operative bounds) is provided to the stack of a PEM electrolyzer, water electrolysis reaction starts, and hydrogen and oxygen are produced, respectively at the cathode and at the anode, following Equation (4.14) and Equation (4.15) [48], [57]:

$$\dot{n}_{H_2 ideal} = \frac{i}{2F} A_{cell} N_{cell} \tag{4.14}$$

$$\dot{n}_{O_2 ideal} = \frac{i}{4F} A_{cell} N_{cell} \tag{4.15}$$

The equations reported above allow to identify the ideal flow of H_2 and O_2 produced, but actually, losses, like hydrogen crossover for example, are happening during electrolyzer functioning [58].

In order to consider these phenomena, an efficiency, called Faraday efficiency, is introduced. It is defined in Equation (4.16) and represents the fraction between the hydrogen produced and the theoretical producible with the same electric power in input [57].

$$\eta_{Faraday} = \frac{\dot{n}_{H_2}}{\dot{n}_{H_2,ideal}} \tag{4.16}$$

Literature around Faraday efficiency for PEM electrolyzer is not wide. To take into account it, a four-parameter model has been considered and reported in Equation (4.17) taken from Yodwong et al. [58].

$$\eta_{Faraday} = (a_1 \cdot p_{cat} - a_2) \left(\frac{I}{A}\right)^b + c \tag{4.17}$$

In Equation (4.17) A is the active area (m^2) of the electrolyzer ($A = A_{cell} N_{cell}$), I is the current of the stack ($I = i \cdot A_{cell}$), while the other parameters are taken from Yodwong et al. [58] and reported in Table 4.2.

a_1	a_2	c
-0.0034	-0.001711	1

Table 4.2 – Parameters of the linear model developed in Yodwong et al. [58].

The model can be extended up to medium pressure, with a value of 30 bar and below, which is of our interest, inside the admitted pressure [58]. Through Faraday's efficiency it is possible to compute the real gas production:

$$\dot{n}_{H_2} = \frac{i}{2F} A_{cell} N_{cell} \eta_{Faraday} \tag{4.18}$$

$$\dot{n}_{O_2} = \frac{i}{4F} A_{cell} N_{cell} \eta_{Faraday} \tag{4.19}$$

4.2.2. Efficiency of H2 production – Effect of Temperature

Given hydrogen and oxygen production, it is possible to assess the performance of an electrolyzer through different indexes, for example the stack efficiency, defined in LHV basis (Equation (4.20)) or in HHV basis (Equation (4.21)) [57].

$$\eta_{stack}^{LHV} = \frac{P_{H_2}}{P_{elec}} = \frac{\dot{m}_{H_2} \cdot LHV_{H2}}{\Delta V \cdot I} \tag{4.20}$$

$$\eta_{stack}^{HHV} = \frac{P_{H_2}}{P_{elec}} = \frac{\dot{m}_{H_2} \cdot HHV_{H2}}{\Delta V \cdot I} \tag{4.21}$$

A comparison with literature’s example has been done with Mohanpurkar et al. [59] and reported in Figure 4.12.

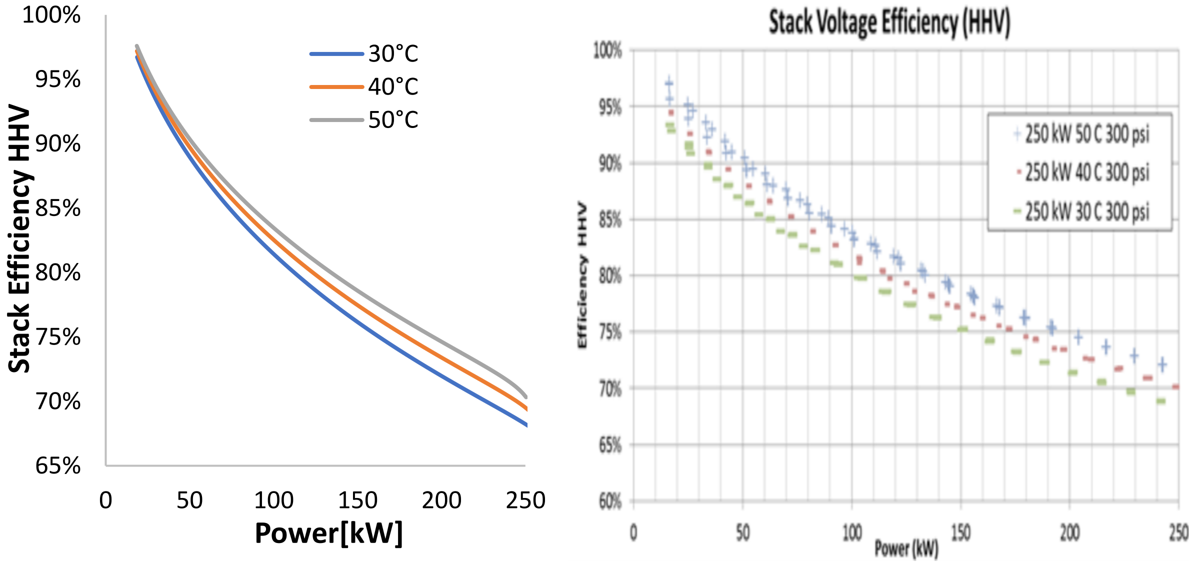

Figure 4.12 – Left: temperature effect on HHV stack efficiency of the modeled PEM electrolyzer (1 atm, 200 cells, 300 cm^2). Right: temperature on HHV stack efficiency from [59].

The trends and the values of the modeled electrolyzer, in the same operating conditions of temperature, pressure and stack power could be considered coherent with the ones in Mohanpurkar et al. [59], hence also from this point of view the developed model could be considered reliable.

4.2.3. Efficiency of H2 production – Effect of Pressure

Another interesting aspect to consider is the effect of pressure on the performance. It is possible to highlight that the main loss in efficiency happens when the electrolyzer is forced to work at pressure higher than the atmospheric one, while the dissipation become smaller if the electrolyzer increases the working pressure from 20 bar to 30 bar, for example.

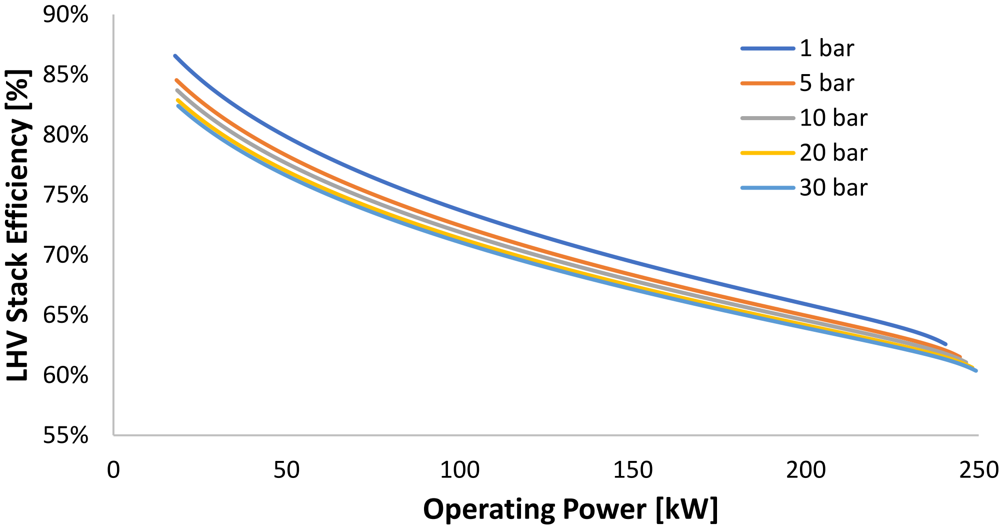

Figure 4.13 - Effect of pressure on stack efficiency based on LHV from the modeled PEM electrolyzer (60 °C, 500 cells, 100 cm²).

4.2.4. Efficiency of H2 production – Effect of cell number and cell area

Moreover, the effect on efficiency of varying cell number should be considered too. Unlike the effect of pressure and temperature, varying cell number affects power too, as it is possible to see in Figure 4.14. Anyway, this does not affect the value of maximum and minimum stack efficiency. Indeed, if Faraday's efficiency is neglected (it has a small influence and only at low current density [58]), stack efficiency does not depend on cell number, because it depends only on cell voltage and other constant value (molar mass, LHV, Faraday's constant), as shown in (4.22), merging Equation (4.21) and Equation (4.14).

$$\eta_{stack}^{LHV} = \frac{\dot{m}_{H_2} \cdot LHV_{H2}}{\Delta V \cdot I} = \frac{\frac{i}{2F} \cdot A_{cell} \cdot N_{cell} \cdot MM \cdot LHV}{i \cdot A_{cell} \cdot V_{cell} \cdot N_{cell}} = \frac{MM \cdot LHV}{2F \cdot V_{cell}} \tag{4.22}$$

Looking to Figure 4.14 where the effect on stack efficiency of cell number and cell area is shown, it is possible to highlight that working at low load is beneficial for an electrolyzer, as already pointed out. Indeed, cell number does not affect the polarization curve, but its variation is mainly related to hydrogen production quantity requirements.

Concerning cell area effect, a trade-off between cell area (thus electrolyzer size) and cost, and electricity purchasing price arises. Meaning that at larger cell area the current density to produce a certain amount of hydrogen is lower, therefore the input power is lower too, reducing the cost of electricity per kilogram of hydrogen produced. Nevertheless, this lower cost is a consequence of the big size of the electrolyzer and thus it is a consequence of the higher investment cost for the technology.

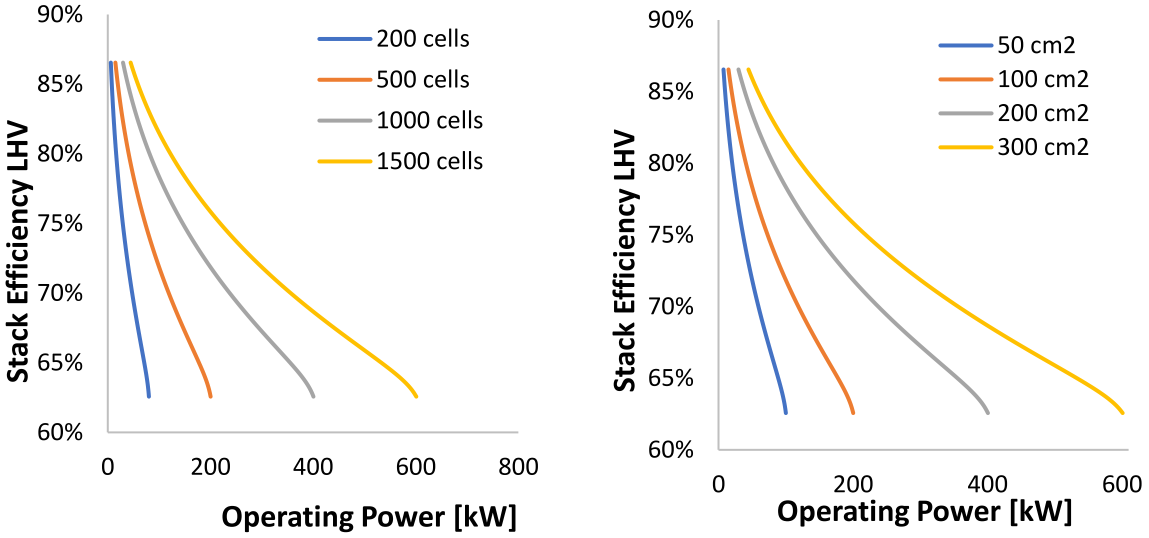

Figure 4.14 – Left: effect of varying cell number on LHV stack efficiency of the modeled PEM electrolyzer (1 atm, 60°C, 100 cm^2). Right: Effect of varying cell area on stack efficiency based on HHV of the modeled PEM electrolyzer (atmospheric pressure, 60°C, 500 cells).

4.3. PEM power – PEM production relations

In order to have an efficient match between the electrolyzer power in input and hydrogen and oxygen production, a logic scheme, and the relations to make it effective, should be modeled. Through different relations, shown in Figure 4.15, it will be possible to compute the hydrogen and oxygen production starting from an input power to the electrolyzer (which will be provided by PV field, by battery storage, or by the grid depending on the configuration chosen and the operating conditions) to find the operative point in the polarization curve. Obviously, the following logic scheme (and relations) could be applied in the other way around too, meaning that once a certain production is required, it is possible to retrieve the input power needed.

$$Power_{PEM}[kW] \leftrightarrow Cell\ Voltage[V] \leftrightarrow Current\ Density\left[\frac{A}{cm^2}\right] \leftrightarrow H_2, O_2\ produced\left[\frac{mol}{s}\right]$$

Figure 4.15 - Logic scheme of H_2, O_2 production from PEM input power.

Each arrow in Figure 4.15 it is representing a relation where the input is the left argument and the output is the right one (or vice versa whether a certain production is required). Each of these relations will be explained in the following sections, but they are computed to be able of having hydrogen and oxygen production once a given input power is provided to the electrolyzer.

The starting point is the input power to the electrolyzer, which should provide us a cell voltage, through which it is possible to have access to the polarization curve, hence to a current density, which allows us to compute H_2 and O_2 production thanks to Equation (4.18) and Equation (4.19).

4.3.1. Cell Voltage – PEM Power relation

Starting from the input power to the electrolyzer, it is necessary to obtain back a cell voltage for any value of input power. In order to do it in an easy and convenient way (the relation should update and be valid even if the cell area, cell number or the operating conditions change) a cubic regression between input power and cell voltage is computed and it is shown in Figure 4.16 and defined in Equation (4.23).

$$V_{cell}(P) = a + b \cdot P + c \cdot P^2 + d \cdot P^3 \tag{4.23}$$

The parameters in Equation (4.23) change if cell number, cell area or operating conditions have been changed, this because the electrolyzer power changes too. Therefore a model which can update itself it is necessary to provide techno-economic analysis based on size and on production of the electrolyzer. The parameters are obtained through "LINEST function" in Excel, and the polynomial has been chosen to be a cubic one because the R^2 index is practically equal to unity.

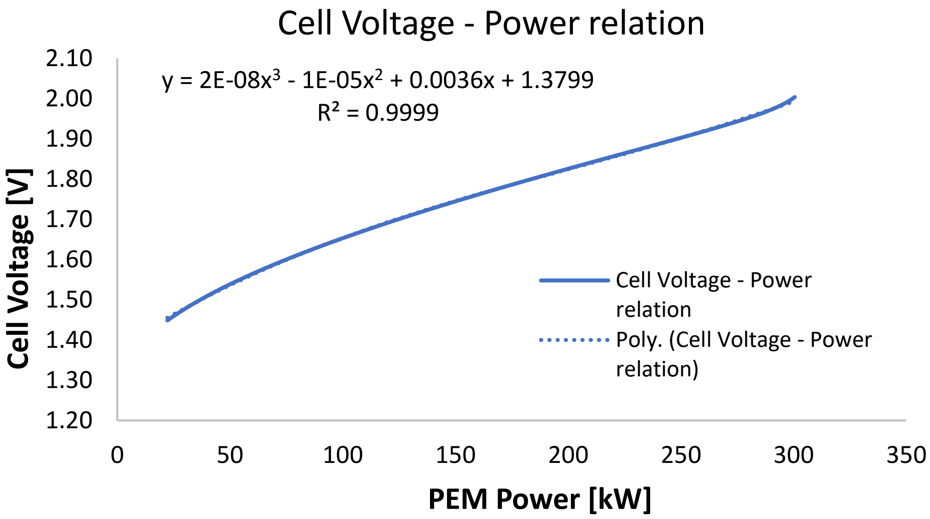

Figure 4.16 - Cell Voltage - PEM Power relation (200 cm², 250 cells, atmospheric pressure, 60°C)

4.3.2. Current density – Cell Voltage relation

Once the cell voltage has been computed, it is possible to enter in the polarization curve and extrapolate the current density value. To do that a current density – cell voltage regression has been done, in order to have, for every possible cell voltage, a given current density. Obviously, also this relation can update itself when cell number, cell area or operating condition are changed.

$$i(V_{cell}) = e + f \cdot V_{cell} + g \cdot V_{cell}^2 + h \cdot V_{cell}^3 \tag{4.24}$$

A cubic polynomial has been chosen to describe this relation too, since R^2 value is close to 1.

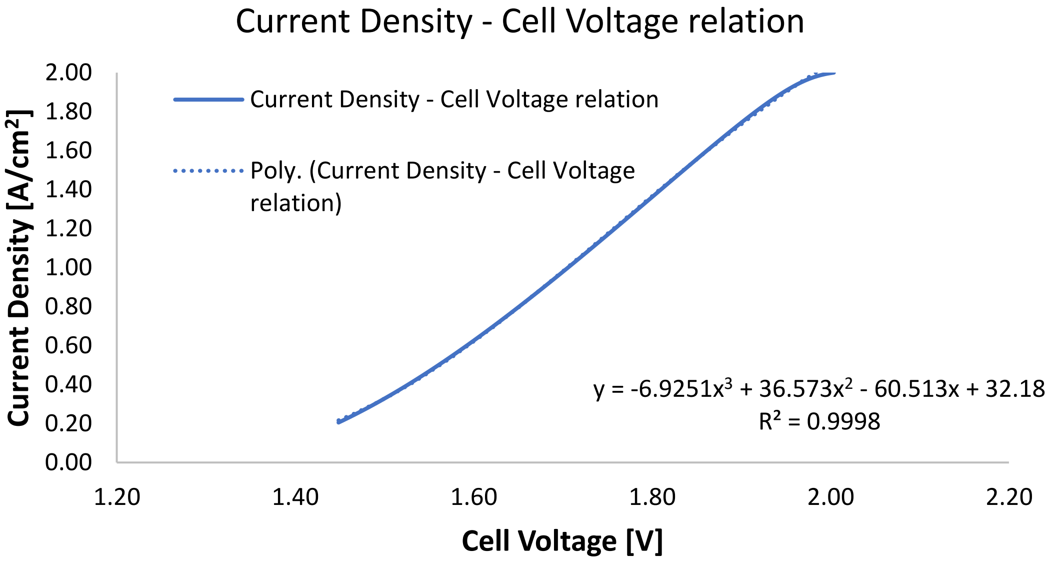

Figure 4.17 – Current Density - Cell Voltage relation (200 cm², 250 cells, atmospheric pressure, 60°C)

4.3.3. Hydrogen and oxygen production

Given the current density produced by a certain input power it is easy to compute the gas production of the electrolyzer. First of all, there is the need to evaluate the Faraday efficiency, secondly by simply applying Equation (4.18) and Equation (4.19) the gas produced by that certain input power is obtained.

4.3.4. Minimum power relation

As written before, the minimum accepted load for electrolyzer is set on hydrogen production, being 10% of the maximum one. The maximum hydrogen production is varying, if cell number, cell area or operating conditions change, and to evaluate the corresponding minimum power associated to the minimum H_2 production, a relation between hydrogen production and power should be defined.

In this way, once that the minimum production is found, it is possible to have the minimum operating power too. This is done through a polynomial regression which allows to find the power corresponding to a certain hydrogen production, expressed in $\frac{Nm_{H_2}^3}{h}$, as shown in Equation (4.25).

$$P\left(\frac{Nm_{H_2}^3}{h}\right) = a + b \cdot \dot{n}_{H_2} + c \cdot \dot{n}_{H_2}^2 \tag{4.25}$$

In this case a quadratic relation offer a good fitting of the data, hence a quadratic polynomial relation, shown in Figure 4.18, is chosen.

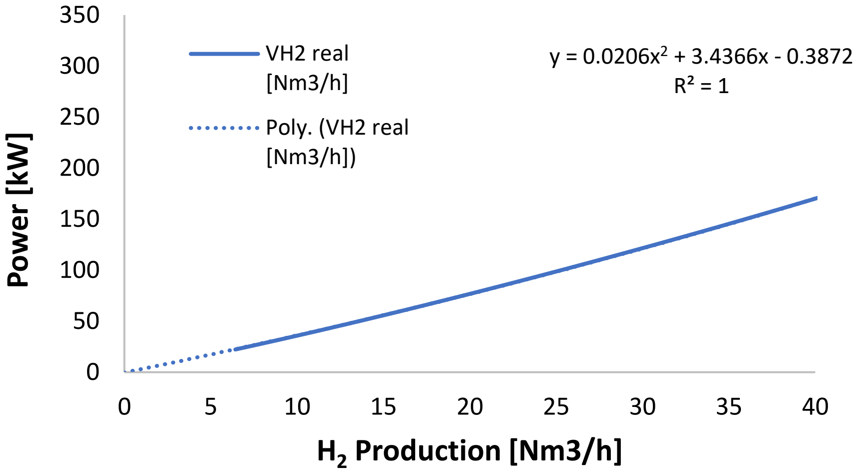

Figure 4.18 – H_2 production - Power relation (200 cm^2, 250 cells, atmospheric pressure, 60°C)

Once that the minimum power is computed, through the third degree polynomial relation, displayed in Equation (4.23), it is possible to retrieve the minimum cell voltage. In the same way, given the minimum cell voltage, also the minimum current density is computed, using Equation (4.24).

Anyway, there are electrical limits in minimum current density and cell voltage to be respected, to preserve PEM lifetime. For the cell voltage a range between 1.4 and 2.5 V should guarantee safe operation [23].While regarding the minimum current density, a value of 0.21 A/cm^2 is reached, and since lower value (0.1 A/cm^2 or 0.05 A/cm^2) are used in different works, also at high pressure, it is considered a safe minimum current density value [44], [60],[19], [61].

4.3.5. Electrolyzer auxiliaries consumption

Beside the electrolyzer consumption it is important to consider auxiliaries too. Balance of Plant (BoP) components are typically [62]:

- Heat management subsystem
- Water management subsystem
- Power conditioning subsystem
- Control subsystem

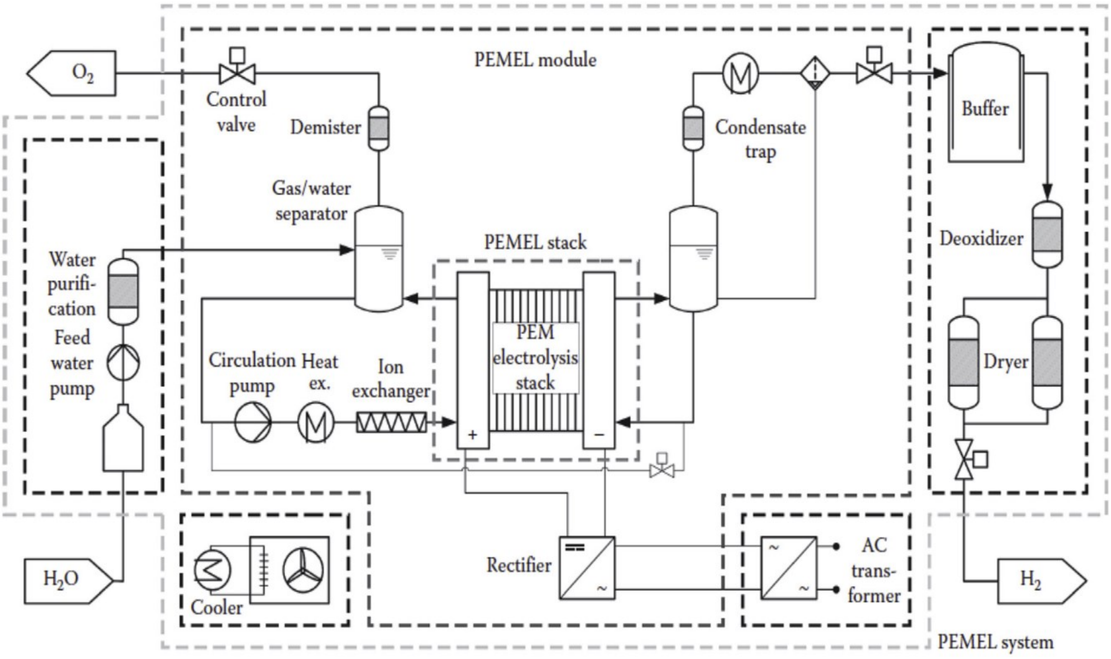
O$_2$
Control valve
Demister
PEMEL module
Condensate trap
Buffer
Gas/water separator
PEMEL stack
Deoxidizer
Water purifi- cation
Feed water pump
Circulation pump
Heat ex.
Ion exchanger
PEM electrolysis stack
+
–
Dryer
H$_2$O
Cooler
Rectifier
AC trans- former
H$_2$
PEMEL system

Figure 4.19 - PEM Electrolyzer system [20].

In order to have a proper estimation of auxiliaries consumption, a commercial Proton Exchange Membrane Electrolyzer datasheet, with size similar on the one of interested, has been taken as reference [63].

From the mentioned datasheet it is possible to point out that water consumption is $1\ L/Nm^3_{H_2}$, while regarding auxiliaries consumption are $0.5\ kWh/Nm^3_{H_2}$, hence the power needed for them is:

$$P_{aux} = 0.5 \left[\frac{kWh}{Nm^3_{H_2}}\right] \cdot \dot{V}_{H_2,real} \left[\frac{Nm^3_{H_2}}{h}\right] \tag{4.26}$$

4.3.6. System Efficiency

Once that the electrolyzer auxiliaries consumption are defined, it is possible to identify the electrolyzer system efficiency, defined as in Equation (4.27). With respect to the load, the trend of the system efficiency is displayed in Figure 4.20. From the chart below, it is possible to see the reduction in efficiency of the modeled electrolyzer if it works at full load, but since renewable energy source have typically an oscillating nature, the increase in performance at partial load is a possibility to exploit in coupling these technologies.

$$\eta_{system}^{LHV} = \frac{\dot{m}_{H_2} \cdot LHV_{H2}}{\Delta V \cdot I + P_{aux}} \tag{4.27}$$

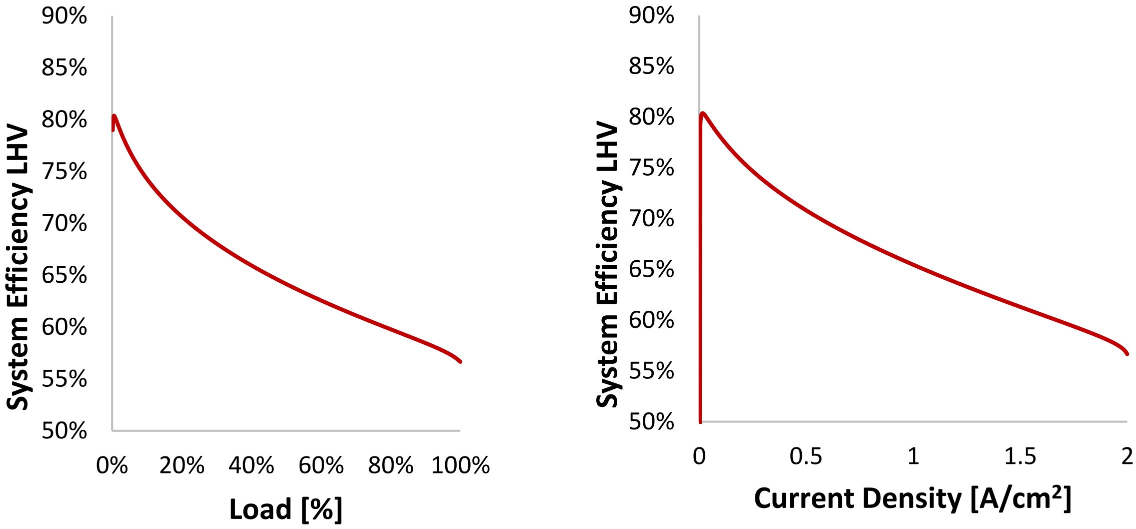

Figure 4.20 – Left: system efficiency as function of PEM load (1 atm, 300 cm^2, 500 cells, 60°C). Right: System efficiency as function of current density (1 atm, 300 cm^2, 500 cells, 60°C).

5 Photovoltaic field and auxiliaries

In this section, the development of the photovoltaic field (PV), which powers the electrolyzer and/or recharge the energy storage and/or inject electricity into the grid is modeled.

Furtherly, the auxiliaries' models, comprising BESS, oxygen tank, CO_2 removal and injection are explained in detail.

5.1. Solar radiation data

In order to compute a hourly year-long simulation of the system a specific tool for solar radiation data, and electricity production estimation, has been used, with a procedure adopted similar to Crespi et al. [31].

Photovoltaic Geographical Information System tool (PVgis tool [64]) has been used to obtain hourly solar radiation data for the whole 2019, which has been taken as reference year. A location must be selected and the choice fallen on Catania, Sicily, south of Italy, where the ATR plant have been supposed to be.

Hourly solar radiation data have been obtained by PVgis through satellite based measurement instruments and calculation, and then validated against ground-level measurements from Baseline Surface Radiation Network (BSRN) station.

PVgis tool provides the possibility to automatically optimize the azimuth and the slope of the panel based on the location chosen; for the geographical area chosen the values are respectively -5° and 34°.

The aforementioned instruments and calculations allow PVgis to produce values of global and beam irradiance on a horizontal plane, hence, since the modules are tilted, the in-plane irradiance must be computed. The model used by PVgis to evaluate the in-plane irradiance is developed and explained in Muneer T. [65]. This value is then adjusted considering the influence of ground elevation (resolution of 90 m) which could provoke shadow and then only diffuse radiation is exploited by the modules.

5.2. Electricity production estimation

Once the in-plane irradiance is calculated it is possible to estimate the electricity produced along the year. To obtain the real PV power output, several corrections should be made to impose real conditions, which of course are different from the STC, like:

- Shallow angle reflection: not all the light which hits the PV module is exploited, indeed, some of it is reflected, and sharper the incidence angle is, greater the reflection will be. This effect is evaluated through [66], [67] and causes a 2-4% loss of sunlight.
- Spectrum changes effect: depending on the meteorological conditions and depending on the hour of the day the sunlight spectrum is changing, and since that the PV modules (depending on the type) is sensitive to different light wavelength range, there is an effect on PV power output. A crystalline silicon PV module is assumed.
- Hourly dependence on irradiance (G_{sun}) and module temperature (T_{mod}): the efficiency of harvesting solar energy by PV module depends on the irradiance and on the module temperature: lower irradiance and high module temperature are detrimental for the performance of the technology. PVgis assumes that PV power depends on the irradiance and on the module temperature following the model detailed in Huld et al. [68] and summed up in Equation (5.1), (5.2), (5.3).

$$P = \frac{G_{sun}}{G_{STC}} \cdot A \cdot \eta(G_{sun}, T_{mod}) = \frac{G_{sun}}{G_{STC}} \cdot A \cdot \eta_{STC} \cdot \eta_{rel}(G_{sun}, T_{mod}) \tag{5.1}$$

$$\begin{gathered} \eta_{rel}(G_{sun}, T_{mod}) = 1 + k_1 \cdot \ln\left(\frac{G_{sun}}{G_{STC}}\right) + k_2 \cdot (T_{mod} - T_{STC}) \cdot \\ \ln\left(\frac{G_{sun}}{G_{STC}}\right)^2 + k_3 \cdot (T_{mod} - T_{STC}) + k_4 \cdot (T_{mod} - T_{STC}) \cdot \ln\left(\frac{G_{sun}}{G_{STC}}\right) + \\ k_5 \cdot (T_{mod} - T_{STC}) \cdot \ln\left(\frac{G_{sun}}{G_{STC}}\right)^2 + k_6 \cdot (T_{mod} - T_{STC})^2 \end{gathered} \tag{5.2}$$

$$T_{mod} = T_a + \frac{G_{sun}}{U_0 + U_1 \cdot W} \tag{5.3}$$

Measurements performed at European Solar Test Installations (ESTI) allowed to obtain the k_1 to k_6 coefficients through a data-fitting, and their values are taken from [64] and detailed in Table 5.1.

k_1	k_2	k_3	k_4	k_5	k_6
-0.017237	-0.040465	-0.004702	0.000149	0.000170	0.000005

Table 5.1 - Crystalline Silicon coefficients for PV power estimation.

The model which describes Equation (5.3) is detailed in Faiman [69]. T_a is the air temperature, W is the wind speed, U_0 and U_1 are coefficients taken in Koehl et al. [70].

- Degradation with age: PVgis, considering the study made by Jordan and Kurz in [71], which evaluates a loss of 0.5% of power per year of operation, assumes a loss of 5% of the original PV power. Indeed with an hypothesis of 0.5% of loss per year, assuming 20 years of lifetime, in the last year there is a downgrade on the original power of 90%. On an average on 20 years the equivalent downgrade would be 95% of the original power, therefore a yearly loss of 5% is assumed.
- System loss: these losses are caused by transformations and transport to properly provide the electric energy generated to the load or to the grid. The main instruments used are inverters, rectifiers and cables of course. PVgis suggests to use a value of 9% of loss, similar to other values used in literature for connecting photovoltaic field to electrolyzer and/or to the grid [72], [73]. These power electronics components will not be described in detail, even if their proper definition is crucial for the system energy management, since the focus of this work is on the analysis of electrical energy and of hydrogen flow.

In order to perform a techno-economic analysis, a dimensionless (kWh_{el}/kWp) photovoltaic hourly generation profile is obtained from PVgis, with the previously mentioned hypothesis.

5.2.1. Land utilization

Once the dimensionless PV generation profile is obtained, there is the need to choose a panel, in order to perform analysis regarding the size and the number of modules to apply. The panel chosen is "Aleo Solar Module P23" ([74]), with a nominal peak power of 325 W_p and an area of 1.755 m^2.

The techno-economic analysis will be performed varying the number of modules, therefore the photovoltaic field dimension will vary, thus the land cost will vary too. It is evident that it is necessary to obtain a specific land utilization per module, to vary the total field area when the number of modules and consequently the field peak power is varied.

The land utilization per module is computed assuming no shadow at noon on 21st December of 2019. From PVgis data the solar altitude at 12.00 a.m. is equal to $\alpha = 26.74°$, while the PV module slope is $\beta = 34°$. The module dimensions are reported in Table 5.2.

Height [m]	Length [m]	Width [m]	Peak Power [kW]
0.035	1.716	1.023	0.325

Table 5.2 - PV module dimensions.

The module land use corresponds to the total area occupied per module and by dividing for the module peak power it is easy to assess a module land use in terms of m^2/kW_p . The procedure to evaluate the land use is detailed in the next set of equations.

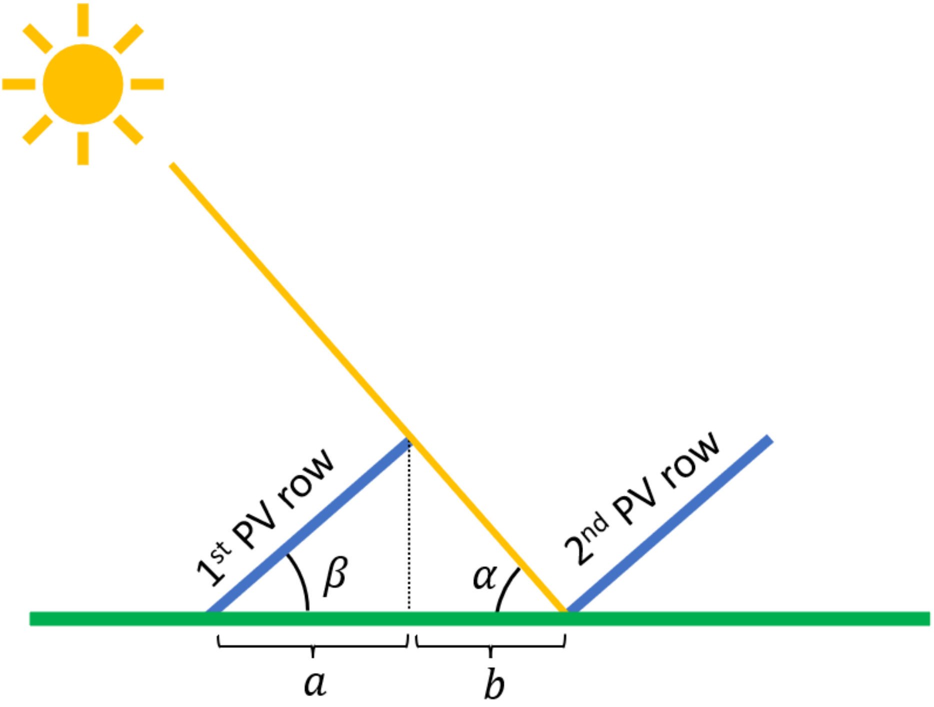

Figure 5.1 - Land use for PV module.

$$a = Module_{length} \cdot \cos(\beta) \tag{5.4}$$

$$b = Module_{length} \cdot \sin(\beta) \cdot \cot(\alpha) \tag{5.5}$$

$$Land_{use} = (a + b) \cdot Module_{width} \tag{5.6}$$

$$Land_{use\ per\ kW} = \frac{Land_{use}}{Module_{peak\ power}} \cong 10.5 \frac{m^2}{kW_p} \tag{5.7}$$

5.3. Battery Energy Storage System

The photovoltaic field is able to produce electricity only during sun hours, therefore a Battery Energy Storage System (BESS) is required, especially in off-grid configuration, to feed the electrolyzer and/or the auxiliaries consumption of the whole plant when there is no sunlight. In order to properly model a BESS, which capacity (kWh) is going to undergo to optimization procedure, several assumptions (typical for Li-ion battery) should be made, and they are reported in Table 5.3.

	Value	Reference
Round-trip efficiency	95%	[75], [76],[77]
Maximum Depth of Discharge (DoD)	90%	[78]
Minimum Possible State of Charge (SoC)	10%	[78]

Table 5.3 - Battery Energy Storage System assumptions adopted.

Round-trip efficiency is used in order to take into account an energy loss when the energy is discharged from the battery to the user, meaning that the energy in output is lower than the energy in input, and this loss is 5%. Regarding the maximum depth of discharge and consequently the minimum possible state of charge, these values are assumed in order to preserve battery lifetime, which has been assumed equal to 10 years [31], [79].

5.4. Oxygen tank

A component that could be useful to add to the plant is an oxygen tank. Indeed, it could be interesting to decouple the oxygen production with respect to the oxygen consumption, letting the electrolyzer works in a variable and flexible operating point, depending on the input power.

When the tank is used (off-grid configuration), the electrolyzer is assumed to produce oxygen at 30 bar, and at that pressure is stored.

If the production of oxygen is lower than the requirement to feed the autothermal reforming, the needed gas is retrieved from the tank, if it is possible. Indeed, withdrawing oxygen from the tank causes a reduction of the vessel pressure and since the membrane reactor works at 12 bar, the minimum tank pressure is limited to 13 bar, meaning that if retrieving oxygen will provoke a reduction of the tank pressure under 13 bar, the withdraw is not allowed.

The model of the oxygen tank is set through applying ideal gas law, considering a constant temperature equal to $T_{tank} = 15°C$. Critical temperature and critical pressure of oxygen are respectively -118.8 °C and 50.43 bar. Reduced temperature and reduced pressure at 15°C and 30 bar, provides values around 1.87 and around 0.6 respectively. With this values the assumptions of considering oxygen as ideal gas could be accepted according to compressibility factor charts.

A yearly profile of the tank evolution is modeled based on the previously mentioned assumption, providing for each hour i, the tank pressure $p_{tank}(i)$, computed with Equation (5.8). As said before, if retrieving oxygen will provoke a pressure $P_{tank}(i)$ greater than 13 bar, then the oxygen is withdrawn.

$$p_{tank}(i) = \frac{[O_2stored(i-1) + O_2prod(i) - O_2feed] \cdot R \cdot T_{tank}}{V_{tank}} \tag{5.8}$$

The tank size is set on the mass of oxygen to contain and consequently this amount will correspond to a certain volume (computed through ideal gas law with the previously mentioned conditions) and to a certain number of autonomy hours, during which the storage could feed the reactor without further production from the PEM electrolyzer.

5.5. CO_2 removal and injection in pipeline

The retentate, after the hydrogen extraction, thanks to membrane reactor is a flow containing mainly CO_2 and H_2O, with trace of N_2, CO, CH_4 and H_2, which is addressed to a catalytic burner in order to ignite the retentate combustion and then to heat up the feed to allow the functioning of the reactor.

The combustion is done in pure oxygen environment, available from the electrolyzer or from the tank, therefore, the flue gas has an high content of water and carbon dioxide, while the molar fraction of oxygen and nitrogen is low. In particular, nitrogen is assumed to be inert, because its content in the retentate is low (its presence is due only to the biogas composition), the combustion is done with pure oxygen as comburent and the burner is embedded of catalyst, therefore NO_x formation is neglected [80].

Once the flue gas stream is cooled down to 35°C, passing through an air cooler, it is directed to a flash at ambient pressure to separate vapor phase and liquid phase. Adopting this solution, the vapor phase is a stream rich in CO_2, with a molar fraction higher than 90%, therefore it can be considered high-purity CO_2 stream [81].

Two different possibilities are analyzed: the first foresees the sale of this stream as it is, hence at 35°C and 1 atmosphere, the second solution is addressed to inject the CO_2 stream in a pipeline, assumed close to the plant.

The injection solution needs a multi-stage compressor in order to bring the rich-CO_2 stream at pipeline conditions (125 bar, 25°C) [82], designed through assumptions provided in Table 5.4.

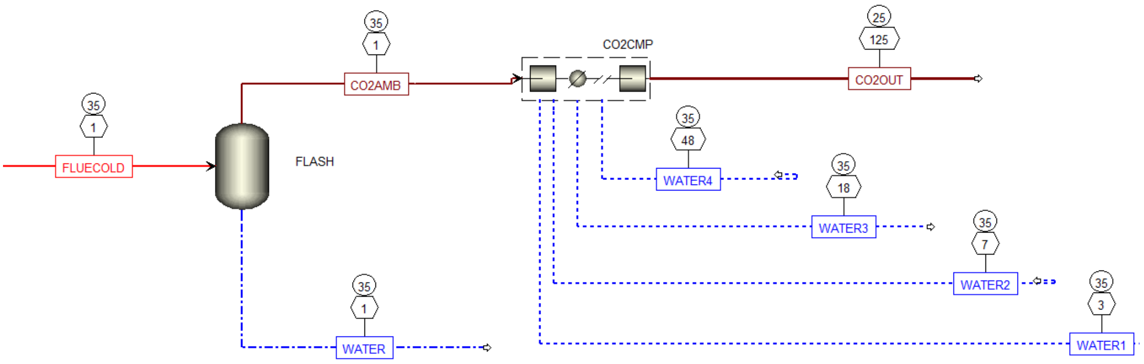
35
1
CO2AMB
CO2CMP
25
125
CO2OUT
35
1
FLUECOLD
FLASH
35
48
WATER4
35
18
WATER3
35
7
WATER2
35
1
WATER
35
3
WATER1

Figure 5.2 - Flue gas track after air cooler: flash separator, compressor and CO_2 injection.

The intercooled compressor has five stage, which works at equal pressure ratio, allowing to avoid temperature greater than 150°C, assumed as maximum temperature admissible by the compressor.

	Pressure ratio	Discharged pressure	Isentropic efficiency	Mechanical efficiency	Cooler outlet temperature
1	2.62	2.65	0.70	0.90	35
2	2.62	6.95	0.70	0.90	35
3	2.62	18.21	0.70	0.90	35
4	2.62	47.72	0.70	0.90	35
5	2.62	125	0.70	0.90	25

Table 5.4 - Design features of CO_2 compressor.

The water removal provides a stream with a CO_2 molar fraction greater than 95%, acceptable value of purity to be injected in a pipeline [82], and thus it is possible to upgrade the classification of the plant from CO_2-neutral to CO_2-negative.

6 Economic analysis

6.1. General description

To properly evaluate the economic performance of an hydrogen producing plant, Levelized Cost of Hydrogen (LCOH) is a common indicator to establish the readiness and the competitiveness of the plant. The methodology adopted to evaluate the LCOH has been taken from G. Di Marcoberardino et al., explicated in Equation (6.1).

$$LCOH = \frac{\sum TPC_c \cdot CCF_c + \sum C_{O\&M,c}}{kg_{H_2} (or\ Nm^3_{H_2})} \tag{6.1}$$

Each plant component c (membrane reactor and auxiliaries, PV field, electrolyzer, energy storage) will be further evaluated, in a single dedicated section.

The plant, in on-grid configuration, foresees the possibility of performing electricity exchanges with the grid, considering revenues too.

The expenditure term involves the purchasing of electricity from the grid (when the configuration allows it) during the year, and it is computed as in Equation (6.2). The purchasing price is set constant along the year (as often used for industrial user) and equal to 120 €/MWh, as in G. Di Marcoberardino et al. [32].

$$Expenditure = \sum_t (E_{from\ grid}(t) \cdot C_{purch}(t)) \tag{6.2}$$

Regarding the revenues, a selling price for the electricity produced by solar field and injected into the grid, when grid exchanges are allowed, is assumed constant along the year and equal to 60 €/MWh [31]. Moreover, a selling of excess oxygen is considered too. Indeed, if there is an excess of oxygen, this happens if the tank is already full or if the final tank level is greater than the initial tank level, this excess is worthy 150 €/tonO_2 [34], [35].

$$Revenues = \sum_t (E_{to\ grid}(t) \cdot C_{sell\ grid}(t)) + ExcessO_2 \cdot C_{O_2} \tag{6.3}$$

The lifetime of the plant has been set equal to 20 years, but the components forming the overall plant have different lifetimes, in particular the electrolyzer and the battery energy storage system have a lifetime of 10 years, thus a replacement cost should be considered. Replacement costs mean additional investment costs in years different from zero, and to take those into account in a one-year analysis, the actualized value at year zero for the component c, with a lifetime shorter than 20 years, has been calculated, as in Equation (6.4), procedure explained in Crespi et al. [31].

$$I_{replace,act,c} = \sum_{t=1}^{Lifetime} \frac{I_{replace,c,t}}{(1+WACC)^t} \tag{6.4}$$

Once that the actualized value at year zero is computed for the electrolyzer and for the battery energy storage system, a sum with the initial investment cost provides an equivalent investment cost (Equation (6.5)), which is practically a TPC for the electrolyzer and BESS part of the plant, but in this way, TPC is evaluate for PV and tank part too.

$$TPC_c = I_{eq,c} = I_{0,c} + I_{replace,act,c} \tag{6.5}$$

The equivalent investment cost is allocated as constant instalment along the whole plant lifetime, finding an annual share of the investment cost for each component. This is done through the Capital Charge Factor (CCF) approach.

Considering the constant instalment along the whole lifetime and the yearly operational cost for the single technology c, an equivalent annual cost can be computed:

$$I_{eq,annual,c} = TPC_c \cdot CCF_c + C_{O\&M,c} \tag{6.6}$$

In order to provide a fair economic analysis of this plant, which is composed by different subsections, two CCF_c are assumed, based on the readiness of the technology. The membrane reactor is not a commercial technology yet, and this has an impact on the valorisation of the investment, that will provoke to adopt $CCF_{ATR} = 16\%$ at which correspond a WACC (Weighted Average Capital Cost) equal to 13.1% [32], [83].

The other subsections of the plant (PV field, BESS, PEM electrolyzer, oxygen tank) are technology which are already available at commercial scale, therefore in literature lower WACC are used to evaluate an investment regarding these technologies [84], [85], [86]. The WACC assumed is equal to 8%, which corresponds to $CCF = 9.24\%$, taken from Crespi et al. [31], since that they foresaw to use the same technologies. This procedure is adopted in order to avoid using a unique CCF value of 16%, that would mean to overpay the already commercial technology.

6.2. Photovoltaic field cost

Photovoltaic field is formed by different components which must be taken into account to properly size the plant and to properly define the cost of this technology.

Electricity generation through PV module is a mature technology, and different literature sources allow to have well defined cost. Anyway differences in investment cost per kW_P could be found, but they are related to the size of the plant (residential vs utility scale) or to the market possibility in that country [87].

Regarding the CAPEX a value of 800 €/kW_P has been assumed (as done in [31]), similar values can be found in [87], [88]. This amount is comprehensive of BoS, inverter and a fixed share of CAPEX is including construction and engineering cost [31].

Operational expenditure should be considered too. Photovoltaic technology foresees mainly a fix share of operational cost during the year, assumed proportional to the size and equal to 13 €/kW_P (adopted in [31]); similar value could be found in literature [87], [88]. The last data needed, to evaluate the annual share of capital cost for PV field, is the lifetime which has been assumed to be 20 years [64].

Investment cost	**Land Cost**	**Fix OPEX**	**Lifetime**
800 €/kW_P	31.50 €/ kW_P	13 €/ kW_P year	20 year

Table 6.1 - Economic features of PV field.

In order to associate a fairer cost to this technology, a land cost should be considered too. This has been taken from [89] and equal to 3 €/m^2 and since the land use is 10.5 m^2/kW_P, as pointed out in paragraph *5.2.1 Land utilization*, the investment cost for land purchasing is 31.50 €/kW_P.

In order to evaluate the annual share of investment cost, the approach is reported in Table 6.2.

Replacement cost $I_{replace,PV,t}$	**Actualized replacement cost** $I_{replace,act,PV}$	**Equivalent investment cost** $I_{eq,PV}$	**Annual Equivalent investment cost** $I_{eq,annual,PV}$
0 €/ kW_P	0 €/ kW_P	831.50 €/ kW_P	76.86 €/ kW_P year

Table 6.2 - Economic evaluation and actualization of PV technology.

An important value to evaluate the techno-economic performance of electricity generation technologies is the LCOE (Levelized Cost Of Electricity). Investors and policy makers commonly use LCOE to assess the profitability of the technology, comparing it to the market prices. Indeed, it represents the average net present cost of electricity generation, and can be computed through Equation (6.7).

$$LCOE\left[\frac{€}{MWh}\right] = \frac{I_{eq,PV}\cdot CCF_{PV} + C_{O\&M}}{E_{PV}} \tag{6.7}$$

6.3. PEM Electrolyzer cost

PEM electrolyzer is a commercial technology, but it has not reached its full degree of maturity and consequently the installation costs are going to decrease in a remarkable way in the future years [23], [90]. PEM electrolyzer system comprises several components to operate (stack, demister, pump…[91]), which are included in a total system cost equal to 1000 €/kW, like installation and engineering cost [31]; similar values could be found in literature in [23], [90].

Operational costs are both fixed (proportional to the size of the electrolyzer) and variables (proportional to hydrogen production). Fix operational cost and lifetime values are taken from Crespi et al., equal to 2% of CAPEX, meaning equal to a value of 20 €/kW, and to 10 years, while for the variable operational expenditures a value of 0.08 €/kgH$_2$ has been assumed [92], since Crespi et al. neglected this contribution.

Investment cost	Fix OPEX	Var OPEX	Lifetime
1000 €/kW	20 €/kW	0.08 €/kgH$_2$	10 year

Table 6.3 – Economic features of PEM Electrolyzer.

As similarly done for PV technology, the annual share of investment cost for PEM technology is evaluated through the previously mentioned approach, explained in Table 6.4, where the replacement cost is taken from Crespi et al. [31] and follow the trend cost for PEM technology in the next years [23], [90].

Replacement cost $I_{replace,PEM,t}$	Actualized replacement cost $I_{replace,act,PEM}$	Equivalent investment cost $I_{eq,PEM}$	Annual Equivalent investment cost $I_{eq,annual,PEM}$
400 €/kW	185.28 €/kW	1185.28 €/kW	109.56 €/kW year

Table 6.4 – Economic evaluation and actualization of PEM technology.

Therefore, depending on the size of the electrolyzer chosen, it is possible to define the final annual equivalent investment cost. The results in Table 6.4 are practically equal to the ones in Crespi et al, showing the correctness of the procedure.

6.4. Battery Energy Storage System cost

Battery costs are assumed proportional to the size too. The investment cost is set equal to 500 €/kWh, comprehensive of installation and engineering cost, taken from Crespi et al. [31], but similar values are also found in [79], [93]. As CAPEX, fix operational expenditure value is taken from [31]; instead, the variable operational cost is taken from [79], since Crespi et al. neglected it. The costs are summarised in Table 6.5.

Investment cost	Fix OPEX	Var OPEX	Lifetime
500 €/kWh	10 €/kWh	0.003 €/kWh	10 year

Table 6.5 - Economic features of BESS technology.

Battery lifetime is lower than the plant one, hence a replacement is foreseen, equal to 300 €/kWh, and then the annual equivalent investment cost can be computed [31].

Replacement cost $I_{replace,BESS,t}$	Actualized replacement cost $I_{replace,act,BESS}$	Equivalent investment cost $I_{eq,BESS}$	Annual Equivalent investment cost $I_{eq,annual,BESS}$
300 €/kWh	138.96 €/kWh	638.96 €/kWh	59.06 €/kWh year

Table 6.6 - Economic evaluation and actualization of BESS technology.

6.5. O_2 Tank cost

The tank cost allows to have a decoupling between electrolyzer oxygen production and membrane reactor oxygen consumption and it is strictly necessary in off-grid configuration.

Oxygen tank cost is assumed from a study of Mayer et al. [94], who considered a value of 300 €/kg, even if the gas stored in their work is hydrogen. This value is considered suitable for this work both in terms of size and in terms of pressure. Actually the cost assumption is conservative when applied to this work, since the pressure in Mayer et al. was 50 bar, while the tank in this work is modelled to withstand to a maximum pressure of 30 bar. In order to obtain an oxygen tank price in €/m^3, to pass by the difference of pressure, ideal gas law is used to understand the value in €/m^3 which corresponds to 300 €/kgH_2. The result provides a value of 1230.90 €/m^3.

Variable operational cost is neglected, while for fixed operational cost a value of 1% of oxygen tank CAPEX is assumed, coherent with [31]. The lifetime is taken from [31] and it is equal to 25 years.

Investment cost	Fix OPEX	Var OPEX	Lifetime
1230.90 €/m³	12.31 €/m³	0 €/m³	25 year

Table 6.7 – Economic features of oxygen tank.

Replacement cost $I_{replace,tank,t}$	Actualized replacement cost $I_{replace,act,tank}$	Equivalent investment cost $I_{eq,tank}$	Annual Equivalent investment cost $I_{eq,annual,tank}$
0 €/m³	0 €/m³	1230.90 €/m³	113.78 €/m³ year

Table 6.8 – Economic evaluation and actualization of oxygen tank.

6.6. ATR cost

The economic analysis of the ATR plant is computed through a bottom-up approach, starting from the cost of the single basic component ($C_{i,2022}$), and adding up the installations cost (TIC), indirect cost (IC) and owner's and contingencies cost (C&OC), in order to identify the Total Plant Cost (TPC) for the ATR plant part [32], [83].

$$TPC_{ATR,plant} = \left(\sum_{i} C_{i,2022}\right) \cdot (1 + \%_{TIC}) \cdot (1 + \%_{IC}) \cdot (1 + \%_{C\&OC}) \tag{6.8}$$

The percentage for the different additional costs have been assumed equal to the ones used in [32] and they are shown in Table 6.9.

$\%_{TIC}$	$\%_{IC}$	$\%_{C\&OC}$
0.65	0.14	0.15

Table 6.9 – Installation, indirect, owner's and contingencies percentage.

6.6.1. Reactor Cost

The cost of the reactor is governed by the amount of material used, which has a specific cost equal to 3.5 €/kg (T316 Stainless Steel) [40]. The formulation of reactor cost is available in Equation (6.9) and it includes labour cost (equal to 7) too.

$$C_{reactor,2022} = Material\ [kg] \cdot Cost_{T316SS} \left[\frac{€}{kg}\right] \cdot ReactorLabourCost \tag{6.9}$$

The amount of material used is related to the volume of the reactor (which is computed as shown in Equation (6.10)) and to its density (8 g/cm^3). The cylindrical reactor has a height H_r equal to 1 m, a diameter D_r, and a thickness t_r, which formulation is shown in Equation (6.11). In order to properly assess the cost of the reactor, the volume is increased of a factor equal to 75%.

$$V_{material}[m^3] = \pi \cdot H_r \cdot \left[\left(\frac{D_r}{2} + t_r\right)^2 - \left(\frac{D_r}{2}\right)\right] + 2 \cdot \pi \cdot t_r \cdot \left(\frac{D_r}{2} + t_r\right)^2 \tag{6.10}$$

$$t_r = P_{r,max} \cdot \frac{D_r}{2\left(S_{stress} \cdot E_{welding} - 0.6 \cdot P_{r,max}\right)} \tag{6.11}$$

In the reactor shell thickness formulation: $P_{r,max}$ is the maximum pressure to withstand (1.8 MPa), E is taken equal to 85% and it is the welding efficiency, while S is the allowable stress given by Equation (6.12):

$$S = \min\left[\frac{UTS}{3.5}; \frac{\sigma_y}{3.5}\right] \tag{6.12}$$

Where UTS and σ_y are respectively the Ultimate Tensile Strength and the yield strength, equal to 480 MPa and 170 MPa, for the material considered. All these data have been taken from MACBETH project [95].

6.6.2. Components cost

The cost of the single basic component $C_{i,2022}$ is computed through Equation (6.13), as explained in [83]. The cost $C_{i,0}$ is retrieved from literature, reports and other sources, for a given size $S_{i,0}$, then it is scaled thanks to the actual size S and scale factor f and it is actualized using CEPCI index for 2022, equal to 607.5.

$$C_{i,2022} = \left(C_{i,0} \cdot \left(\frac{S}{S_{i,0}}\right)^f\right)_y \left(\frac{CEPCI_{2022}}{CEPCI_y}\right) \tag{6.13}$$

The characteristics and assumptions to compute the different $C_{i,2022}$ of the single basic component, are summarized in Table 6.10 and based on the economic analysis and assumptions in Di Marcoberardino et al. [32] and in EU funded project MACBETH [95]. Heat exchangers areas have been computed adopting typical heat transfer coefficient for gas-gas ($U_{g-g} = 60\ W/m^2K$) and gas-liquid/bi-phase ($U_{g-l} = 70\ W/m^2K$).

Component	Scaling Parameter	$S_{i,0}$	$C_{i,0}$ [k€]	f	Ref. Year	$CEPCI_y$	Ref.
Heat Exchangers	Exchange Area [m²]	2	15.5	0.59	2007	525.4	[83]
Air Cooler	Exchange Area [m²]	200	103.214	0.89	2001	394.3	[40]
Biogas Compressor	Power [kW]	5	3.3	0.82	2006	499.6	[83]
Water Pump	Water flow rate [l/h]	90	1.2	0.7	2011	585.7	[83]
Water Demineralizer	Water flow rate [l/h]	90	2.1	0.68	2011	585.7	[83]
Vacuum Pump	Power [kW]	10	9.82	0.44	2001	394.3	[40]
H2 compressor	Power [W]	745.7	1.2	0.3	1987	324	[40]
Burner	-	-	5	-	2013	567.3	[83]

Table 6.10 – Cost assumptions for Autothermal Reforming Membrane Reactor.

6.6.3. O&M Cost

Operation and Maintenance cost comprises two subsection: variable O&M and fix O&M. Fix O&M are computed through Equation (6.14).

$$O\&M_{fix} = TPC_{ATR,plant} \cdot \frac{(\%insurance + \%maintenance)}{100} + LabourCost \qquad (6.14)$$

Where $\%insurance$, $\%maintenance$ and $LabourCost$ values are summarized in Table 6.11.

	Value	Ref.
$\%insurance$	2.5% TPC	[32]
$\%maintenance$	2% TPC	[32]
$LabourCost$	30 [k€/year]	[40]

Table 6.11 - Economic assumptions to compute Fix O&M for ATR plant.

Variable O&M cost includes the voices summarized below in Table 6.12.

	Cost	Ref
Catalyst	540 [k€/m^3]	[32]
Filler	50 [k€/m^3]	[32]
Biogas	0.2712 [€/Nm^3]	[40]
Deionisation Resin	447.07 [€/year]	[32]
Electricity	0.12 [€/kWh]	[32]
Membranes	5.5 [k€/m^2]	[32]

Table 6.12 - Economic assumptions to compute variable O&M for ATR plant.

In order to proper evaluate each item further explanation are provided:

- Catalyst and Filler volume are computed through their mass and density, equal to 2098 kg/m^3 and then divided by their lifetime which is equal to 5 years.
- Biogas purchasing depends on the biogas molar flow used to feed the reactor and on the hours of operation. Biogas specific cost referred to anaerobic digestion process.
- Membranes cost computation needs to consider that they have a lifetime of 5 years, so the yearly cost is evaluated starting from the membranes total area divided by lifetime and then multiplied by the cost, of course, higher the membranes number, higher will be this cost.
- Process water purchasing is affected by the water consumption to feed the reactor and by the operative hours, anyway, its contribution is minimum and it has been neglected.

6.7. CO_2 removal and utilization

As mentioned in section *5.5 CO2 removal and injection in pipeline*, it is possible to burn the retentate in a catalytic burner and, after water separation, a high purity CO_2 flow is obtained. The burner cost and the air cooler are already included in *6.6 ATR cost*, while the CO_2 compressor cost, to pressurize the flue gas stream and to inject it into a pipeline, is evaluated through Equation (6.13), with the same cost function assumed for biogas compressor, reported in Table 6.13.

Component	Scaling Parameter	$S_{i,0}$	$C_{i,0}$ [k€]	f	Ref. Year	$CEPCI_y$	Ref.
CO_2 Compressor	Power [kW]	5	3.3	0.82	2006	499.6	[83]

Table 6.13 - Cost assumptions for CO_2 Compressor.

Carbon dioxide market price is dependent on the purity and on the conditions of the flow. A wide range of selling price is provided in IEA report "*Putting CO_2 to use*", depending on the source and on the purity of the flow, a price even higher than 400 \$/tonCO_2, could be reached for niche market, or a price of 3-15 \$/tonCO_2, if the flow comes from ammonia production, has been pointed out [96]. Other prices can be found in literature, like 50 €/tonCO_2 used by Tremel et al. [97], 10 €/tonCO_2 used by Rivarolo et al. [36], or 35 €/tonCO_2 in Kim et al. [37], and in Alsayegh et al. [98].

The carbon dioxide flow has a CO_2 molar fraction greater than 90% at the outlet of the flash separator, therefore it is possible to label this flow as high-purity carbon dioxide flow [81], moreover, since it is practically at ambient conditions, as in Kim et al., the selling price for CO_2 flow has been assumed equal to 35 €/tonCO_2.

Instead, a higher market price for selling the carbon dioxide rich stream by pipeline injection is considered, and it is assumed equal to 50 €/tonCO_2 [38].

7 Results

In this section the results of the analyses briefly described in chapter *2 Methodology* are presented.

The aim of this work is firstly to quantify the performance improvement by feeding oxygen instead of air to an ATR-FBMR plant, then to assess the techno-economic convenience of integrating the oxygen-fed ATR-FBMR plant with a PEM electrolyzer, in order to produce green hydrogen from biogas. Techno-economic analysis will also detail the introduction of a PV field and of Battery Energy Storage System (BESS). Feeding oxygen to FBMR and to catalytic burner which ignites retentate combustion, provides flue gas mainly composed by water and CO_2, which could be easily separated through water condensation. Two pathways of treating CO_2 have been studied: a selling at ambient condition directly after water separation and an injection through CO_2 compression into a pipeline, generating a carbon-negative plant. The model of CO_2 treatment are explained in *5.5 CO2 removal and injection in pipeline*.

A proper comparison with air used as oxidizing agent should be assessed; therefore, the air-configuration, implemented in MACBETH project, and described in *2.2.1 Air configuration*, is going to be considered the benchmark case. All the configurations are performed in order to produce 100 kgH_2/day, with the same biogas composition and in the same operating condition of temperature and pressure, enlisted in Table 2.1.

As previously mentioned, providing heat for reforming reaction through pure oxygen combustion should raise up the difference of hydrogen partial pressure between retentate side and permeate side, increasing consequently the permeation force, allowing an improvement of the performance.

All the configurations have been implemented in Aspen Plus, a software able to solve heat and mass balances and which includes a wide dataset of properties and equations of state. Membrane Reactor is the heart of the plant: its model has been developed in MACBETH project through Aspen Custom Modeler (ACM) software, which allows to model in detail the operation of the membranes reactor and it can be easily integrated in Aspen Plus. The model has been already presented in chapter *3 Fluidized bed membrane reactor model*.

The comparison will be assessed at different membranes number, verifying that minimum pitch limit described in section *3.2 Features and model* is respected, and highlighting the trend of the main performance parameters.

7.1. Oxygen-air comparison

The configurations are compared by changing membranes number. Membranes number is, obviously, an important parameter, since they perform hydrogen separation. If the membranes number increases, an increase in HRF is observed too, thus, at constant pure hydrogen production, the biogas needed as input is reduced. Therefore, overall biogas purchasing cost is reduced, but the cost of membranes is increased; it is evident the presence of a trade-off.

Besides economic analysis, technical limit concerning membranes number increase arises too.

Indeed, a reduction in separation performance is actually observed when membranes are placed closer than 2 cm by each other (surface-to-surface distance)[30].

However, when membranes number increases, the model foresees an efficiency improvement, with a reduction in biogas and steam consumed. Thus, in order to keep the ratio between gas superficial velocity and the minimum fluidization velocity equal to 1.5, the diameter reactor is reduced, but this reduction limits the space available to place the membranes, providing a maximum number of membranes depending on the reactor diameter.

The comparison must cope with these constraints, and to evaluate the maximum number of membranes ($N_{membrane}^{max}$) that could fit in a given diameter reactor, a polynomial relation has been developed in MACBETH project and it is reported in Equation (7.1)[30]. The simulation, made in Aspen Plus, provides the reactor diameter that respects the Design Specification enlisted in section *2.2 Comparison description between air and oxygen*; thus known the membranes number, which is an Aspen Plus input required, it is possible to obtain the maximum number of membranes which respects the 2 cm distance limit. In Equation (7.1) D_r is the reactor diameter, while d is the sum of the membrane external diameter (1.4 cm) and the minimum distance between two membranes (2 cm).

$$N_{membrane}^{max} = 0.7854\left(\frac{D_r}{d_{membrane}}\right)^2 - 0.2349\left(\frac{D_r}{d_{membrane}}\right) - 2.1429 \tag{7.1}$$

$$d = d_{membrane} + 0.02 = 0.034\ m \tag{7.2}$$

7.1.1. Technical comparison results

For air-case a maximum number of membranes have been suggested to be equal to 147, while for oxygen case simulations have been performed adopting a membranes number from 107 to 123 (with a step of 3), with a maximum number that could fit inside the reactor equal to 122. Thus, a first results is that membranes number in oxygen-fed configuration is reduced.

Besides computing the maximum number of membranes with (7.1) and comparing it with the input membranes number (to verify that the membranes number used as input is lower or equal to the maximum number found), it is possible to identify the membranes distance too, and verifying it to be lower than 2 cm. This could be easily found by manipulating Equation (7.1), making explicit d and, then computing membranes distance through a difference with membrane diameter, as shown in (7.3).

$$Membranes\ Distance = d - d_{membrane} \tag{7.3}$$

The trend of membranes distance at different membranes number is shown in Figure 7.1, pointing out that the maximum membranes number, which respects all the configuration constraints, is 122 for oxygen case. The reactor diameter at which the membrane distance limit is reached is equal to 0.43 m, while for air case is 0.47 m.

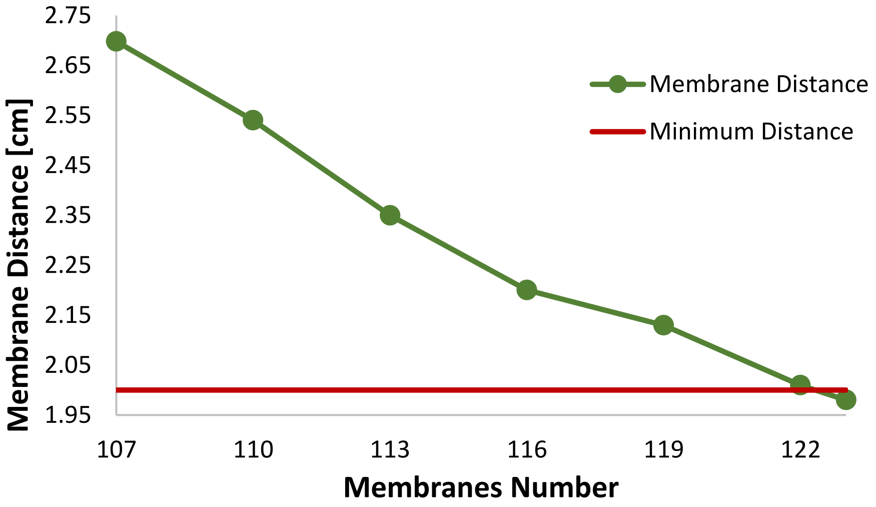

Figure 7.1 - Membranes distance at different membranes number for O_2-case.

System efficiency is the main output goal of this comparison, because it is used to understand the improvement of performance when oxygen is used as oxidizing agent.

Nevertheless, different parameters could be used to assess the performance of a membranes reactor simulation, like HRF or methane conversion; obviously these indexes are related because methane is the main source of hydrogen generation. These values are reported in Figure 7.2, where the membranes number ranges investigated for air case and oxygen case are shown.

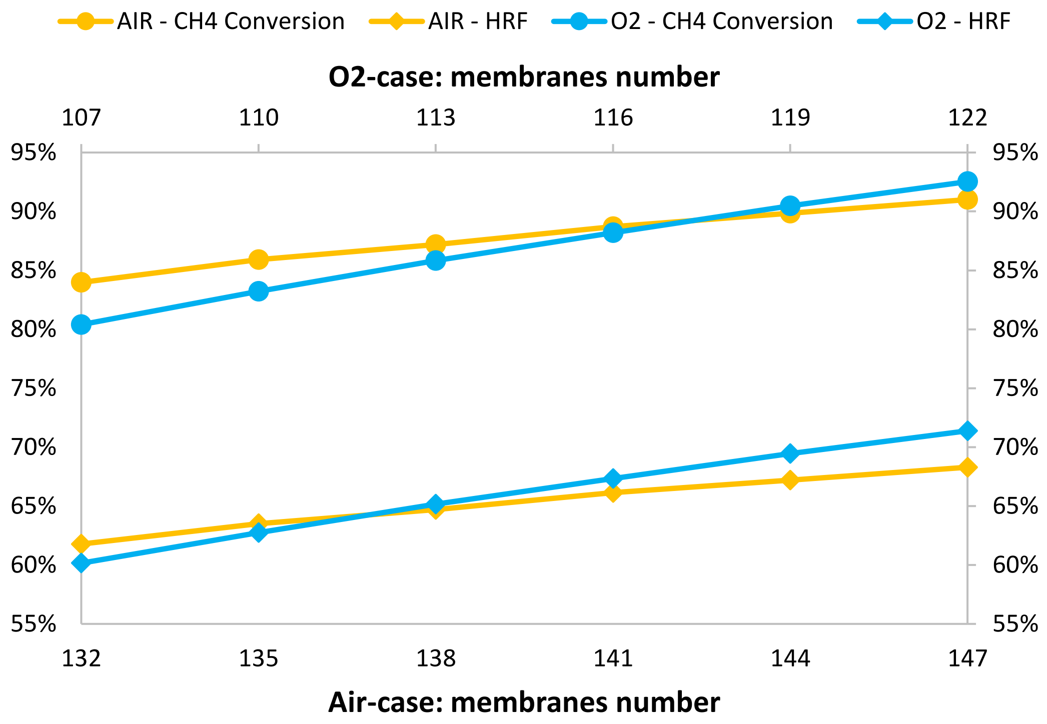

Figure 7.2 - Trend of methane conversion and HRF for air and oxygen configuration.

At maximum membranes' number it is possible to highlight the improvement of reactor performance by feeding oxygen; indeed greater HRF and greater methane conversion is a good first clue for achieving greater efficiency, although further analysis at system level should be done. Therefore, from the achieved values, it is possible to state that oxygen-case in the most performant set-up, provides an higher HRF at lower membranes number.

Membranes Number	HRF	CH_4 Conversion
122 (O_2 case)	71.39%	92.53%
147 (Air case)	68.29%	91.01%

Table 7.1 – HRF and CH_4 conversion in best configuration for the different case.

A relevant aspect to point out is that a greater methane conversion yields to a lower retentate LHV, thus less heat could be unleash by retentate combustion, therefore, the reactor feed would be colder; this limits in a certain way the maximum efficiency of the overall system.

By keeping the steam temperature constant at 700°C, it is possible to depict the trend of feed temperatures and flue gas temperatures in both cases (Figure 7.3).

Feed temperatures are limited by: avoiding to reach ignition temperature (especially in O_2 case) and by the available thermal power for feed preheating (particularly in air configuration).

Flue gas temperature is instead related to methane molar fraction in retentate: higher the methane content is, higher the retentate LHV will be. Methane molar fraction in retentate is affected by methane conversion (higher conversion, lower retentate molar fraction) and by nitrogen presence, which reduces methane molar fraction in air-case. In oxygen-case, due to the absence of nitrogen in oxidizing agent (higher methane retentate molar fraction), and being the combustion performed with pure oxygen as oxidizing agent, the temperature of flue gas from catalytic burner is higher.. Since the overall feed flow is lower, and due to the similar thermal power available (in oxygen-case flue gas temperature is higher but the mass flow rate is lower) it would be possible to increase temperature of the feed or of the steam, increasing the reforming and separation efficiency, but this could happen only in a future when membranes, and steam heat exchangers, could operate at higher temperature. Nowadays membrane reactors operating temperature is still limited at around 500°C, and this constraint is limiting in a more relevant way oxygen case than air-case.

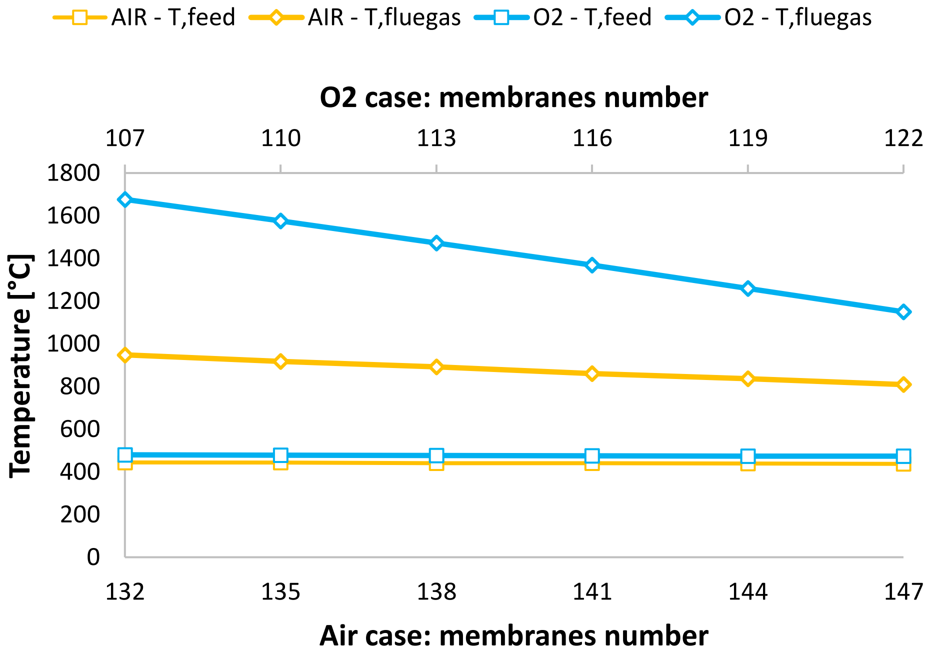

Figure 7.3 - Feed and flue gas temperature in both configurations.

Pursuing the comparison between air and oxygen configuration, steam and biogas consumption are interesting flows to be compared, especially the amount of biogas used, since it has a relevant cost.

By feeding oxygen, a reduction in biogas consumption is observed in Figure 7.4, meaning that, less biogas is needed to produce 100 kgH2/day, highlighting an improvement in performance of membrane reactor.

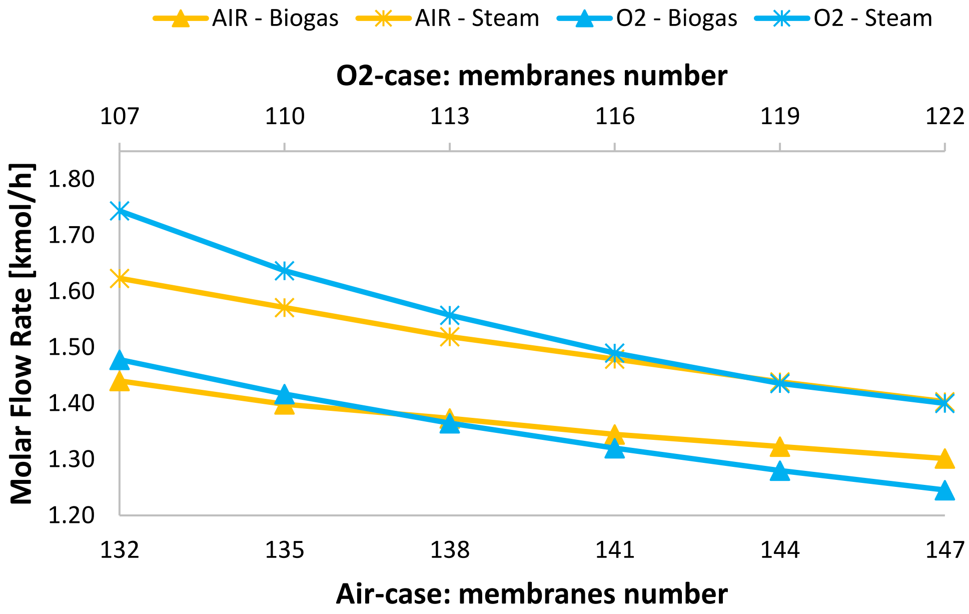

Figure 7.4 - Biogas and steam flows comparison in the two configurations.

Biogas consumption affects the cost, but it affects the efficiency too. Indeed, higher biogas consumption means greater biogas input power and greater auxiliaries consumption.

Auxiliaries consumption is given by: biogas compressor, hydrogen vacuum pump, hydrogen compressor, water pump and by the air cooler electric consumption, assumed to be 1.5% of the heat dissipated, as done in MACBETH project. In air-configuration, an air compressor is obviously involved and the heat is dissipated in two air coolers: Q_{RET} to cool down the flue gas (present in oxygen case too) and Q_{PER} to cool down the permeate before the vacuum pump. Moreover, an addiction of 10% in the whole sum of auxiliaries is accounted for control system [32].

System efficiency is computed as explained in 2 *Methodology* and its computation is reported below.

$$\eta_{sys} = \frac{\dot{m}_{H_2} \cdot LHV_{H_2}}{\dot{m}_{BG,f} \cdot LHV_{BG} + \frac{W_{aux}}{\eta_{el,ref}}} \tag{7.4}$$

The main consumptions, for both cases, in their best configuration (maximum number of membranes in both cases), are below enlisted.

	Unit	Air - case	O_2 - case
$W_{BG,CMP}$	kW	4.25	4.01
$W_{Air,CMP}$	kW	4.13	0
W_{vacuum}	kW	8.18	8.18
$W_{H2,CMP}$	kW	8.42	8.42
$W_{H2O\ PUMP}$	kW	0.01	0.01
Q_{ret}	kW	19.15	15
Q_{perm}	kW	2.36	0
W_{aux}	kW	27.84	22.93
Biogas input power	kW	168.61	161.34

Table 7.2 - Electric and thermal power for both cases in their best configuration.

The results concerning mass flows are reported in Table 7.3, where rich-CO_2 stream is enlisted too, with the electric consumption necessary to be injected into the grid, which is not taken into account in this comparison (but it will be in next analysis), since air-case did not envision it. The overall streams features are further displayed, in Table 7.5 (for oxygen-case) and in Table 7.6 (for air-case).

	Unit	Air - case	O_2 - case
Biogas flow	kmol/h	1.30	1.24
Air/O_2 flow	kmol/h	1.27	0.25
Air/O_2 flow for burner	kmol/h	1.88	0.15
Steam flow	kmol/h	1.40	1.40
H_2 flow	g/s	1.16	1.16
H_2 flow	kg/h	4.17	4.17
CO_2 flow	kg/h	/	51.84
CO_2 compression	kW	/	7.20

Table 7.3 - Streams flows and CO_2 compressor power.

Replacing oxidizing agent from air to oxygen is definitively improving the performance of the hydrogen production plant: the biogas consumed is reduced, thus less input power is provided for having the same output, and as a consequence, a reduction in biogas compressor consumption is detected too. The plant configuration chosen, moreover, allows to dissipate less amount of heat.

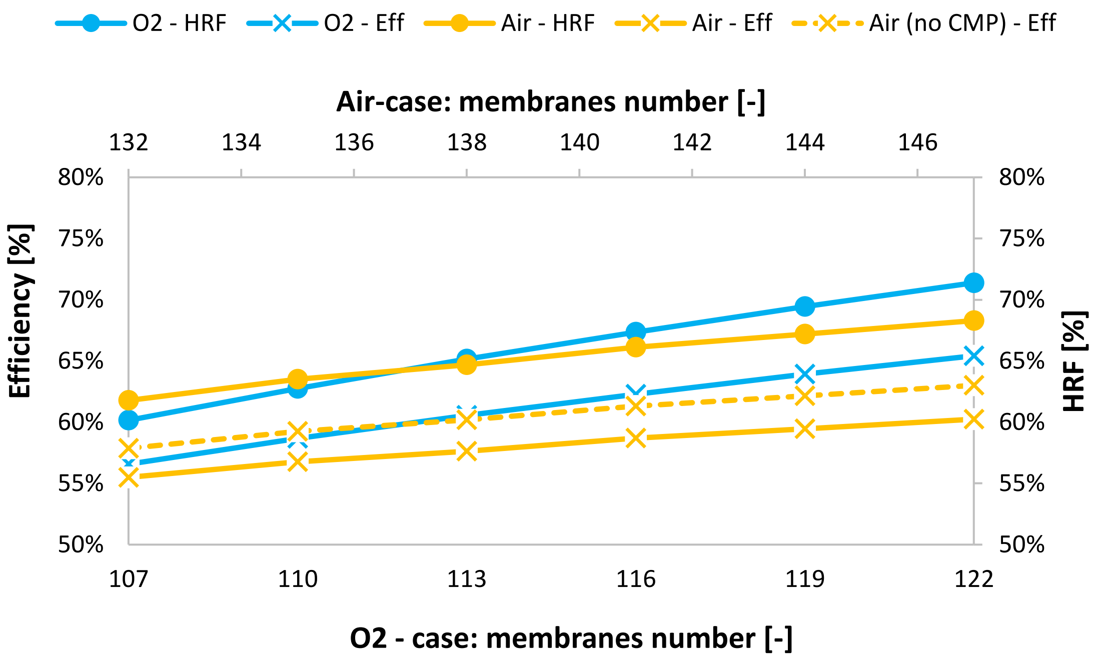

Figure 7.5 - Efficiency and HRF comparison.

In Figure 7.5, the efficiencies at different membranes number are reported. For air case, two efficiencies are reported: the solid line is the real system efficiency, while the dashed one does not take into account air compression, because in oxygen configuration O_2 is considered as given. Even in the case in which air compression is not taken into account, oxygen configuration provides the best performance.

	Air - case	Air – case (without air compressor)	O_2 - case
$\dot{m}_{H_2}$ *produced* $\left[\frac{g}{s}\right]$	1.16	1.16	1.16
Biogas input power [kW]	168.61	168.61	161.34
W_{aux} [kW]	27.84	23.30	22.93
System efficiency	60.25%	63.01%	65.42%

Table 7.4 - Summary of system efficiencies voices.

As a final conclusion, in Table 7.5 and in Table 7.6, all the relevant streams, with their features, of the most performant set-up for oxygen-case and for air-case are reported. Table allows to point out the main benefit of oxygen-case, which is the reduction in biogas consumption, which has a remarkable cost as highlight in section *6.6.3 O&M Cost*. All the technical results of the comparison are enlisted in *Appendix A.1*.

Stream	Flow		T [°C]	P [bar]	Composition (% molar basis)						
	mol/s	g/s			CH_4	H_2O	CO	CO_2	H_2	O_2	N_2
Biogas	0.35	9.07	15	1	58.10	3.10	0	33.90	0	1.10	3.80
O_2 FMBR	0.07	2.19	15	12	0	0	0	0	0	100	0
Steam	0.39	7.01	700	12	0	100	0	0	0	0	0
Feed	0.80	18.27	473.58	12	25.02	49.74	0	14.60	0	9.00	1.64
Retentate	0.53	17.11	500	12	2.84	33.81	1.23	56.11	3.52	0	2.49
O_2 Burner	0.04	1.38	15	13	0	0	0	0	0	100	0
Flue gas	0.56	18.49	1149.79	1	0	40.67	0	56.90	0	0.07	2.35
H_2	0.57	1.16	133.69	20	0	0	0	0	100	0	0

Table 7.5 - Main streams features for oxygen-case in its most performant set-up.

Stream	Flow		T [°C]	P [bar]	Composition (% molar basis)						
	mol/s	g/s			CH_4	H_2O	CO	CO_2	H_2	O_2	N_2
Biogas	0.36	9.39	15	1	58.10	3.10	0	33.90	0	1.10	3.80
Air FBMR	0.35	10.05	15	1	0	0	0	0	0	21.00	79.00
Steam	0.39	7.04	700	12	0	100	0	0	0	0	0
Feed	1.10	26.48	448.32	12	18.97	36.61	0	11.07	0	7.03	26.32
Retentate	0.83	25.32	500	12	2.16	22.22	1.03	36.67	3.00	0	34.92
Air Burner	0.58	16.75	15	1	0	0	0	0	0	21.00	79.00
Flue gas	1.39	42.07	766.05	1	0	17.56	0	23.70	0	5.00	53.74
H_2	0.57	1.16	133.69	20	0	0	0	0	100	0	0

Table 7.6 - Main streams features for air-case in its most performant set-up.

7.1.2. Economic comparison results

Even if it would not be properly correct to compare LCOH of both configurations, since oxygen is assumed as given in oxygen case, several important observations could be done by comparing each cost voices. Through the procedure explained in *6 Economic analysis* and the results provided in *Appendix A* it is possible to compute each cost reported below. In Table 7.7 all the expenditures are enlisted for the best case of each configuration. The difference between TPC and TIC is called as "other costs" in Figure 7.6 and in Figure 7.7, including installation, indirect, owner's and contingencies costs.

CAPEX	Unit	Air - case	O_2 - case
Reactor Cost	k€	10.98	9.10
Heat exchangers cost	k€	14.77	16.77
Air coolers cost	k€	7.75	6.14
Biogas Compressor	k€	3.51	3.35
Air Compressor	k€	0.13	0
Water Pump	k€	0.51	0.51
Water demineralizer	k€	0.62	0.51
Vacuum pump	k€	13.85	13.85
H_2 Compressor	k€	4.66	4.66
Burner	k€	5.35	5.35
Membranes	k€	16	13.28
TIC	k€	78.13	73.52
TPC	k€	169.02	159.04

Table 7.7 - CAPEX for air and oxygen cases, in each best configuration.

The main differences between the two cases could be found in:

- Membranes cost: oxygen case can be performed with lower number of membranes. Obviously, greater membranes number is, higher this cost will be.

- Reactor cost: it depends on the dimensions of the reactor, which is lower for oxygen case, due to the smaller diameter to keep the ratio between gas superficial velocity and minimum fluidization velocity around 1.5.
- Heat exchangers and air coolers: in oxygen configuration a greater number of heat exchangers is used, thus the greater cost is explained, while, on the contrary, in air-case, a second air cooler is used. By increasing membranes' number, this cost is going to increase, due to reduction of temperature between the fluids inside the heat exchanger, increasing the required area.
- Biogas compressor: is slightly lower for oxygen case, since it is related to biogas molar flow consumed. Increasing membrane number this cost will reduce, due to improvements in performance.

The other CAPEX differences are practically negligible. The contributions of the different voices, at different membranes number is depicted in Figure 7.6 for air case and in Figure 7.7 for oxygen case.

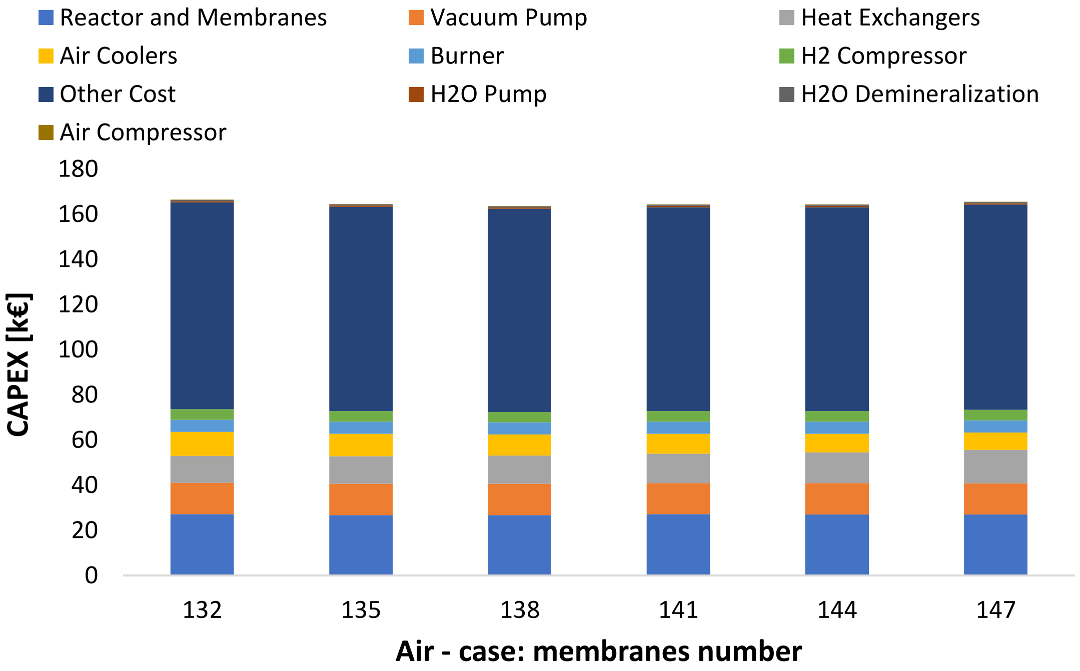

Figure 7.6 - CAPEX contribution at difference membranes number for air-case.

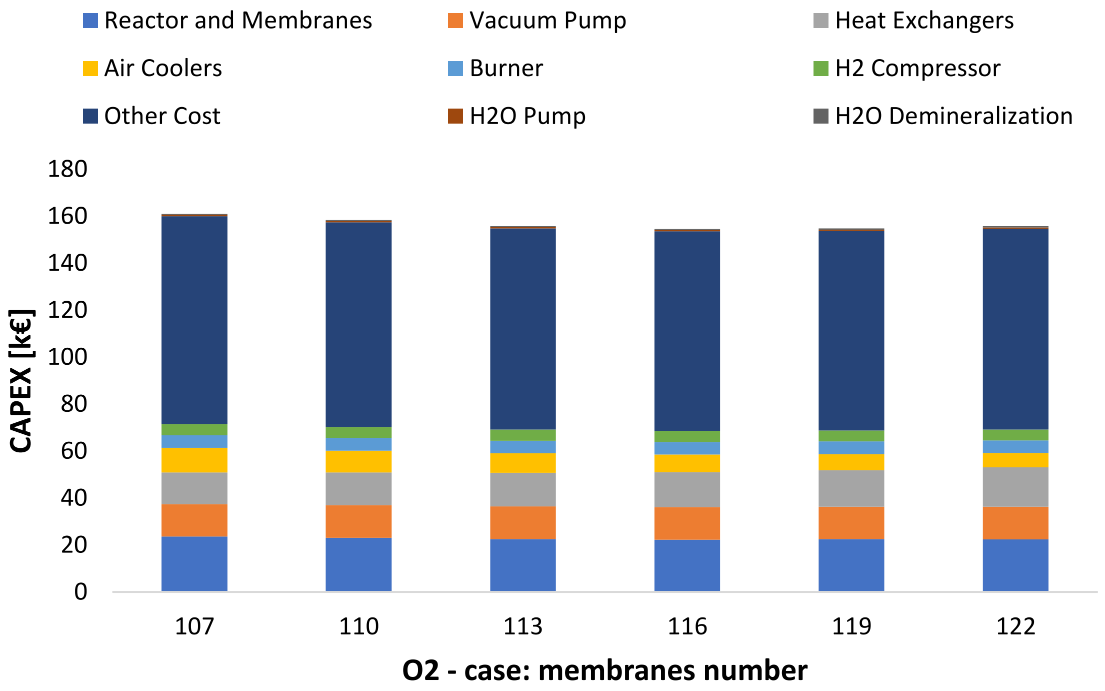

Figure 7.7 - CAPEX contributions value at difference membranes number for oxygen-case.

Regarding operational costs (OPEX), they are divided into fix and variable. Fix OPEX are due to labor cost, maintenance and insurance, as explained in chapter *6 Economic analysis*, while variable OPEX are related to catalyst, filler, biogas, deionization resin, electricity and membranes replacement. In every configuration the biogas is the main cost, remarking that a configuration which minimizes biogas consumption will probably be the one which minimizes LCOH too.

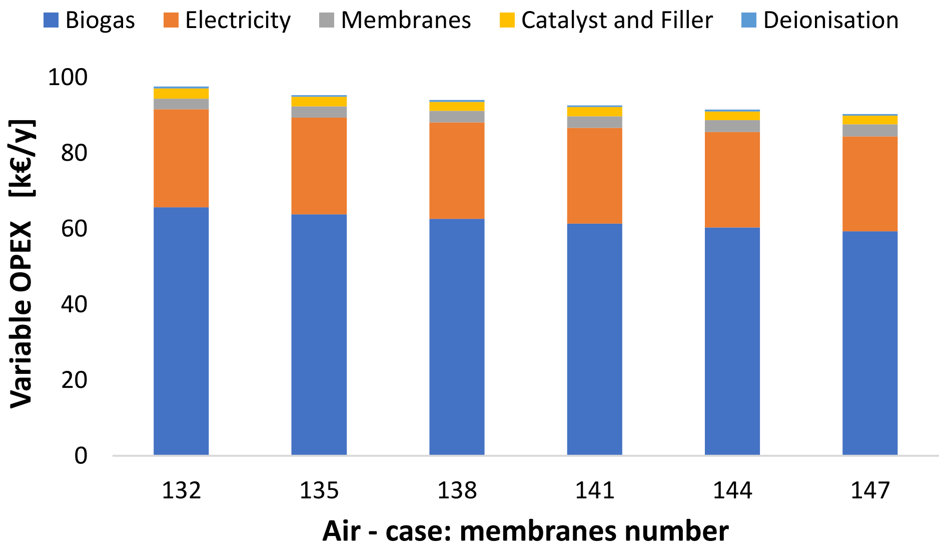

Figure 7.8 - Variable OPEX contributions for air-case varying membranes number.

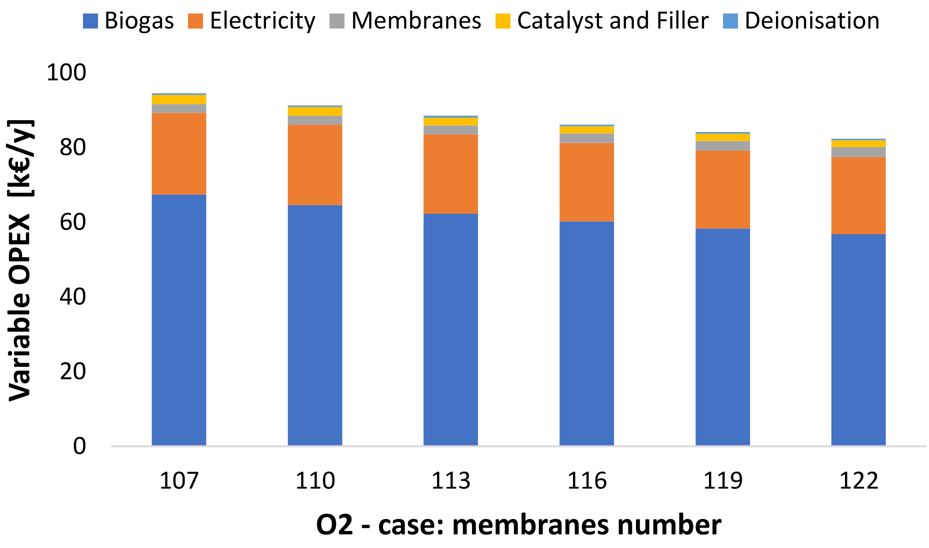

Figure 7.9 - Variable OPEX contributions for O_2 - case.

In Table 7.8 each OPEX voice is reported for the best configuration of each case. Catalyst and filler are reduced at same output production, as well as biogas consumption, due to higher efficiency of oxygen adoption. Electricity cost is lower in oxygen case because the auxiliaries consumption are decreased with respect to air case.

OPEX	Unit	Air - case	O_2 - case
Catalyst and filler	k€/y	2.24	1.81
Biogas	k€/y	59.34	56.78
Deionization Resin	k€/y	0.45	0.45
Electricity	k€/y	25.06	20.64
Membranes	k€/y	3.2	2.66
O&M Var	k€/y	90.29	82.33
O&M Fix	k€/y	37.61	37.16

Table 7.8 – OPEX for air and oxygen cases, in each best configuration.

In order to understand the weight of the operational expenditure, with respect to the CAPEX, on LCOH, Figure 7.10, for air case and Figure 7.11 for oxygen case, are below represented.

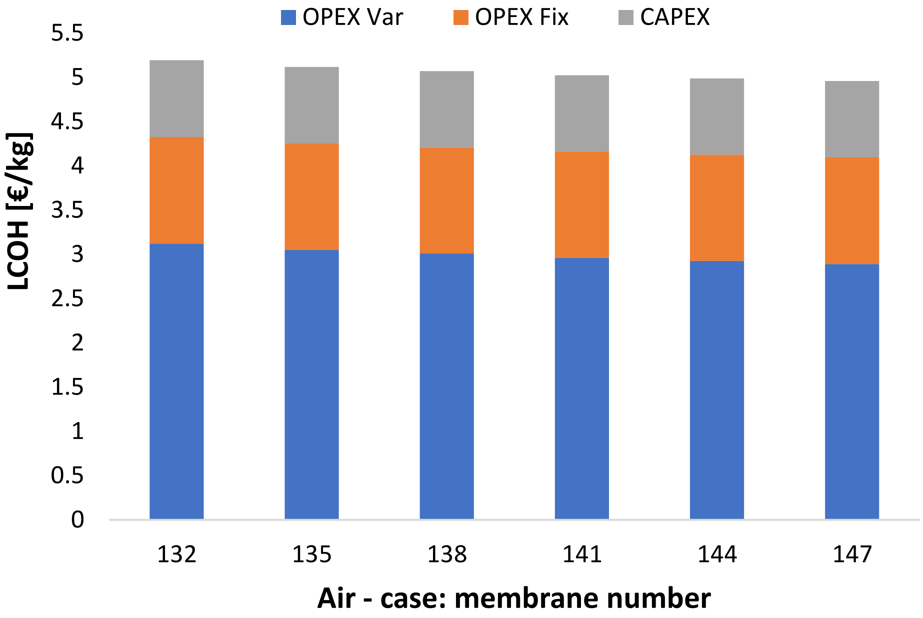

Figure 7.10 - Comparison between CAPEX, variable and fix OPEX for air-case.

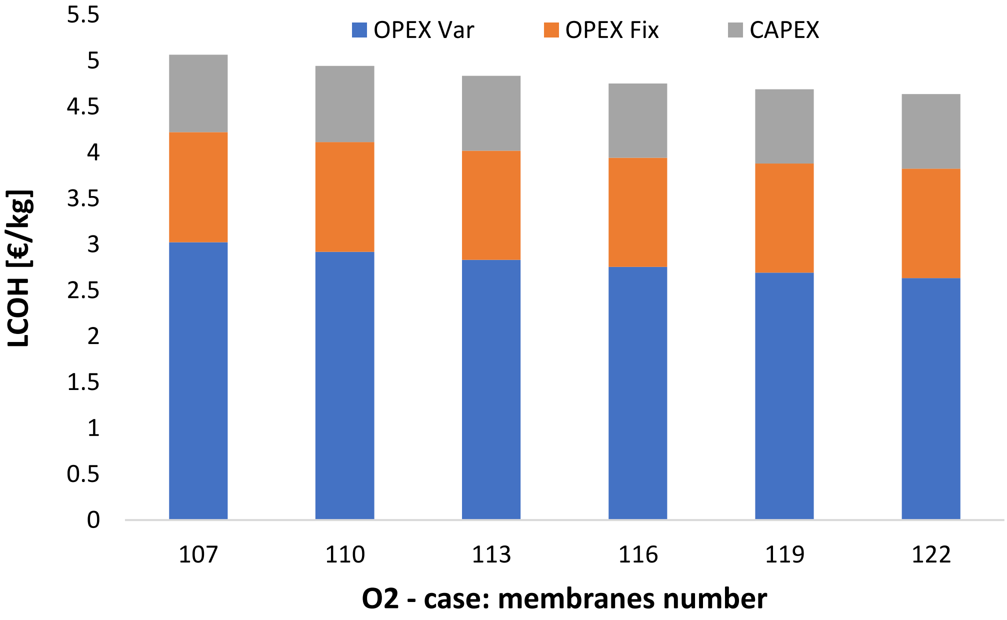

Figure 7.11 - Comparison between CAPEX, variable and fix OPEX for oxygen-case.

OPEX is the major contribution of cost in the studied hydrogen production plant, accounting more than half of total share. Particularly, the main cost in OPEX is the biogas purchasing (around 40% of overall equivalent annual cost), driving the convenience of the plant towards low biogas consumption plant.

The economic analysis is concluded when LCOH values are obtained; they are computed as explained in chapter *6 Economic analysis*, and in Table 7.9, the main results are reported, for the best configuration of oxygen and air-case.

	Unit	Air - case	O_2 - case	Δ	Δ [%]
Total cost	k€/y	154.94	144.93	-10.01	-6.46%
H2 produced	kg/y	31243	31250	+7.00	+0.02%
LCOH	€/kg	4.96	4.64	-0.32	-6.48%

Table 7.9 - LCOH composition, results and comparison between air and oxygen case.

As previously mentioned, it is not properly coherent comparing these LCOHs, but anyway the trend analyzed allows to point out the goodness of replacing oxidizing agent.

In the next analysis oxygen production, by PEM electrolyzer, is going to be taken into account. Different coupling solutions are going to be presented, and all of them considers the same ATR plant configuration, that is the one which maximizes the system efficiency, which FBMR adopts 122 membranes, with a diameter of 0.43 m.

7.2. PEM-ATR configuration

In this section oxygen production through a PEM electrolyzer, which model has been detailed in chapter *4 Electrolyzer*, is added to autothermal reforming plant.

7.2.1. Configuration set-up

A coupling, between the oxygen needed by the autothermal reforming plant and oxygen production, is obviously required. The main goal of PEM electrolyzer is to produce for 7500 hours per year the oxygen needed by membrane reactor, which is practically equal to 0.40 kmolO_2/h, as introduced in Table 7.3.

The operating conditions chosen for electrolyzer operation are 60 °C and 21 bar. The temperature is a typical value for PEM, as described above, while 21 bar has been assumed to bring hydrogen at the same pressure of hydrogen produced by the reactor (20 bar, 1 bar to have a safe gap of operation). Therefore, the oxygen produced is pressurized with respect to its utilization in ATR plant, thus, a valve is placed to bring oxygen at the condition described in *2.2.2 Oxygen configuration*.

In this configuration electricity is retrieved by the grid which should power both the electrolyzer and autothermal reforming plant, with CO_2 compressor addiction whether applied.

In the overall plant, thus, an electrolyzer with its water heater (an additional heat exchanger with burned retentate) to heat up the water needed, and its pump are added. The heat exchanger and the pump are already considered in PEM CAPEX and in auxiliaries consumption, as mentioned in section *6.3 PEM Electrolyzer cost*. Introducing an additional heat exchanger will provide a further cooling down of flow gas, which could reduce the cost of the air cooler, but considering a conservative scenario the heat exchangers cost are considered unvaried with respect to the oxygen case aforementioned.

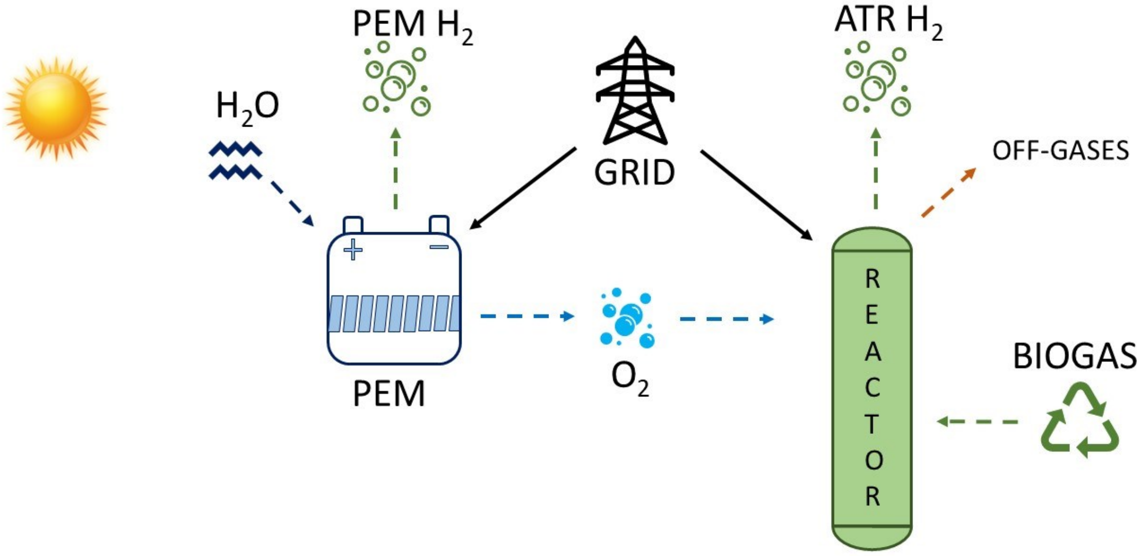

Figure 7.12 – Configuration set-up with PEM introduction.

The electrolyzer, thus, works at constant production (0.40 kmolO_2/h) and depending on the cell number and cell area, a certain current and voltage, thus a certain power retrieved by the grid, is required. In order to preserve the electrolyzer lifetime and to avoid working at too high or too low current density, only a range of admittable current density has been identified as suitable. Therefore, the current density has been limited between 0.5 A/cm^2 and 1.5 A/cm^2. This range is shown in PEM polarization curve too, reported at 60°C and 21 bar for the modeled electrolyzer in Figure 7.13. It is not affected by cell number and cell area, then it is common for every combination of the two aforementioned parameters.

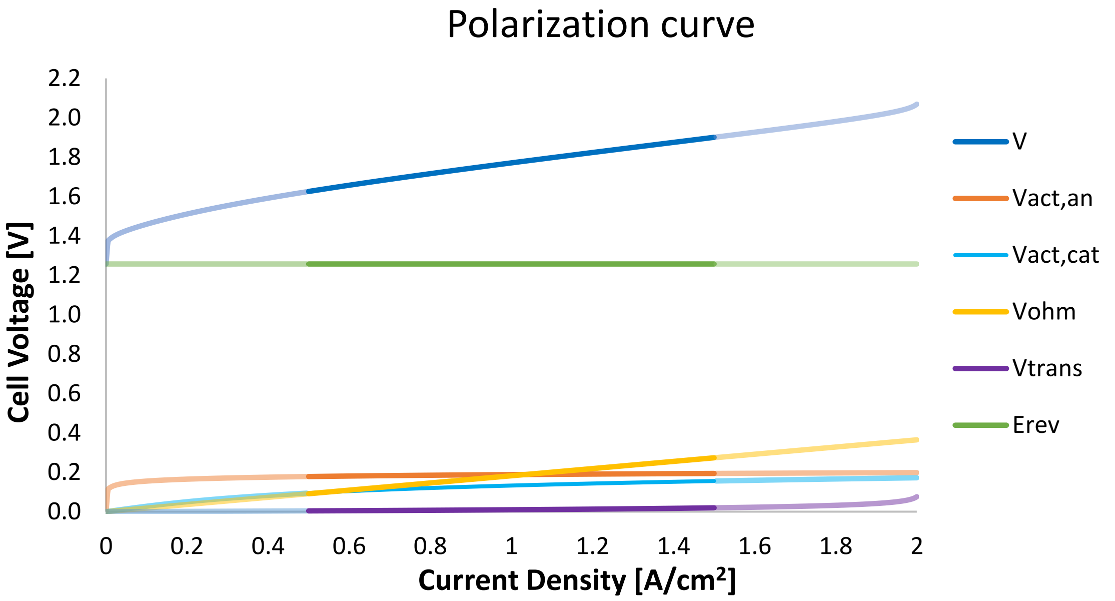

Figure 7.13 - Polarization curve at 60°C and 21 bar.

This range excludes certain combination of cell area and cell number (hence certain range of power), because the oxygen required will be produced at current density outside the range chosen.

Different combinations of cell number and cell area could manage to produce the oxygen needed in the range of current density identified, and the best combination will be chosen to be the one which minimizes the LCOH of the overall plant, considering hydrogen production both from PEM and from membrane reactors.

Higher the electrolyzer power, lower will be its load and greater will be the efficiency, but the cost for the electrolyzer will increase, thus, a trade-off on the electrolyzer size is detected. In order to analyze in an easy and fast way different cell number and cell area combination a code in Visual Basic has been implemented. The code, which consists of evaluating in an automatic way several parameters varying cell area and cell number, allows to identify the best electrolyzer configuration.

Indeed, once that cell area and cell number are fixed, since that oxygen production is known, the correspondent current density, through Equation (4.19), could be computed, then by applying Equation (4.18) hydrogen production is detected. Given the current density, through the logic scheme of relation explained in Figure 4.15, it is possible to obtain cell voltage and power needed. Once that PEM auxiliaries consumption are found, as explained in section *4.3.5 Electrolyzer auxiliaries consumption*, the electricity retrieved by the grid can be easily found, since ATR auxiliaries are always 22.93 kW, explicated in Table 7.2. Whether the configuration foresees the injection of carbon dioxide in a pipeline, CO_2 compressor consumption should be considered too (7.20 kW).

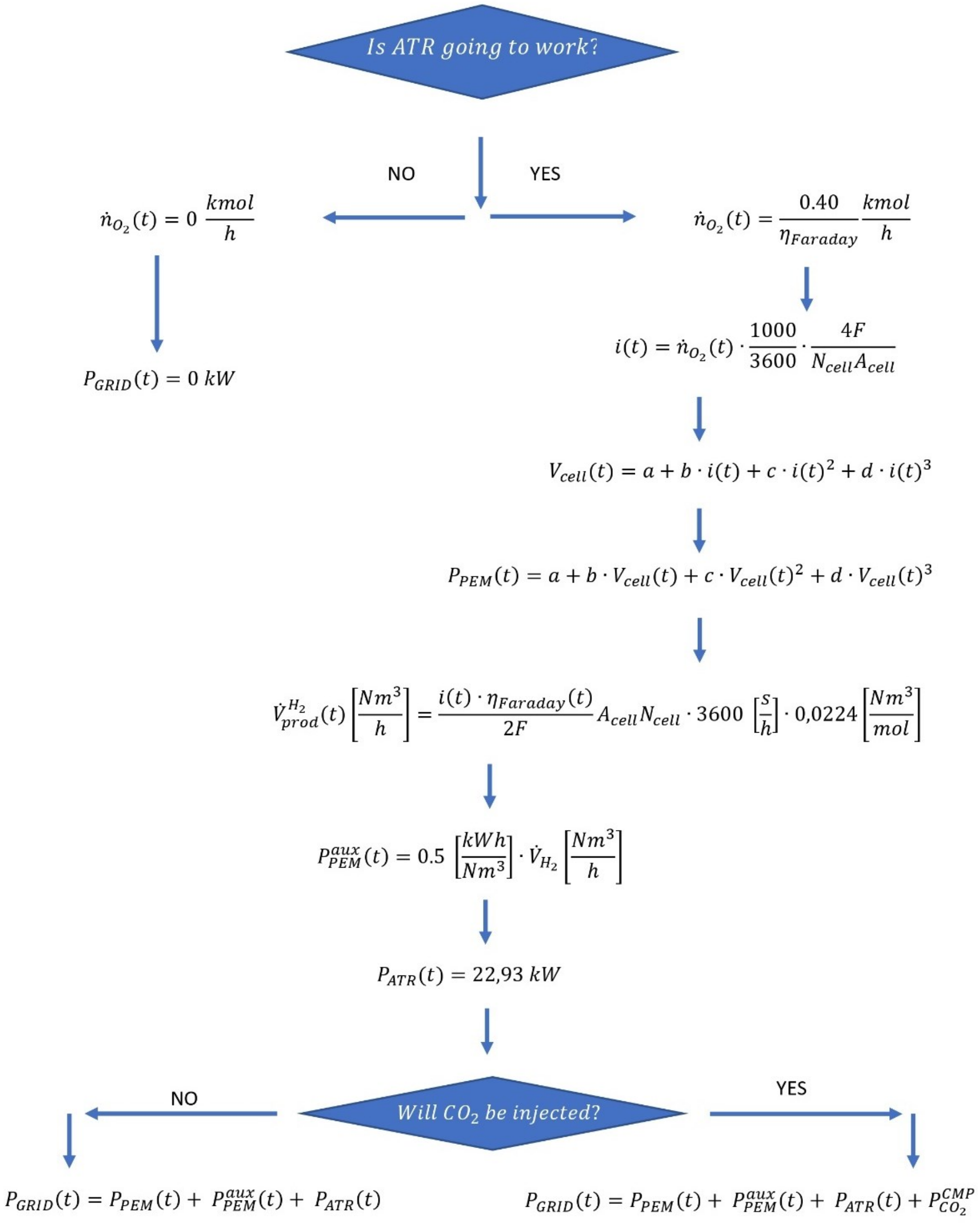
Is ATR going to work?
NO
YES
$\dot{n}_{O_2}(t) = 0\ \frac{kmol}{h}$
$P_{GRID}(t) = 0\ kW$
$\dot{n}_{O_2}(t) = \frac{0.40}{\eta_{Faraday}} \frac{kmol}{h}$
$i(t) = \dot{n}_{O_2}(t) \cdot \frac{1000}{3600} \cdot \frac{4F}{N_{cell} A_{cell}}$
$V_{cell}(t) = a + b \cdot i(t) + c \cdot i(t)^2 + d \cdot i(t)^3$
$P_{PEM}(t) = a + b \cdot V_{cell}(t) + c \cdot V_{cell}(t)^2 + d \cdot V_{cell}(t)^3$
$\dot{V}_{prod}^{H_2}(t) \left[\frac{Nm^3}{h}\right] = \frac{i(t) \cdot \eta_{Faraday}(t)}{2F} A_{cell} N_{cell} \cdot 3600 \left[\frac{s}{h}\right] \cdot 0{,}0224 \left[\frac{Nm^3}{mol}\right]$
$P_{PEM}^{aux}(t) = 0.5 \left[\frac{kWh}{Nm^3}\right] \cdot \dot{V}_{H_2} \left[\frac{Nm^3}{h}\right]$
$P_{ATR}(t) = 22{,}93\ kW$
Will CO_2 be injected?
NO
YES
$P_{GRID}(t) = P_{PEM}(t) + P_{PEM}^{aux}(t) + P_{ATR}(t)$
$P_{GRID}(t) = P_{PEM}(t) + P_{PEM}^{aux}(t) + P_{ATR}(t) + P_{CO_2}^{CMP}$

Figure 7.14 - Flow chart of PEM-ATR configuration.

7.2.2. Results

Visual basic code, with a step of 10 cm^2 and with a step of 10 cells, analyzes different combinations of cell area (range 50-300 cm^2) and cells number (50-800 cells), and it identifies the one which minimizes the LCOH of the whole plant, considering hydrogen production both from PEM and from ATR.

The results from Visual Basic code identify that the power of the electrolyzer which minimizes the LCOH of the whole plant is 96.7 kW, and the combination of cell area and cell number obtained is 113 cells of 300 cm^2.

It is possible to point out that the cell area identified is the maximum of the range investigated (according to Carmo et al.), and it is coherent with the latest trend of enlarging electrolysis cell. Indeed, being the hydrogen production affected by the current, if the cell area is enlarging, at the same current density a greater amount of hydrogen can be produced (besides Faraday's efficiency is greater too).

This fact could be easily understand from losses point of view too. Meaning that, if hydrogen production is fixed, larger cell provides a lower current density, therefore lower ohmic losses are generated.

Cell numbers value is typically affecting PEM electrolyzer stack power and hydrogen production. In this configuration hydrogen production is fixed, since it is fixed oxygen production to feed membranes reactor, thus the main voices which will drive the techno-economic trade-off are PEM investment cost and electricity purchasing from the grid.

Assuming to keep fixed 300 cm^2 as cell area whether cell number increases, PEM stack power is increased too. If this happens the load at which PEM electrolyzer would work is reduced since oxygen production is fixed at 0.40 kmolO_2/h. Lower load are beneficial for PEM electrolyzer efficiency, thus a bigger electrolyzer would minimize the cost for purchasing electricity from the grid, but the investment cost will be remarkable. Optimum cell number is therefore that value which minimizes the overall equivalent annual cost for PEM technology and for electricity withdrawal, and this value is 113 for 300 cm^2 of cell. Cell number and cell area detected as optimum set-up are similar values to the one adopted for PEM electrolyzer stack design in [55]. The electrolyzer identified produces the amount of oxygen needed working at 1.28 A/cm^2, corresponding to a cell voltage around 1.84 V.

The same stack power could be obtained by adopting different combination of cell area and cell number (shown in Table 7.10), but the surplus of hydrogen produced with a larger cell makes the configuration reported the one with the lowest LCOH, both considering the whole plant or considering PEM only. LCOH of PEM and of the whole plant has been computed as described in *6 Economic analysis*. The ATR plant economic analysis remains unchanged with respect to the previous paragraph.

Even if the difference on the overall LCOH (in Table 7.10) is obviously negligible, the table above allows to clearly point out the best combination of cell area and cell number for the PEM stack power which minimizes the cost of hydrogen produced.

Parameters	Values					
N_{CELL}	113	136	170	226	339	678
A_{CELL} [cm2]	300	250	200	150	100	50
H_2 produced by PEM [ton/year]	12.257	12.256	12.253	12.249	12.241	12.218
LCOH PEM [€/kgH_2]	7.6374	7.6383	7.6396	7.6419	7.6463	7.6597
H_2 tot [ton/y]	43.506	43.505	43.502	43.498	43.491	43.467
LCOH Plant [€/kgH_2]	5.4830	5.4832	5.4834	5.4839	5.4847	5.4873

Table 7.10 - Comparison of PEM electrolyzer at the same stack power.

Hydrogen production through electrolyzer, with an LCOH of around 7.64 €/kgH_2 is coherent with literature [3], [92] which considers electricity retrieved from grid. Indeed, besides investment cost, operational costs, and in particular the purchasing of the needed electricity is remarkable.

Once the best configuration is detected, it is interesting to evaluate several technical factor of plant operation, reported in Table 7.11, in order to produce 0.40 kmolO_2/h.

Parameter	Unit	Value
Current density	A/cm^2	1.28
Cell Voltage	V	1.84
PEM overall consumption	kW	89
PEM H_2 produced	kg/day	39.22
PEM Equivalent Hours	h/y	6201
PEM Electrolyzer Efficiency	%	61.20
PEM Efficiency on primary energy	%	27.54
ATR H_2 produced	kg/day	100
ATR Efficiency on primary energy	%	65.42
PEM-ATR consumption	kW	111.85
PEM-ATR consumption with CO_2 compression	kW	119.05
Overall system efficiency	%	47.15
Overall system efficiency with CO_2 compression	%	45.38

Table 7.11 - Technical parameters of the coupling between PEM and ATR.

PEM, ATR and system efficiency are computed according to Equation (2.2), while ATR efficiency on primary energy is taken equal to the one computed for oxygen-case reported in Table 7.4.

Once that cell area is fixed at 300 cm^2 it could be interesting to evaluate how LCOH of the plant is affected by the electrolyzer power in the current density range chosen. In Figure 7.15, LCOH considering CO_2 removal (sold at ambient condition) and CO_2 injection are reported.

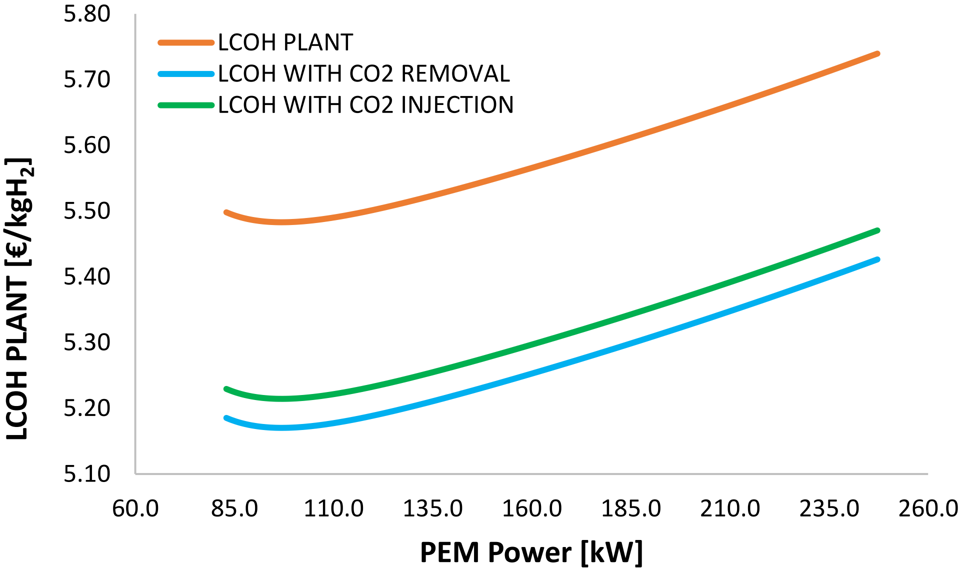

Figure 7.15 - Overall plant LCOH without CO_2 selling, with CO_2 selling at ambient condition, with CO_2 injection and selling.

The economic results of the plant are improving when CO_2 removal and/or injection in pipeline is realized. Rich-CO_2 stream is obtained after water separation, and it is worthy 35 €/tonCO_2, while whether compression and injection of CO_2 is applied, the economic value is 50 €/tonCO_2, but CO_2 compressor and CO_2 compression energy cost should be taken into account, as detailed in *5.5 CO2 removal and injection in pipeline* and in *6.7 CO2 removal and utilization*.

Being assumed 7500 hours per year of operation of autothermal reforming and separation the amount of CO_2 produced is always the same, equal to almost 390 tonCO_2/year, which, whether injection in pipeline is applied, could be considered negative emission. Therefore, in a year, the revenues are fixed, and they could be considered as a constant difference in LCOH of the plant (ΔLCOH) due to CO_2 income, detailed in Table 7.12, where the main voices of CO_2 treatment are highlighted.

	CO_2 yearly flow [ton/y]	CO_2 treatment cost [k€/year]	CO_2 income [k€/year]	ΔLCOH [€/kgH$_2$]
CO_2 Removal	388.8	0	13.6	-0.31
CO_2 Injection	388.8	7.75	11.7	-0.27

Table 7.12 - CO_2 removal and CO_2 injection economic evaluation.

The economic results, therefore, are improved by taking into account CO_2 selling. In particular, whether CO_2 separation and selling at ambient conditions is considered, the LCOH passes from around 5.48 €/kgH$_2$ to 5.17 €/kgH$_2$. While, in carbon negative plant, where CO_2 is injected, the LCOH decreases until to 5.21 €/kgH$_2$, greater than the case where CO_2 is sold at ambient conditions, but in this case there are all the carbon negative benefits to be considered.

As previously mentioned, PEM stack power which minimizes the overall plant is around 96.7 kW, with 113 cells of 300 cm^2. The LCOHs previously mentioned have been assessed according to procedure explained in chapter 6 *Economic analysis*, which voices, reported in Figure 7.16, are available once that PEM power, PEM H_2 production and electricity retrieved by the grid are computed through the yearly hourly simulation.

Grid exchange is not taken into account in Investment Cost, but it is a relevant share in variable OPEX and in the equivalent annual cost too. PEM equivalent annual cost share is a small share because PEM and ATR operational cost are particularly relevant (besides investment cost share) in a year.

As a conclusion, by comparing LCOH in air case, which is 4.96 €/kgH$_2$, with LCOH of oxygen plant with PEM introduction, it is possible to state that, even if CO_2 removal is considered (5.17 €/kgH$_2$ or 5.21 €/kgH$_2$ if injection is applied), it is not convenient from economic point of view producing oxygen by PEM and feeding it to membrane reactor with respect to compress air and feeding it.

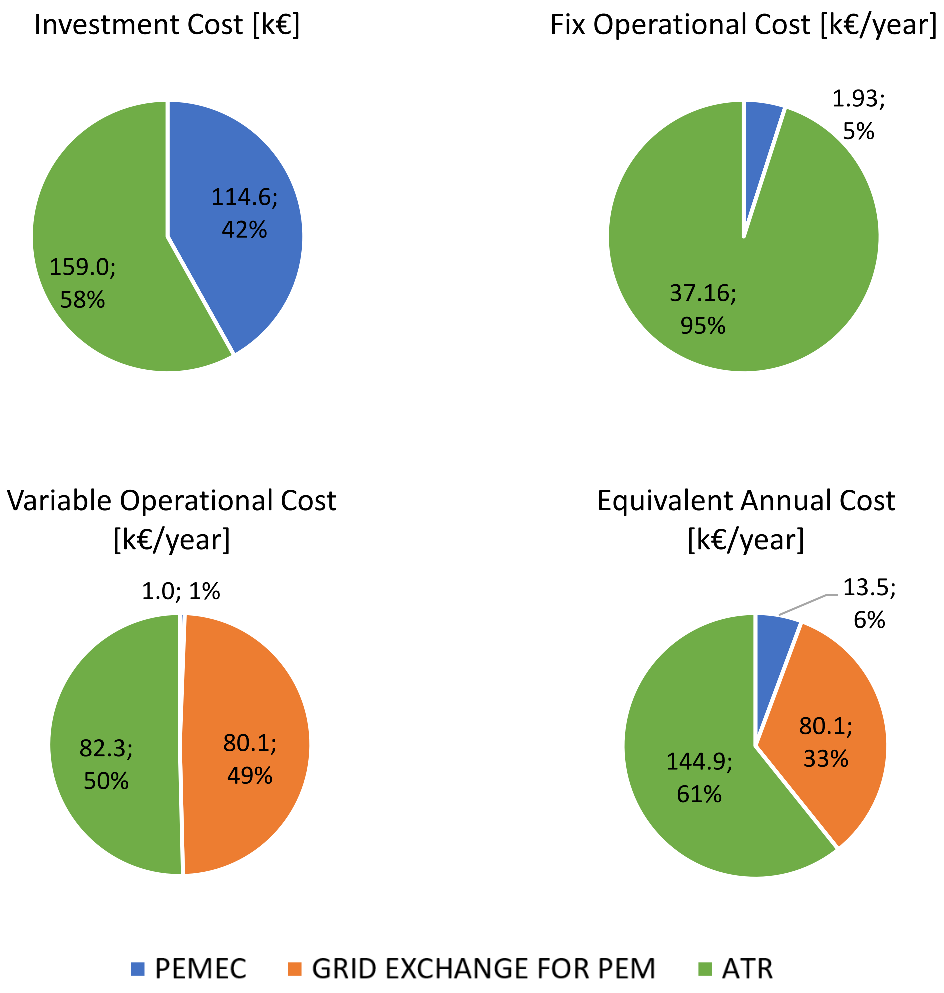

Figure 7.16 - Cost share between PEM (blue), ATR (green) and grid exchange for PEM (orange).

Indeed, besides PEM electrolyzer introduction, which is not a cheap technology yet, the electricity consumption are strongly increased, passing from 27.84 kW for air configurations to an overall consumption of almost 112 kW (119.14 kW if CO_2 injection is applied), having a strong impact on the equivalent annual cost.

	Air-case	PEM-ATR	PEM-ATR (CO_2 - removal)	PEM-ATR (CO_2 – injection)
LCOH [€/kgH_2]	4.96	5.48	5.17	5.21

Table 7.13 - LCOHs comparison between the introduced configurations.

A final remark could be done concerning CO_2 selling price, in particular it could be interesting to identify the CO_2 selling price at which PEM-ATR configurations would reach a break-even with air configuration LCOH. The trend is shown in Figure 7.17, where it is possible to conclude that:

- Whether CO_2 is sold at ambient conditions a value of 60 €/tonCO_2 would be needed to reach the break-even with air configuration LCOH.
- Whether CO_2 is injected into a pipeline CO_2 selling price break-even value is around 78.5 €/tonCO_2.

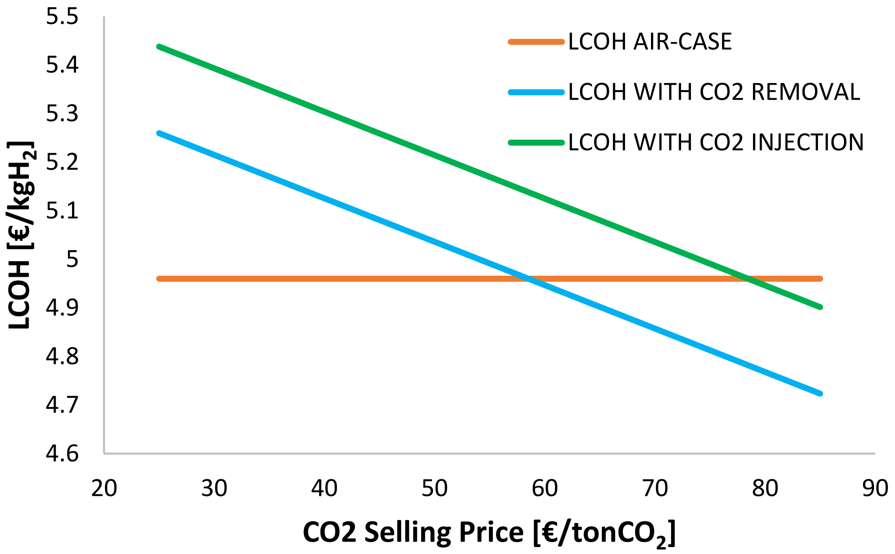

Figure 7.17 - Effect of CO_2 selling price if CO_2 is injected or sold at ambient condition.

Another interesting analysis that could be performed is to identify the cost of PEM electrolyzer technology which allows to have a break-even with air configuration. This analysis should vary both CAPEX and OPEX (only OPEX related to stack power have been analyzed), keeping fixed CO_2 as initial assumptions. Through Excel Solver tool it is possible to set range of variation of the interested cell (CAPEX and OPEX of PEM electrolyzer), and the chosen ranges are reported in Table 7.14. OPEX minimum value has been assumed, according to the same rate of cost reduction of CAPEX (-60%).

Cost	Max (Current value)		Min (2030 forecasting)	
	Value	Ref	Value	Ref
PEM CAPEX [€/kW]	1000	[31]	400	[99]
PEM OPEX [€/kW]	20	[31]	8	

Table 7.14 - Range of CAPEX and OPEX for PEM break-even cost.

Even adopting the minimum value, break-even is not reached, achieving LCOH values of 5.00 €/kgH_2, if CO_2 is sold at ambient condition, and of 5.04 €/kgH_2,if CO_2 is injected. This could be easily explained by looking at Figure 7.16, where the shares of the equivalent annual cost are presented. PEM cost technology accounts only for a value around 6%, indeed the main expenditure due to PEM introduction is concerning electricity purchasing cost. A sensitivity analysis on electricity purchasing price is further presented and detailed in chapter *7.5 Sensitivity analysis on electricity prices*.

7.3. PV-PEM-ATR configuration

Purchasing electricity is a relevant cost share in oxygen feeding plant when PEM electrolyzer is introduced. Photovoltaic energy could reduce the need to retrieve electricity from the grid, reducing the overall cost of electricity. Furthermore, as mentioned in section *5 Photovoltaic field and auxiliaries*, when PV field produces excess electricity with respect to the one needed to feed PEM, its auxiliaries and ATR needs, a selling procedure is applied, worthing 60 €/MWh.

This is the reason behind the choice of introducing a photovoltaic field nearest the hydrogen producing plant, and in this section its implementation and its coupling with PEM electrolyzer and ATR plant is detailed.

7.3.1. Configuration set-up

With a model detailed in *5 Photovoltaic field and auxiliaries* a photovoltaic energy source has been installed nearby the hydrogen producing plant. Solar radiation data taken from PVgis allows easily to compute the hourly yearly profile of electricity generated (kWh/kW$_P$); by taking into account the technology cost (besides installation, engineering, land cost…) it is possible to compute the Levelized Cost Of Electricity (LCOE) of the PV field placed in Catania (Italy) and then comparing it with electricity purchasing price.

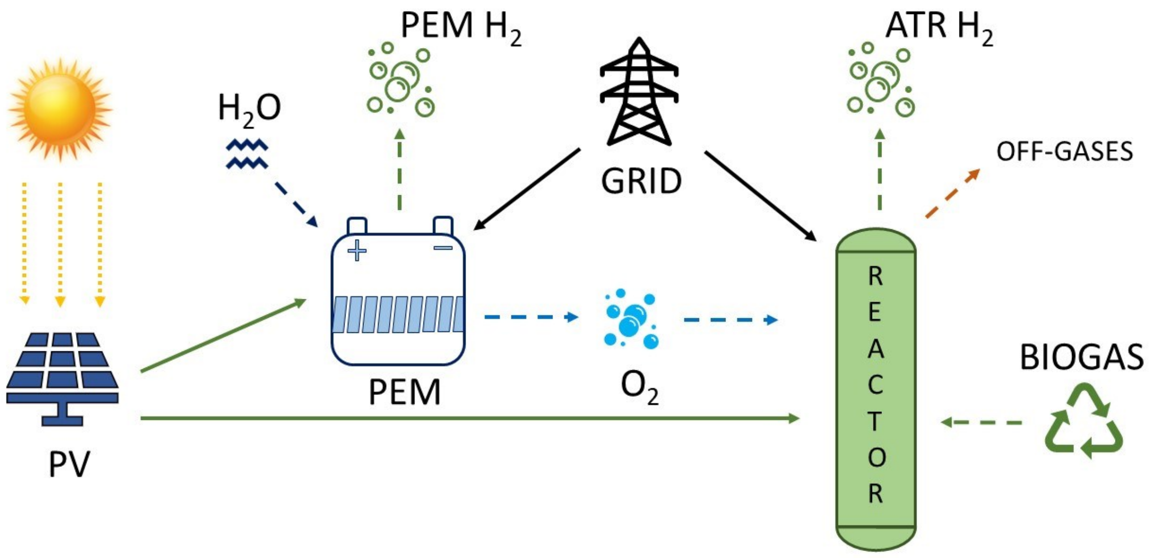

Figure 7.18 - Configuration set-up with introduction of PEM and PV.

The main techno-economic indexes to properly assess the goodness of PV installing are displayed in Table 7.15, with capacity factor and equivalent hours calculation as in Equation (7.5) and in Equation (7.6). The economic assumptions and formulation are detailed in paragraph *6.2 Photovoltaic field cost*.

$$H_{eq}^{PV}\left[\frac{h}{year}\right]=\frac{PV\ Electricity\ produced\ \left[\frac{kWh}{year}\right]}{PV\ Peak\ Power\ [kW]} \tag{7.5}$$

$$CF=\frac{H_{eq}^{PV}\left[\frac{h}{year}\right]}{8760\ \left[\frac{h}{year}\right]} \tag{7.6}$$

Parameter	Unit	Value
Electricity produced	$\frac{kWh}{kW_p \cdot year}$	517.2
Equivalent hours	$\frac{h}{year}$	1591.4
Capacity Factor	%	18.2%
Electricity Produced	$\frac{kWh}{kW_p}$	517.2
LCOE	$\frac{€}{MWh}$	56.5

Table 7.15 - Techno-economic indexes of PV field.

Equivalent hours and as consequence capacity factor are greater than other place in Italy, but they are coherent with the ones reported by other solar radiation data for PV plant installed in Sicily [100]. LCOE is a key parameter to assess the economic feasibility of a power plant, and as declared by International Renewable Energy Agency (IRENA) the obtained value is coherent (even slightly conservative) for current photovoltaic power plant installation [101]. Since LCOE of PV plant installed is lower than electricity purchasing price, it is possible to provide a cheaper electricity to the plant, at least during sun hours.

In order to provide a fair comparison with the previous described cases, FBMR operative hours are set equal to 7500 in a year, in order to consider maintenance (planned or not) and other outages. During functioning hours if PV field produce the whole electricity needed to feed the electrolyzer, its auxiliaries and ATR plant, only photovoltaic energy is used, and when there is an electricity surplus it is even sold. Instead, when the power produced is not sufficient or it is zero, the missing electricity is withdrawn from the grid.

PEM electrolyzer production and ATR consumption are kept constant, as in the previous configuration, thus an yearly hourly profile of electricity, oxygen and hydrogen flow, is easily built.

Known the oxygen required production, it is easy to retrieve back, through the logic scheme in Figure 4.15, the power needed to feed the electrolyzer, and in similar way to the previous configurations, different combinations in terms of PEM cell number, cell area, and number of module (from 80 kW_P to 800 kW_P) have been analyzed through an iterative Visual Basic code, which identifies the configuration which minimizes the LCOH of the whole plant, respecting the constraint on current density, which must be between 0.5 and 1.5 A/cm^2.

7.3.2. Results

The configuration and the size of PEM electrolyzer which minimizes the LCOH of the whole plant is the same of the case in which the electricity is completely retrieved by the grid,. Thus, PEM electrolyzer stack is composed by 113 cells of 300 cm^2, generating a stack power of 96.7 kW. PEM features and characteristics are therefore equal to the ones detailed in Table 7.11.

Analyzing the size of the PV field which minimizes the LCOH of the plant a consideration on the revenues from electricity surplus sold should be made. Since LCOE (56.5 €/MWh) from PV field is lower than the purchasing price assumed (60 €/MWh), whether revenues from electricity selling are considered, the size of the PV plant tends to skyrocket, maximizing the selling of electricity to the grid. This concept could be easily understood by looking to Figure 7.19, whether revenues are taken into account the cost of hydrogen produced is continuously decreasing. Thus, the choice of PV field size is not driven by PV electricity surplus revenues, but the optimum PV field size is chosen to be the one which minimizes the overall plant LCOH without considering PV revenues.

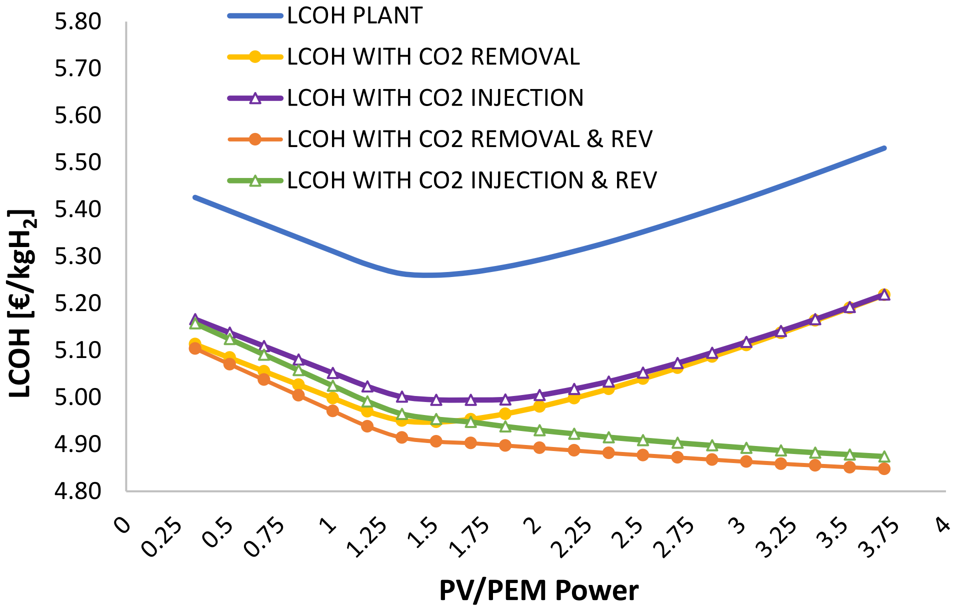

Figure 7.19 - LCOH without CO_2 selling (blue), with CO_2 removal (selling at ambient condition), with CO_2 injection (purple), and adding revenues from electricity selling (orange and green respectively).

The results show that the configuration which provides the lowest LCOH of the overall plant, whether CO_2 is not injected, is obtained adopting 550PV modules (around180 kW_P), providing a ratio between PV power and PEM power equal to1.85. Instead, whether CO_2 is injected into a pipeline, the optimum PV field size is composed by 600 PV modules (around 195 kW_P) with a PV power and PEM power ratio around 2.

Adopting this configuration, independently whether CO_2 is injected or not, economic results concerning hydrogen production are improved with respect to the previous case.

The main voices, for the case where CO_2 is not injected, are summarized in Figure 7.20. It is possible to point out that ATR cost per year is still the main player, accounting for more than 60% of the equivalent annual cost, followed by the grid exchange to feed PEM electrolyzer, which share is around 25%, reduced of 8 percentage point with respect to the case without PV field, as it could be expected since another technology is installed and cheaper electricity is available. However, photovoltaic energy sources is limited by sun availability and powering a plant which has to work for 7500 hours per year requires an high electricity utilization from the grid.

These conclusions are obviously (due to the small difference of size) valid for the case where CO_2 is injected too, which has very similar pie-chart (CO_2 equivalent annual cost is accounting only for 3%).

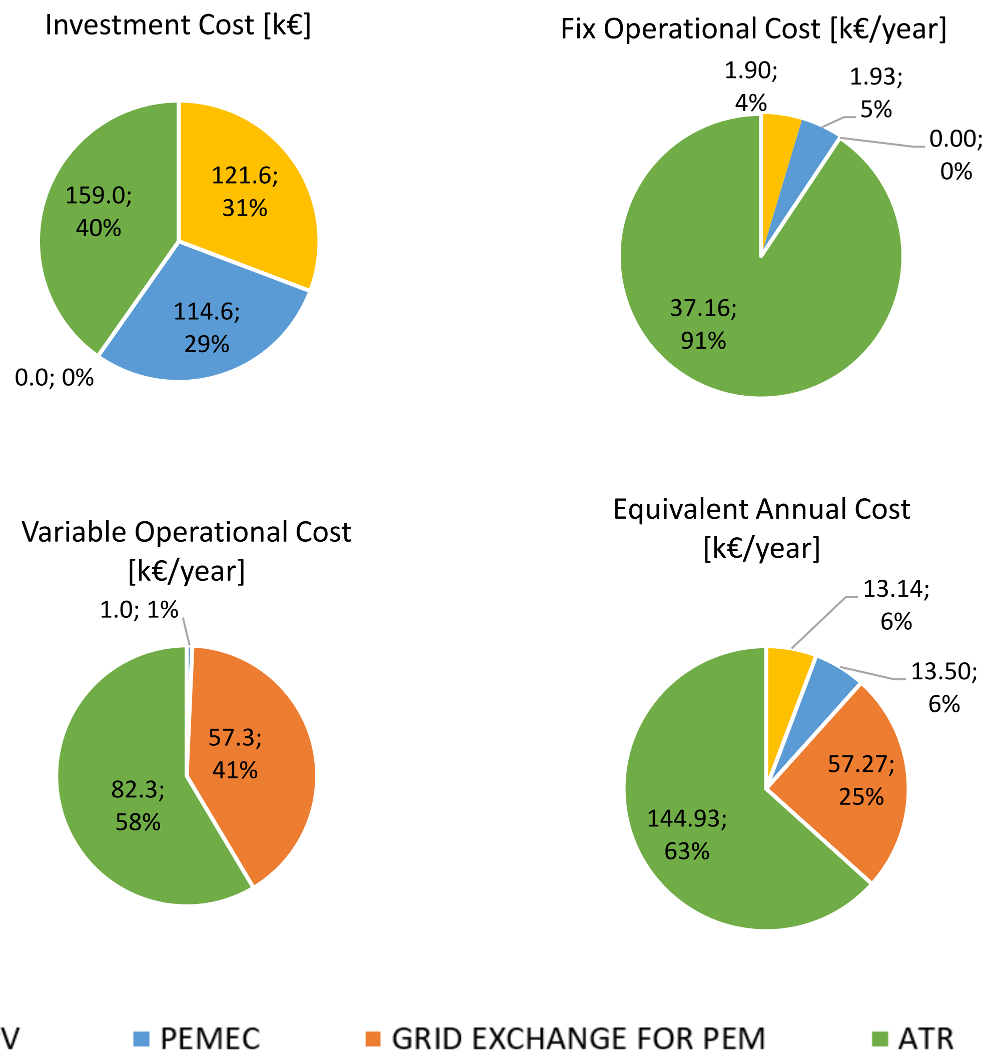

Figure 7.20 - Costs share between PEM (blue), ATR (green), grid exchange for PEM (orange) and PV field (yellow).

Adding photovoltaic energy sources allows to reduce the cost at which the energy is purchased, reducing the LCOH and improving the share of renewable energy used.

The results for the cases introduced are shown in Table 7.16, where LCOHs are compared; a reduction of around 0.-0.28 €/kgH_2 can be pointed out, which correspond to -5.4%, with respect to the case without PV field.

While introducing 195 kW_p in the configuration with CO_2 injection provokes a reduction of -0.29 €/kgH_2, around -5.6%. Due to greater plant consumption, given by CO_2 compressor needs, the reduction of LCOH is greater in the case where carbon dioxide is injected.

The configuration in which CO_2 is sold at ambient conditions, thus without injection, offers the lowest LCOH, even lower to air-case configuration, although the difference is very small (0.07 €/kgH_2), as shown in Table 7.16.

Therefore it is possible to conclude that, in a configuration with 550 PV modules (around 180 kW_P), with a PEM electrolyzer of 96.7 kW, it is possible to realize a plant which is slightly cheaper than air-case.

A note could be done on the economic results of the case in which CO_2 is injected into a pipeline. In this case, indeed, the plant is carbon-negative, with all the environmental benefits related, and it is still cheaper than air-configuration, even if the difference in LCOHs is negligible.

As previously mentioned, revenues from PV electricity, that could be sold to the grid, are not driving PV field size choice, in order to avoid oversizing PV field. Whether they would be taken into account in the previous configuration (180 kW_P and 195 kW_P), the LCOH value would be equal to 4.82 €/kgH_2 and to 4.86 €/kgH_2, respectively for the case in which CO_2 is sold at ambient conditions or if it is injected into a pipeline, as shown in Table 7.16.

Air-case will always be considered the benchmark for the configurations developed in this project but, it is worth to be mentioned that air-case could retrieve energy from a cheaper source like PV field with respect to the grid. Air-case, as already previously pointed out, demands only 27.84 kW and whether PV energy would be available, the electricity cost is reduced, decreasing the LCOH of the plant. An analysis on the PV field that could minimizes air-case LCOH has been performed, and it is displayed in Figure 7.21; the comparison is realized considering the case where CO_2 is sold at ambient conditions, because it is the one with the lowest LCOH.

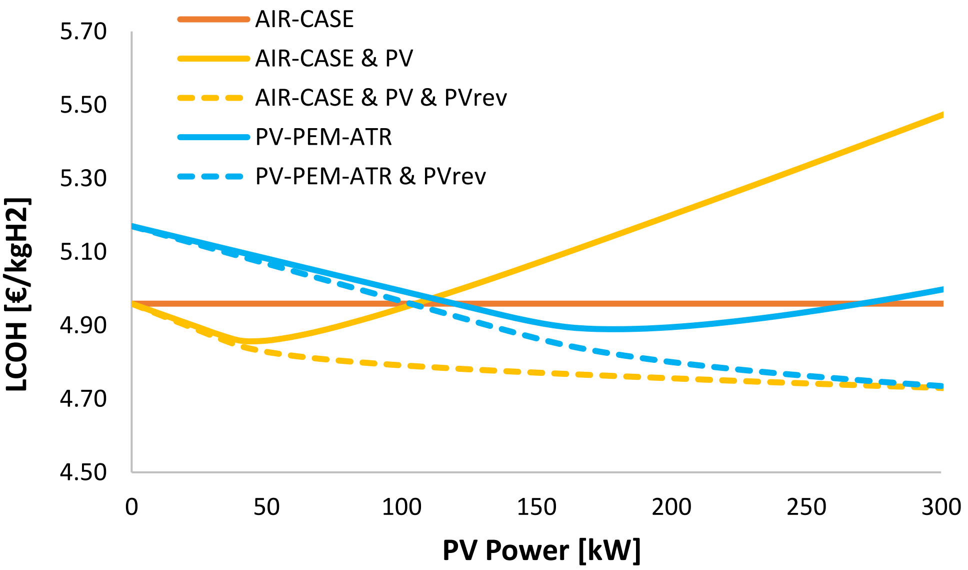

Figure 7.21 – LCOH of air-case varying PV field size.

Photovoltaic field size which minimizes the LCOH of air configuration, is 150 modules, equivalent to 48.8 kW_P, reducing the LCOH from 4.96 €/kgH_2 to 4.86 €/kgH_2 or to 4.83 €/kgH_2 if PV electricity revenues are considered. Thus comparing the LCOHs in Table 7.16 it is possible to point out that the lowest LCOH is achieved when oxygen feeding PEM-ATR plant is assisted by a PV field and PV electricity revenues are taken into account. The economic results among the different configurations are very close to each other, for this reason, a remark could be addressed to carbon-negative plant, which has very close LCOH to air-case but with environmental benefit which are increased.

	LCOH [€/kgH_2]	ΔLCOH with air-case [€/kgH_2]	ΔLCOH [%]
Air case	4.96	/	/
PV – Air case	4.86	-0.10	-2.01%
PV – Air case & PV rev	4.83	-0.13	-2.62%
PEM-ATR (CO_2 removal)	5.17	+0.21	+4.23%
PEM-ATR (CO_2 injection)	5.21	+0.25	+5.04%
PV-PEM-ATR (CO_2 removal)	4.89	-0.07	-1.41%
PV-PEM-ATR (CO_2 injection)	4.92	-0.04	-0.08%
PV-PEM-ATR (CO_2 removal & PV rev)	4.82	-0.14	-2.82%
PV-PEM-ATR (CO_2 injection & PV rev)	4.86	-0.10	-2.02%

Table 7.16 - LCOHs comparison between the introduced configurations.

7.4. PV-BESS-PEM-ATR configuration

From previously described analysis it has been highlighted that electricity purchasing cost is a remarkable share of equivalent annual cost, around 25%, if PV field is installed, and around 33% with the whole electricity retrieved from the grid. In order to reduce the cost at which electricity is bought, photovoltaic field has been introduced, providing cheaper electricity. Pursuing this aim, in this section, Battery Energy Storage System, detailed in section *5.3 Battery Energy Storage System*, has been introduced.

7.4.1. Configuration set-up

Batteries allow to decouple PV electricity production and hydrogen producing plant consumption, in order to store surplus electricity produced during sun hours, reducing electricity taken from the grid. The logic behind the implementation of the yearly hourly profile is that the electrolyzer must produce the exact quantity needed by FBMR (0.40 kmolO_2/h); the power needed to feed the hydrogen producing plant is the one produced by PV field (if available), while during night hours, the electricity is firstly retrieved from BESS up to minimum discharge capacity, then when this limit is reached, the electricity is retrieved by the grid.

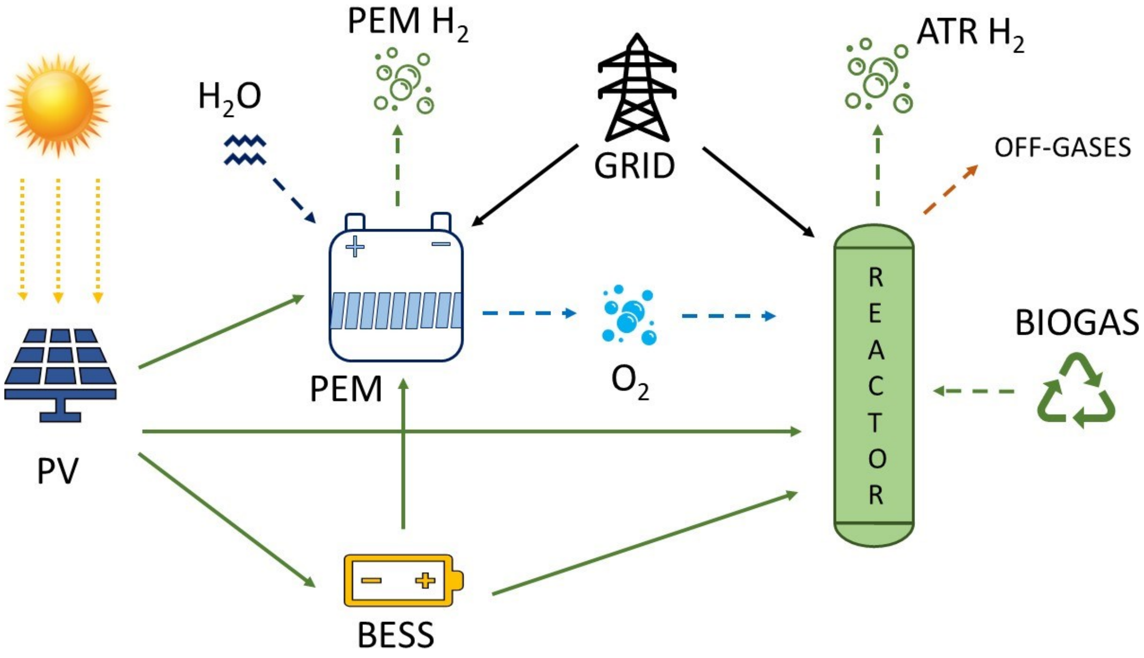

Figure 7.22 - Configuration set-up with introduction of PV, BESS and PEM.

Adopting this procedure the size of the PV field should be increased, in order to always produce surplus electricity, storing it, and using it during night time, minimizing the withdrawal from the grid.

In similar way to the previous cases, once that cell number and cell area are set (this has been done through Visual Basic code to test large number of combinations), known the oxygen production, through the logic scheme in Figure 4.15, it is possible to retrieve the power to feed the electrolyzer. Moreover, different combination of PV power and BESS power (from 50 kWh to 800 kWh) are tested in combination with cell number, cell area and PV modules variation, always considering 7500 operative hours per year and imposing a final battery SoC at least equal to the initial SoC, besides the previously mentioned constraints on current density.

A valuable index that could be useful to define, in order to properly choose a BESS size, is the Hours of Autonomy, which is a number that identifies the number of hours that BESS could feed oxygen production and ATR production, defined in Equation (7.7).

$$Hours\ of\ autonomy = \frac{BESS_{capacity} - BESS_{capacity}^{minimum}}{Total\ Plant\ Power} \tag{7.7}$$

This index allows to understand whether the BESS size tested is oversized or downsized with respect to the plant consumption. Total Plant Power is the sum of the power required by ATR plant and oxygen production plant (PEM and its auxiliaries). This number varies due to PEM size which is varied during Visual Basic code computation. Regarding economic results, as in the previous cases, the procedure has been detailed in *6.4 Battery Energy Storage System cost*.

7.4.2. Results

Visual Basic code provide techno-economic results which are worse than the previous case, with the lowest value slightly lower than 5 €/kgH_2. Regarding PEM size, it has not changed, with the configuration which minimizes LCOH of the whole plant composed by 113 cells of 300 cm^2,therefore, PEM electrolyzer production shares the same features enlisted in Table 7.11.

In Figure 7.23 it is possible to point out that LCOH of the plant is continuously increasing with BESS capacity, with the values displayed that are taking into account CO_2 removal (thus CO_2 selling at ambient condition). Meaning that introducing BESS, and consequently increasing PV field size, it is not convenient from economic point of view. Indeed, BESS is not, currently, a very cheap technology (even if its cost has recently decreased), considering that PV field size should increase too. Furthermore, in a case in which revenues from selling electricity would be accounted, an income would be strongly reduced since the surplus electricity will be stored (until BESS is already full).

The following figures are considering the case where CO_2 is not injected into a pipeline, but it is sold at ambient conditions, because it provides the lowest LCOH and the conclusions are practically identical for both cases.

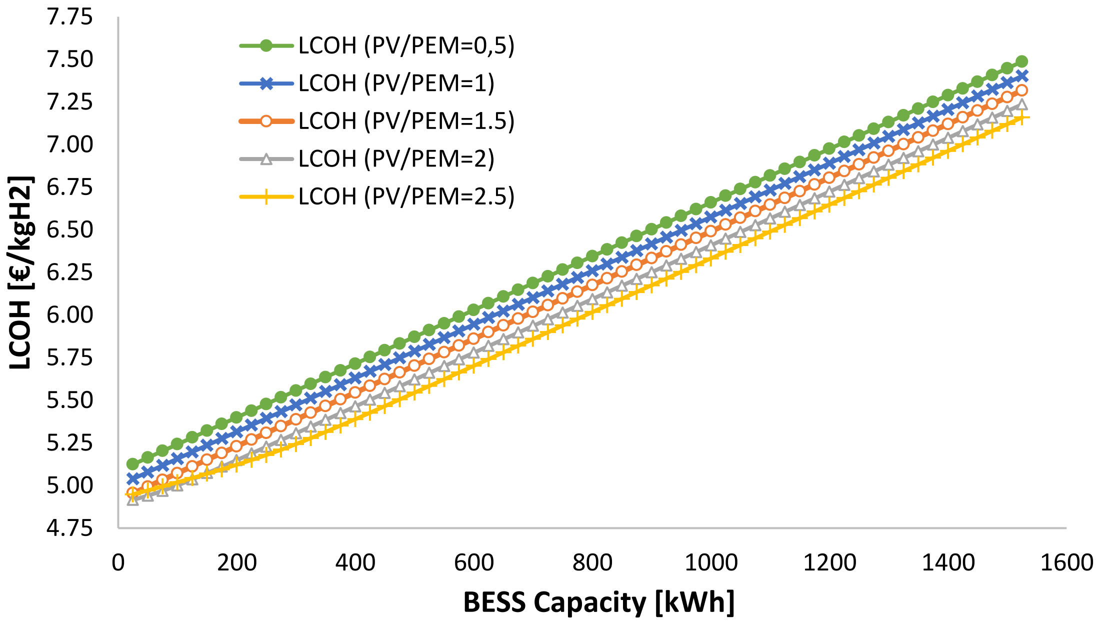

Figure 7.23 - LCOH of the plant at different BESS size and PV size.

The results, shown in Figure 7.23 and enriched in Figure 7.24, show that the best BESS size which minimizes the LCOH of the plant (always displaying results where CO_2 is sold at ambient condition) is 50 kWh, which is the minimum size tested, meaning that introducing BESS in the plant is not economically convenient. This conclusion is valid for the case where CO_2 is injected into pipeline too.

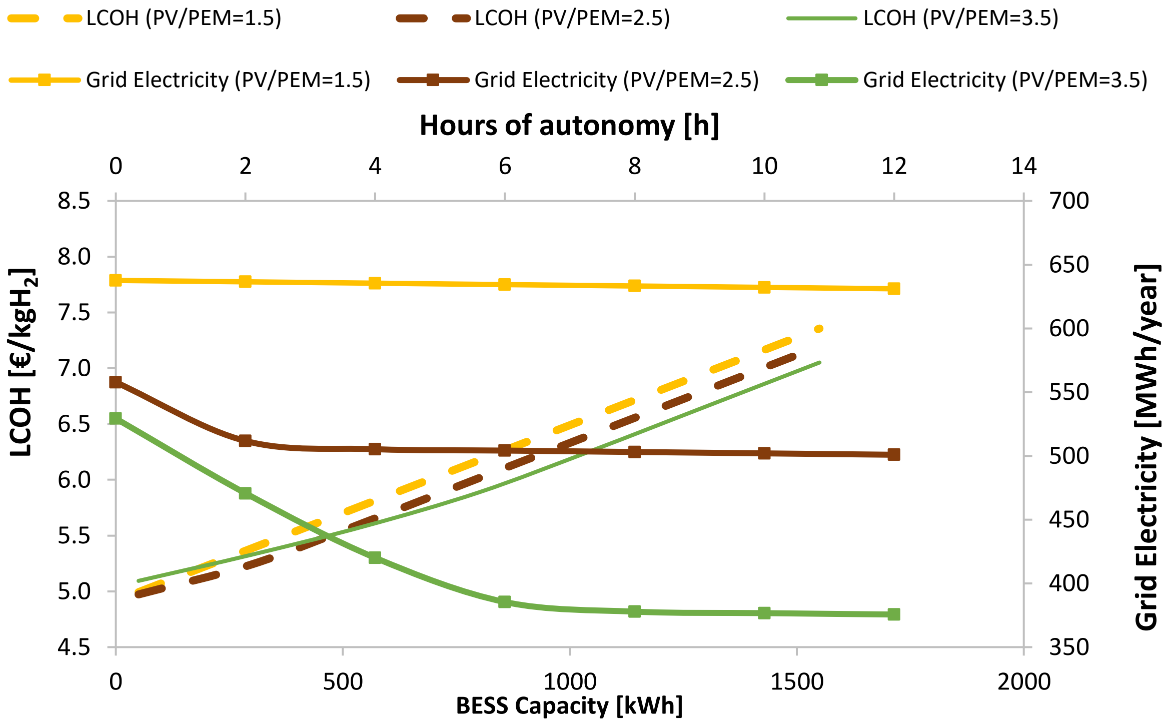

Figure 7.24 - LCOHs and Electricity retrieved from the grid as function of BESS capacity.

The best size of PV, for the case where CO_2 is not injected, is slightly greater than the previous case (195 kW_P against 180 kW_P); this because the minimum BESS size tested is 50 kWh, and not zero, as previously done and the configuration provides an LCOH equal to 4.94 €/kgH_2. Whether CO_2 is going to be injected, CO_2 compressor load should be taken into account, and this additional 7,20 kW slightly increase the optimum PV field size with respect to the case where BESS has not been introduced, up to 211 kW_P. The best configuration with CO_2 injection is, therefore, composed by 211 kW_P and 50 kWh (minimum size tested), providing an LCOH equal to 4.97 €/kgH_2.

BESS affects the amount of electricity withdrawn from the grid along the year, but its effect is appreciated only when PV and BESS size are increased. Indeed, in order to produce electricity surplus during day-time and being able to store it, as shown in Figure 7.24, the electricity retrieved from the grid is reducing only when PV field size and BESS size are big enough to store electricity surplus. Nevertheless, the increase in size of these components do not make BESS introduction economically convenient.

The results, shown in Table 7.17, are not considering CO_2 injection, since the lowest values are reached with CO_2 sold at ambient conditions, but the conclusion are practically the same, the difference between the two case is negligible. It is possible to highlight the worsening of results when BESS is introduced, and being the best configuration the one with smallest BESS size, pie-charts are not going to be displayed.

	Air-case	PEM-ATR (CO_2 removal)	PV-PEM-ATR (CO_2 removal)	PV-BESS-PEM-ATR (CO_2 removal)
LCOH [€/kgH_2]	4.96	5.17	4.89	4.94

Table 7.17 - LCOHs comparison of the best configurations (CO_2 sold at ambient condition) for the different cases.

7.5. Sensitivity analysis on electricity prices

The detailed on-grid configurations results are certainly directly affected by electricity purchasing price; indeed, the share on equivalent annual cost for powering PEM electrolyzer is remarkable, around 25-33%. In this section, a sensitivity analysis on electricity purchasing price is presented on the most performant configuration, which is the one where PEM is partially powered by PV field production, with carbon dioxide sold at ambient condition. In this analysis the electricity selling price is not varied in order to point out the effect of electricity purchasing price only and also because its effect is not as relevant as the purchasing one.

7.5.1. Results

Sensitivity analysis has been performed varying PV field size and electricity purchasing price, both for air-case and for PV-PEM-ATR configuration, with PEM size equal to the optimum found one (stack power equal to 96.7 kW, composed by 113 cells of 300 cm^2).

Sensitivity analysis has been conducted varying PV modules number, from 50 PV modules (around 16 kW$_P$) to 1400 PV modules (around 455 kW), and varying electricity purchasing price between 50 €/MWh to 250 €/MWh, with a step of 50 €/MWh. Results are, obviously, available also for an electricity purchasing price equal to 120 €/MWh, since it is the one assumed for the previous analysis.

By comparing air-case with PV-PEM-ATR one, it is expected that electricity purchasing price will have a greater effect on the latter configuration due to the greater electricity consumption per hour, with respect to air-configuration, also testified by looking at Figure 7.20; indeed PV-PEM-ATR configurations requires around 112 kW, given by 89 kW to feed PEM and its auxiliaries (Table 7.11) and by almost 23 kW to feed ATR plant (Table 7.2), while air-feeding one demands only 27.84 kW.

For this purpose, an initial sensitivity analysis concerning electricity purchasing price has been carried out between air-case and an oxygen configuration without PV field, like the one presented in *7.2 PEM-ATR configuration*; this has been done in order to represent the share of grid withdrawal to feed PEM electrolyzer production, with respect to ATR equivalent annual costs.

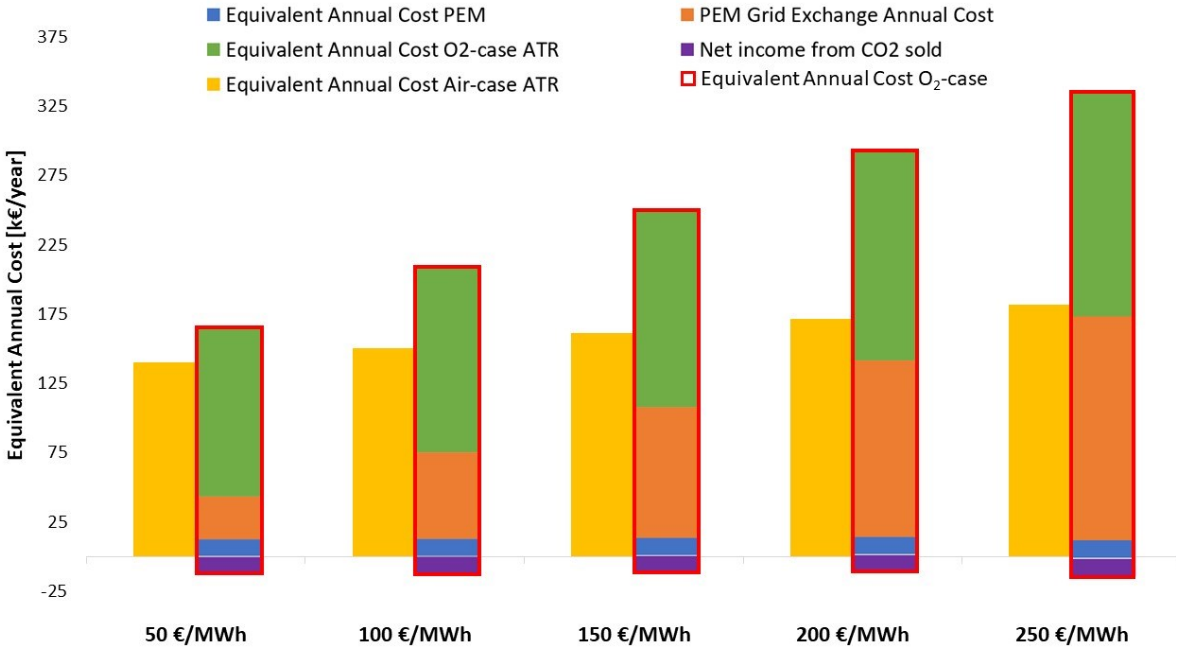

Figure 7.25 - Different Equivalent Annual Costs contributions at different electricity purchasing prices.

Observing Figure 7.25 it is possible to point out the great dependence of PEM overall cost increase due to increase in electricity purchasing price. Indeed, PEM overall cost is given by the equivalent annual cost, which takes into account PEM investment (plus replacement) and electricity retrieving cost to power it. Electricity withdrawal to power PEM electrolyzer is a relevant part of the overall annual cost, and observing Figure 7.25 above, it is possible to assess how much electricity purchasing price affects PEM overall cost, make it comparable to ATR plant at high electricity purchasing cost. Indeed, electricity consumption cost for ATR plant is not a relevant factor (unlike biogas purchasing cost), proved by the relatively small increase in equivalent annual cost of air-case and oxygen reactor part.

Once the great influence on electricity purchasing price on PEM overall annual cost is evaluated, it is possible to compare the best configuration detected, at different electricity purchasing price, as function of PV field size (Figure 7.26).

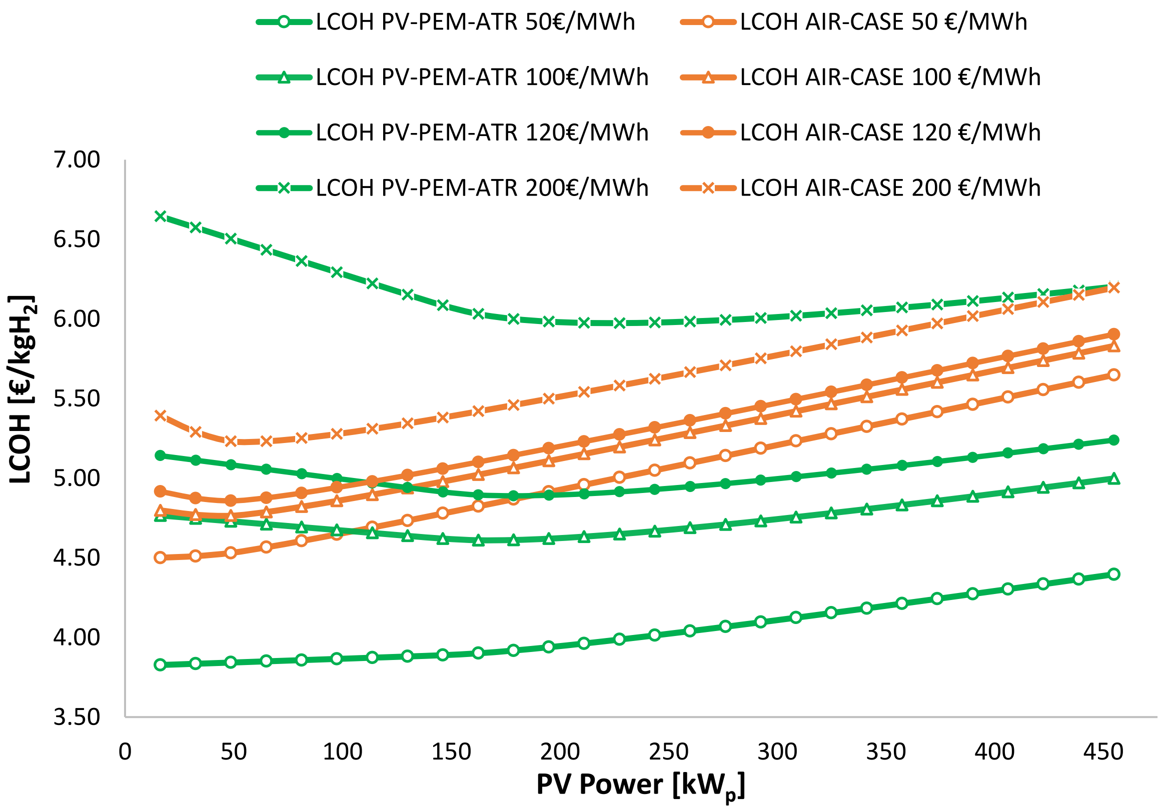

Figure 7.26 - LCOHs of air-case assisted by PV and PV-PEM-ATR cases at different electricity prices and as function of PV field size.

At low electricity cost it is possible to point out that oxygen feeding plant LCOH is always lower than the corresponding air-case. Feeding oxygen is beneficial for ATR plant, both from efficiency and from economic point of view, but the issue arises when oxygen is going to be produced. Grid withdrawal to feed PEM electrolyzer is a remarkable cost in the equivalent annual cost pie-chart, but if low-cost electricity would be available, the overall techno-economic performance could be better than air-case.

This surely happens with an electricity purchasing costs of 50 €/MWh and 100 €/MWh, while the value which makes practically equivalent the two cases is 120 €/MWh, because at their best configurations the cost are equal to 4.83 €/kgH_2 and to 4.82 €/kgH_2, respectively for air-case and for oxygen case, with a negligible difference between the two.

Whenever electricity purchasing price is well above 120 €/MWh, the configuration which minimizes LCOH for air-case will have an LCOH lower than oxygen case in its best configuration, thus 120 €/MWh could be considered a break-even for electricity purchasing price.

7.6. Off-grid configuration

Another interesting option to set-up is an off-grid configuration. In an off-grid configuration it is not possible to retrieve electricity from the national grid, but it has to be supplied by the energy sources and/or by the storage system that are installed inside the (typically small) grid, composed by the local interconnected loads and sources of energy. The impossibility of national grid electricity withdrawal arranges a challenging situation, where the components will be oversized with respect to an on-grid solution.

7.6.1. Configuration set-up

The energy source is provided by a PV field, which electricity production is going to power the PEM electrolyzer, the ATR system and their auxiliaries, but, in the meantime, it is going to be stored in a BESS, in order to partially save it and to use it during night time. Since the whole amount of electricity used is produced by renewable energy sources only, this configuration provides a completely green hydrogen producing plant, and whether CO_2 injection into a pipeline is applied, the whole production system is carbon negative too.

In off-grid configuration an oxygen tank has been introduced and modeled as detailed in *5.4 Oxygen tank*, with the minimum oxygen tank pressure fixed at 13 bar (1 bar over FBMR reactor operating pressure is assumed for safety of supply), meaning that whether oxygen withdrawal will reduce the tank pressure under 13 bar, the withdrawal is not allowed. PEM electrolyzer is therefore working at greater pressure than in the on-grid case, in order to keep pressurized the tank, assumed equal to 30 bar, keeping as operative temperature 60 °C.

Oxygen tank is a strategic component in off-grid configuration, storing the excess oxygen produced with respect to 0.40 kmolO_2/h needed by the ATR plant. Excess oxygen is produced during sun hours, where PV electricity is abundant, when, therefore, PEM electrolyzer is typically producing at maximum power.

Being off-grid, it has been chosen to let PEM electrolyzer production variable according to the input power, which is provided by PV field during sun hours and by BESS during night; same energy sources are foreseen to power ATR auxiliaries.

Therefore, unlike on-grid configuration, where PEM works exactly to satisfy FBMR request, in off-grid configuration, there is a mismatch between oxygen produced and oxygen consumed, this mismatch is going to be stored in the oxygen tank.

However, it could happen that during sun hours the electrolyzer production satisfies the ATR plant requirement and the oxygen tank is already full. When this situation arises the oxygen produced would be wasted, but being a valuable by-product it has been decided to make profits by selling it, at a price equal to 150 €/tonO_2, values assumed in Bellotti et al. [34] for oxygen produced as by-product from PEM electrolyzer operating at 30 bar. A value of 150 €/tonO_2 is indicated as minimum selling price for industrial use of oxygen, but medical oxygen could be more expensive [34]–[36].

A note could be made concerning the surplus oxygen revenues: producing oxygen through PEM electrolyzer is costing more than the selling price, thus, PEM size is not going to be oversized, like it could happen with PV field size if PV electricity revenues would drive PV field size choice.

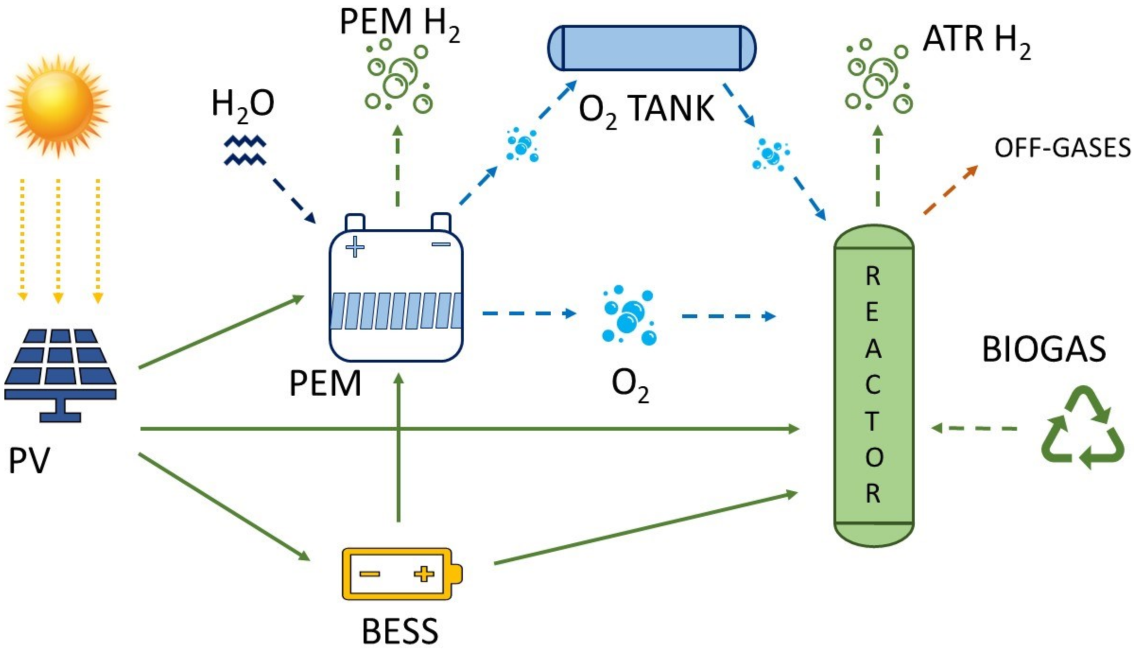

Figure 7.27 - Off-grid configuration set-up.

A coupling between PEM and PV power is therefore necessary, and it has been accomplished by following the logic scheme in Figure 4.15 and the consequent relations defined in *4.3 PEM power – PEM production relations*.

The previously mentioned relations allow to easily compute hydrogen and oxygen production once that the power in input is known, which is decided according to flowchart in *Appendix B.1 Flow-chart*.

Another note should be made concerning the operative hours: being in off-grid configuration they are going to be computed according to size and availability of the energy sources, assuming that the previous constraint of 7500 hours per year is not valid for this configuration.

In order to detect the combination of components size which minimizes the overall LCOH, as in the previous cases, a Visual Basic code has been implemented. The aforementioned code is testing a very big number of combinations of components size, varying PV module number, cell number and cell area of PEM electrolyzer, capacity of BESS and oxygen tank capacity.

Both cases, considering CO_2 injection or not, are going to be tested, since the consumption of CO_2 compressor is more relevant in off-grid configuration, and it will probably require bigger size of PV field and BESS capacity with respect to the case without compressor needs.

The ranges, through which Visual Basic has tested different combinations, are reported in Table 7.18. Values outside the ranges are not considered interesting, due to the trend of LCOH shown in previous simulations and confirmed in charts that are going to be shown in *7.6.2 Results* sections, besides the fact that several constraints must be respected.

In particular, the configurations under test must be compliant to constraints related to: current density, initial and final state of charge of BESS and initial and final percentage of oxygen tank filled.

Being in off-grid configuration, PEM production is dependent on the energy sources in input, therefore, PEM could work, during the day, from its minimum load (around 10% of maximum H2 production, as described in chapter *4 Electrolyzer*), which corresponds to 0.21 A/cm^2, to the maximum current density, kept equal to 1.5 A/cm^2.

PEM cell number and cell area test range is chosen in order to avoid working at minimum load with current density outside the limit here reported. Furthermore, the state of charge of BESS and the percentage of tank filled must be at least equal to the ones at the beginning of the year.

Component	Lower bound	Upper bound
PV modules number	2000 (around 600 kW)	4500 (around 1500 kW)
PEM cell number	150	650
PEM cell area	150 cm^2	300 cm^2
BESS capacity	600 kWh	1400 kWh
O_2 tank capacity	100 kgO_2	600 kgO_2

Table 7.18 - Components size ranges tested.

7.6.2. Results

Off-grid configurations are particularly responsive to loads requirements in terms of energy demand. For this reason it has to be decided to present results in different sections, according to the need of injecting or not CO_2 into a pipeline, although several conclusions are for both cases valid.

7.6.2.1. Off-grid configuration with CO_2 sold at ambient condition

Visual basic code allows to point out the combination of components size which minimizes the LCOH of the overall plant. The results highlight that PV field is equal to 812.5 kW$_p$, which powers a PEM electrolyzer of 258 kW, composed by 300 cells of 300 cm^2. The storage capacity of the best configuration is 800 kWh, which allows to autonomously feed the reactor (producing the oxygen required, powering ATR and all the auxiliaries) for at least 7 hours (whether BESS is fully charged and discharged up to the minimum capacity allowed). Regarding the oxygen tank, the best size is 300 kg, which allows to autonomously feed the ATR plant up to 13 hours. As previously mentioned, in off-grid configuration CO_2 revenues and O_2 revenues are taken into account and, the combination reported in Table 7.19, is the one which minimizes the LCOH considering both incomes.

Component	Unit	Value
PV field	kW$_p$	812.5
PEM electrolyzer	kW	258
BESS capacity	kWh	800
Oxygen tank capacity	kgO_2	300

Table 7.19 - Components size of minimum LCOH configuration, where CO_2 is not injected

Enlarging PV field and BESS capacity allows to increase operative hours of ATR plant up to 7756 hours per year. Even if PEM electrolyzer has a lower number of operative hours its hydrogen production is relevant, contributing to an electrolyzer production of around 17 tons per year; ATR produces around 32 tons per year, thus PEM electrolyzer production increases the overall hydrogen production of about 50%.

Component	Unit	Value
PV field area	m^2	8531
Electricity wasted	$\frac{MWh}{y}$	345
PEM Average Load	%	43.7
PEM Consumption	$\frac{kWh}{kgH_2}$	54
PEM Average Production	$\frac{kgH_2}{day}$	47.3
ATR Average Production	$\frac{kgH_2}{day}$	88.5

Table 7.20 – Features of optimum configurations of off-grid case with CO2 sold at ambient condition.

Hydrogen production are averaged considering 365 days per year, with PEM consumption and average load coherent with data reported by IRENA [23].

In order to understand why this combination of components size is the one which minimizes overall LCOH, several trends are displayed below.

The effect of electrolyzer size is shown in Figure 7.28, where it is possible to appreciate the trend of LCOH and plant operative hours as function of PEM power at different PV field size, considering 800 kWh and 300 kgO_2 as oxygen tank capacity. Electrolyzer size is a fundamental parameter to be properly calibrated, because it has an effect, obviously on oxygen produced, but on the electricity to be addressed to ATR too, affecting operative hours of the whole plant. This is the reason behind the first increase and then decrease of equivalent hours when PEM power start to increase.

From Figure 7.28 it is possible to appreciate the trend of LCOH, and consequently also the reason behind the optimum PEM and PV field size found. Obviously Visual Basic code investigates a larger number of possible combination; in Figure 7.28 only some relevant combinations, even for graphic reasons, are reported, in order to understand the trend of LCOH at different PV field size and PEM size. In particular, it is possible to point out the presence of the best configuration at around 258 kW of PEM stack power and at 813 kW_P PV field size, with a ratio between PV power and PEM power around 3-3.2, as shown in Figure 7.30.

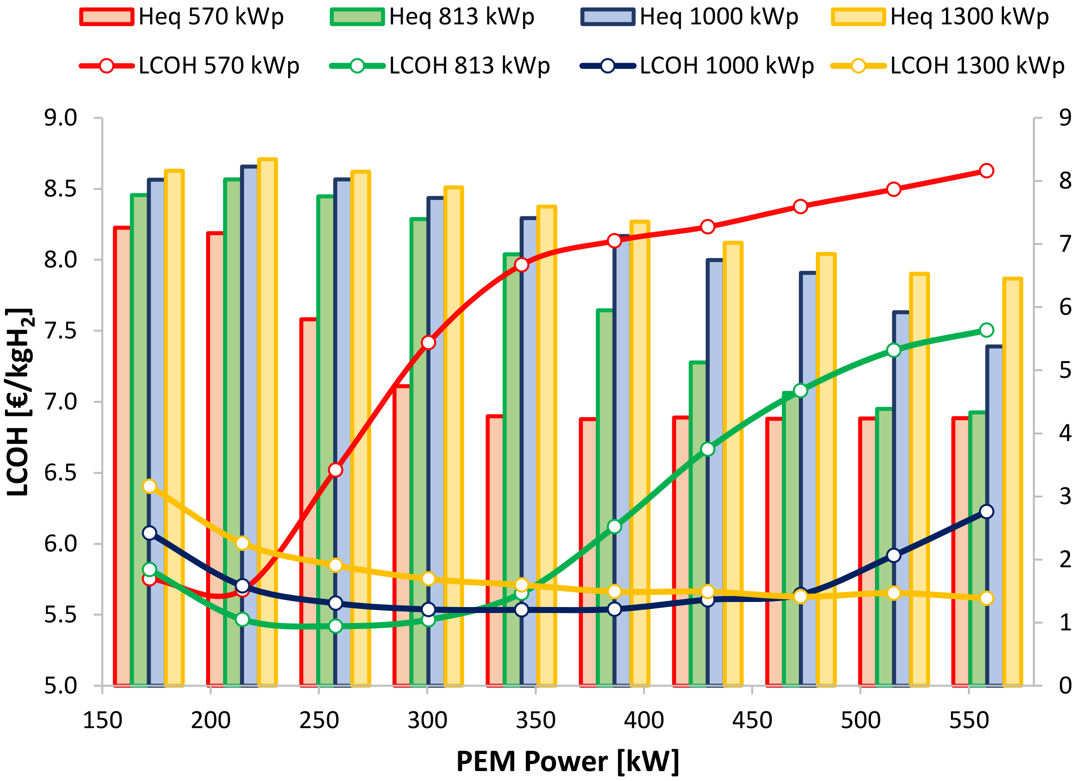

Figure 7.28 - LCOH and plant operative hours as function of PEM power at difference PV field size.

In order to detect the effects of BESS size and oxygen tank size some trends are going to be shown in the next figures.

In Figure 7.29 the effect of varying PV field size at different BESS capacity allows to understand the influence of these features in LCOH of the overall plant. The chart below is built considering a PEM electrolyzer and oxygen tank capacity equal to the ones of the configuration which minimizes the LCOH of the plant (obtained by Visual Basic code results), and those values are common for each tested point.

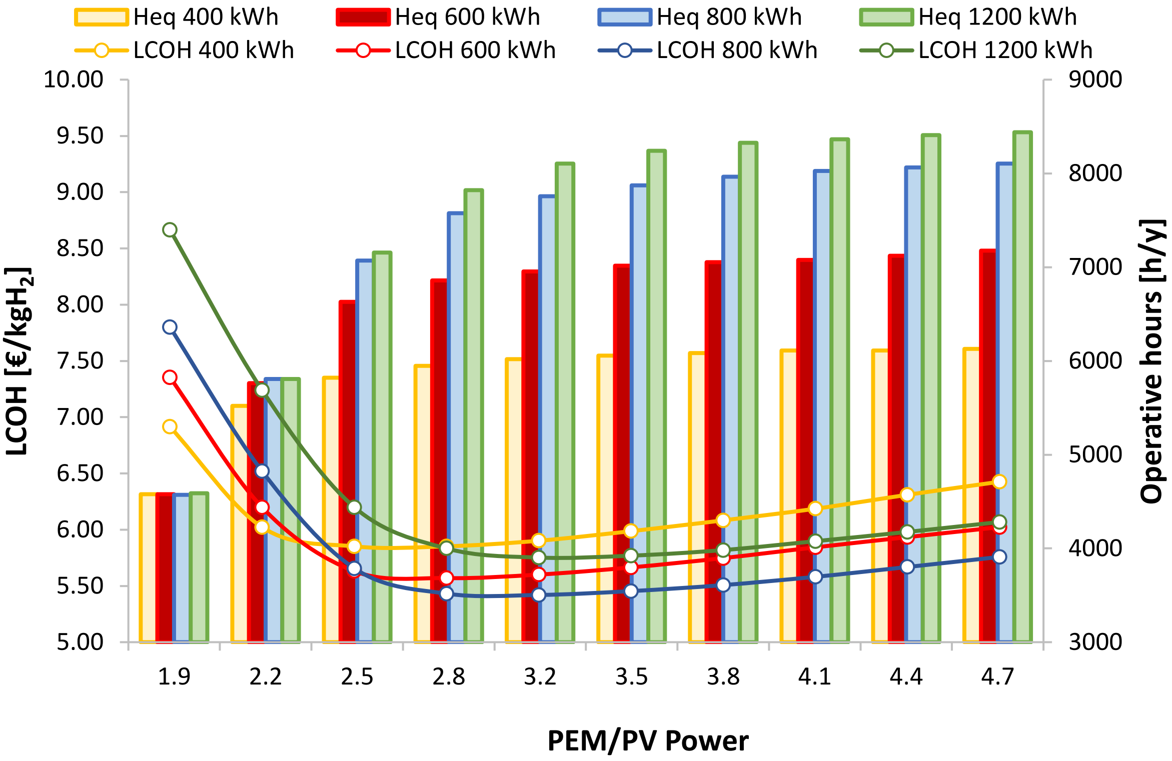

Figure 7.29 - Trend of LCOH and ATR operative hours at different PV and BESS size.

It is evident that an increase of BESS size must be supported by a PV field size which shall be appropriated to feed both BESS and overall plant during sun hours, and that is the reason of low operative hours and high LCOH, at small size of PV, even with big BESS size. Another note to point out is that it is not profitable to increase a lot the capacity of energy storage, because the increase of the cost related to storage growth is not compensated by an increase in operative hours; the operative hours adopting 800 kWh and 1200 kWh are not increased that much to pay back the increase of storage size.

Concerning oxygen tank size effect, Figure 7.30 analyzes the change in LCOH and plant operative hours at different oxygen tank size and at different PV size, adopting 800 kWh as BESS capacity and a PEM electrolyzer composed by 300 cells of 300 cm^2, as the one of the best configuration.

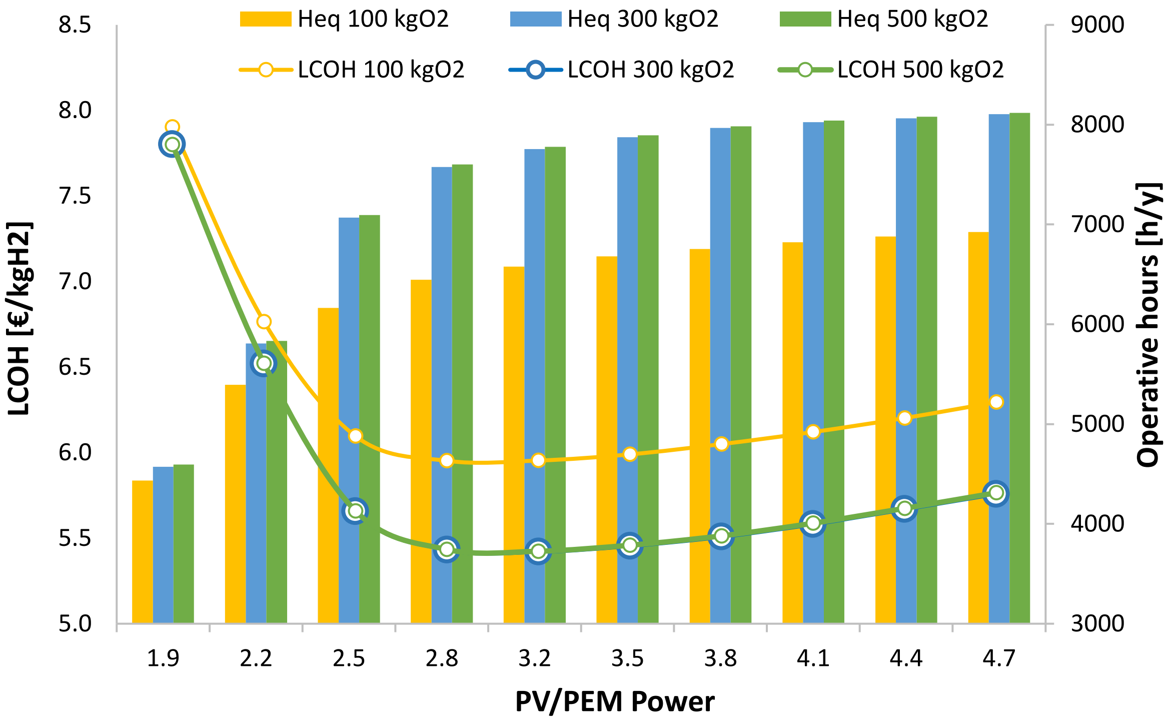

Figure 7.30 - Trend of LCOH and ATR operative hours at different PV and oxygen tank size.

An increase in oxygen tank capacity is relevant once that a certain autonomy hours are granted. This means that if the capacity of the tank allows to store oxygen for at least 7 hours (around 175 kgO_2 as capacity) it provides an high operative hours configuration. Obviously, the greater the size of photovoltaic power is, the greater the operative hours are, and the increase of O_2 tank size from 300 kgO_2 (around 13 hours of autonomy) to 500 kgO_2 (around 22 hours of autonomy) rises the LCOH of the plant due to the bigger tank size and due to lower income from O_2 sold, but, however, in a negligible way.

In Figure 7.31 the trend of LCOH and the trend of oxygen selling income are shown at different oxygen tank capacity and at different PV size. Once a certain FBMR feeding autonomy hours are granted, itis possible to point out the very low impact of oxygen tank in the overall LCOH, due to very big size and cost of the other technology; this can also be detected by analyzing the share of each technology on equivalent annual cost (Figure 7.32).

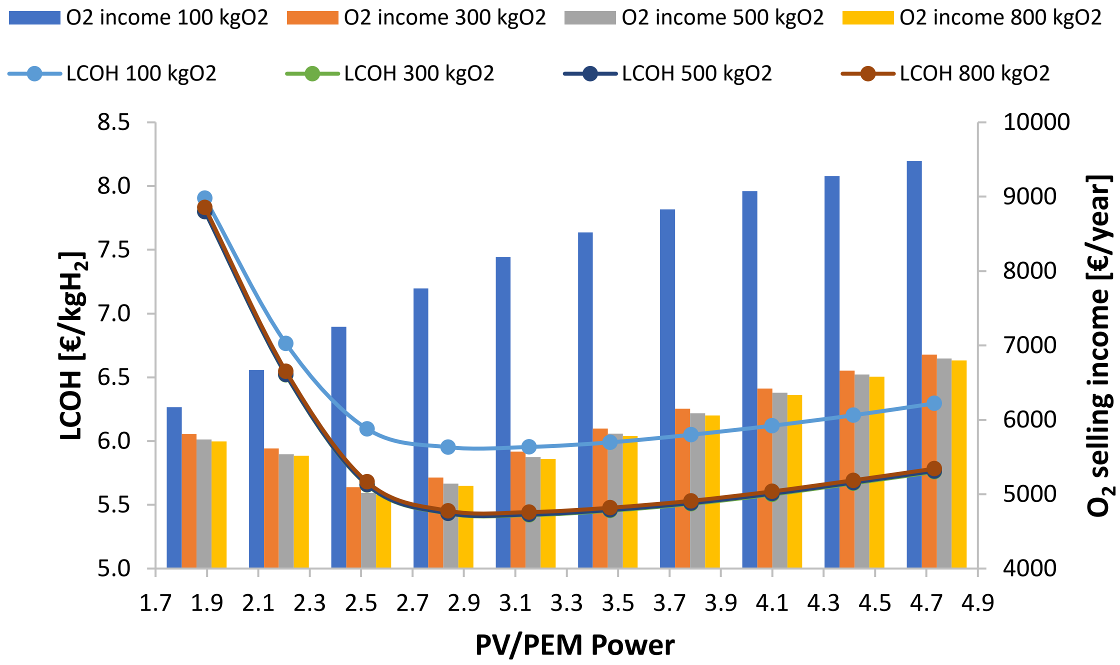

Figure 7.31 - LCOH and income from oxygen selling at different PV field size and tank capacity.

The different shares of voice costs are depicted in pie-charts in Figure 7.32. It is possible to highlight that concerning the investment cost, the main player is the PV field, due to the very big size, which requires an overall big investment cost. Nevertheless, from an equivalent annual cost point of view, autothermal reforming is the main cost due to very big operational costs, which are mainly affected by biogas purchasing cost.

Indeed, in this case variable operational cost are all due to ATR, because there is no withdrawal from the grid to power PEM electrolyzer, which was the other big voice in previous analysis.

Through the previous analysis it is possible to better identify the components size which allows to minimize the LCOH of the overall plant, summarized in Table 7.19. The final value of LCOH is 5.42 €/kgH$_2$, considering CO$_2$ sold at ambient conditions and oxygen surplus revenues, reaching a number of operative hours equal to 7756 hours per year.

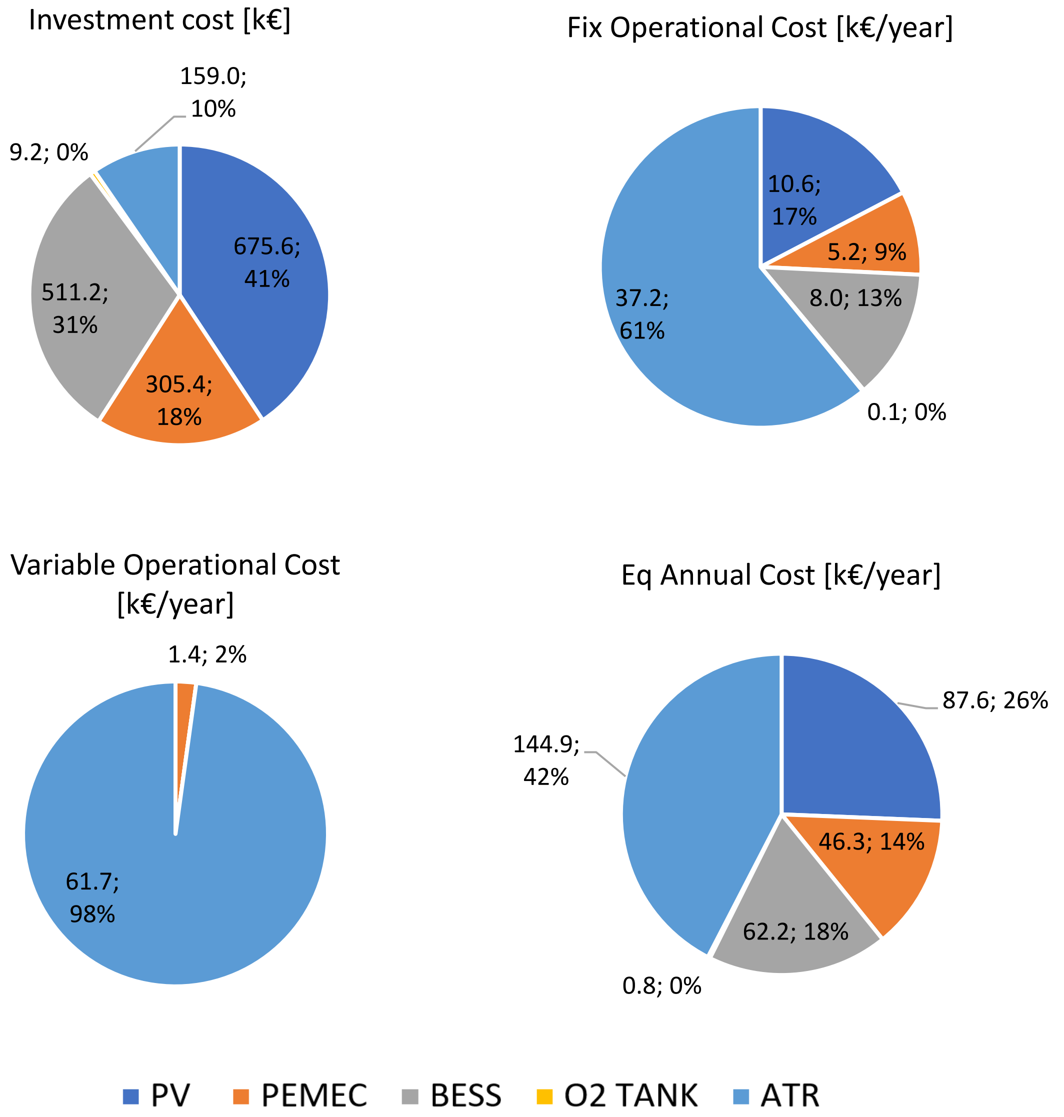

Figure 7.32 - Costs share between PEM (orange), ATR (light blue), BESS (grey) and PV field (blue).

As previously mentioned, when the tank is full, surplus oxygen is sold at 150 €/tonO_2. Due to an overall oxygen that could be sold as by-product equal to 37.1 tonO_2 per year, the LCOH is reduced of almost -0.11 €/kgH_2, since it generates an income around 5.6 k€/year.

Concerning CO_2 selling, it happens at ambient conditions and it provides an income of 14.1 k€/year, generating a difference of -0.29 €/kgH_2. Both revenues allow to reduce the cost of hydrogen generated of a value equal to -0.40 €/kgH_2 (-6.8%), with a contribution given by oxygen surplus revenues of around -1.9%, and given by carbon dioxide selling, which accounts for a reduction of around -4.9%.

	Unit	Value	ΔLCOH
LCOH without revenues	€/kgH_2	5.82	/
LCOH with CO_2 selling only	€/kgH_2	5.53	-0.29
LCOH with O_2 surplus selling only	€/kgH_2	5.71	-0.11
LCOH with both revenues	€/kgH_2	5.42	-0.40

Table 7.21 - Summary of LCOHs and contributions of revenues for off-grid case without CO_2 injection.

Due to the size of components, which is larger than on-grid case, off-grid configurations are typically more expensive than on-grid ones, even if CO_2 and O_2 revenues are taken into account, nevertheless in this case all the energy used is 100% renewable and the plant generating a completely green hydrogen.

As a conclusion, it has been demonstrated that off-grid configuration could be a practical and feasible solution for all those hydrogen-consuming applications which have particular problems of hydrogen transport and storage but that have sun and biogas availability.

7.6.2.2. Off-grid configuration with CO_2 injection

CO_2 injection requires an additional power consumption in order to compress CO_2 up to pipeline condition. This additional load is, obviously, has a bigger impact in an off-grid configuration than in an on-grid one, due to impossibility of electricity withdrawal, and, as a consequence, the components size of the configuration which minimizes the LCOH of the overall plant, could be different from the previous configuration.

In order to power CO_2 compressor, around 7.20 kW are required, thus, small differences in the components size of the configuration which minimizes the LCOH of the overall plant could be expected.

Visual basic code, analyzing a very large number of combinations, provides an overall LCOH equal to 5.64 €/kgH_2, obtained adopting 2500 PV modules, corresponding to 812.5 kW_p and 215 kW as stack power of PEM electrolyzer, composed by 250 cells of 300 cm^2 (according to the manufacturer it could be divided in more stacks).

Battery energy storage system capacity is greater than the previous case, equal to 900 kWh, which guarantees 7 hours of autonomy of the hydrogen producing plant; oxygen tank capacity is around 300 kgO_2, corresponding to 13 hours of autonomy. As previously mentioned these sizes are minimizing the LCOH of the plant considering CO_2 and surplus oxygen revenues too.

It is possible to point out small differences between the components size of the best configuration whether CO_2 is injected or not. This is due to techno-economic constraints due to availability of electricity. In order to better understand why this configuration is the best one for this case, a comparison between three interesting configurations are provided.

The first aim is to test the components size of the configuration which minimizes the LCOH of the case in which CO_2 is not injected, since just the CO_2 compressor is added, it could be a possible solution. Then a configuration with the same components size of the configuration which minimizes the LCOH of the case in which CO_2 is not injected, but with an increase BESS, equal to 900 kWh, is tested. The increase of storage capacity is due to the additional load with respect to the previous configuration, due to CO_2 compression. The last configuration detailed is the output of Visual Basic code, which tested a very large number of combinations, and it provides as output the combination reported above.

	Best configuration if CO_2 is not injected	Middle configuration	Best configuration if CO_2 is injected
PV power [kW_P]	812.5	812.5	812.5
PEM cells number	300	300	250
PEM cells area [cm^2]	300	300	300
BESS capacity [kWh]	800	900	900
Tank capacity [kgO_2]	300	300	300
ATR operative hours [h/y]	6996	7391	7775
Total Equivalent Annual Cost [k€/y]	264.6	271	267.5
H2 produced by PEM [$tonH_2/y$]	16.91	17.13	15.03
H2 produced by ATR [$tonH_2/y$]	29.15	30.80	32.40
H2 produced by plant [$tonH_2/y$]	46.05	47.30	47.43
LCOH with CO_2 & O_2 revenues	5.75	5.65	5.64

Table 7.22 - Comparison of configurations with CO_2 injection.

Due to the additional load given by CO_2 compressor the optimum BESS capacity is increased with respect to the case without compression, from 800 kWh to 900 kWh, which provides at least 7 autonomy hours of powering PEM and ATR plant, against 6 autonomy hours that would have been provided by 800 kWh. Increasing the operative hours of ATR plant generates a lower LCOH, due to the techno-economic convenience of providing an high operative hours to membrane reactors.

Adopting the "Middle configuration", in Table 7.22, provides a configuration with 900 kWh as BESS capacity. but with the same electrolyzer power (258 kW) of the optimum set-up in which CO_2 is sold at ambient condition. This components size provokes a greater equivalent annual cost and lower overall H_2 production. Thus, it is possible to point out that the configuration adopted in the case CO_2 is not injected is not performant as the one in output from Visual Basic, which details are in Table 7.23.

Component	Unit	Value
PV field	kW_p	812.5
PEM electrolyzer	kW	215
BESS capacity	kWh	900
Oxygen tank capacity	kgO_2	300

Table 7.23 - Components size of minimum LCOH configuration, where CO_2 is injected. Same as the third configuration in Table 7.22.

Adopting these components size, the operative hours for biogas autothermal reforming plant is equal to 7775 hours per year, sustained by an hydrogen production from PEM electrolyzer too. Summing up both hydrogen production the yearly value is around 47.43 tons/year, provided by a configuration with features enlisted in Table 7.24.

Component	Unit	Value
PV field area	m^2	8531
Electricity wasted	$\frac{MWh}{y}$	233.4
PEM Average Load	%	43.9
PEM Consumption	$\frac{kWh}{kgH_2}$	54.1
PEM Average Production	$\frac{kgH_2}{day}$	41.2
ATR Average Production	$\frac{kgH_2}{day}$	88.8

Table 7.24 - Features of off-grid configuration with CO_2 injection.

ATR and PEM production are average values considering 365 days per year; if only actual operative hours would be accounted, a value around 100 kgH_2/day would be found for ATR, similarly to on-grid cases, where 7500 h/y were imposed. PEM consumption and features, they are coherent with values reported by IRENA in [23].

The charts analyzing BESS and oxygen tank effect are very similar, in terms of conclusions, to the ones of the case where CO_2 injection is not applied, thus, they are not shown for this case too.

The equivalent annual cost provides the real weight of the single technology investment, since it considers investment cost amortization and operational costs. Due to the big size of the considered configuration, the equivalent annual cost share of each technology is more softly divided than on-grid case, exception made for CO_2 injection cost, which is practically negligible since it considers only CO_2 compressor cost. Investment cost is dominated by PV field investment in this case too. Anyway, the very high operational cost of ATR plant, especially for biogas purchasing, provides that the main voice concerning the equivalent annual cost is related to ATR.

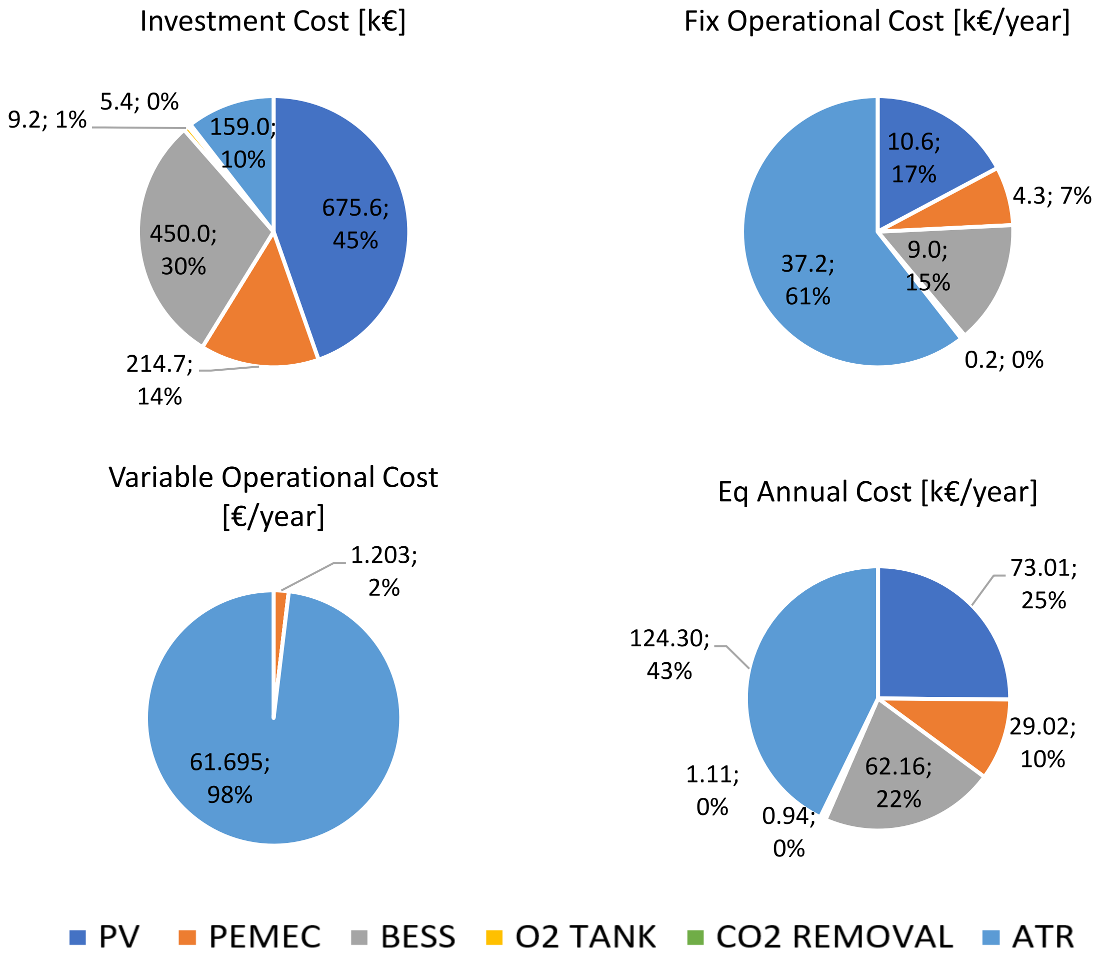

Figure 7.33 - Costs share between PEM (orange), ATR (light blue), BESS (grey) and PV field (blue), CO_2 removal (green).

In order to provide a deeper analysis, the effects of CO_2 revenues and oxygen surplus income are highlighted in Table 7.26 and they are depicted in Figure 7.34.

In Figure 7.34 the contributions of CO_2 and O_2 revenues, in terms of k€/year, at different PEM size are shown. The shown chart is built considering variable PEM size, but fixed PV size, BESS capacity and oxygen tank capacity, which sizes are taken equal to the ones which minimizes the LCOH of the overall plant. A reducing trend with increasing PEM power can be detected up to 215 kW; at greater power the increase in PEM size and reduction of ATR operative hours (to which CO_2 income trend is related) make LCOH raises again.

Concerning oxygen selling income, is obvious that at greater PEM power, the oxygen surplus is increasing, thus revenues do too.

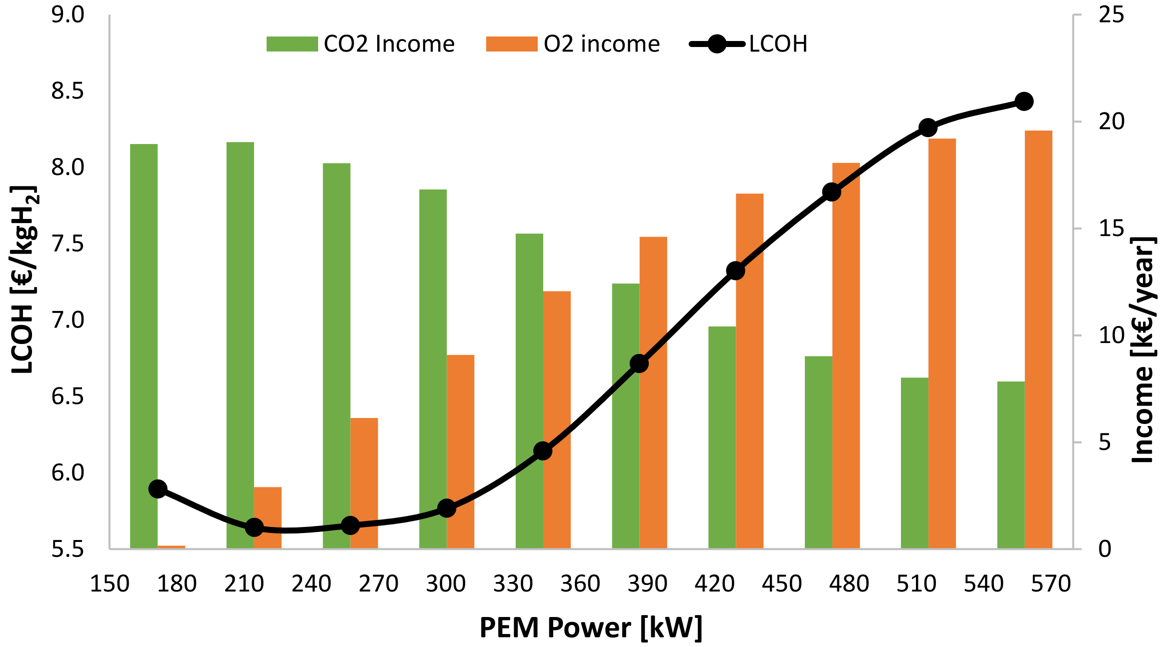

Figure 7.34 - LCOH and incomes from CO_2 and O_2 at different PEM power.

Considering the best configuration, injecting CO_2 (403 tons per year) into the pipeline provides a net income slightly greater than 19 k€/year, which consists in a reduction of around -0.43 €/kgH₂ (-6.9%). Oxygen, being a by-product, is generating income (2.9 k€/year) without expenditures, with a yearly generation of around 19.3 tonO_2, providing a reduction of -0.06 €/kgH_2 (-1%). Accounting both revenues there is a reduction in LCOH of the overall plant equal to -0.49 €/kgH_2 (-7.9%), with a value which is still greater than on-grid configurations.

A comparison between revenues effect in case in which CO_2 is not injected with respect to the case where CO_2 is injected is provided in Table 7.25.

Carbon dioxide income is related to CO_2 yearly flow, which is totally dependent on ATR operative hours; thus, greater the functioning hours of ATR are, greater the CO_2 selling flow will be, therefore, greater the income will be.

	CO_2 is sold at ambient conditions	CO_2 is injected
CO_2 market price [€/ton]	35	50
O_2 market price [€/ton]	150	150
CO_2 yearly flow [ton/y]	402.05	403.03
O_2 yearly sold [ton/y]	37.1	19.3
CO_2 Net Income [k€/y]	14.1	19
O_2 Net Income [k€/y]	5.6	2.9
CO_2 Effect on LCOH [€/kgH_2]	-0.28	-0.43
CO_2 Effect on LCOH [%]	-4.9%	-6.9%
O_2 Effect on LCOH [€/kgH_2]	-0.11	-0.06
O_2 Effect on LCOH [%]	-1.9%	-1%

Table 7.25 - Revenues effect comparison between off-grid cases.

Oxygen selling flow obviously depends on PEM production, since the tank capacity is the same for both case. PEM stack power is greater for the case in which CO_2 is not injected, thus that case has the greater income from O_2 selling.

	Unit	Value	ΔLCOH
LCOH without revenues	€/kgH_2	6.13	/
LCOH with CO_2 selling only	€/kgH_2	5.70	-0.43
LCOH with O2 surplus selling only	€/kgH_2	6.07	-0.06
LCOH with both revenues	€/kgH_2	5.64	-0.49

Table 7.26 - Summary of LCOHs and contributions of revenues for off-grid case with CO_2 injection.

As conclusion, in Table 7.26, LCOHs have been reported. They are slightly greater than the case without CO_2 injection, but in this case, it is possible to take into account the fact that the plant is carbon negative.

.

8 Conclusion

The developed thesis work focused on assessing techno-economic analysis of a green hydrogen producing plant from biogas, through autothermal reforming assisted by fluidized bed membranes reactor, assumed to be placed in Catania, Italy.

The innovation of this project is concerning the evaluation of performance improvement by feeding pure oxygen (instead of air) to perform autothermal reforming in FBMR and assessing the coupling with a PEM electrolyzer in different configuration. The techno-economic convenience of introducing auxiliaries technology like PV solar field and BESS has been assessed. Feeding pure oxygen to FBMR and to a catalytic burner, which ignites retentate combustion, provides a flue gas stream mainly composed by water and carbon-dioxide, thus, CO_2 could be easily separated. Two CO_2 separation possibilities have been detailed in *5.5 CO2 removal and injection in pipeline*. The first foresees the selling of rich-CO_2 stream at ambient condition, directly after water separation, while in the second solution, after water separation, CO_2 is compressed and injected into a pipeline, generating a carbon-negative plant solution.

In this context, FBMR is the core technology of this work, and PEM electrolyzer has been introduced in order to generate oxygen at small-scale to feed ATR plant.

Membranes reactor goal is to produce and to separate hydrogen from autothermal reforming product stream. The flux of separated hydrogen is driven from hydrogen partial pressure difference between the two sides of the membrane, as explained by Richardson's Equation (3.5) [30]. Feeding oxygen, instead of air, is increasing retentate hydrogen partial pressure, due to the absence of nitrogen in retentate stream, therefore, the hydrogen partial pressure difference is increased.

Thus, the first aim of this work has been to quantify the performance improvement by changing autothermal reforming oxidizing agent from air to oxygen. For this purpose, a comparison with an air-feeding plant has been done. The air-case has been developed in EU funded project MACBETH and it has been chosen as benchmark for the oxygen configurations developed in this work, with an LCOH value equal to 4.96 €/kgH_2.

The comparison has been performed at same operating conditions, with the same pure hydrogen production target (100 kgH_2/day) and at the same biogas composition (assumed to be taken from anaerobic digester with methane molar fraction equal to 58.1%), enlisted in Table 2.1 and Table 2.2. FBMR model is the heart of the plant and it has been modelled in Aspen Custom Modeler, software integrable in Aspen Plus, where ATR-FBMR plant functioning has been simulated. FBMR model has been described in chapter *3 Fluidized bed membrane reactor model* and it has been developed through different projects [17], [39], [30], [40].

The comparison has been conducted at different membranes number, through Aspen Plus, as described in section *2.2 Comparison description between air and oxygen*, verifying to always be compliant with a technical constraint identified by experiment results, which detected loss of membrane separation capability if membranes pitch distance is lower than 2 cm. Different KPIs drove the comparison, but the most relevant technical ones are the Hydrogen Recovery Factor (HRF) and the system efficiency, computed as in Equation (2.1) and in Equation (2.2), respectively. From an economic point of view LCOH (computed as in Equation (2.3)) is the most important indicator because it quantifies the levelized cost of hydrogen produced and separated.

Simulation results affirms that increasing membranes number provides a higher HRF of the reactor, thus the input biogas required is reduced, increasing consequently system efficiency too. Nevertheless, two technical issues could arise at increasing membranes number. The first is related to the lower LHV of retentate stream, while the second is concerning the minimum distance pitch between adjacent membranes.

Retentate stream is going to be burned to provide lower thermal power to heat up the feed, which temperature will be lower at FBMR inlet reducing consequently the efficiency.

However, this possible reduction in efficiency is not observed among the membranes number range tested, because pitch distance technical limit is reached at lower number of membranes. Increasing membranes number provides a greater HRF, thus a lower amount of biogas, and consequently a lower amount of steam (to keep S/C around 3) is necessary. Therefore, the amount of feed is reducing at increasing membranes number and in order to keep the ratio between gas superficial velocity and minimum fluidization velocity around 1.5 the reactor diameter is reducing too. Decreasing the diameter provokes a reduction in available space for membranes, with the limit of minimum membranes distance pitch of 2 cm which is reached with 122 membranes and 147 membranes, for oxygen-case and air-case respectively.

By adopting the number of membranes which minimizes the LCOH of each case (oxygen-case and air-case) it is possible to identify an improvement of FBMR performance concerning HRF and system efficiency, as detailed in Table 8.1. Thus by feeding oxygen, considering the most performant solution (122 membranes adopted) a higher HRF has been achieved at lower membranes number.

Membranes Number	HRF	System efficiency
122 (lowest O_2 case LCOH)	71.39%	65.42%
147 (lowest air case LCOH)	68.29%	60.25%

Table 8.1 - HRF and system efficiency comparison for the best configuration of air-case and oxygen-case.

From this first analysis it has been possible to certify, as expected, the improvement of technical performance of an oxygen-fed FBMR with respect to an air-case one.

Economic analysis at different membranes number identifies that the configurations with the lowest LCOH are the one with the maximum allowed number of membranes. Indeed, as shown in detail in paragraph *7.1.2 Economic comparison results,* variable O&M cost (mainly due to biogas purchasing cost) is a relevant share of equivalent annual cost. Increasing membranes number, as previously said, is raising up the efficiency and it is reducing biogas consumption, but a trade-off with hydrogen selective membranes arises, meaning that greater the membranes number is, lower biogas purchasing cost will be, but on the other hand, membranes cost would increase.

In this first comparison oxygen has been assumed as granted a priori and directly mixed with the FBMR feed, therefore, it would not be properly correct to compare LCOHs of these configurations.

For this purpose, a Proton Exchange Membrane (PEM) electrolyzer has been introduced, in chapter *7.2 PEM-ATR configuration*, and its oxygen production has been coupled with FBMR needs. ATR-FBMR configurations assumed (to assess the different couplings) is the set-up which maximizes plant performance from air-O_2 analysis, thus adopting 122 membranes and a diameter reactor of 0.43 m.

Since retentate burned, in oxygen case, is almost entirely composed by water and carbon dioxide, two CO_2 separation possibilities have been implemented as detailed in *5.5 CO2 removal and injection in pipeline*. In a configuration flue gas from catalytic burner, after being used to heat up the feed, are going to be separated through water condensation, in order to isolate a CO_2-rich stream and selling it at ambient conditions, worthing 35 €/tonCO_2 [37]. In a second configuration a CO_2 compressor after water condensation has been introduced to inject CO_2 into a pipeline (125 bar, 25°C) [82], with a revenues of 50 €/tonCO_2 [38]. Details on carbon dioxide revenues and compressor are explained in *6.7 CO2 removal and utilization* and in *6.6 ATR cost*, respectively.

In coupling configurations PEM electrolyzer, which model and fundamental equations have been detailed in *4 Electrolyzer*, shall provide the exact quantity of oxygen needed for feeding FBMR (0.40 kmolO_2/h, as enlisted in Table 7.3) for 7500 hours per year (ATR plant operative hours). The operating condition of PEM electrolyzer production have been set equal to 21 bar (to mix hydrogen from PEM with the one from ATR which is at 20 bar) and 60°C (typical temperature for PEM electrolyzer [21]). Operating in this condition a polarization curve, shown in Figure 7.13, is found according to the model developed and the electrolyzer features chosen (membrane thickness, ECD…). In the polarization curve it is possible to appreciate the current density limits adopted for PEM electrolyzer production. The range of current density admitted is between 0.5 A/cm^2 to 1.5 A/cm^2, in order to preserve PEM lifetime avoiding constantly working at too extreme conditions.

The electrolyzer production is therefore set by ATR needs and once cell number and cell area have been detected, through logic scheme (shown in Figure 4.15) and through the relations developed in *4.3 PEM power – PEM production relations*, it is possible to identify the power to be withdrawn from the grid to feed PEM electrolyzer. The relations, hereabove mentioned, allow to easily test every combination of cell number and cell area given as input. To identify a preferred PEM configuration design, which must be compliant with the mentioned constraints, a Visual Basic code to test a very large number of cell area and cell number combination has been implemented. A trade-off arises for PEM electrolyzer too. At increasing stack power the efficiency of the electrolyzer increases, therefore, a lower amount of electricity is retrieved from the grid, but PEM CAPEX and OPEX cost, which is related to the power as detailed in *6.3 PEM Electrolyzer cost*, are increasing.

Visual Basic code tested a very large number of different combinations and an optimum size, corresponding to 96.7 kW of PEM electrolyzer, composed of 113 cells of 300 cm^2, has been found, working at 1.28 A/cm^2 and 1.84 V. Indeed, this size is the one which minimizes the overall LCOH of the plant as shown in Figure 7.15. The performance details of PEM electrolyzer operation have been reported in Table 7.11, while the performance details of ATR plant have not changed since the oxygen is fed at the same condition of oxygen-air comparison.

Overall plant LCOH is equal to 5.48 €/kgH$_2$, but economic revenues from CO$_2$ selling at ambient condition or by injection into a pipeline provides an economic improvement. Selling carbon dioxide at ambient conditions provides a difference in LCOH equal to -0.31 €/kgH$_2$, while selling it through pipeline injection, besides all the environmental benefits of being carbon-negative, provides a reduction equal to -0.27 €/kgH$_2$. LCOH of the overall plant is reduced to 5.17 €/kgH$_2$, whether CO$_2$ is sold at ambient condition, and to 5.21 €/kgH$_2$, whether CO$_2$ is injected.

The economic comparison with air-case LCOH, equal to 4.96 €/kgH$_2$ affirms that, with the hypothesis assumed in this work, air-case is providing a cheaper green hydrogen with respect to a configuration where a PEM electrolyzer is coupled with FBMR fed by oxygen, but the coupling feasibility has been positively demonstrated.

An interesting results to point out is concerning a break-even analysis on CO_2 selling price and PEM electrolyzer CAPEX and OPEX reduction, to provide an LCOH equivalent solution with respect to air-case.

A trend concerning LCOH variation at different CO_2 selling price is shown in Figure 7.17, where it is possible to highlight that CO_2 break-even selling price is equal to 60 €/tonCO_2, if it is sold at ambient condition, or equal to 78.5 €/tonCO_2, if it is injected into a pipeline.

Concerning PEM electrolyzer CAPEX and OPEX a range between current values and 2030 expected costs [99] has been analyzed to reach a break-even solution with air-case. Nevertheless an expected reduction of investment and operational cost of -60%, a break-even with air-case is not achieved, reaching values of 5.00 €/kgH_2, if CO_2 is sold at ambient condition, and of 5.04 €/kgH_2 if CO_2 is injected. Indeed, by looking at Figure 7.16, it is possible to emphasize the relevant share of equivalent annual cost for electricity purchasing, which share is around 33% with respect to a value of 6% for PEM (including investment, replacement and operational cost without electricity purchasing cost). Thus, an important improvement would be remarked by feeding cheaper electricity to PEM-ATR plant with respect to the electricity retrieved from the grid, which cost has been assumed to be 120 €/MWh [32]. Supplying a cheaper electricity could have a bigger impact than the one that it would have in air-case, due to the remarkably lower power consumption (oxygen-case consumes around 4 times more than air-case).

In order to reduce electricity purchasing cost, which is a relevant share of equivalent annual cost, a PV field has been assumed to be installed nearby the plant in order to assist PEM-ATR plant. Taking solar radiation data from PVgis, with the detailed model of PV field explained in *5 Photovoltaic field and auxiliaries*, it is possible to compute an yearly hourly PV electricity generation profile $\left(\frac{kWh}{kW_p}\right)$ according to the chosen size of PV field peak power. Depending on solar radiation data, and on the economic assumptions for PV technology detailed in *6.2 Photovoltaic field cost*, it is possible to compute relevant indicators for PV field performance, especially capacity factor, equal to 18.2% (other data in Table 7.15) and LCOE equal to 56.5 €/MWh, coherent (even slightly conservative) with values reported by IRENA in [101]. Being LCOE lower than electricity purchasing price (assumed to be 120 €/MWh [32]) PV field installation allows to reduce electricity yearly expenditure.

Operative hours have been assumed to be equal to the previous configurations (7500 hours per year), providing a fair comparison. A Visual Basic code, to test different combination of PV field size, PEM cell number and cell area, has been developed, in order to identify the optimum combination of components size which minimizes the overall plant LCOH.

Results are shown in *7.3.2 Results*, where it is possible to point out that PEM electrolyzer size which minimizes the overall plant is not changed, being 96.7 kW, composed of 113 cells of 300 cm^2 (thus it has the same performance of the previous case, enlisted in Table 7.11), while the optimum PV field size identified is 180 kW$_P$, or 195 kW$_P$, whether CO_2 compression and injection is taken into account. These components size provides a ratio between PV power and PEM power equal to 1.85 and 2, respectively. A chart with LCOH as a function of PV power and PEM power ratio is displayed in Figure 7.19.

As expected, overall plant LCOH is decreasing by introducing PV electricity, with results, summarized in Table 7.16, which values are equal to 4.89 €/kgH$_2$ and 4.92 €/kgH$_2$ if CO_2 is sold at ambient condition or if it is injected into a pipeline, respectively. These values does not consider revenues from PV electricity sold to the grid, indeed due to the fact that LCOE is lower than the electricity selling cost (assumed to be 60 €/MWh [31]), if the PV field size choice would be driven by PV electricity revenues, there would be an oversizing of PV field, changing its goal from assisting the plant to making revenues by selling electricity; thus, the values reported above are the ones which does not take into account PV electricity revenues, but CO_2 revenues only. If PV electricity revenues would be taken into account in the configuration with 180 kW$_P$ and 195 kW$_P$, an LCOH equal to 4.82 €/kgH$_2$ and equal to 4.86 €/kgH$_2$ would be reached.

By comparing them to the benchmark case (LCOH equal to 4.96 €/kgH$_2$) it is clear that (a small) improvement is detected. However, a fairer comparison would be provided if air-case would be powered by PV field too.

For this purpose, an economic analysis on air-case when it is partially powered by a PV field has been developed. Results shown that the optimum PV field size for air-case, which consumes 27.84 kW, is around 50 kW$_P$, providing an LCOH reduction of -0.10 €/kgH$_2$, passing from 4.96 €/kgH$_2$ to 4.86 €/kgH$_2$. This reduction is only given by having available a cheaper electricity; when revenues form PV electricity selling to the grid are considered the value, always accounting 50 kW$_P$, decreases to 4.83 €/kgH$_2$. LCOHs results as function of PV field size are displayed in Figure 7.21.

Pursuing the aim of avoiding to withdraw expensive electricity from the grid, in *7.4 PV-BESS-PEM-ATR configuration*, a Battery Energy Storage System (BESS), modeled in *5.3 Battery Energy Storage System*, is introduced. Also in this case, a Visual Basic code has been implemented to test a large number of combinations varying BESS capacity, PV field peak power size, PEM cell number and cell area, in order to identify the components size which minimizes the overall plant LCOH and that is compliant with the different constraints introduced. ATR plant operative hours have always been assumed to be 7500 hours per year, to be fairly compared with the previous cases. Battery system has the aim to store surplus PV electricity, up to its capacity, during sun hours, and then releasing it during night time, reducing the withdrawal from the grid. Indeed, the plant is firstly powered by BESS and then when battery state of charge is at possible minimum, grid electricity is retrieved. Anyway, adopting this logic, PV field should be increased in size and BESS, which cost is not currently low, is introduced. This provides a worsening in overall LCOH plant with respect to the case where PEM-ATR plant is assisted by PV field only. The results are shown in Figure 7.23 and enlisted in Table 7.17 (for the case where CO_2 is sold at ambient condition), pointing out that the lowest LCOH is reached for a BESS size equal to 50 kWh, which is the minimum value tested; thus, it is possible to emphasize that introducing a battery storage is not convenient from LCOH point of view.

As pointed out in these analysis, the impact of electricity purchasing price is relevant. Thus, a sensitivity analysis on the most performant configuration (PEM-ATR plant assisted by PV field, with CO_2 sold at ambient condition) varying electricity purchasing price has been conducted in paragraph *7.5 Sensitivity analysis on electricity prices*, analyzing a range of price from 50 €/MWh to 250 €/MWh with a 50 €/MWh step; results are available for 120 €/MWh too, since this value is the one assumed for the previous analysis. In Figure 7.25 it is evident the relevance of electricity purchasing cost share on equivalent annual cost at different electricity purchasing price, where, for high electricity price, the share, which accounts for PEM electricity withdrawal, is relevant such the ATR one.

The most interesting results are shown in Figure 7.26, where it is possible to point out that 120 €/MWh is practically a break-even electricity price between air-case and oxygen one. Whether electricity purchasing price would be lower than this value, PEM-ATR plant assisted by PV field is producing a cheaper hydrogen with respect to air-case configuration.

A final analysis is considering the possibility of producing hydrogen off-grid, without possibility of electricity withdrawal from the national grid. In analogous way with the previous analysis, two CO_2 separation and selling possibilities (in a case at ambient condition, and in a second case through pipeline injection), are considered and detailed in chapter *7.6 Off-grid configuration*. Electricity is provided by PV field during the day, and by BESS during night hours, but unlike on-grid configuration, PEM oxygen production is not perfectly coupled with ATR needs, but oxygen production could be stored in an under-pressure tank, in order to provide a decoupling between PEM production and ATR plant consumption, allowing PEM to produce surplus oxygen during sun hours, when PV electricity is largely available.

Oxygen tank has been modeled as detailed in *5.4 Oxygen tank*, and it works with a minimum pressure equal to 13 bar, in order to always ensure a safe supply to ATR, which operates at 12 bar. In order to properly supply oxygen to the tank, PEM electrolyzer production is set at 30 bar (keeping 60°C as operating temperature). Furthermore, according to PEM and tank size, it is possible to experience hours in which a surplus of oxygen is detected, meaning that the tank is already full and ATR is properly fed. When an oxygen surplus is identified, oxygen has been considered as by-product and it is sold at 150 €/tonO_2, as reported by [34]–[36]. Thus off-grid configuration could expect incomes both from CO_2 and from O_2 selling.

In off-grid context, due to variable PEM production, depending on input power provided by PV field or by BESS, a logic behind the choice of input power is needed, and it is explained according to flowchart reported in *Appendix B.1 Flow-chart*. Once that input power is defined, through logic scheme in Figure 4.15 and through the relations developed in *4.3 PEM power – PEM production relations*, it is possible to identify PEM oxygen and hydrogen production.

In order to test large number of combinations of different components size a Visual Basic code has been developed, in order to easily compute LCOH and other important parameters of the overall plant at different combinations of PV field peak power, BESS capacity, oxygen tank, PEM cell number and cell area.

According to the fact that carbon dioxide is sold at ambient conditions or if it is injected into a pipeline, the results are reported in two different sections which are *7.6.2.1 Off-grid configuration* and *7.6.2.1 Off-grid configuration with CO2 sold at ambient condition.*

Several trends have been shown in order to understand the effect of the different components size on overall LCOH. Concerning the case in which CO_2 is sold at ambient conditions, in Figure 7.28 the effects of PEM size, as function of different PV size, on LCOH and on ATR operative hours are shown. At low PEM size a small amount of ATR operative hours is granted due to low oxygen production, while at high PEM size, the power to be addressed to PEM electrolyzer is high, thus less power is available to feed ATR plant, therefore, plant operative hours are reduced.

Battery capacity effect is shown, at different PV size, in Figure 7.29, pointing out the economical choice of choosing a capacity greater than the one which guarantees 7 hours of autonomy (800 kWh or 900 kWh according if CO_2 is sold at ambient condition or it needs to be compressed for pipeline injection).

Oxygen tank size has a small effect from equivalent annual cost as shown in Figure 7.32 and in Figure 7.33, therefore, also the effect on LCOH (if a tank capacity which ensure at least 7 hours of FBMR feeding is chosen) will be small, and it is displayed in Figure 7.30 as function of PV/PEM power ratio. Another aspect concerning oxygen tank is related to oxygen income from selling surplus oxygen, its trend is shown in Figure 7.31. From these mentioned charts it is possible to conclude that the optimum tank size for both the case in which CO_2 is injected or not, is around 300 kgO_2.

The other optimum components size are similar in both cases too. In particular the best PV peak power is 812.5 kW_P for both configurations, while PEM power is slightly lower in CO_2 injection cases, which has also a greater battery capacity. Indeed, a large electrolyzer is absorbing a larger power that could be fed ATR, reducing its operative hours.

Whether CO_2 is sold at ambient conditions an LCOH equal to 5.42 €/kgH_2 is reached, with a PV field of 812.5 kW_P, a PEM stack power equal to 258 kW, 800 kWh of BESS capacity and 300 kgO_2 of oxygen tank; the components size chosen is ensuring 7756 ATR plant operative hours per year. In this configuration CO_2 sold provides a LCOH reduction of -0.28 €/kgH_2, while oxygen selling income generates a reduction equal to -0.11 €/kgH_2.

If CO_2 is injected into a pipeline an LCOH equal to 5.64 €/kgH_2 is achieved, adopting 812.5 kW_P, a PEM electrolyzer with 215 kW of stack power, 900 kWh of BESS capacity and an oxygen tank of 300 kgO_2. In this configuration oxygen income provides a reduction of -0.06 €/kgH_2, while CO_2 injection provides a reduction equal to -0.43 €/kgH_2, due to the greater ATR operative hours equal to 7775 hours per year.

In order to summarize all the components size which minimize the LCOHs of the different configurations and the corresponding LCOH, Table 8.2 has been reported, pointing out the comparison between the case in which CO2 is sold at ambient conditions (Case A) and the case in which CO2 is injected into pipeline (Case B).

Case name	**PEM [kW]**		**PV [kW_P]**		**BESS [kWh]**		**O_2 tank [kg]**		**LCOH [€/kgH_2]**		**LCOH - PV revenues [€/kgH_2]**	
AIR CASE	/		/		/		/		4.96		/	
PV-AIR CASE	/		48.8		/		/		4.86		4.83	
	Case A	Case B	Case A	Case B	Case A	Case B	Case A	Case B	Case A	Case B	Case A	Case B
PEM-ATR	96.7		/		/		/		5.17	5.21	/	
PV-PEM-ATR	96.7		180	195	/		/		4.89	4.92	4.82	4.86
PV-BESS-PEM-ATR	96.7		195	211	50		/		4.94	4.97	4.86	4.88
OFF-GRID	258	215	812.5	812.5	800	900	300		5.42	5.64	/	

Table 8.2 - LCOHs and components size of the best configuration for each case, with CO_2 sold at ambient condition (case A) and CO_2 injected in pipeline (Case B).

As final conclusion it is possible to point out that:

- The configurations which provide the best techno-economic performance (lowest LCOH) are generated by PEM-ATR plant assisted by a PV field.
- The mentioned configurations (PV-PEM-ATR in Table 8.2) provide LCOHs, equal to 4.89 €/kgH_2 and to 4.92 €/kgH_2 (if CO_2 is sold at ambient condition or if it is injected), which are lower than air-feeding reference case, which value is

4.96 €/kgH_2, and really close to 4.86 €/kgH_2, value of air-case assisted by PV field.

- Whether surplus PV electricity revenues are taken into account in the previously best configuration mentioned, results equal to 4.82 €/kgH_2 and to 4.86 €/kgH_2 (if CO_2 is sold at ambient condition or if it is injected) have been achieved, and they should be compared with 4.83 €/kgH_2 of air-case assisted by PV field, which includes revenues from surplus PV electricity.
- Particularly interesting is the economic results of PV-PEM-ATR configuration with CO_2 injection, which, besides generating the environmental benefits of being a carbon-negative plant, provides an LCOH value really close to air-case (4.86 €/kgH_2 compared to 4.83 €/kgH_2)

From these evidences it is possible to highlight that in their best configurations oxygen-case provides techno-economic performance practically equivalent to air-case and the coupling with PEM electrolyzer, especially when the plant is assisted by PV field, is performing in a remarkable way. A note could be done concerning carbon-negative plant, which provides LCOH really close to air-configuration, but includes all the environmental benefits of being a carbon-negative plant.

Bibliography

[1] IEA, "Net Zero by 2050: A Roadmap for the Global Energy Sector," *Int. Energy Agency*, p. 224, 2021, [Online]. Available: https://www.iea.org/reports/net-zero-by-2050.

[2] P. M. Falcone, M. Hiete, and A. Sapio, "Hydrogen economy and sustainable development goals: Review and policy insights," *Curr. Opin. Green Sustain. Chem.*, vol. 31, p. 100506, 2021, doi: 10.1016/j.cogsc.2021.100506.

[3] I. Renewable and E. Agency, *"Hydrogen from renewable power: Technology outlook for the energy transition (2018)", IRENA, available at https://www.irena.org/publications/2018/Sep/Hydrogen-from-renewable-power [Accessed : 29-Nov.-2019]*, no. September. 2018.

[4] "Global Hydrogen Review 2021," *Glob. Hydrog. Rev. 2022*, 2021, doi: 10.1787/a15b8442-en.

[5] A. M. Oliveira, R. R. Beswick, and Y. Yan, "A green hydrogen economy for a renewable energy society," *Curr. Opin. Chem. Eng.*, vol. 33, p. 100701, 2021, doi: 10.1016/j.coche.2021.100701.

[6] S. K. Bhatia, H. S. Joo, and Y. H. Yang, "Biowaste-to-bioenergy using biological methods – A mini-review," *Energy Convers. Manag.*, vol. 177, no. October, pp. 640–660, 2018, doi: 10.1016/j.enconman.2018.09.090.

[7] International Energy Agency, "'Outlook for biogas and biomethane. Prospects for organic growth.,'" *IEA Publ.*, pp. 1–93, 2020.

[8] U. of M. Vindis, P. (Faculty of Agriculture and Life Sciences, U. of M. Mursec, B. (Faculty of Agriculture and Life Sciences, U. of M. Janzekovic, M. (Faculty of Agriculture and Life Sciences, and U. of M. Cus, F. (Faculty of Mechanical Engineering, "The impact of mesophilic and thermophilic anaerobic digestion on biogas production," *J. Achiev. Mater. Manuf. Eng.*, vol. 36, no. 2, pp. 23–26, 2009, [Online]. Available: https://citeseerx.ist.psu.edu/document?repid=rep1&type=pdf&doi=05b6450b15729d6a0d5c5031aae9c3bcc0606c0b.

[9] S. N. B. Villadsen, P. L. Fosbøl, I. Angelidaki, J. M. Woodley, L. P. Nielsen, and

P. Møller, “The Potential of Biogas; the Solution to Energy Storage,” *ChemSusChem*, vol. 12, no. 10, pp. 2147–2153, 2019, doi: 10.1002/cssc.201900100.

[10] A. Brunetti, A. Caravella, E. Drioli, and G. Barbieri, “Membrane Reactors for Hydrogen Production.pdf,” in *Membrane Engineering for the Treatment of Gases: Gas-separation Issues Combined with Membrane Reactors, Volume 2*, E. Drioli, G. Barbieri, and A. Brunetta, Eds. Royal Society of Chemistry, 2017, pp. 1–29.

[11] N. Lu and D. Xie, “Novel Membrane Reactor Concepts for Hydrogen Production from Hydrocarbons: A Review,” *Int. J. Chem. React. Eng.*, vol. 14, no. 1, pp. 1–31, 2016, doi: 10.1515/ijcre-2015-0050.

[12] G. Di Marcoberardino, X. Liao, A. Dauriat, M. Binotti, and G. Manzolini, “Life cycle assessment and economic analysis of an innovative biogas membrane reformer for hydrogen production,” *Processes*, vol. 7, no. 2, 2019, doi: 10.3390/pr7020086.

[13] F. Gallucci, E. Fernandez, P. Corengia, and M. van Sint Annaland, “Recent advances on membranes and membrane reactors for hydrogen production,” *Chem. Eng. Sci.*, vol. 92, pp. 40–66, 2013, doi: 10.1016/j.ces.2013.01.008.

[14] M. De Falco, L. Marrelli, and I. Gaetano, *Membrane Reactor for Hydrogen Production Processes*. 2011.

[15] G. Iaquaniello, E. Palo, A. Salladini, and B. Morico, “Membrane reactors for hydrogen production,” *Curr. Trends Futur. Dev. Membr. Recent Adv. Met. Membr.*, vol. 2, pp. 261–292, 2020, doi: 10.1016/B978-0-12-818332-8.00011-9.

[16] T. Y. Amiri, K. Ghasemzageh, and A. Iulianelli, “Membrane reactors for sustainable hydrogen production through steam reforming of hydrocarbons: A review,” *Chem. Eng. Process. - Process Intensif.*, vol. 157, no. August, p. 108148, 2020, doi: 10.1016/j.cep.2020.108148.

[17] S. Foresti, G. Di Marcoberardino, G. Manzolini, N. De Nooijer, F. Gallucci, and M. van Sint Annaland, “A comprehensive model of a fluidized bed membrane reactor for small-scale hydrogen production,” *Chem. Eng. Process. - Process Intensif.*, vol. 127, no. February, pp. 136–144, 2018, doi: 10.1016/j.cep.2018.01.018.

[18] G. Di Marcoberardino, F. Gallucci, G. Manzolini, and M. van Sint Annaland, “Definition of validated membrane reactor model for 5 kW power output CHP system for different natural gas compositions,” *Int. J. Hydrogen Energy*, vol. 41, no. 42, pp. 19141–19153, 2016, doi: 10.1016/j.ijhydene.2016.07.102.

[19] D. S. Falcão and A. M. F. R. Pinto, “A review on PEM electrolyzer modelling: Guidelines for beginners,” *J. Clean. Prod.*, vol. 261, 2020, doi: 10.1016/j.jclepro.2020.121184.

[20] S. A. Grigoriev, V. N. Fateev, D. G. Bessarabov, and P. Millet, “Current status, research trends, and challenges in water electrolysis science and technology,”

Int. J. Hydrogen Energy, vol. 45, no. 49, pp. 26036–26058, 2020, doi: 10.1016/j.ijhydene.2020.03.109.

[21] M. Carmo, D. L. Fritz, J. Mergel, and D. Stolten, "A comprehensive review on PEM water electrolysis," *Int. J. Hydrogen Energy*, vol. 38, no. 12, pp. 4901–4934, 2013, doi: 10.1016/j.ijhydene.2013.01.151.

[22] M. Yu, E. Budiyanto, and H. Tüysüz, "Principles of Water Electrolysis and Recent Progress in Cobalt-, Nickel-, and Iron-Based Oxides for the Oxygen Evolution Reaction," *Angew. Chemie - Int. Ed.*, vol. 61, no. 1, 2022, doi: 10.1002/anie.202103824.

[23] IRENA, *Green Hydrogen Cost Reduction*. 2020.

[24] IRENA (International Renewable Energy Agency), *Global Hydrogen Trade to Meet the 1.5°C Climate Goal: Trade Outlook for 2050 and Way Forward*. 2022.

[25] L. El Chaar, L. A. Lamont, and N. El Zein, "Review of photovoltaic technologies," *Renew. Sustain. Energy Rev.*, vol. 15, no. 5, pp. 2165–2175, 2011, doi: 10.1016/j.rser.2011.01.004.

[26] A. S. Al-Ezzi and M. N. M. Ansari, "Photovoltaic Solar Cells: A Review," *Appl. Syst. Innov.*, vol. 5, no. 4, pp. 1–17, 2022, doi: 10.3390/asi5040067.

[27] International Renewable Energy Agency (IRENA), *Future of solar photovoltaic: Deployment, investment, technology, grid integration and socio-economic aspects*, vol. November. 2019.

[28] D. D. B. Mesquita, J. Lucas De Silva, H. S. Moreira, M. Kitayama, and M. G. Villalva, "A review and analysis of technologies applied in PV modules," *2019 IEEE PES Conf. Innov. Smart Grid Technol. ISGT Lat. Am. 2019*, no. November, 2019, doi: 10.1109/ISGT-LA.2019.8895369.

[29] IRENA, *Future of solar photovoltaic: Deployment, investment, technology, grid integration and socio-economic aspects (A Global Energy Transformation: paper)*, vol. November. 2019.

[30] M. Ongis, G. Di Marcoberardino, M. Baiguini, F. Gallucci, and M. Binotti, "Optimization of small-scale hydrogen production with membrane reactors," pp. 1–26, 2023.

[31] E. Crespi, P. Colbertaldo, G. Guandalini, and S. Campanari, "Design of hybrid power-to-power systems for continuous clean PV-based energy supply," *Int. J. Hydrogen Energy*, vol. 46, no. 26, pp. 13691–13708, 2021, doi: 10.1016/j.ijhydene.2020.09.152.

[32] G. Di Marcoberardino, S. Foresti, M. Binotti, and G. Manzolini, "Potentiality of a biogas membrane reformer for decentralized hydrogen production," *Chem. Eng. Process. - Process Intensif.*, vol. 129, no. August 2017, pp. 131–141, 2018, doi:

10.1016/j.cep.2018.04.023.

[33] J. U. Steinle and E. U. Franck, "High pressure combustion - ignition temperatures to 1000 bar," *Berichte der Bunsengesellschaft/Physical Chem. Chem. Phys.*, vol. 99, no. 1, pp. 66–73, 1995, doi: 10.1002/bbpc.19950990110.

[34] D. Bellotti, A. Sorce, M. Rivarolo, and L. Magistri, "Techno-economic analysis for the integration of a power to fuel system with a CCS coal power plant," *J. CO2 Util.*, vol. 33, no. March, pp. 262–272, 2019, doi: 10.1016/j.jcou.2019.05.019.

[35] D. Bellotti, M. Rivarolo, and L. Magistri, "Economic feasibility of methanol synthesis as a method for CO2 reduction and energy storage," *Energy Procedia*, vol. 158, no. 2018, pp. 4721–4728, 2019, doi: 10.1016/j.egypro.2019.01.730.

[36] M. Rivarolo, D. Bellotti, L. Magistri, and A. F. Massardo, "Feasibility study of methanol production from different renewable sources and thermo-economic analysis," *Int. J. Hydrogen Energy*, vol. 41, no. 4, pp. 2105–2116, 2016, doi: 10.1016/j.ijhydene.2015.12.128.

[37] J. Kim, C. A. Henao, J. E. Miller, and E. Stechel, "Methanol production from CO2 using solar-thermal energy: process development and techno-economic analysis," no. September, 2011, doi: 10.1039/C1EE01311D.

[38] A. Bhardwaj, C. McCormick, and J. Friedmann, "Opportunities and limits of CO2 utilization pathways: Techno-economics, critical infrastructure needs, and policy priorities," *Abstr. Pap. 262nd ACS Natl. Meet. Expo. Atlanta, GA, United States, August 22-26, 2021*, no. May, 2021.

[39] G. Di Marcoberardino, F. Gallucci, G. Manzolini, and M. van Sint Annaland, "Definition of validated membrane reactor model for 5 kW power output CHP system for different natural gas compositions," *Int. J. Hydrogen Energy*, vol. 41, no. 42, pp. 19141–19153, 2016, doi: 10.1016/j.ijhydene.2016.07.102.

[40] M. Ongis, G. Di, G. Manzolini, F. Gallucci, and M. Binotti, "Membrane reactors for green hydrogen production from biogas and biomethane : A techno-economic assessment," *Int. J. Hydrogen Energy*, no. xxxx, pp. 1–16, 2023, doi: 10.1016/j.ijhydene.2023.01.310.

[41] M. E. Demir and I. Dincer, "Development of a hybrid solar thermal system with TEG and PEM electrolyzer for hydrogen and power production," *Int. J. Hydrogen Energy*, vol. 42, no. 51, pp. 30044–30056, 2017, doi: 10.1016/j.ijhydene.2017.09.001.

[42] B. Han, S. M. Steen, J. Mo, and F. Y. Zhang, "Electrochemical performance modeling of a proton exchange membrane electrolyzer cell for hydrogen energy," *Int. J. Hydrogen Energy*, vol. 40, no. 22, pp. 7006–7016, 2015, doi: 10.1016/j.ijhydene.2015.03.164.

[43] E. T. Ojong, J. T. H. Kwan, A. Nouri-Khorasani, A. Bonakdarpour, D. P. Wilkinson, and T. Smolinka, "Development of an experimentally validated

semi-empirical fully-coupled performance model of a PEM electrolysis cell with a 3-D structured porous transport layer," *Int. J. Hydrogen Energy*, vol. 42, no. 41, pp. 25831–25847, 2017, doi: 10.1016/j.ijhydene.2017.08.183.

[44] F. Marangio, M. Santarelli, and M. Calì, "Theoretical model and experimental analysis of a high pressure PEM water electrolyser for hydrogen production," *Int. J. Hydrogen Energy*, vol. 34, no. 3, pp. 1143–1158, 2009, doi: 10.1016/j.ijhydene.2008.11.083.

[45] S. Shiva Kumar and V. Himabindu, "Hydrogen production by PEM water electrolysis – A review," *Mater. Sci. Energy Technol.*, vol. 2, no. 3, pp. 442–454, 2019, doi: 10.1016/j.mset.2019.03.002.

[46] D. Saebea, Y. Patcharavorachot, V. Hacker, S. Assabumrungrat, A. Arpornwichanop, and S. Authayanun, "Analysis of unbalanced pressure PEM electrolyzer for high pressure hydrogen production," *Chem. Eng. Trans.*, vol. 57, pp. 1615–1620, 2017, doi: 10.3303/CET1757270.

[47] S. Toghyani, S. Fakhradini, E. Afshari, E. Baniasadi, M. Y. Abdollahzadeh Jamalabadi, and M. Safdari Shadloo, "Optimization of operating parameters of a polymer exchange membrane electrolyzer," *Int. J. Hydrogen Energy*, vol. 44, no. 13, pp. 6403–6414, 2019, doi: 10.1016/j.ijhydene.2019.01.186.

[48] V. Liso, G. Savoia, S. S. Araya, G. Cinti, and S. K. Kær, "Modelling and experimental analysis of a polymer electrolyte membrane water electrolysis cell at different operating temperatures," *Energies*, vol. 11, no. 12, 2018, doi: 10.3390/en11123273.

[49] A. S. Tijani, N. A. Binti Kamarudin, and F. A. Binti Mazlan, "Investigation of the effect of charge transfer coefficient (CTC) on the operating voltage of polymer electrolyte membrane (PEM) electrolyzer," *Int. J. Hydrogen Energy*, vol. 43, no. 19, pp. 9119–9132, 2018, doi: 10.1016/j.ijhydene.2018.03.111.

[50] E. W. Saeed and E. G. Warkozek, "Modeling and Analysis of Renewable PEM Fuel Cell System," *Energy Procedia*, vol. 74, pp. 87–101, 2015, doi: 10.1016/j.egypro.2015.07.527.

[51] R. Hancke, T. Holm, and Ø. Ulleberg, "The case for high-pressure PEM water electrolysis," *Energy Convers. Manag.*, vol. 261, no. December 2021, 2022, doi: 10.1016/j.enconman.2022.115642.

[52] C. Y. Biaku, N. V. Dale, M. D. Mann, H. Salehfar, A. J. Peters, and T. Han, "A semiempirical study of the temperature dependence of the anode charge transfer coefficient of a 6 kW PEM electrolyzer," *Int. J. Hydrogen Energy*, vol. 33, no. 16, pp. 4247–4254, 2008, doi: 10.1016/j.ijhydene.2008.06.006.

[53] F. M. Sapountzi, J. M. Gracia, C. J. K. Weststrate, H. O. A. Fredriksson, and J. W. H. Niemantsverdriet, "Electrocatalysts for the generation of hydrogen , oxygen

and synthesis gas," *Prog. Energy Combust. Sci.*, vol. 58, pp. 1–35, 2017, doi: 10.1016/j.pecs.2016.09.001.

[54] O. Schmidt, A. Gambhir, I. Staffell, A. Hawkes, J. Nelson, and S. Few, "Future cost and performance of water electrolysis: An expert elicitation study," *Int. J. Hydrogen Energy*, vol. 42, no. 52, pp. 30470–30492, 2017, doi: 10.1016/j.ijhydene.2017.10.045.

[55] A. Mayyas *et al.*, "Manufacturing Cost Analysis for Proton Exchange Membrane Water Electrolyzers," *Natl. Renew. Energy Lab.*, no. August, p. 65, 2019, [Online]. Available: https://www.nrel.gov/docs/fy10osti/72740.pdf.%0Ahttps://www.nrel.gov/docs/fy10osti/72740.pdf.

[56] L. Allidières, A. Brisse, P. Millet, S. Valentin, and M. Zeller, "On the ability of pem water electrolysers to provide power grid services," *Int. J. Hydrogen Energy*, vol. 44, no. 20, pp. 9690–9700, 2019, doi: 10.1016/j.ijhydene.2018.11.186.

[57] J. J. C. Mancera, F. S. Manzano, J. M. Andújar, F. J. Vivas, and A. J. Calderón, "An optimized balance of plant for a medium-size PEM electrolyzer. Design, control and physical implementation," *Electron.*, vol. 9, no. 5, 2020, doi: 10.3390/electronics9050871.

[58] B. Yodwong, D. Guilbert, M. Phattanasak, W. Kaewmanee, M. Hinaje, and G. Vitale, "Faraday's efficiency modeling of a proton exchange membrane electrolyzer based on experimental data," *Energies*, vol. 13, no. 18, pp. 1–14, 2020, doi: 10.3390/en13184792.

[59] M. Mohanpurkar *et al.*, "Electrolyzers enhancing flexibility in electric grids," *Energies*, vol. 10, no. 11, p. 1DUMMU, 2017, doi: 10.3390/en10111836.

[60] Q. Cacciuttolo, J. Vulliet, V. Lair, M. Cassir, and A. Ringuedé, "Effect of pressure on high temperature steam electrolysis: Model and experimental tests," *Int. J. Hydrogen Energy*, vol. 40, no. 35, pp. 11378–11384, 2015, doi: 10.1016/j.ijhydene.2015.04.034.

[61] A. H. A. Rahim, A. S. Tijani, F. H. Shukri, S. Hanapi, and K. I. Sainan, "Mathematical modelling and simulation analysis of PEM electrolyzer system for hydrogen production," *IET Semin. Dig.*, vol. 2014, no. CP659, 2014, doi: 10.1049/cp.2014.1466.

[62] N. Briguglio *et al.*, "Design and testing of a compact PEM electrolyzer system," *Int. J. Hydrogen Energy*, vol. 38, no. 26, pp. 11519–11529, 2013, doi: 10.1016/j.ijhydene.2013.04.091.

[63] "H2B2 EL20N," 2003. https://www.h2b2.es/wp-content/uploads/2022/01/211125_H2B2-EL20N-Datasheet.pdf.

[64] EU Science Hub, "PVgis tool." https://re.jrc.ec.europa.eu/pvg_tools/en/.

[65] T. Muneer, “Solar radiation model for Europe,” *Build. Serv. Eng. Res. Technol.*, vol. 11, no. 4, pp. 153–163, 1990, doi: 10.1177/014362449001100405.

[66] N. Martin and J. M. Ruiz, “Calculation of the PV modules angular losses under field conditions by means of an analytical model,” *Sol. Energy Mater. Sol. Cells*, vol. 110, p. 154, 2001, doi: 10.1016/j.solmat.2012.11.002.

[67] N. Martin and J. M. Ruiz, “Corrigendum to ‘Calculation of the PV modules angular losses under field conditions by means of an analytical model’ [Sol. Energy Mater. Sol. Cells 70 (1) (2001) 25–38] (S0927024800004086) (10.1016/S0927-0248(00)00408-6)),” *Sol. Energy Mater. Sol. Cells*, vol. 110, no. March 2013, p. 154, 2013, doi: 10.1016/j.solmat.2012.11.002.

[68] T. Huld *et al.*, “A power-rating model for crystalline silicon PV modules,” *Sol. Energy Mater. Sol. Cells*, vol. 95, no. 12, pp. 3359–3369, 2011, doi: 10.1016/j.solmat.2011.07.026.

[69] D. Faiman, “Assessing the Outdoor Operating Temperature of Photovoltaic Modules,” *Prog. Photovoltaics Res. Appl.*, vol. 16, no. 1, pp. 307–315, 2008, doi: 10.1002/pip.

[70] M. Koehl, M. Heck, S. Wiesmeier, and J. Wirth, “Modeling of the nominal operating cell temperature based on outdoor weathering,” *Sol. Energy Mater. Sol. Cells*, vol. 95, no. 7, pp. 1638–1646, 2011, doi: 10.1016/j.solmat.2011.01.020.

[71] D. C. Jordan and S. R. Kurtz, “Photovoltaic Degradation Rates—an Analytical Review,” *Prog. Photovoltaics Res. Appl.*, vol. 21, no. 1, pp. 12–29, 2011, doi: 10.1002/pip.

[72] A. Mohammadi and M. Mehrpooya, “A comprehensive review on coupling different types of electrolyzer to renewable energy sources,” *Energy*, vol. 158, pp. 632–655, 2018, doi: 10.1016/j.energy.2018.06.073.

[73] F. Gutiérrez-Martín, L. Amodio, and M. Pagano, “Hydrogen production by water electrolysis and off-grid solar PV,” *Int. J. Hydrogen Energy*, vol. 46, no. 57, pp. 29038–29048, 2021, doi: 10.1016/j.ijhydene.2020.09.098.

[74] “Aleo Solar Module P23.” https://www.aleo-solar.com/app/uploads/sites/6/2016/02/P23_320-325W_EN_web.pdf.

[75] T. Feehally, A. J. Forsyth, R. Todd, S. Liu, and N. K. Noyanbayev, “Efficiency Analysis of a High Power Grid-connected Battery Energy Storage System,” *IET Int. Conf. Power Electron. Mach. Drives*, pp. 1–6, 2018.

[76] I. Renewable, “Lithium-ion Battery Test Centre.” https://batterytestcentre.com.au/project/lithium-ion/.

[77] M. Steilen and L. Jörissen, “Hydrogen Conversion into Electricity and Thermal Energy by Fuel Cells: Use of H2-Systems and Batteries,” *Electrochem. Energy*

Storage Renew. Sources Grid Balanc., pp. 143–158, 2015, doi: 10.1016/B978-0-444-62616-5.00010-3.

[78] Y. Liu, Y. G. Liao, and M. C. Lai, "Effects of Depth-of-Discharge, Ambient Temperature, and Aging on the Internal Resistance of Lithium-Ion Battery Cell," *Int. Conf. Electr. Comput. Energy Technol. ICECET 2021*, no. December, pp. 9–10, 2021, doi: 10.1109/ICECET52533.2021.9698495.

[79] DOE, "Energy Storage Technology and Cost Characterization Report 2019," *Report*, no. July, pp. 1–120, 2019, [Online]. Available: https://www.energy.gov/eere/water/downloads/energy-storage-technology-and-cost-characterization-report.

[80] B. Raho, G. Colangelo, M. Milanese, and A. De Risi, "A Critical Analysis of the Oxy-Combustion Process : From Mathematical Models to Combustion Product Analysis," 2022.

[81] N. E. T. L. (NETL), "Cost of Capturing CO2 from Industrial Sources," 2014. [Online]. Available: https://www.netl.doe.gov/projects/files/CostofCapturingCO2fromIndustrialSources_011014.pdf.

[82] S. P. Peletiri, N. Rahmanian, and I. M. Mujtaba, "CO2 Pipeline design: A review," *Energies*, vol. 11, no. 9, 2018, doi: 10.3390/en11092184.

[83] G. Di Marcoberardino, D. Vitali, F. Spinelli, M. Binotti, and G. Manzolini, "Green hydrogen production from raw biogas: A techno-economic investigation of conventional processes using pressure swing adsorption unit," *Processes*, vol. 6, no. 3, 2018, doi: 10.3390/pr6030019.

[84] J. Hinkley *et al.*, "Cost Assessment of Hydrogen Production from PV and Electrolysis," *CSIRO Energy*, no. March, pp. 1–35, 2016, [Online]. Available: http://arena.gov.au/files/2016/05/Assessment-of-the-cost-of-hydrogen-from-PV.pdf.

[85] F. Gallardo, J. García, A. Monforti Ferrario, G. Comodi, and J. N. Chiu, "Assessing sizing optimality of OFF-GRID AC-linked solar PV-PEM systems for hydrogen production," *Int. J. Hydrogen Energy*, vol. 47, no. 64, pp. 27303–27325, 2022, doi: 10.1016/j.ijhydene.2022.06.098.

[86] F. I. Gallardo, A. Monforti Ferrario, M. Lamagna, E. Bocci, D. Astiaso Garcia, and T. E. Baeza-Jeria, "A Techno-Economic Analysis of solar hydrogen production by electrolysis in the north of Chile and the case of exportation from Atacama Desert to Japan," *Int. J. Hydrogen Energy*, vol. 46, no. 26, pp. 13709–13728, 2021, doi: 10.1016/j.ijhydene.2020.07.050.

[87] IRENA, *Renewable Power Generation Costs in 2020*. 2020.

[88] E. Vartiainen, G. Masson, C. Breyer, D. Moser, and E. Román Medina, "Impact

of weighted average cost of capital, capital expenditure, and other parameters on future utility-scale PV levelised cost of electricity," *Prog. Photovoltaics Res. Appl.*, vol. 28, no. 6, pp. 439–453, 2020, doi: 10.1002/pip.3189.

[89] S. Giuliano, M. Puppe, and K. Noureldin, "Power-to-heat in CSP systems for capacity expansion," *AIP Conf. Proc.*, vol. 2126, no. July, 2019, doi: 10.1063/1.5117589.

[90] A. Patonia and R. Poudineh, *Cost-competitive green hydrogen: how to lower the cost of electrolysers?*, no. January. 2022.

[91] M. Ruth, A. Mayyas, and M. Mann, "Manufacturing Competitiveness Analysis for PEM and Alkaline Water Electrolysis Systems," *Fuel Cell Semin. Energy Expo.*, pp. 5–11, 2017, [Online]. Available: https://www.osti.gov/servlets/purl/1550788.

[92] A. Christensen, "Assessment of Hydrogen Production Costs from Electrolysis: United States and Europe," *Int. Counc. Clean Transp.*, pp. 1–73, 2020, [Online]. Available: https://theicct.org/sites/default/files/publications/final_icct2020_assessment_of_hydrogen_production_costs v2.pdf.

[93] L. Mauler, F. Duffner, W. G. Zeier, and J. Leker, "Battery cost forecasting: A review of methods and results with an outlook to 2050," *Energy Environ. Sci.*, vol. 14, no. 9, pp. 4712–4739, 2021, doi: 10.1039/d1ee01530c.

[94] T. Mayer, M. Semmel, M. A. Guerrero Morales, K. M. Schmidt, A. Bauer, and J. Wind, "Techno-economic evaluation of hydrogen refueling stations with liquid or gaseous stored hydrogen," *Int. J. Hydrogen Energy*, vol. 44, no. 47, pp. 25809–25833, 2019, doi: 10.1016/j.ijhydene.2019.08.051.

[95] "EU project MACBETH." https://www.macbeth-project.eu/.

[96] IEA, "Putting CO 2 to Use," no. September, 2019, [Online]. Available: https://www.iea.org/reports/putting-co2-to-use.

[97] A. Tremel, P. Wasserscheid, M. Baldauf, and T. Hammer, "ScienceDirect Techno-economic analysis for the synthesis of liquid and gaseous fuels based on hydrogen production via electrolysis," *Int. J. Hydrogen Energy*, vol. 40, no. 35, pp. 11457–11464, 2015, doi: 10.1016/j.ijhydene.2015.01.097.

[98] S. Alsayegh, J. R. Johnson, B. Ohs, and M. Wessling, "Methanol production via direct carbon dioxide hydrogenation using hydrogen from photocatalytic water splitting : Process development and techno-economic analysis," *J. Clean. Prod.*, vol. 208, pp. 1446–1458, 2019, doi: 10.1016/j.jclepro.2018.10.132.

[99] A. H. Reksten, M. S. Thomassen, S. Møller-Holst, and K. Sundseth, "Projecting the future cost of PEM and alkaline water electrolysers; a CAPEX model including electrolyser plant size and technology development," *Int. J. Hydrogen Energy*, vol. 47, no. 90, pp. 38106–38113, 2022, doi: 10.1016/j.ijhydene.2022.08.306.

[100] Solargis, “Global Solar Atlas 2.0 - Solar resource maps of Italy,” 2020. ttps://solargis.com/maps-and-gis-data/download/italy.

[101] IRENA, *Renewable Power Generation Costs in 2021*. 2022.

A Appendix A

A.1. Oxygen-air comparison

In this section the values obtained as output for oxygen-case and air-case in their respective best performance configurations (i.e. with 122 and 147 membranes respectively) have been reported. The economic values have been obtained through the procedure explained in chapter *6.6 ATR cost*.

PARAMETERS	UNITS	O2 CASE
SCR	-	3.03
H2SEP	kmol/h	2.07
QDUTY	kW	-0.01
CH4CONV	-	0.93
HRF	-	0.71
HRFSTAR	-	0.87
SEPFACT	-	0.97
H2PROD	kmol/h	2.13
SOLIDS	kg	64.47
UMIN	m/s	1.55
UMAX	m/s	2.31
DILFAC	-	2
DIAMREAC	m	0.43
MEMSAREA	m2	2.41
CATALYST	kg	32.24
FBG	kmol/h	1.25
FSTEAM		1.40
FO2		0.25
FRET		1.90
QEVAP	kW	14.72
QECO2		1.42
QFEEDHX		2.98
QSH		3.90
QECO1		3.94
QPREO2		0.22
QSH1		3.80
QCO2COOL		15.00
WBGCMP		4.01
QBGCMP		-1.42

PARAMETERS	UNITS	AIR CASE
SCR	-	2.99
H2SEP	kmol/h	2.07
QDUTY	kW	0.00
CH4CONV	-	91.01%
HRF	-	68.29%
HRFSTAR	-	0.84
SEPFACT	-	0.96
H2PROD	kmol/h	2.16
SOLIDS	kg	79.82
UMIN	m/s	1.59
UMAX	m/s	2.10
DILFAC	-	2
DIAMREAC	m	0.47
MEMSAREA	m2	2.91
CATALYST	kg	39.91
FBG	kmol/h	1.30
FSTEAM		1.40
FAIR		1.27
FRET		3.01
QPREHX	kW	0.00
QECO		-5.39
QECO2		-0.07
QEVA		-14.74
QSH		-7.72
QPER		2.36
QRET		19.15
WBGCMP		4.25
QBGCMP		-1.30

WCO2CMP		7.20
QCO2CMP		-10.37
WVACUUM		8.18
QVACUUM		-6.45
WWATPMP		0.01
WH2CMP		8.42
QH2CMP		-6.08
TFEED	°C	473.58
TSTEAM		700
TFLUEGAS		1149.8
WATREC	kmol/h	0.82
UAEVAP	kW/K	0.029
UAECO2		0.009
UAFEEDHX		0.015
UASH		0.008
UAECO1		0.060
UAPREO2		0.001
UASH1		0.056
UACO2COOL		0.31
LMTD EVAP	°C	515.54
LMTD ECO2		163.09
LMTD FEEDHX		196.64
LMTD SH		506.48
LMTD ECO1		65.73
LMTD PREO2		180.49
LMTD SH1		67.89
LMTD CO2COOL		48.39
NBG	kmol/h	1.25
NO2		0.25
NO2B		0.15
NWATER		1.40
MBG	kg/s	0.00907
MH2		0.00116
WATSPLIT		/
MCO2	kg/h	51.8371
Auxiliaries	MW	0.023
Efficiency	%	**65.42%**

WAIRCMP		4.13
QAIRCMP		-2.18
WVACUUM		8.18
QVACUUM		-6.45
WWATPMP		0.01
WH2CMP		8.42
QH2CMP		-6.08
TFEED	°C	437.33
TSTEAM		700
TFLUEGAS		809.00
WATREC	kmol/h	0.625
UAPREBAM	kW/K	0.039
UAAIRB		0.000
UAECO		0.023
UAECO2		0.000
UAEVA		0.048
UASH		0.032
UACOOLH2		0.035
UACOLRET		0.368
MITABAMX	°C	71.97
MITAAIRB		275.11
MITAECO		165.88
MITAECO2		641.75
MITAEVA		191.61
MITASH		109.00
MITAQPER		20.00
MITAQRET		20
NBG	kmol/h	1.30
NAIR		1.27
NAIRB		1.88
NWATER		1.40
MBG	kg/s	0.009478
MH2		0.001157
WATSPLIT	-	1
MCO2	kg/h	/
Auxiliaries	MW	0.02784
Efficiency	%	**60.25%**

Table A.1 - Technical results of oxygen-air comparison in each best case.

PARAMETERS	UNITS	O2 CASE
INTERNAL VOLUME	m3	0.1473
THICKNESS	m	0.0152
MATERIAL	m3	0.0464
MATERIAL	kg	371.47

PARAMETERS	AIR CASE
INTERNAL VOLUME	0.1747
THICKNESS	0.0166
MATERIAL	0.0560
MATERIAL	448.23

REACTOR COST	k€	9.10
AREA EVAP	m2	0.4078
AREA ECO2	m2	0.1244
AREA FEEDHX	m2	0.2526
AREA SH	m2	0.1283
AREA ECO1	m2	0.8564
AREA PREO2	m2	0.0201
AREA SH1	m2	0.9340
AREA CO2COOL	m2	5.1661
COST HX	k€	16.77
COST Air Cooler (CO2 HX)	k€	6.14
BG CMP	(k€)	3.35
CO2 CMP	(k€)	5.41
WATER PMP	(k€)	0.51
WATER DEMIN	(k€)	0.51
VACUUM PMP	(k€)	13.85
H2 CMP	(k€)	4.66
BURNER	(k€)	5.35
MEMBRANES	(k€)	13.28
TIC	(k€)	73.52
TPC	(k€)	159.04
V_CAT	(m3/y)	0.0031
V_FILLER	(m3/y)	0.0031
CAT & FILLER	(k€/y)	1.81
N_BG	(Nmc/y)	209360.20
COSTO BG	(k€/y)	56.78
DEIONISATION	(k€/y)	0.45
ELECTRICITY	(k€/y)	20.64
MEMBRANES	(k€/y)	2.66
O&M VAR	(k€/y)	82.33
O&M FIXED	(k€/y)	37.16
TOTAL COST	(€/y)	144933.31
M_H2	(kg/y)	31249.21
COP	(€/kg)	4.64

REACTOR COST	10.98
AREA BAMX	0.6563
AREA PAIR	0.0001
AREA ECO	0.3293
AREA ECO2	0.0013
AREA EVA	0.6810
AREA SH	0.5265
AREA QPERM	0.5800
AREA QRET	6.1340
COST HX (no air)	14.77
COST Air C	7.75
BG CMP	3.51
AIR CMP	0.13
WATER PMP	0.51
WATER DEMIN	0.62
VACUUM PMP	13.85
H2 CMP	4.66
BURNER	5.35
MEMBRANES	16.00
TIC	78.13
TPC	169.01
V_CAT	0.00380
V_FILLER	0.00380
CAT & FILLER	2.24
N_BG	218793.51
COSTO BG	59.34
DEIONISATION	0.45
ELECTRICITY	25.06
MEMBRANES	3.20
O&M VAR	90.29
O&M FIXED	37.61
TOTAL COST	154936.09
M_H2	31242.65
COP	4.96

Table A.2 - Economic results of oxygen-air comparison in each best case.

B Appendix B

In this section, the flow-chart in order to provide the input power to PEM electrolyzer as function of energy available in off-grid configuration is displayed. Once the power is known through the logic scheme in Figure 4.15 it is easy to identify H_2 and O_2 production.

B.1. Flow-chart

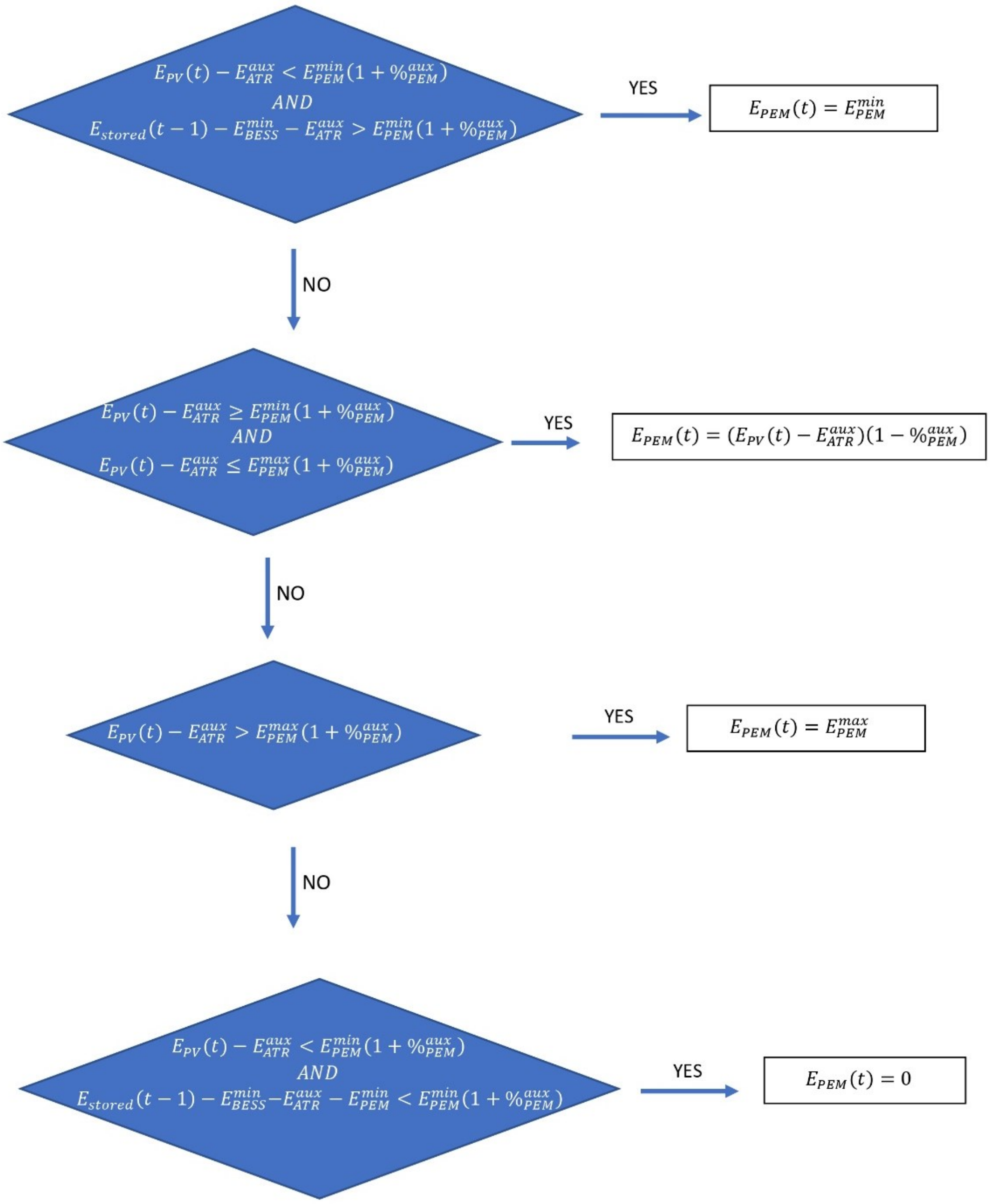
$E_{PV}(t) - E_{ATR}^{aux} < E_{PEM}^{min}(1 + \%_{PEM}^{aux})$
AND
$E_{stored}(t-1) - E_{BESS}^{min} - E_{ATR}^{aux} > E_{PEM}^{min}(1 + \%_{PEM}^{aux})$
YES
$E_{PEM}(t) = E_{PEM}^{min}$
NO
$E_{PV}(t) - E_{ATR}^{aux} \geq E_{PEM}^{min}(1 + \%_{PEM}^{aux})$
AND
$E_{PV}(t) - E_{ATR}^{aux} \leq E_{PEM}^{max}(1 + \%_{PEM}^{aux})$
YES
$E_{PEM}(t) = (E_{PV}(t) - E_{ATR}^{aux})(1 - \%_{PEM}^{aux})$
NO
$E_{PV}(t) - E_{ATR}^{aux} > E_{PEM}^{max}(1 + \%_{PEM}^{aux})$
YES
$E_{PEM}(t) = E_{PEM}^{max}$
NO
$E_{PV}(t) - E_{ATR}^{aux} < E_{PEM}^{min}(1 + \%_{PEM}^{aux})$
AND
$E_{stored}(t-1) - E_{BESS}^{min} - E_{ATR}^{aux} - E_{PEM}^{min} < E_{PEM}^{min}(1 + \%_{PEM}^{aux})$
YES
$E_{PEM}(t) = 0$

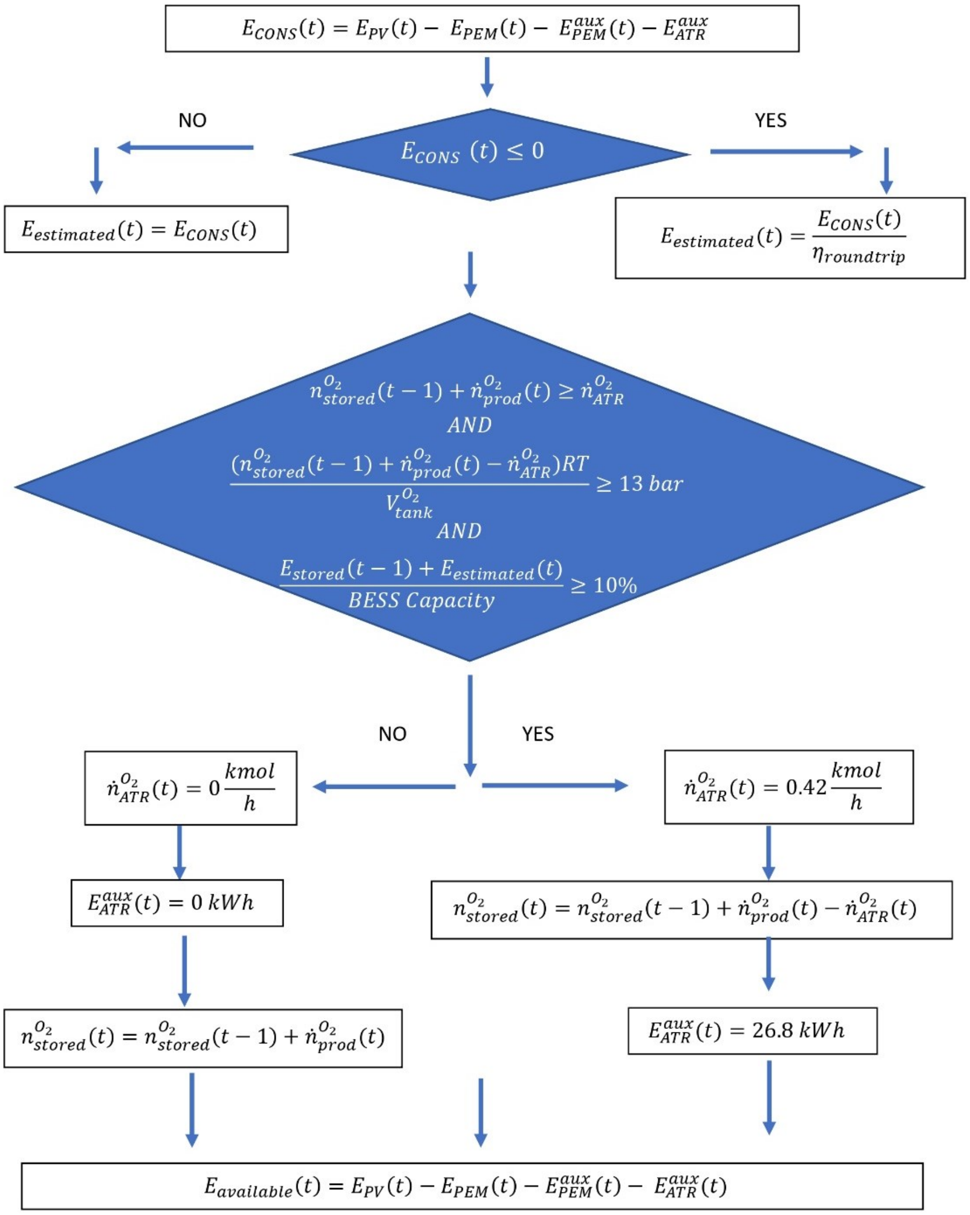
$E_{CONS}(t) = E_{PV}(t) - E_{PEM}(t) - E_{PEM}^{aux}(t) - E_{ATR}^{aux}$
NO
YES
$E_{CONS}\ (t) \leq 0$
$E_{estimated}(t) = E_{CONS}(t)$
$E_{estimated}(t) = \frac{E_{CONS}(t)}{\eta_{roundtrip}}$
$n_{stored}^{O_2}(t-1) + \dot{n}_{prod}^{O_2}(t) \geq \dot{n}_{ATR}^{O_2}$
AND
$\frac{(n_{stored}^{O_2}(t-1) + \dot{n}_{prod}^{O_2}(t) - \dot{n}_{ATR}^{O_2})RT}{V_{tank}^{O_2}} \geq 13\ bar$
AND
$\frac{E_{stored}(t-1) + E_{estimated}(t)}{BESS\ Capacity} \geq 10\%$
NO
YES
$\dot{n}_{ATR}^{O_2}(t) = 0\frac{kmol}{h}$
$\dot{n}_{ATR}^{O_2}(t) = 0.42\frac{kmol}{h}$
$E_{ATR}^{aux}(t) = 0\ kWh$
$n_{stored}^{O_2}(t) = n_{stored}^{O_2}(t-1) + \dot{n}_{prod}^{O_2}(t) - \dot{n}_{ATR}^{O_2}(t)$
$n_{stored}^{O_2}(t) = n_{stored}^{O_2}(t-1) + \dot{n}_{prod}^{O_2}(t)$
$E_{ATR}^{aux}(t) = 26.8\ kWh$
$E_{available}(t) = E_{PV}(t) - E_{PEM}(t) - E_{PEM}^{aux}(t) - E_{ATR}^{aux}(t)$

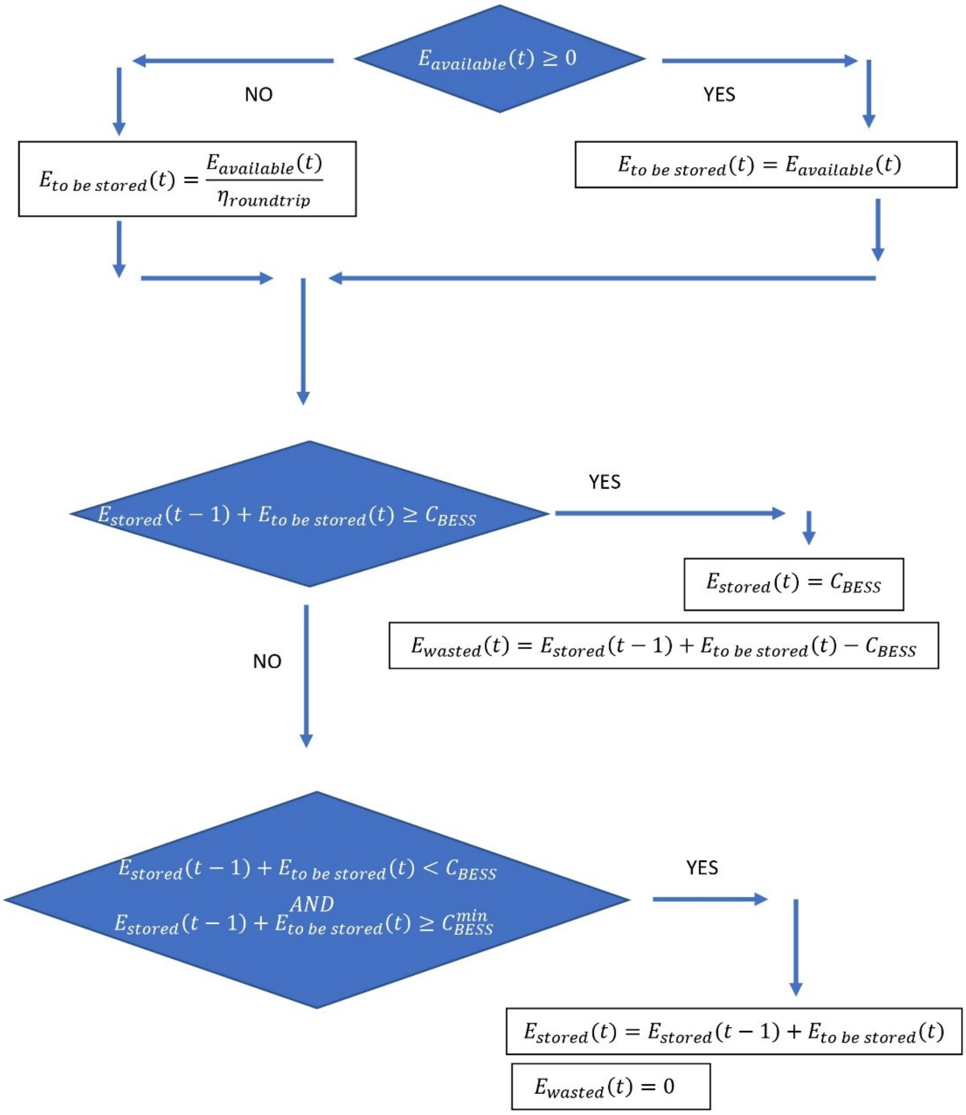
$E_{available}(t) \geq 0$
NO
YES
$E_{to\ be\ stored}(t) = \frac{E_{available}(t)}{\eta_{roundtrip}}$
$E_{to\ be\ stored}(t) = E_{available}(t)$
$E_{stored}(t-1) + E_{to\ be\ stored}(t) \geq C_{BESS}$
YES
$E_{stored}(t) = C_{BESS}$
$E_{wasted}(t) = E_{stored}(t-1) + E_{to\ be\ stored}(t) - C_{BESS}$
NO
$E_{stored}(t-1) + E_{to\ be\ stored}(t) < C_{BESS}$
AND
$E_{stored}(t-1) + E_{to\ be\ stored}(t) \geq C_{BESS}^{min}$
YES
$E_{stored}(t) = E_{stored}(t-1) + E_{to\ be\ stored}(t)$
$E_{wasted}(t) = 0$

Figure B.1 - Flow-chart for off-grid configuration.

List of Figures

Figure 1.1 - Hydrogen demand by sector (2000-2020) [4]. 3

Figure 1.2 - Energy demand prevision according to NZE scenario (adapted from “Global Hydrogen Review”, 2021 [4]). 3

Figure 1.3 – LCOH by technology in 2020, and in the NZE scenario, 2030 and 2050 [4]. 5

Figure 1.4 - Anaerobic digestion process [6]. 7

Figure 1.5 - Hydrogen production through SR (“Membrane Reactor for Hydrogen Production”, 2017 [10]). 9

Figure 1.6 - Comparison of traditional reforming process and membrane reactor-assisted process, taken from [12]. 10

Figure 1.7 - Packed bed MR (“Membrane Reactor for Hydrogen Production”, 2017 [10]). 13

Figure 1.8 - Fluidized bed MR scheme [18]. 14

Figure 1.9 - Alkaline water electrolysis cell [23]. 17

Figure 1.10 – Proton Exchange Membrane (PEM) water electrolysis cell [23]. 18

Figure 1.11 – Thermodynamic parameters change with temperature [20]. 19

Figure 1.12 - Solid Oxide water electrolysis cell [23]. 20

Figure 1.13 - Anion Exchange Membrane water electrolysis cell [24]. 21

Figure 1.14 – Solar cell p-n junction [26]. 22

Figure 1.15 - Mono-crystalline and poly-crystalline cell [28]. 24

Figure 1.16 - Comparison of a conventional cell (a) and a PERC cell (b) [28]. 24

Figure 2.1 - ATR plant in air configuration, taken from MACBETH Project. 33

Figure 2.2 - ATR plant in oxygen configuration. 36

Figure 2.3 - Sketch of on-grid complete configuration. 39

Figure 2.4 - Sketch of off-grid configuration. 40

Figure 3.1 – FBMR layout with modeled region contoured in red, with catalyst (black dots) and membranes (in white) clearly represented. Layout adapted taken from [30]. 45

Figure 4.1 - Example of polarization curve at 80°C and 1 bar [43]. 50

Figure 4.2 – Left: $E0$ at standard pressure as function of cell temperature. Right: effect of varying pressure (at cathode only, at anode only, both) at standard temperature. 51

Figure 4.3 - Contribution in terms of overvoltage of activation losses. 53

Figure 4.4 - Ohmic losses at different temperature. 54

Figure 4.5 - Diffusion overpotential contribution. 55

Figure 4.6 - Polarization curve and contribution of the different losses at 60 °C and 1 atm 55

Figure 4.7 - Losses contributions at 60 °C, 1 atm and at different current density 56

Figure 4.8 – Left: effect of temperature at 1 atm on the modeled polarization curve. Right: effect of temperature at 1 atm in [42]. 57

Figure 4.9 – Left: cathode pressure effect on the modeled polarization curve at 80°C and anode at 1 atm. Right: cathode pressure effect at 80°C and anode at 1 atm in [42]. 58

Figure 4.10 – Left: anode ECD effect on the modeled polarization curve at 80 °C, anode at 1 atm, cathode at 13.6 atm. Right: anode ECD effect on polarization curve at 80 °C, anode at 1 atm, cathode at 13.6 atm in [42]. 59

Figure 4.11 - Left: cathode ECD on the modeled polarization curve at 80 °C, anode at 1 atm, cathode at 13.6 atm. Right: cathode ECD on polarization curve at 80 °C, anode at 1 atm, cathode at 13.6 atm in [42]. 59

Figure 4.12 – Left: temperature effect on HHV stack efficiency of the modeled PEM electrolyzer (1 atm, 200 cells, 300 cm^2). Right: temperature on HHV stack efficiency from [59]. 61

Figure 4.13 - Effect of pressure on stack efficiency based on LHV from the modeled PEM electrolyzer (60 °C, 500 cells, 100 cm^2). 62

Figure 4.14 – Left: effect of varying cell number on LHV stack efficiency of the modeled PEM electrolyzer (1 atm, 60°C, 100 cm^2). Right: Effect of varying cell area on stack efficiency based on HHV of the modeled PEM electrolyzer (atmospheric pressure, 60°C, 500 cells). 63

Figure 4.15 - Logic scheme of H_2, O_2 production from PEM input power. 63

Figure 4.16 - Cell Voltage - PEM Power relation (200 cm^2, 250 cells, atmospheric pressure, 60°C) 64

Figure 4.17 – Current Density - Cell Voltage relation (200 cm^2, 250 cells, atmospheric pressure, 60°C) 65

Figure 4.18 – H_2 production - Power relation (200 cm^2, 250 cells, atmospheric pressure, 60°C) 66

Figure 4.19 - PEM Electrolyzer system [20]. 67

Figure 4.20 – Left: system efficiency as function of PEM load (1 atm, 300 cm^2, 500 cells, 60°C). Right: System efficiency as function of current density (1 atm, 300 cm^2, 500 cells, 60°C). 68

Figure 5.1 - Land use for PV module. 72

Figure 5.2 - Flue gas track after air cooler: flash separator, compressor and CO_2 injection. 75

Figure 7.1 - Membranes distance at different membranes number for O_2-case. 89

Figure 7.2 - Trend of methane conversion and HRF for air and oxygen configuration. 90

Figure 7.3 - Feed and flue gas temperature in both configurations. 91

Figure 7.4 - Biogas and steam flows comparison in the two configurations. 92

Figure 7.5 - Efficiency and HRF comparison. 94

Figure 7.6 - CAPEX contribution at difference membranes number for air-case. 97

Figure 7.7 - CAPEX contributions value at difference membranes number for oxygen-case. 98

Figure 7.8 - Variable OPEX contributions for air-case varying membranes number. 98

Figure 7.9 - Variable OPEX contributions for O_2 - case. 99

Figure 7.10 - Comparison between CAPEX, variable and fix OPEX for air-case. 100

Figure 7.11 - Comparison between CAPEX, variable and fix OPEX for oxygen-case. 100

Figure 7.12 – Configuration set-up with PEM introduction. 102

Figure 7.13 - Polarization curve at 60°C and 21 bar. 103

Figure 7.14 - Flow chart of PEM-ATR configuration. 104

Figure 7.15 - Overall plant LCOH without CO_2 selling, with CO_2 selling at ambient condition, with CO_2 injection and selling. 107

Figure 7.16 - Cost share between PEM (blue), ATR (green) and grid exchange for PEM (orange). 109

Figure 7.17 - Effect of CO_2 selling price if CO_2 is injected or sold at ambient condition. 110

Figure 7.18 - Configuration set-up with introduction of PEM and PV. 111

Figure 7.19 - LCOH without CO_2 selling (blue), with CO_2 removal (selling at ambient condition), with CO_2 injection (purple), and adding revenues from electricity selling (orange and green respectively). 114

Figure 7.20 - Costs share between PEM (blue), ATR (green), grid exchange for PEM (orange) and PV field (yellow). 115

Figure 7.21 – LCOH of air-case varying PV field size. 116

Figure 7.22 - Configuration set-up with introduction of PV, BESS and PEM. 118

Figure 7.23 - LCOH of the plant at different BESS size and PV size. 120

Figure 7.24 - LCOHs and Electricity retrieved from the grid as function of BESS capacity. 120

Figure 7.25 - Different Equivalent Annual Costs contributions at different electricity purchasing prices. 122

Figure 7.26 - LCOHs of air-case assisted by PV and PV-PEM-ATR cases at different electricity prices and as function of PV field size. 123

Figure 7.27 - Off-grid configuration set-up. 125

Figure 7.28 - LCOH and plant operative hours as function of PEM power at difference PV field size. 129

Figure 7.29 - Trend of LCOH and ATR operative hours at different PV and BESS size. 130

Figure 7.30 - Trend of LCOH and ATR operative hours at different PV and oxygen tank size. 131

Figure 7.31 - LCOH and income from oxygen selling at different PV field size and tank capacity. 132

Figure 7.32 - Costs share between PEM (orange), ATR (light blue), BESS (grey) and PV field (blue). 133

Figure 7.33 - Costs share between PEM (orange), ATR (light blue), BESS (grey) and PV field (blue), CO_2 removal (green). 137

Figure 7.34 - LCOH and incomes from CO_2 and O_2 at different PEM power. 138

Figure B.1 - Flow-chart for off-grid configuration. 168

List of Tables

Table 1.1 - Half-reactions in different electrolyte type. 15

Table 1.2 - Comparison of the different electrolyzer technologies. 20

Table 2.1 - Operating conditions to compare air and oxygen as feed. 29

Table 2.2 - Biogas composition and characteristic. 29

Table 2.3 - Input parameter to simulate air compression. 31

Table 2.4 - Input parameter to simulate biogas compression. 32

Table 2.5 - Features of hydrogen compressor. 32

Table 2.6 - Constraints imposed in air-case, with Design-Specification tool. 34

Table 2.7 - Features of CO_2 compressor. 35

Table 2.8 - Constraints imposed in oxygen configuration, with Design-Specification tool. 35

Table 2.9 - Summary of the cases analyzed. 40

Table 3.1 - Double-skin membranes parameters used in Richardson equation [30] 44

Table 4.1 - Exchange current density values tested in [42]. 58

Table 4.2 – Parameters of the linear model developed in Yodwong et al. [58]. 60

Table 5.1 - Crystalline Silicon coefficients for PV power estimation. 70

Table 5.2 - PV module dimensions. 71

Table 5.3 - Battery Energy Storage System assumptions adopted. 73

Table 5.4 - Design features of CO_2 compressor. 75

Table 6.1 - Economic features of PV field. 79

Table 6.2 - Economic evaluation and actualization of PV technology. 79

Table 6.3 – Economic features of PEM Electrolyzer. 80

Table 6.4 – Economic evaluation and actualization of PEM technology. 80

Table 6.5 - Economic features of BESS technology. 81

Table 6.6 - Economic evaluation and actualization of BESS technology. 81

Table 6.7 – Economic features of oxygen tank.. 82

Table 6.8 – Economic evaluation and actualization of oxygen tank. 82

Table 6.9 – Installation, indirect, owner’s and contingencies percentage. 82

Table 6.10 – Cost assumptions for Autothermal Reforming Membrane Reactor. .. 84

Table 6.11 - Economic assumptions to compute Fix O&M for ATR plant. 84

Table 6.12 - Economic assumptions to compute variable O&M for ATR plant. 85

Table 6.13 - Cost assumptions for CO_2 Compressor.. 86

Table 7.1 – HRF and CH_4 conversion in best configuration for the different case.. 90

Table 7.2 - Electric and thermal power for both cases in their best configuration.. 93

Table 7.3 - Streams flows and CO_2 compressor power. 93

Table 7.4 - Summary of system efficiencies voices. 94

Table 7.5 - Main streams features for oxygen-case in its most performant set-up.. 95

Table 7.6 - Main streams features for air-case in its most performant set-up.......... 95

Table 7.7 - CAPEX for air and oxygen cases, in each best configuration. 96

Table 7.8 – OPEX for air and oxygen cases, in each best configuration. 99

Table 7.9 - LCOH composition, results and comparison between air and oxygen case. 101

Table 7.10 - Comparison of PEM electrolyzer at the same stack power. 106

Table 7.11 - Technical parameters of the coupling between PEM and ATR. 106

Table 7.12 - CO_2 removal and CO_2 injection economic evaluation......................... 108

Table 7.13 - LCOHs comparison between the introduced configurations. 109

Table 7.14 - Range of CAPEX and OPEX for PEM break-even cost. 110

Table 7.15 - Techno-economic indexes of PV field.. 112

Table 7.16 - LCOHs comparison between the introduced configurations. 117

Table 7.17 - LCOHs comparison of the best configurations (CO_2 sold at ambient condition) for the different cases. 121

Table 7.18 - Components size ranges tested. 127

Table 7.19 - Components size of minimum LCOH configuration, where CO_2 is not injected 127

Table 7.20 – Features of optimum configurations of off-grid case with CO2 sold at ambient condition. 128

Table 7.21 - Summary of LCOHs and contributions of revenues for off-grid case without CO_2 injection. 134

Table 7.22 - Comparison of configurations with CO_2 injection. 135

Table 7.23 - Components size of minimum LCOH configuration, where CO_2 is injected. Same as the third configuration in Table 7.22. 136

Table 7.24 - Features of off-grid configuration with CO_2 injection. 136

Table 7.25 - Revenues effect comparison between off-grid cases. 139

Table 7.26 - Summary of LCOHs and contributions of revenues for off-grid case with CO_2 injection. 139

Table 8.1 - HRF and system efficiency comparison for the best configuration of air-case and oxygen-case. 143

Table 8.2 - LCOHs and components size of the best configuration for each case, with CO_2 sold at ambient condition (case A) and CO_2 injected in pipeline (Case B). 149

Table A.1 - Technical results of oxygen-air comparison in each best case. 162

Table A.2 - Economic results of oxygen-air comparison in each best case. 163

List of symbols

Parameter	Description	Unit
$\%_{C\&OC}$	% of owner's and contingencies cost	%
$\%_{IC}$	% of indirect cost	%
$\%_{TIC}$	% of installation cost	%
A	Reactor cross section area	m^2
A_{cell}	PEM Cell Area	cm^2
a	PEM membrane water activity	$[-]$
a_1	Parameter for PEM Faraday efficiency computation	$[-]$
a_2	Parameter for PEM Faraday efficiency computation	$[-]$
b	Parameter for PEM Faraday efficiency computation	$[-]$
C	Molar concentration	$\frac{kmol}{m^3}$
$C_{i,2022}$	Single basic component cost	€
CF	PV Capacity Factor	%
c	Parameter for PEM Faraday efficiency computation	$[-]$
D_r	Reactor diameter	m
$d_{membrane}$	Membranes internal diameter	cm
d	Membranes pitch distance	cm
E	PEM Reversible cell voltage	V

E_0	Reversible voltage at standard pressure for PEM polarization curve	V
E_a	Activation Energy	$\frac{kJ}{mol}$
$E_{from\ grid}$	Electric energy retrieved from the grid	MWh
$E_{to\ grid}$	Electric energy injected into the grid	MWh
E_{PV}	Electric energy produced by PV field	MWh
$E_{welding}$	FBMR welding efficiency	%
F	Faraday constant	$\frac{s \cdot A}{mol}$
F_{H_2}	Total moles of hydrogen permeated at each axial position z	$\frac{kmol}{h \cdot m}$
f	Scale factor	$[-]$
G	Gibbs free energy	$\frac{kJ}{mol}$
G_{sun}	Solar irradiance	$\frac{W}{m^2}$
H_{eq}^{PV}	PV equivalent hours	h/y
H_r	Reactor Height	m
h	Molar enthalpy	$\frac{kJ}{kmol}$
I	PEM overall current	A
$I_{0,c}$	Investment cost	€
$I_{eq,annual,c}$	Equivalent annual investment cost	$\frac{€}{y}$
$I_{replace,act,c}$	Actualized replacement cost	€
$I_{replace,c,t}$	Replacement cost at year t	€

i	Current density of PEM electrolyzer	$\frac{A}{cm^2}$
i_{lim}	PEM Current density limit	$\frac{A}{cm^2}$
i_0	PEM Exchange current density	$\frac{A}{cm^2}$
$J_{H_2}^{Permeating}$	Hydrogen flux through the membrane	$\frac{kmol}{h \cdot m^2}$
K	Equilibrium constant	$[-]$
K_{be}	Exchange coefficient between bubble and emulsion FBMR phases	$\frac{1}{h}$
k_i	PV electricity production coefficient	$[-]$
$\dot{m}$	Mass flow rate	$\frac{kg}{s}$
N	Number	$[-]$
NR	Number of chemical reactions considered	$[-]$
n	Exponent in hydrogen flux expression	$[-]$
n_{el}	Number of electrons transferred in water electrolysis reaction	$[-]$
$\dot{n}$	Molar flow rate	$\frac{kmol}{h}$
P	Power	kW
P_{GRID}	Electric power retrieved from the grid	kW
$P_{H_2}^0$	Pre-exponential factor of membrane permeability	$\frac{mol}{s \cdot m \cdot bar^{0.5}}$
$P_{r,max}$	Maximum pressure to withstand for FBMR reactor	MPa
p	Pressure	bar
p_i	Partial pressure of component i	bar

Q	Exchanged heat power	kW
R	Universal gas constant	$\frac{kJ}{mol \cdot K}$
$r_{R,j}$	Reaction rate of reaction j	$\frac{kmol}{h \cdot kg_{cat}}$
S	Components size	x
S_{stress}	FBMR allowable stress to withstand	MPa
T	Temperature	K
t_r	Reactor thickness	m
t_{SL}	Thickness of membrane selective layer	μm
U_0	coefficient describing the effect of the radiation on the module temperature in the Faiman mode	$\frac{W}{°C \cdot m}$
U_1	coefficient describing the cooling by the wind in the Faiman model	$\frac{W \cdot s}{°C \cdot m^3}$
U_{g-g}	heat transfer coefficient for gas-gas	$\frac{W}{m^2K}$
U_{l-g}	heat transfer coefficient for gas-liquid/bi-phase	$\frac{W}{m^2K}$
UTS	Ultimate Tensile Strength	MPa
u	Velocity	$\frac{m}{s}$
V	Cell voltage	V
$\dot{V}$	Volumetric flow	$\frac{Nm^3}{h}$
W	Wind speed for PV electricity generation computation	m/s
W_{aux}	Auxiliary power consumption	kW
x	Molar fraction	$[-]$

z	Axial coordinate along the reactor	m
z_{el}	mole number of electrons transferred to fulfill the reactions	$[-]$
	Greek Letters	
α	Activity	$[-]$
$\alpha_{a/c}$	Charge transfer coefficient at the anode or at the cathode	$[-]$
β	Compression ratio	$[-]$
δ_m	PEM membrane thickness	m
λ_m	PEM membrane hydration	$[-]$
$\nu_{j,i}$	Stoichiometric coefficient of species i in reaction j	$[-]$
ρ_p	Density	$\frac{kg}{m^3}$
σ_m	PEM membrane conductivity	$\frac{S}{cm}$
σ_y	yield strength	MPa
Δ	Difference	x
ΔV	PEM Overall voltage	V
ε	Void fraction	$[-]$
δ	Fraction of phase (wake or emulsion or bubble)	$[-]$
η	Efficiency	%

Subscripts

R	Parameter value for the reactor
SL	Selective layer of the membrane
a	Parameter in ambient condition

a/an	Parameter related to anode of PEM electrolyzer
act	Parameter related to reaction activation
aux	Parameter related to system auxiliaries
ATR	Parameter related to ATR plant
$reactor$	Parameter related to FBMR
$material$	Parameter related to FBMR material
b	Parameter in bubble phase
BG	Parameter related to biogas in input
CMP	Parameter related to compressors
fix	Parameter related to fix OPEX
c	Parameter related to component c
c/cat	Parameter related to cathode of PEM electrolyzer
$cell$	Parameter related to PEM electrolyzer cell
e	Parameter in emulsion phase
el/PEM	Parameter related to electrolyzer variable
$elec$	Parameter related to electric variable
$feed$	Parameter valid for the feed stream
g	Parameter valid for gaseous phase
i	Parameter valid for chemical component (or species)
in	Parameter at the reactor/system inlet
j	Parameter related to chemical reaction j
l	Parameter valid for liquid phase
m	Parameter related to membrane of MR

mf	In minimum fluidization conditions
mod	Parameter related to PV module
ohm	Parameter related to ohmic loss in PEM
ox	Parameter related to oxidated species
p	Parameter of a single catalyst particle
stc	Parameter in Standard Test Conditions
$perm$	Parameter related to permeation process
$tank$	Parameter related to oxygen tank
var	Parameter related to variable OPEX
$perm$	Parameter related to the permeation process
$O\&M$	Parameter related to O&M
$purch$	Parameter related to electricity purchasing
$permeate$	Parameter related to permeate side
ref	Parameter of reference or in reference condition
$retentate$	Parameter related to retentate side
$replace$	Parameter related to replacement cost
rev	Parameter related to reversible process
eq	Parameter related to equivalent annual cost
act	Actualized Parameter
$stack$	Parameter related to PEM electrolyzer stack
sys	Parameter related to overall system
th	Parameter related to thermoneutral voltage
$trans$	Parameter related to transport loss in PEM

w	Parameter in wake phase

Acronyms

1D	Monodimensional
ACM	Aspen Custom Modeler
AD	Anaerobic Digestion
AEM	Anion Exchange Membrane
APV	Agrophotovoltaic
ATAG	Air Transport Action Group
ATR	Autothermal Reforming
BESS	Battery Energy Storage System
BG	Biogas
BIPV	Building-Integrated photovoltaic solar panel
BSRN	Baseline Surface Radiation Network
BtB	Biowaste-to-Bioenergy
C&OC	Owner's and Contingencies Cost
CAPEX	Capital Expenditure
CCF	Carrying Charge Factor
CCS	Carbon Capture and Storage
CCUS	Carbon Capture Utilization and Storage
CEPCI	Chemical Engineering Plant Cost Index
CHP	Combined Heat and Power

CIGS	Copper-Indium-Gallium-Diselenide
DF	Dilution Factor
DS	Design-Specification
ECO	Economizer
ESTI	European Solar Test Installations
EU	European Union
EVAP	Evaporator
FBMR	Fluidized Bed Membrane Reactor
GHG	Greenhouse gases
HER	Hydrogen Evolution Reaction
HRF	Hydrogen Recovery Factor
HT	High Temperature
IC	Indirect Cost
IEA	International Energy Agency
IRENA	International Renewable Energy Agency
KPI	Key Performance Indicator
LCOE	Levelized Cost Of Electricity
LCOH	Levelized Cost Of Hydrogen
LHV	Lower Heating Value
LT	Low Temperature
MACBETH	Membranes And Catalysts Beyond Economic and Technological Hurdles
MR	Membrane Reactor

MSW	Municipal Solid Waste
NZE	Net Zero Emission
O&M	Operation and Maintenance
OCV	Open Circuit Voltage
OER	Oxygen Evolution Reaction
OPEX	Operational Expenditure
PEM	Proton Exchange Membranes or Polymer Electrolyte Membrane
PERC	Passivated Emitter and Rear Cell
PIS	Process Intensification Strategy
PSA	Pressure Swing Adsorption
PSA	Pressure Swing Adsorption
PV	Photovoltaic
S/C	Steam-Carbon-Ratio
SH	Superheater
SoC	State of Charge
SOEC	Solid Oxide Electrolyzer
SR	Steam Reforming
STEPS	Stated Policies Scenario
TIC	Installations Cost
TPC	Total Plant Cost
UTS	Ultimate Tensile Strength
VFAs	Volatile Fatty Acids

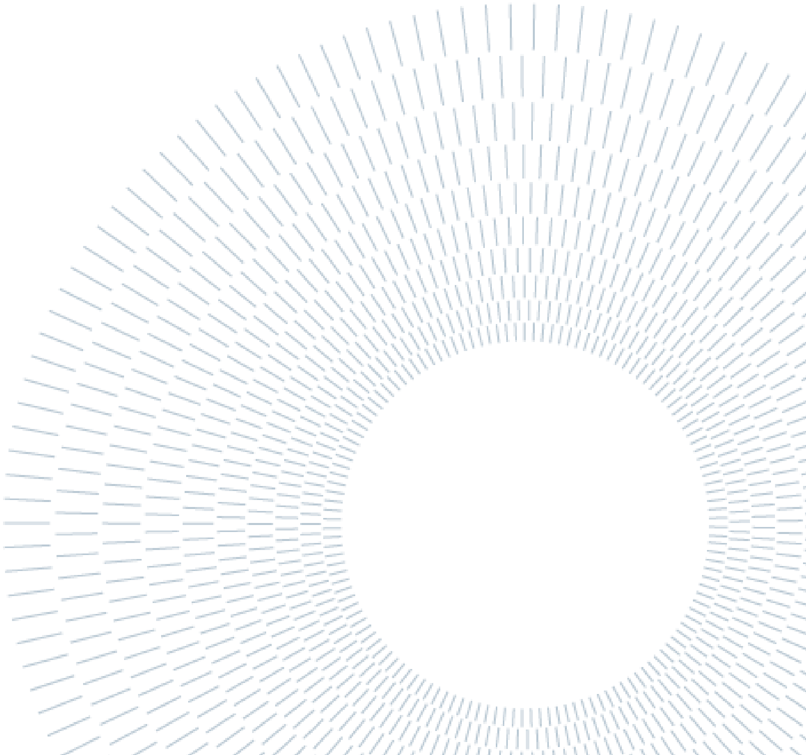WGS	Water Gas Shift